Title

Photoactive Nitric Oxide Delivery Systems based on Metal Nitrosyl-Biomaterial Composites

Author

Heilman, Brandon James

Publication Date

2015

UNIVERSITY OF CALIFORNIA

SANTA CRUZ

Photoactive Nitric Oxide Delivery Systems based on Metal Nitrosyl-Biomaterial Composites

A dissertation submitted in partial satisfaction
of the requirements for the degree of

DOCTOR OF PHILOSOPHY

in

CHEMISTRY AND BIOCHEMISTRY

by

Brandon James Heilman

March 2015

The Dissertation of Brandon J. Heilman
is approved:

Professor Scott R. J. Oliver, Chair

Professor Pradip K. Mascharak, Advisor

Professor Theodore R. Holman

Tyrus Miller
Vice Provost and Dean of Graduate Students

Table of Contents

List of Figures……………………………………………………………………x

List of Tables…………………………………………………………………xvii

Abstract………………………………………………………………………xviii

Acknowledgments……………………………………………………………xxi

Chapter 1. Introduction

1.1 Nitric Oxide in Mammalian Biology……………………………………2

1.1.1 Enzymatic NO production by Nitric Oxide Synthase

1.1.2 NO Production by eNOS and nNOS

1.1.3 NO Production by iNOS

1.1.4 The Direct Effects of NO

1.1.5 The Indirect Effects of NO

1.2 Cytotoxic Effects of Elevated NO……………………………………19

1.2.1 Inhibition of Mitochondrial Function by NO

1.2.2 NO-mediated Targeting of DNA and Induction of Apoptosis

1.3 NO, ROS, and RNS Detoxification……………………………………23

1.3.1 Microbial Stress Responses to NO

1.3.2 NO and Oxidative Stress

1.4 Therapeutic Intervention in NO-mediated Pathways……………………29

1.4.1 NO Donors as Biophysiological Tools in the Indentification of EDRF

1.4.2 Calcium Channel Blockers

1.4.3 ACE-Inhibitors

1.4.4 L-Arginine Supplementation

1.5 Exogenous NO Donors…………………………………………………..34

1.5.1 Organic Nitrite and Nitrate Esters

1.5.2 N-Diazeniumdiolates

1.5.3 S-Nitrosothiols

1.6 Metal Nitrosyls as NO Donors……………………………………………38

1.6.1 Sodium Nitroprusside

1.6.2 Iron-sulfur-nitrosyl Complexes

1.6.3 Photoactive Metal Nitrosyls Derived from Ligands with Carboxamido-*N* Donors

1.6.4 Metal Nitrosyls Derived from the Pentadentate Ligand, $PaPy_3H$

1.6.5 Metal Nitrosyls Derived from the Tetradentate Ligand, bpbH_2

1.7 NO-Delivery Systems……………………………………………………50

1.7.1 NO-releasing Iron-oxide Magnetic Nanoparticles

1.7.2 NO releasing Gold Nanoparticles

1.7.3 NIR Activated Up-Converting Nanocrystals

1.7.4 NO-donating Material Composites with Incorporated Metal Nitrosyl

1.7.5 Site-specific Delivery of Photo-controlled NO

1.8 Thesis Outline………………………………………………………………65

Chapter 2. Synthesis, Characterization, and Light Activated Antibiotic Application of a Composite Material (PUX-NO) Derived from Polyurethane and Silica Xerogel with Embedded manganese Nitrosyl {Mn-NO}

2.1 Background ……………………………………………………………...85

2.2 Synthesis and optimization PUX-NO film………………………………97

2.2.1 Encapsulation of {Mn-NO} in silica xerogel particles

2.2.2 Optimization of the Moisture Content of PUX-NO Films to Achieve Maximum NO Release

2.2.3 Optimization of material properties that enhance NO release

2.2.4 Stability of PUX-NO films under various storage conditions

2.3 Light-activated NO release from PUX-NO films………………………102

2.3.1 NO Photo-release Rate and Duration from PUX-NO

2.3.2 Visualization of the Diffusion of NO Released from PUX-NO in an Agar Matrix

2.5 Optimal Storage Conditions for PUX-NO Films..........................106

2.5 Antibacterial Properties of PUX-NO Films................................108

2.5.1 Antimicrobial Activity of PUX-NO Films using a Modified Agar Diffusion Method

2.5.2 Antimicrobial Activity of PUX-NO Films against *Escherichia Coli* using the Agar Overlay Method

2.6 Merits of PUX-NO as an Antimicrobial Occlusive Film Dressing......114

2.6.2 Broad Spectrum Antimicrobial Activity of PUX-NO Films

2.7 Conclusions..120

Chapter 3 – Light-Triggered Eradication of *Acinetobacter baumannii* by Means of NO Delivery from a Porous Material with an Entrapped Metal Nitrosyl

3.1 Background..133

3.2 Synthesis of {Mn-NO}@MCM-41..141

3.3 Characterization of {Mn-NO}@MCM-41.................................144

3.3.1 Determination of the {Mn-NO} Content of {Mn-NO}@MCM-41

3.3.2 Stability of the {Mn-NO}@MCM-41 Host-Guest Interaction Under Physiological Conditions

3.3.3 FTIR spectra of $\{Mn\text{-}NO\}_{200}$@Si-MCM-41 and $\{Mn\text{-}NO\}_{200}$@Al-MCM-41

3.3.4 Diffuse Reflactance Spectra of the {Mn-NO}@MCM-41 Materials

3.3.5 Probing the Pore Environment of {Mn-NO}@MCM-41 by N_2 Sorption Isometry

3.3.6 PXRD and TEM Analysis of the {Mn-NO}@MCM-41 Structures

3.3.7 SEM-EDX Elemental Mapping of {Mn-NO}@MCM-41

3.4 NO Photorelease from {Mn-NO}@MCM-41..............................165

3.4.1 NO Releasing Capacities of {Mn-NO}@MCM-41 under Steady Illumination

3.5 Antimicrobial effects of {Mn-NO}@MCM-41 against *A. baumannii*...171

3.5.1 Skin and Soft-Tissue Infection Model for Antimicrobial Testing

3.5.2 The Antimicrobial Efficacy of {Mn-NO}@MCM-41 against*A. baumannii*

3.6 Conclusions..180

Chapter 4 – Enhanced Cytotoxic Effect Observed Damage to Hyphal Form Through Light-Induced Delivery Of Nitric Oxide To *Candida Albicans* Colonies

4.1 Introduction……………………………………………………198

4.2 NO-donating materials: {Mn-NO}@Al-MCM-41 and PUX-NO……...201

4.3 Growth Conditions for *C. albicans and S. cerevisiae*…………………208

4.3.1 Morphologically Selective Growth of *C. albicans* in Liquid Media

4.3.2 Morphologically Selective Growth of *C. albicans* in Soft Agar

4.4 Antimicrobial Effect of Photorealeased NO from {Mn-NO}@Al-MCM-41 on *C. albicans*……………………………………………………212

4.5 Sensitivity of S. cerevisiae Mutants Lacking Key Components of the Nitrosative Stress Response to Photo-released NO..………………………217

4.6 Conclusions…………………………………………………………..220

4.7 Experimental Methods……………………………………………….220

Appendix A. The Effects of Equatorial Ligand Planarity on the Stability and NO Photorelease of Dye-Tethered Ruthenium Nitrosyls

A.1 Background……………………………………………………….232

A.2 Syntheses of $H_2(OMe)_2bQb$ and $H_2(OMe)_2IQ1$………………………..240

A.3 Syntheses and Characterization of Cl-Bound Nitrosyls………………..241

A.3.1 - Structure of $[((OMe)_2bpb)Ru(NO)(Cl)]$

A.3.2 X-ray Crystal Structure of $[((OMe)_2IQ1)Ru(NO)(Cl)]$

A.5 Comparison of Electronic Absorption Spectra of the Cl^- bound Ruthenium Nitrosyls…………………………………………………………244

A.6 Syntheses and Structures of Dye Conjugated Metal Nitrosyls………...246

A.6.1 X-ray crystal structure of [((OMe)$_2$bpb)Ru(NO)(Resf)]

A.6.2 Structural Characterization of [((OMe)$_2$IQ1)Ru(NO)(Resf)]

A.6.3 Electron Absorption Spectra of [((OMe)$_2$bpb)Ru(NO)(Resf)] and [((OMe)$_2$IQ1)Ru(NO)(Resf)]

A.6.4 Stability of Dye-Bound Metal Nitrosyls in Aqueous Solvents

A.7 Visible Light Triggered NO-Photorelease from the Cl$^-$ and Dye-bound Metal Nitrosyls..254

A.8 Fluorescence Properties of Free-Dye and Metal Bound-Dye.............256

A.9 Conclusions..258

A.10 Experimental Section..259

A.11 Experimental Data..265

List of Figures

Chapter 1.

Figure 1.1. Reaction catalyzed by nitric oxide synthases

Figure 1.2. Bacterial NO detoxification systems

Figure 1.3. Schematic representation of the mechanism of NO-release from *N*-diazeniumdiolates

Figure 1.4. Decomposition pathways of the S-nitrosothiol

Figure 1.5. Schematic of metal nitrosyls with $PaPy_3^-$ type ligands.

Figure 1.6. Structure of H_2bpb^{2-} type ligands

Figure 1.7. "Turn on" fluorescence upon NO photorelase from [Ru(Me_2bpb)(FlEt)(NO)] (**8**) in aqueous media.

Figure 1.8. Schematic representation of the synthesis of magnetic Fe_3O_4 nanoparticles with *S*-nitroso functionalized mercaptosuccinic acid (MSA) or dimercaptosuccinic acid (DMSA) ligands.

Figure 1.9. 2-mercapto-5-nitro benzimidazole functionalized gold nanoparticles that release NO upon visible-light irradiation.

Figure 1.10. Copolymerization of the vinyl group of [RuCl(P-salen)(NO)] (10) in a methacyralate matrix afforded the photoactive NO-donating material **P-10**.

Figure 1.11. Light-triggered NO release from the sol-gel, $\{Mn\text{-}NO\}^6$ composite **3•SG**

Chapter 2.

Figure 2.1. Wound re-epithelialization under moist conditions produced by an occlusive film dressing

Figure 2.2. Chemical structure of Tecoflex® SG-80A thermoplastic polyurethane chains

Figure 2.3. Schematic of the synthesis of PUX-NO films

Figure 2.4. NO photo-release rates from PUX-NO films in PBS buffer at 25°C as measured by an NO-specific electrode.

Figure 2.5. The diffusion of NO released from PUX-NO films was visualized in an agar matrix by the formation of a pink azo-dye from the Griess reagent.

Figure 2.6. Antimicrobial effects of NO photoreleased upon illumination of PUX-NO films on bacteria inoculated on the surface of TSB agar plates

Figure 2.7. Antimicrobial activity of PUX-NO films $\{Mn\text{-}NO\}^6$ against *E. coli* colonies suspended in a 1.1 mm thick layer of soft agar

Chapter 3.

Figure 3.1. Schematic depicting the synthesis of PMOs with a crystal-like arrangement of the bridging organic units R in the pore walls

Figure 3.2. Leaching of {Mn-NO} from the mesopores of $\{Mn\text{-}NO\}_{200}$@Si-MCM-41 and $\{Mn\text{-}NO\}_{200}$@Al-MCM-41 during soaking in a physiologically relevant saline solution (10 mg sample in 2 mL of 137 mM NaCl)

Figure 3.3. FTIR spectra of [Mn(PaPy$_3$)(NO)](ClO$_4$), Si-MCM-41 (dotted line) and {Mn-NO}$_{200}$@Si-MCM-41 (solid line) in the region from 1200 to 1800 cm^{-1} (inset, structure of [Mn(PaPy3)(NO)](ClO4)).

Figure 3.4. Diffuse reflectance UV-vis spectra of {Mn-NO} (dashed line), {Mn-NO}$_{200}$@Al-MCM-41 (dash-dot line) and {Mn-NO}$_{200}$@Si-MCM-41(solid line).

Figure 3.5. N$_2$ adsorption (solid lines with triangles) and desorption isotherms (dotted lines) of {Mn-NO}$_{200}$@Si-MCM-41 (red trace, open triangles) and {Mn-NO}$_{200}$@Al-MCM-41 (maroon trace, filled triangles).

Figure 3.6. Schematics of N$_2$ adsorption data and phenomena

Figure 3.7. PXRD analysis of the unloaded and loaded MCM-41 materials

Figure 3.8. TEM micrographs of {Mn-NO}$_{200}$@Al-MCM-41 particles along the pore axis demonstrating the retention of the MCM-41 host structure after {Mn-NO} loading.

Figure 3.9. Cross-sectional SEM-EDX elemental mapping of {Mn-NO}$_{200}$@Al-MCM-41

Figure 3.10 Light-triggered NO release from {Mn-NO}@MCM-41 as measured by an NO-specific electrode

Figure 3.11. Effects of NO photoreleased from {Mn-NO}200@Al-MCM-41 on *A. baumannii* colonies.

Figure 3.12. Antibacterial effects of photoreleased NO from 50 mg of {Mn-NO}$_{200}$@Al-MCM-41 after 1.5 h illumination against drug susceptible *A. baumannii*.

Chapter 4.

Figure 4.1. Infection of a reconstructed skin equivalent with *C. albicans* wild-type (right) and Δ*cph1* Δ*efg1* null mutant (right) lacking necessary factors for hyphal or pseudohyphal morphogenesis.

Figure 4.2. Color filtered image of a Griess agar plate showing the diffusion of photo-released NO from **PUX-NO** films.

Figure 4.3. Micrographs of *C. albicans* polymorphs induced under specific conditions for the growth of hyphal, pseudohyphal and yeast phases in 1.0% (w/v) soft agar cast on top of hard YPD agar plate.

Figure 4.4. Antifungal effects of NO released from photolyzed (**A**), 10 (**B**), 14(**C**) and 16 mg (**D**) {Mn-NO}@Al-MCM-41 under illuminattion with 100 mW cm^{-2} visible light for 1 h.

Figure 4.5. Micrographs showing the effects of a moderate dose of NO (photoreleased from {Mn-NO}@Al-MCM-41) on the pure yeast form (top panel) and pure hyphal form (bottom panel) of *C. albicans*.

Figure 4.6. Effects of NO photoreleased by **PUX-NO** films against wild-type, ΔYHB1, and ΔSSU1 mutants of *S. cerevisiae* grown in soft agar cast on YPD plates.

Appendix A.

Figure A.1. Structure of $[M(PaPy_3)(NO)(Cl)]^{n+}$

Figure A.2. Schematic and corresponding electronic absorption spectra of $\{Ru\text{-}NO\}^6$ nitrosyls derived from the tetradentate, dicarboxamide ligands Me_2bpb^{2-}, Me_2bQb^{2-}, and $(OMe)_2bQb^{2-}$ with Cl^- or $Resf^-$ bound *trans* to NO.

Figure A.3. Reaction scheme for the synthesis of $H_2(OMe)_2bpb$ (structures with solid lines) and $H_2(OMe)_2IQ1$ (structures from combination of solid and dashed lines).

Figure A.4. X-ray crystal structures of $[((OMe)_2bQb)Ru(NO)(Cl)]$[16] (left) and $[((OMe)_2IQ1)Ru(NO)(Cl)]$ (right)

Figure A.5. Electronic absorption spectra of $[(Me_2bpb)Ru(NO)(Cl)]$, $[((OMe)_2bpb)Ru(NO)(Cl)]$, $[(Me_2bQb)Ru(NO)(Cl)]$, $[((OMe)_2bQb)Ru(NO)(Cl)]$, and $[((OMe)_2IQ1)Ru(NO)(Cl)]$ in DMF.

Figure A.6. Thermal ellipsoid (probability level 50%) plot of $[((OMe)_2bpb)Ru(NO)(Resf)]$ with select atom-labeling. H atoms are omitted for the sake of clarity.

Figure A.7. Thermal ellipsoid (probability level 50%) plot of $[((OMe)_2IQ1)Ru(NO)(Resf)]$ with selected atom-labeling. H atoms are omitted for the sake of clarity.

Figure A.8. Electronic absorption spectra for the Cl^- and dye-bound nitrosyls, $[((OMe)_2bpb)Ru(NO)(Cl)]$ and $[((OMe)_2bpb)Ru(NO)(Resf)]$ (left panel) and $[((OMe)_2IQ1)Ru(NO)(Cl)]$ and $[((OMe)_2IQ1)Ru(NO)(Resf)]$ (right panel).

Figure A.9. Electronic absorption spectra of (left) pyridine based dye-sensitized nitrosyls $[(Me_2bpb)Ru(NO)(Resf)]$ and $[((OMe)_2bpb)Ru(NO)(Resf)]$ in $CHCl_3$ (middle) quinoline based dye-sensitized nitrosyls $[(Me_2bQb)Ru(NO)(Resf)]$, $[((OMe)_2bQb)Ru(NO)(Resf)]$ and $[((OMe)_2IQ1)Ru(NO)(Resf)]$ in $CHCl_3$ (right) free deprotonated Resorufin dye in DMF.

Figure A.10. Changes in the electronic absorption spectrum of $[((OMe)_2IQ1)Ru(NO)(Resf)]$ in MeCN following illumination with visible light. Inset: NO-amperogram of $[((OMe)_2IQ1)Ru(NO)(Resf)]$ in $MeCN/H_2O$ exposed to increasing periods of light, as indicated (in seconds).

Figure A.11. Fluorescence emission spectrum of $[((OMe)_2IQ1)Ru(NO)(Resf)]$ and $[(Me_2bpb)Ru(NO)(Resf)]$ in MeCN (λ_{ex}= 490 nm).

Figure A.12. IR spectra of $H_2(OMe)_2bpb$ (KBr Pellet).

Figure A.13. ^{1}H-NMR spectra of $H_2(OMe)_2bpb$ (3.8-10.5 ppm) in $CDCl_3$ at 298 K

Figure A.14. IR spectra of $H_2(OMe)_2IQ1$ (KBr Pellet).

Figure A.15. ^{1}H-NMR spectra of $H_2(OMe)_2IQ1$ (3.8-10.5 ppm) in $CDCl_3$ at 298 K

Figure A.16. IR spectra of $[((OMe)_2bpb)Ru(NO)(Cl)]$ (KBr Pellet).

Figure A.17. ^{1}H-NMR spectra of $[((OMe)_2bpb)Ru(NO)(Cl)]$ (3.8-10.5 ppm) in $CDCl_3$ at 298 K.

Figure A.18. IR spectra of [((OMe)$_2$IQ1)Ru(NO)(Cl)] (KBr Pellet).

Figure A.19. ^{1}H-NMR spectrum (7.7-11.0 ppm) of [((OMe)$_2$IQ1)Ru(NO)(Cl)] in CDCl$_3$ at 298 K

Figure A.20. IR spectrum of [((OMe)$_2$bpb)Ru(NO)(Resf)] (KBr pellet).

Figure A.21. ^{1}H-NMR spectrum (5.5-9.0 ppm) of [((OMe)$_2$bpb)Ru(NO)(Resf)] in CDCl$_3$ at 298 K.

Figure A.22. IR spectrum of [((OMe)$_2$IQ1)Ru(NO)(Resf)] (KBr pellet).

Figure A.23. ^{1}H-NMR spectrum (5.1-10.4 ppm) of [((OMe)$_2$IQ1)Ru(NO)(Resf)] in CDCl$_3$ at 298 K.

List of Tables

Chapter 2.

Table 2.1. Moisture content (q(%)) of PUX-NO films after storage for 3 months under various conditions.

Chapter 3.

Table 3.1 Elemental analysis of the {Mn-NO} content of the loaded Si-MCM-41 and Al-MCM-41 materials

Table 3.2. Average pore diameter, specific surface area (SSA), and cumulative pore volume of $\{Mn\text{-}NO\}_{200}$@Si-MCM-41, $\{Mn\text{-}NO\}_{200}$@Al-MCM-41 and the unloaded host materials.

Table 3.3. van der Waals dimensions of $[Mn(PaPy_3)(NO)]^+$

Abstract

Photoactive Nitric Oxide Delivery Systems based on Metal Nitrosyl-Biomaterial Composites

Brandon James Heilman

Gaseous NO has been recognized as a potent antibiotic even against highly drug-resistant pathogens such as methicillin-resistant *Staphylococcus aureus* (MRSA) in both animal and human studies. However, difficulties in the delivery of the toxic (and reactive) gas demands innovative techniques to deliver NO in a controlled manner to malignant sites throughout the body. Metal nitrosyls reported by our group have demonstrated rapid NO release under the complete control of visible and NIR light. Careful incorporation of these photoactive nitrosyls into polymer matrices has afforded a set of nitrosyl–polymer composites in order to localize the NO-donors at a targeted site, ensure reliable NO release kinetics *in vivo*, and prevent potentially cytotoxic interactions of the metal nitrosyl or its reaction-products with the treatment site. The work presented in this thesis was pursued to derive clinically relevant NO-delivery systems and demonstrate their utility for the treatment of infection.

In chapter 2, an NO-releasing polyurethane film (PUX-NO) is described with dispersed xerogel particles containing up to 3 mol% of $[Mn(PaPy_3)(NO)](ClO_4)$ entrapped in a silica matrix and swelled with excess moisture. The polyurethane based xerogel-nitrosyl (PUX-NO) films demonstrated rapid NO photorelease upon illumination with low-power visible light which was sufficient to eradicate clinically relevant loads (10^5 CFU mL^{-1}) of several gram-positive and gram-negative pathogenic

bacteria, including a strain of methicillin-resistant of *S. aureus*. The results of this study suggest that PUX-NO films are suitable for use as a NO-releasing occlusive film for the treatment of skin and soft-tissue infections or chronic, non-healing wounds. Since the NO-release rate from the films can be modulated by simple adjustment of the intensity of the light source, the films could be used to first clear the microbial burden from the wound site using high fluxes of NO, and then, provide a moderate, sustained flux of NO in order to accelerate the wound healing process and mitigate the potential for recurrent infections.

Chapter 3 details the incorporation of a photoactive Mn nitrosyl in the mesopores of a MCM-41 type silicate to afford {Mn-NO}@MCM-41. To increase the interaction between the nitrosyl and the MCM-41 pore walls, an aluminosilicate-based material (Al-MCM-41) was used with 3 mol% Al^{III} substituted for tetrahedral Si^{IV} sites, which introduced negative point charges capable of electrostatically binding the cationic nitrosyl. Homegenous loading of the Mn nitrosyl (up to 25 wt.%) throughout the hexagonally packed, uni-dimensional mesopores of the Al-MCM-41 particles was determined using various analytical techniques including ICP-MS, FAAS, PXRD, N_2 sorption isometry, UV-vis DRS, FTIR, and SEM-EDX. Exposure of {Mn-NO}@Al-MCM-41 to visible light of similar intensity to sunlight on a bright day (100 mW cm^{-2}) released high fluxes of NO that effectively eradicated a multi-drug resistant strain of *Acinetobacter baumannii.*

In another study, described in Chapter 4, the powdery material was used to demonstrate the effect of NO on the dimorphic fungal pathogen, *Candida albicans*.

Since the virulence of *C. albicans* is dependent on the ability of the fungus to switch growth from an ovoid yeast form to an elongated hyphal form, careful studies of the dose-dependent effect of NO released from {Mn-NO}@Al-MCM-41 on morphologically pure cultures of *C. albicans* in the yeast and hyphal forms have revealed that the hyphal form is more susceptible to NO. Results of this work suggest that photo-activated NO-donating materials of this type could prevent commensal populations of *C. albicans* from invading vulnerable tissue by blocking the over-growth of the tissue penetrating hyphal form of the fungus.

Acknowledgements

I would like to thank my research advisor, Prof. Pradip Mascharak, for providing the support, time and encouragement necessary to complete the research presented in this thesis. I'm especially thankful for his resourceful ideas and passion about science throughout my PhD research. He has been a remarkable mentor, providing me the necessary tools to not only excel in the laboratory, but also in the more subtle aspects of a scientific career.

I would also like to thank my other thesis committee members: Prof. Scott Oliver, for the insight and guidance he provided at weekly research group meetings and also during collaborative research projects, and Prof. Ted Holman for his guidance in the laboratory and his humor outside the laboratory. I greatly appreciate the time my committee members, including the outside member Prof. Fitnat Ylidz, gave for my second year seminar, oral exam, and thesis defense.

Over the years I have worked with talented crystallographers including Dr. David Rogow, Dr. Honghan Fei, and Dr. Yashar Abdollahian in the collection and solving of X-ray data. I would like to thank each of them for their help and guidance.

I had the pleasure of collaborating with Prof. Scott Oliver and Dr. Jessica St. John on the work presented in Chapter 3. I would like to thank them for the contributions and perspectives they provided for this scientific work.

I want to acknowledge all of the help and support I have received from my fellow labmates, past: Dr. Genevieve Halpenny, Dr. Nicole Fry and Dr. Margarita Gonzales, and present: Tara deBoer and Samantha Carrington. I would especially like to thank Dr.

Genevieve Halpenny for taking me under her wing when I first joined the lab. She was a great mentor, always willing to share her wealth of knowledge and experience. I would also like to acknowledge the encouragement and support provided by Tara deBoer in the preparation of my thesis defense.

I would like to thank the undergraduate students whom I have mentored in the lab Abegail Tadle and Luis Pimental. They were both a lot of fun, a lot of work, and bright scientists.

Lastly, I owe an enduring debt of gratitude to my family: my parents, Larry and Sandi Heilman, and siblings, Becky, Cindy, Chris and Amanda; their love and support has carried me to, through, and past graduate school. I share all my achievements with them.

Chapter 1

Introduction

1.1 Nitric Oxide in Mammalian Biology

The unique physicochemical properties and versatile reactivity of the free radical, nitric oxide (NO), allow this simple diatomic molecule to regulate an impressive number of physiological and pathophysiological processes. Since the nearly simultaneous discoveries of Louis J. Ignarro and Salvador Moncada in 1987 identifying NO as the endogenously produced endothelium derived relaxation factor (EDRF), the list of physiological processes regulated by NO has expanded considerably.[1,2] Paradoxically, the proposed function of NO as an endogenously produced regulatory molecule was preceded by the establishment of NO as a side product of fossil fuel combustion and precursor to the toxic pollutants, NO_2 (smog) and HNO_3 (acid rain).[3] Yet, under physiological conditions, NO proves to be remarkably adept for transient paracrine and autocrine signaling. The lipophilicity and Stokes' radius of NO are comparable to those of O_2 and CO, permitting the rapid diffusion of NO across cellular and tissue membranes independent of transport proteins or channels.[4] Furthermore, the slight dipole of NO greatly enhances its diffusion and solubility in water compared to O_2 and CO. Thus, NO is able to iso-topically diffuse from its point of biosynthesis, suffering minimal inhibition from inter- or intracellular barriers, and rapidly activate nearby receptors. With a diffusion coefficient of 3×10^{-5} cm^2 s^{-1} at 37°C (rat cerebral cortex) and a half-life of ~5 s, NO production from a single source will effectively transmit a paracrine signal over a range of 100 um, an area encompassing nearly 10^5 cells.[5] Contrary to conventional bio-signaling molecules that activate specific receptor molecules through structurally determined intermolecular forces, the biological effects of NO manifest through chemical reactions with target molecules. The chemical reactivity of NO in biological systems is concentration dependent with a marked distinction between the **direct** reaction of NO with target molecules which dominant at sub-micromolar concentrations of NO, and the **indirect** reaction of NO with target molecules following redox processing to form a reactive nitrogen species (RNS) observed extensively when [NO] > 1 μM.[6]

1.1.1 Enzymatic NO production by Nitric Oxide Synthase

The kinetically relevant, direct reactions of NO at sub-micromolar concentrations are limited by the radical nature of NO and involve substrates with an unpaired electron, namely the nitrosylation of transition metal centers and radical-radical combination reactions.[7] The primary biological target of NO at nM concentrations is also the primary effector of NO-based signaling pathways, the Fe(II) heme-center of soluble guanylate cyclase (sGC).[8] sGC activity is regulated by

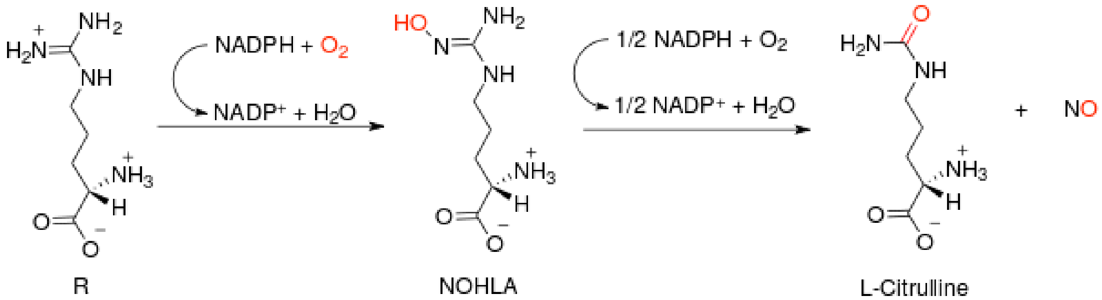

Figure **1.1**. Nitric oxide synthases produce NO by catalyzing a five-electron oxidation of a guanidino nitrogen of L-arginine (L-Arg), producing N^{ω}-hydroxy-L-arginine (NOHLA) as an intermediate, and consuming 2 mol of O_2 and 1.5 mol of NADPH per mole of NO formed.

enzymatically derived NO produced by nitric oxide synthase (NOS) isoforms expressed predominantly by neuronal (nNOS) and endothelial (eNOS) cells. The NOS enzymes catalyze a five electron oxidation of the guanidine group of L-arginine producing just one equivalent of NO and L-citrulline while consuming two equivalents of O_2 and 1.5 equivalents of NADPH (Figure 1.1).[9] The catalytic cycle of NOS involves two successive monoxygenation reactions producing N^{ω}-hydroxy-L-arginine (NOHLA) as an intermediate after the consumption of one equivalent of O_2 and NADPH. The rate of NO production by eNOS and nNOS is regulated by the Ca^{2+}-dependent binding of calmodulin (CaM) to an inter-domain "latch" which holds the oxygenase and NADPH-binding reductase domains in electronic contact. Thus, intracellular [Ca^{2+}] serves as a primary regulator of eNOS and nNOS activity, and thus, NO-dependent signaling processes. The increased CaM binding affinity of the inter-domain latch of nNOS (2 nM CaM) compared to that of eNOS (4 nM CaM) translates into a nearly two-fold increase in the rate of NO production by nNOS compared to eNOS.[10] A third, inducibly expressed NOS isoform (iNOS), binds CaM irreversibly (0.1 nM CaM) and has full catalytic activity under all physiologically relevant [Ca^{2+}]. iNOS expression is primarily induced by immunostimulants originating endogenously (*e.g.* interferon-γ) or exogenously (*e.g.* lipopolysaccharides, a component of bacterial cell walls) and is the greatest in phagocytic cells (although expression has been observed in nearly all nucleated mammalian cells).[11]

1.1.2 NO Production by eNOS and nNOS

NO production by eNOS within the epithelium sustains a basal concentration of ~1 nM NO in the blood plasma. [12] Even at such low concentrations, the primary effector of NO-signaling, soluble guanylate cyclase (sGC), is sufficiently nitrosylated (activated) to regulate vascular smooth muscle contractility and inhibit blood platelet adhesion. In response to physiological signals, eNOS can also generate much greater pulses of NO (>100 nM [NO]) as observed upon the rapid release of intracellular Ca^{2+} stores by epithelial cells in response to the shear stress exerted by turbulent flowing blood at constricted sites in the vasculature. During such events, NO acts as a rapid secondary messenger and amplifies the signal initiated at the point of shear stress on the epithelium in order to locally integrate the dilatory response of the surrounding smooth muscle, preventing catastrophic outcomes such as vessel failure or myocardial infarction. Although eNOS regulates vascular tone throughout most of the body, eNOS is not found in the peripheral blood vessels; instead, vascular tone is controlled by NO released from nNOS located within neural cells that have innervated the vascular smooth muscle membrane.[13] In the cerebral tissue, NO production by nNOS not only contributes to the control of blood flow but also functions in a variety of physiological processes including neurotransmission, neurogenesis, and antioxidant buffering. During high frequency neurotransmission, nNOS activity can alter neural plasticity by modulating long-term potentiation through the activation of sGC/PKG pathways in the hippocampus and regulating catecholamine release (such as dopamine) in the striatum.[14] In contrast to the low nM [NO] required for physiological signaling by eNOS, the activation of certain dopamine releasing pathways requires [NO] > 200 nM, likely to prevent the un-regulated release of dopamine by distal sources of NO. Since nNOS can generate NO levels 100 times higher than those associated with eNOS activity, the location and the microenvironment in the vicinity of nNOS are vital to inhibit the diffusion of high concentrations of NO to sensitive components of the cerebrum. The failure of such NO buffering systems in the cerebrum has been implicated in the neurodegenerative effects associated with nNOS activity. Pharmacological efforts to mitigate the cytotoxic components of nNOS activity are complicated by the often conflicting pathophysiological roles of nNOS activity, *c.f.* the ability of NO to both attenuate and potentiate brain damage during ischemia/reperfussion.[15] In addition, the dysregulation or malfunction of nNOS have been identified as potential etiological factors of certain neurodegenerative conditions such as Parkinson's disease.

1.1.3 NO Production by iNOS

The genes encoding iNOS are induced by various factors including, products of gram-negative and gram-positive bacteria, interferon-gamma (IFN-γ), interleukin-l (IL-1), and tumor necrosis factor (TNF).[16] Different combinations of these agents have shown synergism in their ability to induce iNOS activity at the transcriptional level. For example, the amount of NO detected from macrophages activated with IFN-γ + (TNF or IL-1β) was 10 times less than that of IFN-γ + LPS activated macrophages despite similar amounts of iNOS expression.[17] This observation has been attributed to the influence of the activator on the translocation of iNOS to different subcellular compartments since cytokine activation results in the translocation of iNOS to mostly cytosolic regions while LPS activation results in the translocation of iNOS almost exclusively to the hydrophobic interior of the cellular membrane where O_2 levels are highest (an often limiting substrate of NOS activity. The K_m of O_2 is one of the major differences between the NOS isoforms and provides insight into the physiological role of each isoform.d The K_m for nNOS is 350 µM ,iNOS is 135 µM, and eNOS is 23 µM, reflecting the increased rate of co-precipitation of the NOS isoforms with the cellular membrane (with eNOS being the only integral transmembrane isoform, where O_2 levels are highest) during fractionation.[18] The seemingly trivial decrease in the distance between the source of NO and the targeted site as a result of the translocation of iNOS to the cellular membrane can actually have a significant impact on the effective [NO] at the targeted location since NO diffusing from a single source dilutes within a spherical space defined by the cube of its radius such that at a distance of one cell length there is an 8-fold dilution in [NO] and at two lengths a 27-fold dilution.[19] Since the phosphorylation and activation of the tumor suppressor protein p53 requires several hours of exposure to [NO] > 400 nM, the proximity of iNOS within activated leukocytes to the nucleus of genetically compromised cells targeted for apoptosis is critical during the anti-tumor reponse.[20] Simarily, when leukocytes surround a targeted pathogen, the orientation of iNOS within each cell can determine the intersectional area of NO fluxes, and thus, determine [NO] felt by the microbial target.[21]

1.1.4 The Direct Effects of NO

The important substrates for direct reaction with free-radical NO are limited to some metal complexes and other free radicals. The range of metal-centered biological molecules targed by NO can be easily identified by considering the similarities between NO, CO and O_2, thus, any heme-enzyme that reacts with oxygen or CO will be a potential target for NO binding as well.[22] This criterion dictates that the high spin 5-coordinate heme-enzyme that bind and/or activate O_2, such as cytochrome oxidase, the cytochrome P-450 superfamily and hemoglobin/myoglobin; while, the corollary suggests that 6-coordinate low spin heme-proteins (e.g. cytochromes b and c) that in general react poorly with oxygen will not be potential substrates for NO binding (and therefore CO).[23] The activation of sGC by NO occurs through the rapid nitrosylation of the low-spin Fe(II) center of the enzyme's heme prosthetic group.[24] Although the EC_{50} of NO binding to sGC is ~100 nM, the affinity of NO for the enzyme's heme iron-center results in appreciable sGC activation at [NO] < 1 nM. The strong donation of electron density from the singly occupied molecular orbital of NO (SOMO) through a σ-bonding interaction (p*NO+dz2) with the Fe(II) center of the active state enzyme weakens the σ-bond of the trans-coordinated His ligand.[25] The subsequent dissociation of the distal His ligand (which maybe catalyzed by an additional NO molecule under elevated [NO]) invokes favorable changes in the structure of the enzyme's N-terminus cyclase domain, increasing the enzymatic activity by nearly 200-fold. While dissociation of NO from the five-coordinate species is biologically irreversible (k_{off} 10^{4-} s^{-1}), the binding of GTP in the presence of Mg^{2+} (a cofactor for catalytic activity) appears to reposition the His ligand for re-ligation to the distal binding site, markedly increasing k_{off} of NO (0.05 s^{-1}). [26] Catalytically active sGC catalyzes the cyclization of guanosine triphosphate (GTP) forming the secondary messenger, cyclic-guanosine monophosphate (cGMP). The production of cGMP regulates the activity of cGMP-dependent protein kinases (cGMP-PK) which exert their biological influence through the phosphorylation of certain contractile proteins or by regulating gene expression.[27] The downstream effects of cGMP-PK activation control a variety of vital physiological processes including vascular tone, platelet function, neurotransmission, cellular differentiation, and apoptosis. The binding of NO by sGC can be inhibited during periods of oxidative stress as a result of the oxidation of Fe(II)-sGC to the ferric enzyme with a concomitant distortion of the heme unit from the expected coplanar geometry.[28] Reaction of ferric sGC with NO through a reductive nitrosylation mechanism restores the Fe(II) center with attendant flattening of the heme ring. The increased affinity of NO for ferrous over ferric centers is reflected in both a faster on rate *and* a slower off rate; in some cases the dissociation rate is so slow ($<10^{-5}$ s^{-1}) that structural modifications within the heme-pocket of certain ferrous hemeproteins, such as cytochrome oxidase, may have evolved to accelerate NO dissociation.[29] There is clear evidence that even physiological [NO] (low nM) can inhibit respiration by rapid binding to cytochrome c oxidase, the terminal enzyme in the mitochondrial respiratory electron transport chain.[30] The binuclear heme-copper active site of the oxygen reduction domain of cytochrome c oxidase shows an increased affinity for NO binding compared to similar hemeproteins. For example, the rate of NO binding to the heme-center of the family of cytochrome P450s is reduced nearly 10 fold compared to cytochrome c oxidase and is similar to that of the NOS isoforms. This difference can be explained by the *trans*-effect of the distal ligand on the coordination of the proximal site by NO.[31] Since *trans*-coordinated ligands occupying the distal and proximal axial sites form σ-bonding interactions with the same Fe(II)-centered AO ($3d_{z2}$), the coordination of strong σ-donor NO to the proximal site is inhibited by the occupation of the Fe($3d_{z2}$) orbital by strong σ-donors in the distal coordination site (such as Cys^- in cytochrome P450s and NOSs) while NO binding at the proximal site can cause a significant decrease in the σ-bonding interactions between Fe(II) and weak σ-donors occupying the distal site (such as His in cytochrome c oxidase and sGC) resulting in *trans*-labilization of the distal ligand.[32]

Cell-free hemoglobin (Hb-Fe(II)) containing a distal Cys^- ligand shows similar NO-binding kinetics to other Cys^- ligated hemeproteins with a rapid on rate ($k_{on} = 1.8 \times 10^7\ s^{-1}$) but a considerably slower off rate ($k_{off} = 1.8 \times 10^{-5}\ s^{-1}$), allowing nitrosylation to kinetically outcompete O_2 for binding to HbFe(II).[33] However, under physiological conditions with $[O_2] > [NO]$, the irreversible oxidation of NO by oxyhemoglobin (HbFe(II)-O_2, R-state) producing met-Hb (ferric, inactive) and NO_3^-

$$\text{HbFe(II)-O}_2 + \text{NO}\cdot \rightarrow \text{Fe(III)} + \text{NO}_3^- \qquad k = 3 \times 10^7\ M^{-1}\ s^{-1} \quad (1)$$

is the dominant reaction of NO with cell-free oxyhemoglobin. In most tissue, cells are within 50–300 μm (between 1 to 30 cell lengths) from a blood vessel.[34] Since NO diffuses as much as 5–10 cell lengths in 1s, the rapid diffusion of NO to a blood vessel has been postulated as a kinetic determinant of the life-time of NO by rapid consumption following Eq. (1), especially in the presence of high levels of cell-free hemoglobin as occurs in pathologies caused by the transfusion of improperly stored/aged blood or the lysis of erythrocytes by the protozoa, *Plasmodium* (aka malaria parasite).[35] The accumulation of met-Hb (inactive form) in the presence of elevated [NO] as a result of improper therapeutic administration of NO or pathological NO production by iNOS associated with inflammation can result in a fatal condition known as methemoglobemia due to the inability of metHb to function in O_2 transport. However, the localization of eNOS to the intercellular junction between the endothelium and the vascular smooth muscle, distal to the lumen, favors diffusion of NO to the smooth muscle resulting in sGC activation over Hb-mediated consumption. In addition, several physiological mechanisms attenuate the rate of Eq. (1) with intracellular hemoglobin in flowing blood by nearly 100 to 600-fold compared to the rate of Eq. (1) determined with cell-free Hb in static solutions, and reduce the influence of blood vessels on the local concentration and diffusion of NO.[36] These include diffusional boundaries around the erythrocyte, the lack of red blood cells in the fluid boundary-layer along the endothelial wall in laminar flowing blood, and competing reactions which lead to the formation of nitrosothiols (RSNO) and/or nitrite within the structure of hemoglobin. The discovery of RSNO in hemoglobin isolated from mammalian erythrocytes has led most investigators to accept a revised model to describe the influence of NO on blood-tissue oxygenation which postulates a critical role for RSNO as an allosteric modulator of O_2 binding and release by Hb through the following process: (a) the flow oxygenated blood to areas of low tissue P_{O2} promotes the release O_2 from oxyhemoglobin and generates deoxyhemoglobin which is readily nitrosylated producing HbFe(II)-NO:

$$\mathrm{HbFe(II)} + \mathrm{NO\cdot} \rightarrow \mathrm{HbFe(II)\text{-}NO} \qquad k = 2 \times 10^{7}\ \mathrm{M^{-1}\ s^{-1}} \quad (2)$$

(b) the return of the deoxygenated blood to the lungs where high P_{O2} drives the conversion of HbFe(II)-NO in the 'tense' T state to *S*-nitroso-HbFe(II)-O_2 in the 'relaxed' R state, and (c) the oxygenated blood again flows to sites of low P_{O2} (such as peripheral tissue) causing the dissociation of O_2 from *S*-nitroso-HbFe(II)-O_2 and subsequent decomposition of RSNO producing HbFe(II)-NO which prevents O_2 recombination with HbFe(II) thus increasing tissue oxygenation and generates free NO which functions as an EDRF to increase the flow of oxygenated blood to sites of low P_{O2}.[37]

The upper limit of NO flux released from iNOS can generate local [NO] in the micromolar range and produce significant levels of the biomarkers that result from the indirect chemistry mediated by RNS.[38] Through various levels of regulation including post-translational modifications, lower fluxes are also observed from iNOS associated with [NO] in the 100’s of nM. These concentrations of NO can promote a mixture of direct and indirect effects. The direct reactions of NO in the lower concentration range generated by leukocytes perform a variety of proliferative and cytoprotective functions that can actually mitigate the damage caused by chronic inflammation.[39] Matrix metalloproteinases (MMPs) excreted by macrophages are important mediators of inflammation, angiogenesis, wound response, and cancer metastasis. Exposure of purified latent MMP-9 to activated macrophages resulted in a [NO]-dependent (> 500 nM) increase in enzymatic activity through the activation of translational regulatory pathways functioning at the mRNA level; while, an irreversible inactivation of the enzyme was observed at higher [NO] (> 1 μM) as a result of RNS mediated protein modifications similar to those produced by HOCl.[40] While NO does not directly modify organic substrates at an appreciable rate, NO can be transformed into an efficient nitrosative species through the reductive nitrosylation of Fe(III)-centers to form Fe(II)-NO^+, a nitrosonium (NO^+) adduct.[41] NO demonstrates a variable affinity for Fe(III) centers, dependent on the metal's ligand sphere and can approach $10^7\ M^{-1}\ s^{-1}$ when the distal coordination site is free as in catalase.[41] In addition to the nitrosylation of ferric and ferrous iron, NO rapidly reacts with metallo-oxo species (especially hypervalent iron) formed by the oxidation of metal centers with strong oxidants such as H_2O_2,[42]

$$\mathrm{Fe(II)} + \mathrm{H_2O_2} \rightarrow \mathrm{Fe(IV){=}O} + \mathrm{NO} \rightarrow \mathrm{Fe(II)} + \mathrm{NO_2^-} \qquad (3)$$

$$\mathrm{Fe(III)} + \mathrm{H_2O_2} \rightarrow \mathrm{Fe(V){=}O} + \mathrm{NO} \rightarrow \mathrm{Fe(III)} + \mathrm{NO_2^-} \qquad (4)$$

Many of the cytotoxic reactions of peroxides occur through the oxidation of metal centers through Eqs. (3) and (4) producing hypervalent metals which either directly oxidize substrates or decompose releasing intracellular free metals which can cause considerable cellular damage through their ability to promote hydroxyl radical formation through Fenton chemistry. Thus, the scavenging of hypervalent metals by NO can greatly attenuate peroxide-mediated cellular damage.[43] NO can also provide cytoprotection from the oxidative damage associated with lipid peroxidation (specifically polyunsaturated fatty acids) catalyzed by the non-heme Fe(III)-center of lipoxygenase.[44] While NO binding to the active Fe(III) form of lipoxygenase occurs rather slowly, NO can effectively regulate the activity of lipoxygenase by stabilizing the reduced form of the enzyme through direct nitrosylation of the Fe(II) center forming the stabile, inactive Fe(II)-NO species. NO may also mitigate peroxidative damage by terminating uncontrolled lipid-radical chain reactions through a radical-radical combination reaction that proceeds at a diffusion-limited rate.[45] The formation of lipid radicals ($L^{\cdot}$) is initiated by the abstraction of an allylic hydrogen by oxidizing free-radicals, namely hydroxyl radical ($^{\cdot}OH$). Subsequent addition of $^3O_2$ produces a peroxyl-lipid ($LOO^{\cdot}$**)** which is capable of intra- or inter-molecular hydrogen-abstraction, propagating the radical process.[46] Peroxyl-lipids can also form as a side-product of lipoxygenase activity and are able to severely damage and destabilize cellular membranes in the absence of chain-breaking antioxidants such as a-tocopherol (vitamin E) or NO. The formation of peroxyl-radical by lipoxygenase has been shown to alter the fluidity and permeability of the mitochondrial membrane leading to the formation of pore-like structures which dissipate the mitochondrial potential and allow cytochrome *c* release.[1,47] Interestingly, the release of cytochrome c from the mitochondria is a very strong pro-apoptotic signal which is also promoted by sustained, high fluxes of NO. Due to the relatively low redox potential of NO ($E^o = -0.8$ V for the $NO^{\cdot}/{}^3NO^-$ couple and -0.35 V for the $NO^{\cdot}/{}^1NO^-$ couple), it requires oxidative processing to a more strongly oxidizing species in order to alter the permeability of the mitochondrial membrane. In this regard, NO is unique amongst free-radicals, such as the highly oxidative free-radicals, NO_2, F·, Cl·, and ·OH with E° = 1.04, 3.6, 2.41, and 1.9 V, respectively.[48]

1.1.5 The Indirect Effects of NO

The indirect effects of NO in biology proceed through a two-step process involving: (1) the oxidative processing of NO by (a) O_2 or (b) O_2^- forming reactive nitrogen species (RNS) and (2) the reaction of RNS with biological targets resulting in nitrosative (addition of NO^+) or oxidatitive modifications.[49] Oxidative modifications of biological targets by RNS usually involve electron transfer, hydrogen atom abstraction, and oxygen atom-transfer (oxygen atom insertion, addition, transfer, or hydroxylation). Based on inaccuracies or misinterpretation of experimental data, it had been previously postulated that the nitroxyl anion, NO^-, played a significant role in NO-dependent processes and was formed through the following one-electron reduction:

$$NO\cdot + e^- \rightarrow {}^3NO^- \quad E^\circ = -0.8 \text{ V vs NHE, pH 7} \qquad (5)$$

A revision of the reduction potential from the historical value of +0.39 V established that NO is generally not a good oxidant considering the typical biological reducing agents.[48] Thus, NO^- production (present as HNO pKa 11.4 ± 3.4) is not likely to occur at an appreciable rate and neither HNO or ${}^3NO^-$ (triplet ground state, similar to O_2) have been observed *in vivo*. In contrast, the autoxidation of NO by O_2 is physiologically relevant and produces nitrite as a stable end product in aqueous solutions, however, the rate-limiting step of this process produces the radical oxidant NO_2 according to Eq. (6).[50]

$$2NO\cdot + O_2 \rightarrow 2NO_2 \qquad (6)$$

Since (6) is second order with respect to NO and first with respect to O_2, this reaction proceeds at a negligible rate, except in the presence of high concentrations of NO in a well oxygenated medium. Due to the hydrophobicity of both NO and O_2, they tend to accumulate in the lipid fraction of a cell producing concentrations that are up to 10 times higher than those in the aqueous phase.[51] Thus, a considerable acceleration of (6) is observed in lipophilic environments such as the interior of lipid membranes where the hydrophobic product, nitrogen dioxide (NO_2), must rapidly diffuse to avoid scavenging by additional NO through the rapid radical-radical combination reaction:

$$NO\cdot + NO_2 \rightarrow N_2O_3 \qquad (7)$$

The diffusion limited rate of (7) at $> 10^9\ M^{-1}\ s^{-1}$, in addition to the high concentration of NO required to facilitate NO autoxidation through (6), greatly decrease the life-time of NO_2 and its contributions to the cytotoxic effects exhibited by RNS.[52] Current experimental evidence suggests that N_2O_3, dinitrogen trioxide, is the predominant RNS formed from the autoxidation of NO in biological systems.[53] The balance between reactions 2 and 3 is a critical determinant of the ability of RNS to transform biological molecules through oxidation (NO_2, $E^o = 1.04$ V) or nitrosation (N_2O_3, $E^o = 0.8$ V).[54] While NO_2 is able to diffuse several cell lengths after formation, N_2O_3 is a transient species that readily decomposes upon contact with aqueous solutions ($\tau_{1/2} \sim 1$ ms) forming nitrite,[52]

$$N_2O_3 + H_2O \rightarrow NO_2^- + 2H^+ \quad (8)$$

However, RNS formation through NO autoxidation by O_2 is mostly confined to hydrophobic compartments where the reduced availability of water greatly increases the lifetime of N_2O_3. For example, typical production of 1 μM [NO] in the aqueous phase surrounding an activated macrophage would result in membrane [NO] as high as 10 μM where 1-5% of the total NO produced by the macrophage would undergo autoxidation reaction.[55]

Another route for the oxidation of NO to form RNS, occurs through the rapid reaction of NO with the free-radical anion, superoxide O_2^-, at the diffusion-controlled rate of $6.2 \times 10^9\ M^{-1}\ s^{-1}$,[52] according to :

$$O_2^- + NO\cdot \rightarrow ONOO^- \qquad (9)$$

The remarkable speed of this reaction allows NO to effectively compete with copper, zinc superoxide dismutase (SOD, predominant mammalian isoform except in the mitochondria) which catalyzes the disproportionation of O_2^- at half the rate of Eq. (9). However, the intracellular concentration of SOD is sufficient (3-15 μM) to inhibit the reaction between O_2^- and NO by > 50% and limit the interference of Eq. (9) with NO-based signaling processes when [NO] < 1 μM.[56] At sites of pathogen invasion, inflammatory signals trigger the activation of NADPH oxidase in phagocytic cells to catalyze the reduction of O_2 to O_2^-.[57] The co-localization of this enzyme with iNOS at the cellular membrane and within the phagosome enhances peroxynitrite formation during inflammation. Since O_2^- is anionic, peroxynitrite formation from the reaction of

NO and O_2^- occurs exclusively in aqueous environments where it forms stabilizing intramolecular bonds that increase the lifetime of peroxynitrite by preventing its protonation to form peroxynitrous acid which rapidly decomposes to radical species (Eq. (10), 30%) or nitrate (Eq (11), 70%).[58]

$$\text{HONOO} \rightarrow \text{HO}\cdot + \text{NO}_2 \qquad (10)$$

$$\text{HONOO} \rightarrow \text{(isomerization)} \rightarrow \text{H}^+ + \text{NO}_3^- \qquad (11)$$

However, the major pathway for peroxynitrite scavenging is through its reaction with CO_2 forming the anion $ONOOCO_2^-$ which decomposes within 15 ms to a radical complex, $NO_2/CO_3^{\cdot -}$.

$$\text{ONOO}^- + \text{CO}_2 \rightarrow \text{ONOOCO}_2^- \qquad (12)$$

$$\text{ONOOCO}_2^- \rightarrow \text{NO}_2/\text{CO}_3^{\cdot -} \qquad (13)$$

$$\text{NO}_2/\text{CO}_3^{\cdot -} + \text{NO}\cdot + \text{H}_2\text{O} \rightarrow \text{HCO}_3^- + \text{HNO}_2 + \text{NO}_2 \qquad (14)$$

Eq. (14) shows how high fluxes of NO can alter peroxynitrite chemistry towards a nitrosative form through NO_2 formation which can then react with another molecule of NO to form N_2O_3 according to Eq. (7). Thus, high fluxes of NO can shift the redox balance and the indirect effects of NO from oxidative (NO_2 and $ONOO^-$) to nitrosative (N_2O_3). In addition, an imbalance between NO and O_2^- fluxes leading to higher local $[O_2^-]$ can also deplete peroxynitrite levels through:

$$\text{HOONO} + \text{O}^{2-} + \text{H}^+ \rightarrow \text{O}_2 + \text{NO}_2 + \text{H}_2\text{O} \qquad (15)$$

The NO_2 produced through Eq. (15) rapidly diffuses through the intramembrane space where elevated [NO] can drive N_2O_3 formation Eq. (7) and tip the balance towards nitrosative stress.

1.2 Cytotoxic Effects of Elevated NO

While elevated NO can have a direct cytotoxic effect on cells by disrupting the activity of hemoproteins, the cytotoxic potential of NO mostly arises through its reaction with O_2^- or O_2 to form RNS.[59] Conversion to various oxidative (NO_2 and $ONOO^-$) and nitrosative (N_2O_3) congeners confers on NO the potential to invoke a broad range of reversible and irreversible modifications of various cellular targets. Owing to the high level of reactive oxygen species at sites of infection and neoplasm from the activation of macrophage NADPH oxidase and the high metabolic activity of the replicating cells, the production of elevated [NO] (in the range of 1-5 μM) by iNOS results in significant RNS-mediated damage of DNA, the mitochondria and iron-centered enzymes; activation of pro-apoptotic proteins, including PARP and p53; and disruption of energy metabolism and Ca^{2+} homeostasis.[60] Prolonged exposure to elevated [NO] can overwhelm cellular repair pathways by directly inhibiting/damaging repair enzymes, or by depleting cellular energy levels through the activation of energy intensive NO-detoxification and repair systems and the inhibition of metabolic pathways. The eventual failure of cellular repair systems during continued exposure to elevated [NO] results in the rapid accumulation of cellular damage which activates apoptotic or necrotic pathways leading to cell death. Cell death is described using two distinct pathways: apoptosis, in which cells deliberately activate a built-in death program, and necrosis, which describes the uncontrolled and rapid death of the cell. The actual process by which cell death occurs is perhaps best described as a continuum between necrosis and apoptosis with the contribution of each extreme determined by the extent of cellular damage. If the damage is moderate, a cell might be able to repair itself during growth arrest induced by activated p53 in the nucleus, but if not, p53 is likely to induce apoptosis. If NO-induced stress sufficiently depletes ATP or inactivates pro-apoptotic caspases, cellular resources will be insufficient to carry out apoptosis and the cell will die by necrosis. Single celled organisms are not likely to initiate cell-death under the criteria outlined for apoptosis since they do not have the same obligations of cells in a multi-cellular organism.[61] However, because of vital differences in biological processes, prokaryotes exhibit increased sensitivity to NO and undergo cell-death more rapidly compared to mammalian cells exposed to the same [NO]. The enhanced sensitivity of prokaryotes to NO and RNS can be explained by their relatively higher abundance of Fe/S clusters, which can be degraded by reaction with NO or RNS resulting in mobilization of free iron. The released iron can then bind, oxidize and fragment (through OH production) microbial DNA in the cytosol.

1.2.1 Inhibition of Mitochondrial Function by NO

The targeting of mitochondrial components by NO and its oxidation products greatly impairs energy production through various mechanisms including the nitrosylation of heme-a_3 and inhibition of cytochrome c oxidase; the oxidation and degradation of Fe-S centers in respiratory chain complexes I, II and III, and citric acid cycle enzymes such as aconitase; S-nitrosylation of GAPDH which impairs glycolysis; and the oxidation of mitochondrial thiols and NAD(P)H inducing Ca^{2+} efflux from the mitochondria and initiating a mitochondrial permeability transition (PT).[63] PT is a process that forms 2-3 nm in diameter pores through the mitochondrial membrane and dissipates the membrane potential. Furthermore, $ONOO^-$ has been shown to inactivate mitochondrial Mn-SOD, increasing local O_2^- availability and driving $ONOO^-$ production causing further oxidative damage to mitochondrial components.[64] The rapid oxidation of mitochondrial components by $ONOO^-$ can also drive PT. The critical depletion of ATP stores by repair pathways and the impairment of ATP production as a result of PT can significantly impair Ca^{2+}-ATPase function and effectively eliminate the ability of the mitochondria to maintain a transmembrane calcium gradient. The inability of the damaged mitochondria to regulate cytoplasmic $[Ca^{2+}]$ is exacerbated by the rapid efflux of Ca^{2+} stores from the permeated mitochondria following PT, resulting in a severe disruption of intracellular Ca^{2+} homeostasis.[65] Such rapid degradation of cellular function often results in cell-death through necrosis due to the impairment of apoptotic machinery or the depletion of ATP levels below the threshold necessary to carry out apoptosis.

1.2.2 NO-mediated Targeting of DNA and Induction of Apoptosis

NO and related RNS at high levels can cause DNA damage, including alkylation and subsequent deamination, which can lead to GC to AT, GC to CG, and GC to TA mutations. The deamination of DNA base-pairs and single strand breaks that result from nitrosative damage of DNA activates intensive DNA repair pathways that also produces a heavy strain on cellular energy levels which works concertedly with mitochondrial inhibition to stress cells. DNA damage by NO can increase the amount of the apoptosis mediator, p53, in the nucleus by activating kinases that phosphorylate p53 and inhibit the protein's otherwise rapid proteolysis.[66] The accumulation of a certain level of p53 activity in the nucleus permits the enzyme to block the G1/S transition in the cell cycle and provide adequate time for the repair of damaged DNA before replication recommences; however, severe DNA damage that surpasses the capacity of repair pathways, without posing an imminent risk of necrosis, will prompt p53 to activate apoptotic pathways and commit the cell to apoptosis.[67] In both cases, p53 functions primarily at the transcriptional level, increasing the expression of proteins involved in DNA repair or apoptosis. As outlined above, DNA repair is an energy intensive process and requires the concerted activity of several enzymes to carry out a single function.[68] DNA repair enzymes are actively targeted by NO at different levels and through various mechanisms, *e.g.* the inhibition of ribonucleotide reductase by the combination of NO with a critical tyrosyl radical at the active site which blocks the supply of deoxyribonucleotides necessary for the replacement of damaged DNA.[69] Other key DNA repair proteins, such as AGT, Ogg1, APE1, and DNA-PKcs, are targets of S-nitrosylation by RNS, with modulation their activity, stability, and localization.

1.3 NO, ROS, and RNS Detoxification

1.3.1 Microbial Stress Responses to NO

Since NO demonstrates cytotoxicity at high (μM) concentrations, mechanisms to detoxify NO are crucial to many biological systems.[70] In mammals, the elimination of excess NO is accomplished predominantly through oxidation by oxyhemoglobin.[71] However, this system can be overwhelmed leading to a toxic accumulation of methemoglobin. Denitrifying bacteria and fungi are known to reduce NO to N_2O during denitrification, where nitrate is reduced in a multistep process to either N_2 (bacteria) or N_2O (fungi), as shown: [72]

$$NO_3^- \rightarrow NO_2^- \rightarrow NO \rightarrow N_2O \text{ (fungi)} \rightarrow N_2 \text{ (bacteria)} \qquad (16)$$

Although the reduction of NO_3^- provides a means of anaerobic respiration for fungi and bacteria, the reduction of NO during denitrification does not contribute to the proton gradient or ATP production, but rather, serves only to prevent the accumulation of toxic levels of NO. The reduction of NO is catalyzed by a class of enzymes called nitric oxide reductases (NOR), through the following:

$$2NO + 2e^- + 2H^+ \rightarrow N_2O + H_2O \qquad (17)$$

Two structurally distinct NORs - norV, a flavodiiron protein, and norBC, a dinuclear iron-heme/non-heme protein – have been identified in anaerobically respiring bacteria.[73] Recently, the genome of the enterohemorrhagic *Escherichia coli* (EHEC) strain responsible for a 2011 outbreak in Germany, which resulted in the highest incidence of hemolytic-uremic syndrome on record, was reported to contain a functional norV gene which was required full virulence.[74] In aerobically respiring bacteria, NO detoxification is commonly achieved by conserved flavohemoglobins which catalyze the oxidation of NO to NO_3^-.[75] Common mechanisms by which anaerobically and aerobically respiring bacteria detoxify NO/RNS are shown in Figure 1.2. Stevanin and colleagues found that a mutant strain of Salmonella typhimurium defective for the gene encoding the flavohemoglobin, hmp with NO dioxygenase activity, had reduced survival time when co-cultured with human macrophages

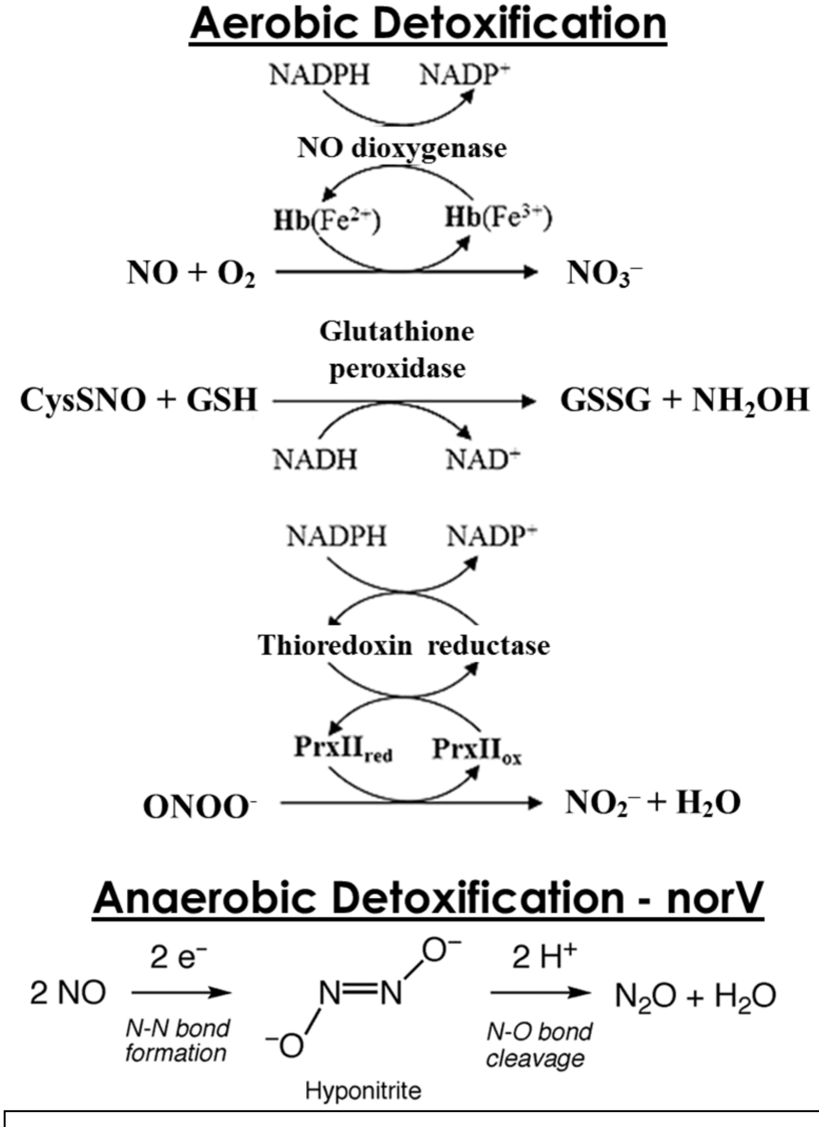

Figure **1.2**. Bacterial NO and RNS detoxification systems.

compared to wild-type.[76] Recently, a similar effect was shown *in vivo* with Δhmp *S. typhimurium* suffering attenuated virulence in a mouse model while iNOS inhibition restored the mutants virulence.[77] Using an experimentally derived and confirmed kinetic model of NO consumption pathways in a liquid culture of *E. coli*, the computer simulated fate of 8-10 μM NO showed that dioxygenation of NO by hmp accounted for 98% of intracellular consumption of NO by aerobically cultured wild-type and ΔnorV strains while the reduction of NO by norV consumed 93% of intracellular NO upon the loss of hmp function by anaerobically cultured wild-type strains compared to a 14% contribution from norV for Δhmp cultured under aerobic conditions.[78] Exposure of pathogenic organisms to NO can result in the up-regulation of a variety of genes that do not provide direct detoxification of NO but rather confer resistance to NO through metabolic or repair activity. A screen of the genes up-regulated under NO-induced stress using a genetic library of *M. tuberculosis* found that deletion of proteasome components (mpa and pafA) or a nucleotide excision repair (uvrB) gene increased the sensitivity of the mutant strains to NO *in vitro* and reduced their virulence in mouse infection models.[79] The proteasome components where shown to function in the metabolic processing of damaged proteins. In addition to enzymatic defense mechanisms, microbes are also known to produce low-molecular-weight thiols in order to sequester NO in a stable nitrosothiol form. A variety of low-molecular-weight thiols have been identified in the cytoplasmic fraction of enteric pathogens and provide effective NO sequestration when present at high intracellular concentrations, such as trypanosothione (excreted by trypanosomes and leishmania), pyocyanin (a pigment of

P. aeruginosa), and homocysteine.[80] While exposure of liquid cultures containing 10^5 cfu mL^{-1} to 200 ppm of NO for 2-6 h was sufficient to eradicate *Staphylococcus* sp., *Pseudomonas aeruginosa*, *Serratia* sp., *Klebsiella* sp. strains, *Enterobacter* sp., *Acinetobacter* sp., *E. coli*, Group B *Streptoccocus*, and *Candida albicans*, the high intracellular concentration of mycothiol present in *M. smegmatis*, a model organism for the causative agent of tuberculosis, provided effective NO sequestration to the same 4 h, 200 ppm dose but was ineffective when the exposure time was double (10 h).[81] Although NO-detoxifying enzymes can provide an effective defense even if the exposure time is increased, rapid saturation of NO-detoxification enzymes can be achieved by increasing the rate of NO delivery and [NO] in the surrounding media. For example, increasing the rate of NO delivery in the above described model of *E. coli* dramatically decreased the rate of NO dioxygenation by hmp from 78.1% in the presence of 9 μM NO to 8.4% in the presence of 34 μM NO due to the competitive inhibition of O_2 binding to the heme active site by NO.[79] The inhibition of hmp activity resulted in a 15-fold increase in the amount of NO consumed by reaction with Fe-S clusters which became the major cellular target in the absence of hmp activity. Since the reported simulations did not include an exogenous source of superoxide, the production of O_2^- by activated leukocytes at O_2-deficient sites of infection could further reduce NO consumption by hmp through the oxidation of NO to RNS and the potential inhibition of hmp by RNS-mediated damage.[82] In light of the importance of NO detoxification systems to the virulence of clinically relevant pathogens, pharmaceutical approaches to inhibit such systems are a plausible alternative to antibiotic therapies for the treatment of infection in immunocompotent patients or as an adjunct to exogenous NO-delivery in order to sensitize resilient infections.[83]

1.3.2 NO and Oxidative Stress

Experimental evidence suggests that NOS activity maybe up-regulated to provide antioxidant defense against endogenously produced ROS during certain pathological conditions.[84] In order for NO to function as a cytoprotectant during oxidative stress, the RNS generated from the reaction between NO and O_2^-, namely $ONOO^-$ and its derived products, must be less perturbing or cytotoxic to the organism than the direct reaction of O_2^- or alternative ROS derived from it, such as hydroxyl radical-related Fe-H_2O_2 complexes, hypochlorous acid, and chloroamines. Another determinant to consider is the cellular resources consumed during the metabolic processing of excess NO and its reaction products, and the impact that will have on the capacity of NADPH-dependent repair and glutathione-dependent antioxidant systems which provide important ROS defense.[84] The glutathione redox buffer centers on the oxidation of the reduced tri-peptide (GSH) by damaging ROS/RNS forming a disulfide (GSSG), according to:[85]

$$2GSH + [O] \rightarrow GSSG + 2e^- \qquad (18)$$

The glutathione redox buffer is one of the most important mammalian defenses against oxidative stress caused by ROS and RNS and comprises a considerable portion of the total antioxidant capacity (TAOC) of mammalian cells.[86] The TOAC provided by the glutathione redox system can be approximated by only considering the contributions of the free-thiol (E_{hc} = GSSG, 2H$^+$/2GSH, where E_{hc} is the half-cell potential for the couple) and the glutathione reducing enzyme, thioredoxin reductase, as a function of its reducing cofactor, NADPH (E_{hc} = NADP$^+$, H$^+$/NADPH). Following the calculations of Schafer and Buettner,[87] the Nerst equation gives E_{hc} (GSSG/2GSH) = −240 mV and E_{hc} (NADP$^+$, H$^+$/NADPH) = −370 mV, and considering a typical cell that contains [GSH] ≈ 5 mM and [NADPH] ≈ 0.1 mM, the TOAC is approximately:

$$\text{TOAC} = (5\text{ mM x -240 mV}) + (0.1\text{ mM x -370 mV}) \qquad (19)$$

Thus, the total half-cell potential of the glutathione redox buffer in a static cell will be -1240 mV mM. It should be noted that this value does not account for the influence of catabolic processes to restore [NADPH], the ability of thioredoxin to increase GSH/GSSG through thiol-disulfide exchange with proteins, and the synthesis of new GSH by glutathione synthase. However, this value was useful for establishing a correlation between the potential and fate of leukemia cells after exposure to different [H_2O_2] in order to achieve E_{hc} ~ 240 mV and promote proliferation; E_{hc} ~ 200 mV and differentiation; and E_{hc} ~ 170 mV and death (using [H_2O_2] = 9-30 μM to induce a +72 mV change with subsequent apoptosis while [H_2O_2] ≥ 100 μM caused rapid necrosis). Since oxidative RNS, such as NO_2 and $ONOO^-$, are known to increase cellular [GSSG], similar to H_2O_2, the ability of NO to promote the proliferation and differentiation of keratinocytes, while at the same concentration, eradicating microbial pathogens (which have a lower TOAC), maybe mediated by changes in the cellular potential of these organisms. The lower TOAC of microbial cells (compared to mammalian cells) results in increased sensitivity to elevated NO and provides a firm basis for reducing the microbial burden of infected wounds by the targeted delivery of a controlled dose of NO.[88]

1.4 Therapeutic Intervention in NO-pathways

NO-releasing drugs are pharmacologically active compounds that have the potential to treat pathological conditions resulting from a quantitative or functional NO deficiency.[89] NO insufficiency may result from a net deficit of NO in the tissue, impaired NO availability, altered NOS activity, or the inhibition of NO mediated responses.[90] In such cases, a decrease in effective [NO] diminishes the regulatory influence of NO-based signaling or weakens the immune response to the detriment of cellular and/or tissue function. The decreased [NO] that results from the dysregulation or malfunction of eNOS has been implicated in the underlying pathophysiology of cardiovascular diseases while the impaired function of iNOS is associated with immunodeficient or autoimmune disorders.[91,92] In such cases, the modulation of NO bioactivity has been achieved by the administration of NO donors which function as sources or surrogates of NO in order to restore the regulatory effects of NO.[89] Pharmaceutical agents that modulate NO-dependent pathways have also been utilized to both restore vascular function and decrease the harmful effects of NO over-production. NO production by eNOS and iNOS (under pathological conditions) can function as a beneficial vasodilatory agent as well as a cytoprotective/anti-inflammatory agent to inhibit the adhesion of activated neutrophils to endothelial walls and preventing the subsequent release of cytotoxic ROS.[90] Conversely, an unregulated increase in plasma or tissue [NO] also has pro-inflammatory effects which include hyper-vasodilation, cellular edema, cytotoxic damage, and the release of cytokines.[93] Consideration of the multifaceted effects of NO in cardiovascular and immunological health is necessary to properly guide current administration of available NO-releasing drugs and to instruct future choices in the development of new pharmaceutical agents.[94]

1.4.1 NO Donors as Biophysiological Tools in the Indentification of EDRF

The therapeutic use of exogenous NO was first reported in 1867 by Thomas Lauder Bruton, who noted that insufflation of amyl nitrate caused rapid relief of angina pectoris in ischemic patients.[95] Although the vasodilatory property of alkyl nitrates was thought to play a role in the observed effects, the exact pharmacological effect of nitrovasodilators (a misnomer) wasn't identified until nearly a century later following two paramount discoveries. The first breakthrough came in 1977, when Ferid Murad and co-workers reported that free NO was produced during the decomposition of several commonly used nitrovasodilators under physiologically relevant conditions along with the nearly identical vasodilatory properties of the NO-releasing nitrovasodilators and $NO_{(g)}$.[96] In the next decade, the work of Luis Ignarro and Robert Furchgott demonstrated that the vasodilatory property of $NO_{(g)}$ result from the nitrosylation and activation of sGC to initiate a signal cascade leading to relaxation of the vascular smooth muscle and dilation of the blood vessel.[97] The identification of NO as a regulatory molecule stimulated further investigation eventually establishing the biological effects of NO in blood pressure regulation, neurotransmission, cellular protection, innate immune response, and cellular apoptosis.[98] It is now evident that NO is enzymatically produced as part of the evolutionary choice for the armamentarium of our body's own defenses against infection and neoplastic proliferation.[99] This knowledge has inspired researchers to emulate the natural immune response at malignant sites through the targeted delivery of cytotoxic doses of NO from molecular stores under controlled conditions.[100]

1.4.2 Calcium Channel Blockers

1,4-Dihydropyridine calcium channel blockers (CCBs) have been used for many years to relieve chronic angina pectoris and hypertension and include the FDA labeled drugs nifedipine, nitrendipine, and lacidipine.[101] 1,4-Dihydropyridine CCBs function at the level of intracellular Ca^{2+} in the vascular smooth muscle by inhibiting the flow of current at L-type calcium channels, reducing intracellular [Ca^{2+}] thereby inducing smooth muscle relaxation. This effect is also supplemented by the ability of 1,4-Dihydropyridine CCBs to induce NO release from the vascular endothelium.[102] This class of compounds can also restore impaired endothelium-derived vasodilatory pathways by increasing NO availability through an antioxidant effect that prevents NO-scavenging by ROS.[103] While 1,4-dihydropyridine CCBs function primarily by inhibiting L-type calcium current in the vascular smooth muscle to promote vasorelaxation, CCBs are also believed to promote vasorelaxation through a secondary, indirect mechanism that functions by inducing NO release from the vascular endothelium.[104]

1.4.3 ACE-Inhibitors

Angiotensin-converting enzyme "ACE" converts angiotensin I (ANGI) to angiotensin II (ANGII), and degrades Bradykinin. ANGII is a peptide-based hormone that promotes vasoconstriction and a subsequent increase in blood pressure.[105] Bradykinin is another peptide hormone that stimulates endothelial cells to release vasodilating substances, in particular, NO. Due to the decrease in ANGII and the increase in brandykinin that results from blocking ACE activity, drugs known as ACE inhibitors are used to lower blood pressure and promote the release of endothelial NO.[106] Additionally, ACE inhibitors increase the bioavailability of NO through an indirect antioxidant effect involving the inhibition of ANGII synthesis which is known to stimulate superoxide production.[107] The ability of ACE inhibitors to modulate NO-production via bradykinin are still not fully understood but possible mechanisms include: (a) inhibition of ACE catalyzed catabolism of kinins; (b) interference in kinin degradation pathways activated by ANG-derivatives and (c) direct potentiation of kinin receptor response on bradykinin stimulation.

1.4.4 L-Arginine Supplementation

Oxidative modification of LDL (oxLDL) can disturb vasorelaxation or act directly against vasodilating substances.[108] OxLDL may impair the uptake of L-arginine and, along with native LDL, uncouple eNOS activated pathways.[109] Interestingly, physiological differences can affect arterial segments from different regions. NO produced by iNOS may inhibit the oxidation of LDL and, thus, have a protective role during LDL oxidation.[108] L-arginine administration partially restores endothelium-dependent vasodilation in cases of hypercholesterolemia and dilates coronary stenosis in patients with chronic hypertensive disorder (CHD).[110] L-arginine supplementation for six months also improves the function of coronary small-vessels and is associated with a significant improvement in symptoms. Therefore, L-arginine administration could be a therapeutic option for patients with endothelial dysfunction and non-obstructive CHD. L-arginine supplementation has been shown to provide significant clinical improvement in the dilation of diseased arteries in more than 70% of treated patients with CHD.[111]

1.5 Exogenous NO Donors

The desire to modulate NO concentrations at targeted locations through activation of exogenously derived, stable sources of NO has inspired research in the area of designed molecules that release NO on demand (NO donors).[112] A variety of molecular structures are known to decompose and release free NO, following activation by oxidants, thiols heat, pH, light, or enzymatic processing. A few of those compounds with favorable NO release properties have been developed for clinical application, including alkyl nitrates, *S*-nitrosothiols, *N*-diazeniumdiolates (NONOates) and metal nitrosyls. The delivery of NO to a specific biological target requires the ability to localize a sufficient concentration of the NO donor at a specific site and initiate NO-release in a controlled or at least predictable manner. Although control over enzymatic pathways or biological conditions such as heat, pH, or redox state in the body is extremely difficult, light provides a particularly convenient trigger to activate NO release from molecular stores.[113] Over the past few years, a variety of photoactived NO donors have been synthesized and their NO delivery capacities have been reported.[114] In order to localize NO-donors within a specific site, they have been incorporated into biocompatible matrices, yielding NO–donating composite materials.[115] Such composites have shown utility as a coating for implantable medical devices to prevent biofouling, and are promising antineoplastic and anti-microbial agents, as demonstrate by results obtained *in vitro* and in animal models. Photoactivated NO-donating composite materials are especially well-suited for the controlled delivery of high doses of NO to malignant sites of microbial infection and neoplasia while retaining the photoproducts within the host matrix.[116]

1.5.1 Organic Nitrite and Nitrate Esters

Organic nitrate esters, such as nitroglycerin, pentaerithrityl tetranitrate, isosorbide triinitrate, and nicorandil, represent the prototypical class of nitrovasodilators and have been used for many years to regulate blood pressure in the treatment of cardiovascular diseases.[117] Organic nitrite esters, such as amyl nitrite and isobutyl nitrite, are a similar class of compounds that induce rapid vasodilation upon inhalation. Organic nitrate esters are pro-drugs requiring enzymatic reduction and denitration by mitochondrial aldehyde dehydrogenase to generate bioactive NO. Complications during therapeutic administration of organic nitrate esters are common and include potentially adverse hemodynamic effects, drug tolerance, lack of selectivity, and limited bioavailability.[118] The contraindications of nitrates limit their therapeutic utility with extra consideration given to the development of cross-tolerance to endothelium-derived NO that may involve increased oxidative inactivation of endogenously produced NO and the “uncoupling” of eNOS activity with vasorelaxing pathways.[118b] Low-molecular-weight thiols, ascorbate, L-arginine, tetrahydrobiopterin, hydralazine, angiotensin converting enzyme (ACE) inhibitors, and folate have been successfully used to reverse or prevent nitrate tolerance.[119]

1.5.2 *N*-Diazeniumdiolates

N-diazeniumdiolate (NONOates) functionalities spontaneously decompose generating two equivalents of NO under physiological conditions.[112c] The NO releasing dissociation reaction follows a simple pseudo-first-order rate laws, but in some cases the rate can be markedly effected by the formation of bimolecular complexes at higher concentrations and by the presence of metal ions. Although a variety of nucleophiles including sulfur, oxygen, aromatic and aliphatic carbon, and nitrogen centers can be modified with the $[N(O)NO]^-$ group, *N*-Diazeniumdiolates prepared by the reaction of primary or secondary amines with NO at elevated pressure are of particular interest due

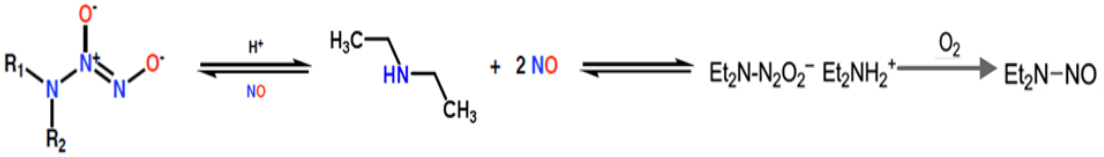

Figure **1.3**. Schematic representation of the mechanism of NO-release from diethylamino-*N*-diazeniumdiolate following hydration, and the mechanism by which *N*-diazeniumdiolates are converted to carcinogenic *N*-nitrosamines, in aqueous solutions.

to their ability to spontaneously release NO. The *N*-bound $[N(O)NO]^-$ derivative of diethylamine, (*Z*)-1-(*N*,*N*-diethylamino)-diazen-1-ium-1,2-diolate (DEA/NO), prepared by Drago and co-workers in 1960 was the first reported *N*-diazeniumdiolate to spontaneously release free NO in aqueous solutions.[120] By varying the nature of the R groups attached to the amine, it is possible to modulate the rate and duration of NO release from the resulting *N*-diazeniumdiolates with half-lives ranging from 1.8 s for proline-*N*-diazeniumdiolate (PROLI/ NO) to 20 h for bis(2-amino-ethyl)-amine-*N*-diazeniumdiolate (DETA/NO), as determined at 37ºC in pH 7.4 PBS.[112c] NMR studies have revealed that the NO released from *N*-diazeniumdiolates can be autoxidized to the nitrosating agent, N_2O_3, which can then recombine with the free amine to form potentially carcinogenic *N*-nitroso species, according to the pathway shown in Figure **1.3**.[121] In light of the known carcinogenicity of certain secondary N-nitrosoamines, researchers have focused on developing *N*-diazeniumdiolates whose corresponding *N*-nitroso derivatives are considered non-carcinogenic, for example PROLI/NO whose potential metabolite *N*-nitrosoproline is a normal constituent of human urine, or by covalently attaching the *N*-diazeniumdiolate functionality to insoluble matrices that limit the limit the release of any byproducts, including nitrosated species. Examples from the literature of NO-donating materials functionalized with *N*-diazeniumdiolate groups are presented below.

1.5.3 *S*-Nitrosothiols

S-nitrosothiols (RSNO) are a class of naturally occurring and synthetic NO-donating compounds that are synthesized by the nitrosation of reduced thiols.

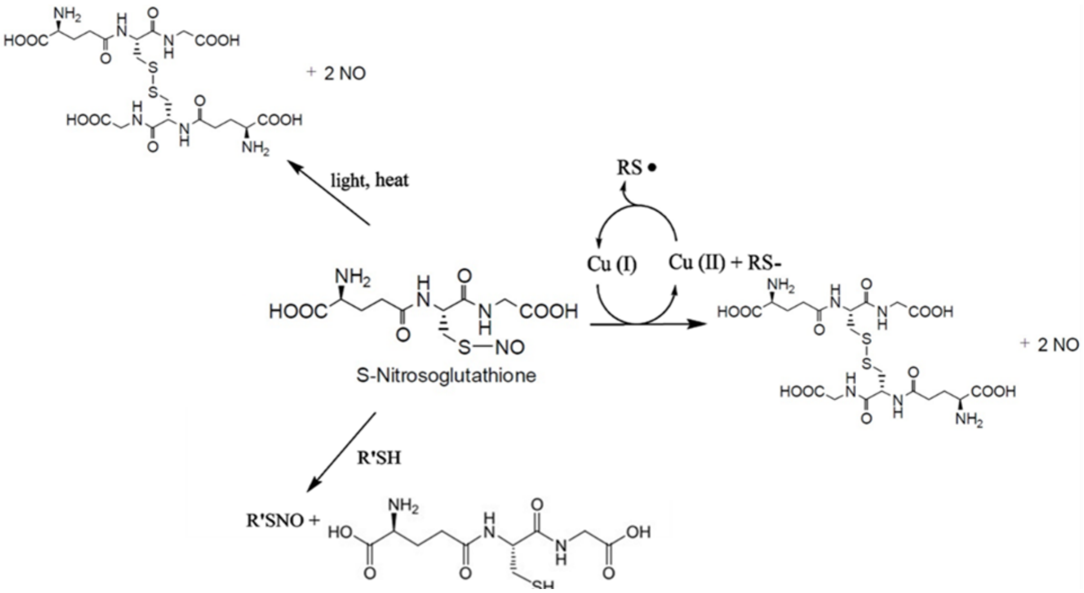

Figure **1.4**. Decomposition pathways of the S-nitrosothiol, S-nitrosoglutathione. Free NO is released in the presence of light, heat, and transition metal ions, producing a thiyl radical that rapidly combines with a nearby S-nitrosothiol producing free NO and a disulfide bond. S-nitrosothiols also donate NO to another free thiol through a trans-nitrosation reaction, provided more stable compounds are produced.

Commonly used NO donors from this class of compounds include *S*-nitroso-glutathione, *S*-nitroso-N-acetylpenicillamine, and *S*-nitroso-albumin.[122] In some cases, investigators have chosen to modify existing pharmacological agents with *S*-nitrosothiol groups in an effort to exploit the properties of the parent compound. Through appropriate selection of the R group, the stability of *S*-nitrosothiols can be modified to promote NO release upon stimulation with heat, pH, light, transition metal ions, and other thiols.[123] *S*-nitrosothiols also donate NO by a trans-nitrosation mechanism involving the transfer of NO to another free thiol, if a more stable compound is produced (Figure **1.4**).[124] *S*- nitrosothiols have potential clinical utility as NO donors, distinct from current NO-donating therapeutics, based on their ability to gain access to the intracellular compartment by the catalytic action of plasma membrane-bound protein disulfide isomerase and associated trans-nitrosation reactions. Additional advantages of *S*-nitrosothiols, over existing NO donors, are their limited potential for inducing oxidant stress and NO-tolerance in vascular cells, which are common side-effects associated with the long-term administration of organic nitrates and SNP.[125] Initial small clinical studies suggest potential benefits from *S*-nitrosothiol administration in a variety of cardiovascular disorders.[126]

1.6 Metal Nitrosyls as NO Donors

Metal complexes are well-suited for pro-drug approaches for therapeutic applications since the metal center can bind and carry drug molecules as ligands and release them under controlled conditions.[113,127] Despite the enormous success of cis-platin (*cis*-[PtCl2(NH3)2]) as an anticancer drug and sodium nitroprusside as a vasodilatory agent, metal complexes have not been widely exploited by the pharmaceutical research community.[128] Metal nitrosyls are formed by the binding of NO to transition metal centers through two distinct binding modes depending on the oxidation state of the metal.[129] With metals in a low oxidation state, NO forms nitrosyls with a bent M-N-O bond angle (140^o). Formally, NO is considered as a one-electron donor in such cases. In the case of metals in a higher oxidation state, NO transfers its unpaired electron to the partially empty out-of-plane d orbital of the metal along with a lone pair to form a linear M-N-O bond (usually 170-180°) between the metal and the nitrogen atom (*linear* M-NO bond). In such cases, NO is considered as a three-electron donor in such cases and acts more as an NO^+ unit. The variability of the electron density transferred from NO to the metal center can make it difficult to assign the oxidation states of both NO and the metal center in linear metal nitrosyls. A special notation was devised in 1974 by Enemark and Feltham to denote a metal–NO bond, $\{M\text{-}NO\}^n$, where n is.the total number of electrons in the metal d plus the NO π^* orbital.[130] For example, $\{Ru\text{-}NO\}^6$ could represent one of the two possible combinations of formal oxidation states of the metal center and NO, namely, Ru(III)-NO or Ru(II)-NO^+. Depending on the nature of the metal nitrosyl bond, NO lability can be stimulated by light through photo-excitation of a MLCT band that transfers electron density from metal centered orbitals to low-energy excited state MOs with strong metal-NO anti-bonding character.[114] The energy required to activate such behavior can be varied by smart selection of the ligand sphere.

1.6.1 Sodium Nitroprusside

The $\{Fe\text{-}NO\}^6$ nitrosyl, sodium nitroprusside ($Na_2[Fe(CN)_5(NO)]$, SNP), contains a Fe(III) coordinated nitrosyl group with a near linear Fe-N-O bond angle which completes an octahedral ligand set with five other strong, σ-donating CN^- ligands.[115,131] The mechanism of *in vivo* NO release is a two-step process beginning with a one-electron reduction of the Fe(III) center by endogenous reductants, namely thiols like glutathione, to afford a semistable ferrous species that readily loses the *trans*-coordinated CN^- ligand to relieve excess negative charge at the metal center.[133] The pentacoordinated intermediate $[Fe(CN)^4(NO)]^{2-}$ eventually decomposes to afford free NO. SNP has been in clinical use as a vasodilatory drug (Nitropress) for quite some time (FDA approval in 1974), and remains an effective, reliable, and commonly used drug for the rapid reduction of significant arterial hypertension regardless of the etiology.[132] It is one of the most commonly used vasodilators for intraoperative control of blood pressure. The utility of SNP is limited by the need to administer it parenterally, its ability to induce NO tolerance in the vascular smooth muscle, and the potential for the development of thiocyanate toxicity with prolonged administration (especially in rhodanase-deficient individuals).[134] Severe toxicity due to the loss of CN^- co-ligands has been observed in patients with compromised liver and renal function.[135] Careful attention to infusion rates, particularly in patients at risk for depleted thiosulfate stores, is mandatory, and the use of other drugs in conjunction with or instead of SNP must is always considered. Despite its toxicity, SNP is popular because it is often the most effective drug in certain clinical cases, most notably to relieve cranial pressure during traumatic brain injury.[136]

NO photo-release from SNP is observed following absorption of 420 nm light with an efficient quantum yield of NO release, ⎞$_{420}$ = 0.201 ± 0.007.[137] Excitation of a MLCT photoband results in the formal transfer of an electron to NO^+ producing an intermediate Fe(III)-NO species that rapidly releases free NO in solution.[138] The solvent-assisted decomposition of the $[Fe(CN)_5]^{2-}$ photo-product results in the release of free CN^- and produces the Fe(II)-Fe(III) pigment, Prussian blue. Thus, loss of ancillary CN^- following both the “dark” and the “light-assisted” modes of NO release complicates the clinical administration of SNP.

1.6.2 Iron-sulfur-nitrosyl Complexes

Synthetic iron–sulfur cluster nitrosyl complexes like Roussin’s red salt (RRS, $[Fe_2S_2(NO)_4]^{2-}$), Roussin’s black salt (RBS, $[Fe_4S_3(NO)_7]^-$), and tetranitrosyltetra-m3-sulfido-tetrairon ($[(Fe(NO)S)_4]^-$) are analogous to the protein iron–sulfur clusters that function as electron “transformers” to mediate electron transfer between donor and acceptor groups during enzymatic redox catalysis.[139] These complexes have bright colors in solution due to strong absorption bands in the visible region. NO photorelease from Fe-S cluster nitrosyl complexes has been studied extensively by Ford *et al.*[140] Irradiation of RRS with 546 nm light in aerobic aqueous solution results in NO release (quantum yield values $\phi_{546} = 0.14–0.40$) and the quantitative production of RBS. The less-photoactive RBS ($\phi_{546} = 0.001–0.004$) undergoes photodecomposition to give mixed Fe(III) precipitates and free NO. Irradiation of RBS and $[(Fe(NO)S)_4]^-$ with a low-power laser at 515 nm (and 458 nm) resulted in the release of sufficient NO to induce vasorelaxation in rat aorta muscle rings during tissue bath experiments.[139] In addition, photo-delivery of NO from RRS greatly sensitized hypoxic cultures of Chinese hamster V79 cells to γ-radiation-induced damage.[141] However, further investigation of the potential utility of Fe-S cluster nitrosyl complexes as biologically acceptable NO donors in radiation oncology had limited success due to the severe toxicity observed with these complexes.

1.6.3 Photoactive Metal Nitrosyls Derived from Ligands with Carboxamido-*N* Donors

Although the photolability of NO from transition metal nitrosyls has been demonstrated in a variety of systems, our laboratory has focused on the synthesis of physiologically stable transition metal nitrosyls that demonstrate rapid NO photorelease upon stimulation with low-power light (in the mW range) of selected wavelengths.[142,143] During the past few years, we have developed a series of designed ligands with peripheral functionalities that could be systematically altered using theoretical predictions based on DFT calculations to tune the photoactivity of the metal nitrosyls and progressively red-shift the photoband (electronic transition that leads to NO release) across the UV, visible and near-infrared (NIR) regions from 350 to 1000 nm.[144] Our synthetic efforts have focused on two sets of ligand scaffolds, namely those derived from the pentadentate ligand frame, $PaPy_3H$, containing a single carboxamido-*N* donor and the tetradentate ligand frame, H_2bpb, containing two carboxamido-*N* donors (H's are dissociable carboxamide protons). The pentadentate ligand design provides enhanced chelation to substitutionally labile metal centers which has allowed the synthesis of stable Mn nitrosyls with remarkably high quantum yields and photoactivity in the visible and NIR region up to 1000 nm. The tetradentate ligand design has been used to isolate highly stable Ru nitrosyls that are capable of tightly binding a functional ligand at the open sixth coordinate site *trans* to NO. Thus far, we have utilized the open sixth site to coordinate ligands functionalized with a vinyl group that copolymerizes with chain forming monomers to provide a covalent tether between the metal nitrosyl and the polymer chains, and photosensitizing fluorescent dyes that absorb light and transfer the harvested photo-energy to the M-NO unit in order to enhance the quantum efficiency and sensitivity to lower energy light of NO photorelease. As described below, the fluorescence of the dye-sensitized metal nitrosyls allows easy tracking of the NO-donor in the cellular matrix and provides an on/off signal for NO release. Metal nitrosyls derived from bpb^{2-} and $PaPy_3^{--}$, as well as composite materials containing these NO donors, have been successfully employed for the light-controlled delivery of cytotoxic doses of NO to cancer cells and microbial pathogens in several *in vitro* experiments.[115]

1.6.4 Metal Nitrosyls Derived from the Pentadentate Ligand, $PaPy_3H$

The pentadentate ligand, $PaPy_3H$ (*N*,*N*-*bis*(2-pyridylmethyl)amine-*N*-ethyl-2-pyridine-2-carboxamide), was the first designed ligand used in our laboratory for the successful synthesis of metal nitrosyls that release NO under the control of low-power visible light.[145] This ligand includes features observed in the metal-chelating locus of the microbial enzyme nitrile hydratase (Fe-NHase), which exhibits rapid photorelease of NO from its Fe(III) centre upon exposure to visible light (sunlight in Nature) to initiate diurnal activity.[146] These features include (i) a unique deprotonated carboxamido-*N* donor group that serves to stabilize the Fe(III) oxidation state observed in the natural enzyme and (ii) a negatively charged donor (thiolate in the case of Fe-NHase) *trans* to NO which could promote photorelease through the *trans*-labilization effect. Upon reaction with $NO_{(g)}$, the Fe(III) complex derived from the deprotonated $PaPy_3^-$ ligand afforded $[Fe(PaPy_3)(NO)]^{2+}$ (**1**, Figure 1.5), which was the first reported metal nitrosyl to readily release NO upon illumination with low-power visible light ($\phi_{500} = 0.185$).[145] Although the results of this study demonstrated the capability of the $PaPy_3H$ ligand to afford a photoactive metal nitrosyl, the iron nitrosyl **1** showed limited stability in aqueous solutions. Replacement of the Fe-center of **1** with its more stable, second row congener, Ru, afforded the $\{Ru\text{-}NO\}^6$ nitrosyl, $[Ru(PaPy_3)(NO)]^{2+}$ (**2**, Figure 1.5), which demonstrated excellent stability under biological conditions and released NO upon illumination with low-power UV light (5–20mW).[147] The structural integrity of **2** permitted its use in biological assays including the delivery NO to myoglobin and reduced cytochrome *c* oxidase (74), papain (a cysteine protease) (75), and sGC (76) in rat aorta muscle rings to promote vasorelaxation in tissue bath experiments.[148] Therapeutic development of this nitrosyl was not pursued, however, due to the detrimental effects of UV light to biological systems. The isoelectronic Mn(II) nitrosyl, $[Mn(PaPy_3)(NO)]^+$ (**3**, Figure 1.5), demonstrated more covalent binding of NO as a result of the lower oxidation state of the group 7 metal center.[149] Thus, **3** is very stable in biological media, yet, demonstrates visible light photoactivity due to the lower energy electronic transitions of first row transition metals. Further red-shift of the NO-releasing photoband was achieved by extending the conjugation of the ligand frame through substitution of the pyridine donor (Py) with a quinoline ring (Q), as in the Mn(II) nitrosyl $[Mn(PaPy_2Q)(NO)]^+$ (**4**, Figure 1.5).[150] **4** was the first reported metal nitrosyl to demonstrate stability under biological conditions and low-power NIR light (2mW) activation up to 900 nm. The efficient photorelease of NO from the $\{M\text{-}NO\}^6$ complexes of the $PaPy_3^-$/$PaPy_2Q^-$ ligands upon exposure to visible light ($\phi_{550} =$

0.38 and 0.70 for **3** and **4**, respectively) and NIR-light (**4)** are quite in contrast to the modest photoactivity of the corresponding $\{Ru\text{-}NO\}^6$ complex (**2**) that is limited to the UV region. Density functional theory (DFT) and time-dependent DFT (TD–DFT) studies on the $[M(PaPy_3)(NO)]^{n+}$ (M=Fe, Ru, Mn) series of nitrosyls indicate that irradiation of these $\{M\text{-}NO\}^6$ species with 350–500 nm light activates NO photorelease through a *direct mechanism* involving excitation of symmetry-allowed electronic electronic transition(s) originating in $d_\pi(M)$-π^*(NO) bonding orbital with partial carboxamide character and populate orbitals with $d_\pi(M)$-π^*(NO) anti-bonding character.[144] In the case of the Mn nitrosyls, an additional *indirect method* for NO photorelease occurs by visible and NIR light excitation of an initial low-energy, symmetry-allowed MLCT transition originating in the non-bonding d_{xy}(Mn) orbital and populating orbitals with predominantly equatorial ligand, Py/Q(π), character. These orbitals are energetically matched with a triplet excited-state with $d_\pi(M)$-π^*(NO) anti-bonding character which permits intersystem crossing and population of NO dissociating states that are inaccessible through direct photo-excitation due to their

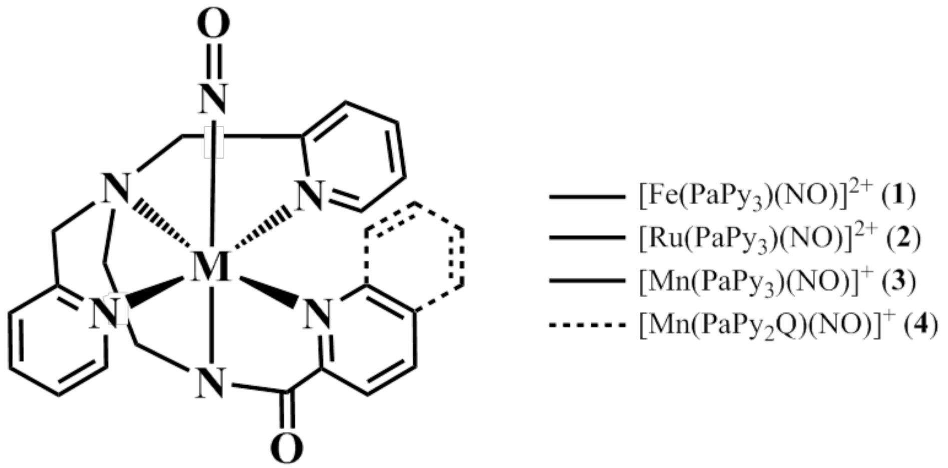

Figure **1.5**. Schematic of metal nitrosyls with $PaPy_3^-$ type ligands.

symmetry-forbidden nature.[151] The intimate involvement of ligand-centered orbitals in the indirect mechanism of NO photorelease from these Mn nitrosyls allows adjustment of the photoactivity to the desired wavelength of light through judicious modification of the ligand frame.[143] For example, we have now synthesized Schiff base ligands with imine-N donors conjugated to a Py ($SBPy_3$) or a Q ($SBPy_2Q$) donor. The metal nitrosyls derived from these designed Schiff base ligands, namely $[Mn(SBPy_3)(NO)]^{2+}$ (**5**) and $[Mn(SBPy_2Q)(NO)]^{2+}$ (**6**), demonstrate enhanced NO photorelease kinetics in comparison with the carboxamide-based nitrosyls **1**–**4** and sensitivity to low-power (5–20 mW) light up to 1000 nm.[152] However, the low stability of the Schiff base Mn-nitrosyls in aqueous solutions has limited investigations to organic solvents thus far.

1.6.5 Metal Nitrosyls Derived from the Tetradentate Ligand, H_2bpb

The tetradentate ligand frame, 1,2-*bis*(pyridine-2-carboxamido)-benzene (H_2bpb^{2-}, Figure 1.6) and its derivates have been used in the synthesis of stable Ru nitrosyls with an open coordination site that can bind a third, functional ligand *trans* to NO.[153] Deprotonated bpb^{2-} coordinates metal centers in a planar fashion, similar to naturally occurring porphyrins with four N-donor atoms and two delocalized electrons across a conjugated set of aromatic rings. Ru nitrosyls derived from bpb^{2-} and related ligands containing systematic peripheral substitutions have shown that a progressive red-shift of the λ_{max} of the photoband can be achieved by careful selection of the

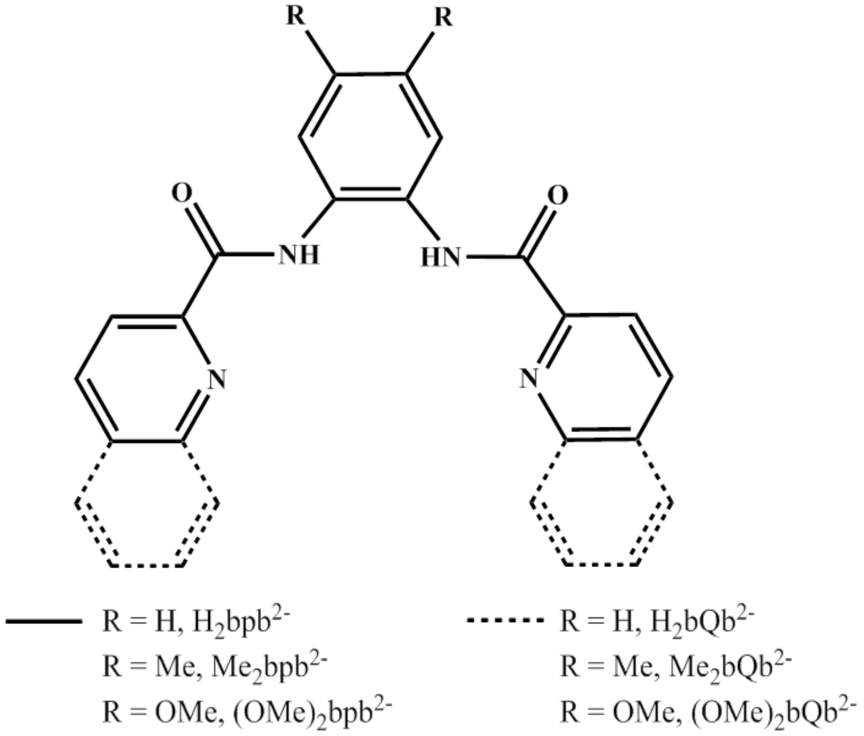

Figure **1.6**. Structure of bpb^{2-} type ligands

substituents. Attachment of electron-donating groups of increasing donor strength (H < Me < OMe) to the phenyl ring of the phenylenedicarboxamide (PDA) region of the ligand frame causes a red-shift of the π(Ru–NO) → π*(Ru–NO) transition.[153,154] This transition can be further red-shifted by extending electron conjugation in the ligand frame through the substitution of pyridine donors with quinoline (Q) or isoquinoline (IQ1) groups.[154] The appropriate combination(s) of substituents lowers the energy of NO releasing electronic transitions by the contribution of ligand character into the ground state (π(Ru–NO)) and excited state (π*(Ru–NO)). [143] Although early attempts to alter the equatorial ligand frame of Ru nitrosyls successfully lowered the energy of the photoband into the visible region, the impact on the quantum efficiency of NO release was quite modest (ϕ_{500} =0.01–0.05), and hence the designed nitrosyls were not effective for the delivery of the high doses of NO that are necessary to induce cytotoxic effects in malignant cells and pathogens. Additional photosensitization was achieved by the *direct* coordination of dye chromophores (as light-harvesting antennae) to the metal center of the Ru nitrosyls.[155] For example, when the fluorescent dye, resorufin (Resf; ε_{600} =105 000 M^{-1} cm^{-1}), was directly attached to the Ru center of the metal nitrosyls, enhanced NO photorelease was observed with a quantum yield at 500nm (ϕ_{500}) in the range of 0.20–0.30.[156] The enhanced photoactivty of dye-sensitized nitrosyls results from the effective intermixing of strong Resf $\pi \rightarrow \pi^*$ transition(s) with metal nitrosyl transitions responsible for NO photorelease. The utility of the dye-tethered Ru nitrosyls in combating malignancy was demonstrated *in vitro*. When MDA-MB-231 human breast cancer cells were incubated with the Resf-tethered Ru nitrosyl [(Me_2bpb)Ru(NO)(Resf)] (**7**), uptake of the NO donor was visualized by the red fluorescence of the diamagnetic NO-bound nitrosyl. No loss of viability was observed when these cells were kept in the dark. However, exposure of the cells to visible light (300mW) for 1 min was followed by the immediate release of NO from **7** and the eventual apoptosis of the cells after 6 h (as indicated by DNA fragmentation and cell wall blebbing). Complete loss of viability was noted within 24 h. These results demonstrate that selective NO delivery to malignant sites can be achieved with designed metal nitrosyls under the complete control of light. Another advantage of the dye-tethered nitrosyls is the ability to track their bio-distribution of down to the cellular level and monitor NO photorelease by the loss of the fluorescent signal. Upon NO photorelease, the diamagnetic Ru nitrosyl is converted into a paramagnetic Ru(III)

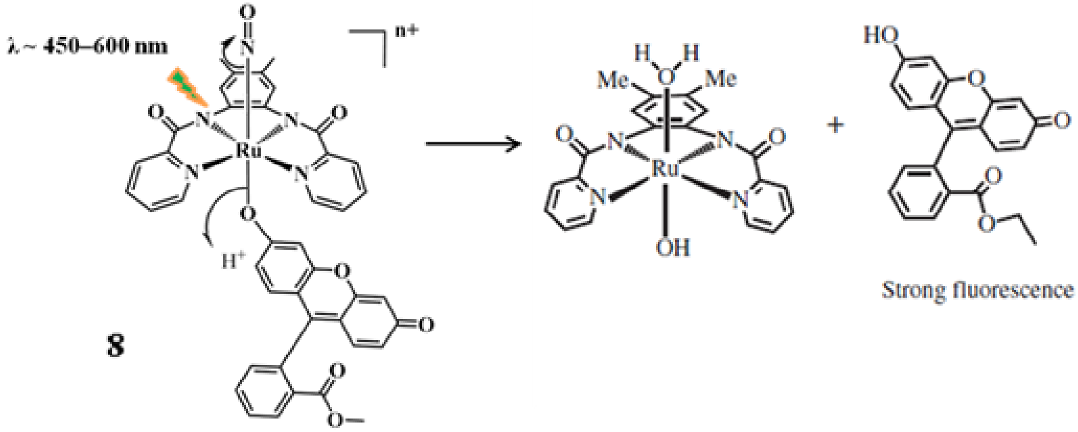

8

Figure **1.7**. "Turn on" fluorescence upon NO photorelase from [Ru(Me_2bpb)(FlEt)(NO)] (**8**) in aqueous media.

photoproduct that quenches the fluorescence of the attached Resf. We have recently reported an improved system that demonstrates 'turn on' fluorescence following NO photorelease from [Ru(Me_2bpb)(FlEt)(NO)] (**8**, Figure 1.7) in aqueous media due to solvent assisted-displacement of the weakly bound dye, fluorescein ethyl ester (FlEt), from the aquated Ru(III) photoproduct.[157] The free FlEt fluorophore demonstrates a dramatic rise in fluorescence compared to the dye conjugated nitrosyl, **8**, providing a 'turn on' signal for NO photorelease in aqueous (biological) solutions.

1.7 NO-Delivery Systems

There has been considerable long-term interest in the development of NO-delivery systems that can be used to localize NO-donors to a targeted site, modulate the kinetics of NO release from molecular stores, and minimize potentially cytotoxic interactions between NO-donors or their reaction-products and the treatment site.[115,158] Since NO is short lived, highly reactive and diffuses only a short distance *in vivo*, NO-donors have been incorporated into various biocompatible matrices that can be applied directly to the treatment site and localize the desired amount of the NO-donor in proximity of the downstream target(s). Numerous NO-donating composite materials have been reported using a range of biocompatible scaffolds, including fabricated biomolecules, dendrimers, liposomes, inorganic and organic nanoparticles, semiconductor quantum dots, carbon nanotubes, and mesoporous ordered materials.[115,116] Biological molecules, such as fibrin and herapin, have been functionalized with NO-donating groups and processed to afford an NO-releasing material that that can be coated onto implantable medical devices in order to prevent biofouling.[159] The appendage of *N*-diazeniumdiolate groups to cross-linked polyetheleneimine microspheres was reported to extend the half-life of NO-release to 51 hours.[160] Application of the microspheres to vascular grafts prevented thrombosis and restenosis formation in animal models. Similarly, bovine serum albumin (BSA) can be covalently modified to bear multiple RSNO groups, which possess vasodilatory and anti-adhesive properties.[161] The advantages of this material include the avidity of the sub-endothelial matrix for albumin, a long half-life *in vivo*, and the ability of *S*-nitrosothiols to serve as a local depot of NO via trans-nitrosation reactions mediated by low-molecular-weight *S*-nitrosothiol intermediates. Sol-gel chemistry provides a convenient route for the incorporation of *S*-nitrosothiol and *N*-diazeniumdiolate NO-releasing groups into a readily cast silica matrix for the coating of implanted devices and sensors.[162] Sol-gel derived from the co-condensation of an amine functionalized silane, *N*-(6-aminohexyl)-*N*-aminopropyltrimethoxysilane, and an alkyltrimethoxysilane, isobutyltrimethoxysilane, was used to coat medical-grade stainless steel implants with a thin layer of silica containing covalently tethered primary amines.[163] Following curing and drying, the free amine were exposed to $NO_{(g)}$ forming NO-releasing *N*-diazeniumdiolate groups. The tissue surrounding the *N*-diazeniumdiolate functionalized implants demonstrated reduced foreign body response and improved vascularization in a rat model.[164] Although the NO released from such coatings has been reported to reduce biofouling of indwelling devices, the brittleness of dehydrated sol-gels can result in potentially fatal fragmentation making such coatings inappropriate for vascular implants.[115] However, it may be possible to improve the durability of sol-gels by blending or coating them with appropriate biocompatible materials, such as polyurethane (described in Chapter 2).[165]

Porous materials, such as silicate-based molecular sieves and aluminosilicate-based zeolites, are an attractive option as carriers for NO-donors since the silicate/aluminosilicate matrices are chemically and biologically inert and exhibit no toxicity in the body.[166] One of the first NO-donating porous materials was described by Wheatley and co-workers in 2006 and was constructed by the coordination of NO to Co- or Zn-exchanged sites in a zeolite-A framework.[167] The Zn-substituted zeolite-A had a NO adsorption capacity of 1 mmol of NO per gram of zeolite-A and demonstrated quantitative release of the adsorbed NO over a period of ~40 min from the hydrolysis of the metal-NO bond in the presence of moisture-rich air. Unfortunately, the inexorable release of NO from this material under biological conditions is not suitable for the delivery of cytotoxic doses of NO in the treatment of infection and neoplasia.

Since the biological effects of NO are strictly dependent on the site, rate, and duration of NO-release, NO-delivery systems that are responsive to stimulation by extracorporeal sources, such as electromagnetic fields, light, or ultrasound, are well suited for the therapeutic delivery of NO to diseased sites throughout the body.[115] Furthermore, the stable microenvironment provided by the material scaffold ensures that the photochemical release of NO will proceed in a predictable manner with reliable, sustained pharmacokinetics that are unaffected by physiological parameters such as temperature, pH and ionic strength.[168] In particular, light provides a convenient, orthogonal stimulus for activating matrix confined therapeutic agents with excellent spatiotemporal control.[169]

1.7.1 NO-releasing Iron-oxide Magnetic Nanoparticles

Magnetic iron-oxide nanoparticles (MNPs) are often used as smart drug delivery vehicles to carry and deliver surface attached ligands or pharmaceutical agents embedded within the iron-oxide matrix for certain biomedical applications.[170] Magnetic nanoparticles can potentially be guided to a targeted site within the body using a focused magnetic field in order to deliver bioactive agents directly to the desired site. Seabra *et al.* have recently reported an iron-oxide nanoparticle-based device as a new strategy for the targeted delivery of NO for biomedical applications (Figure 1.8).[171] A co-precipitation technique with ferric and ferrous chlorides under alkaline conditions was used for the synthesis of Fe_3O_4 MNPs. The washed MNPs were then suspended in oleic acid which coated the surface of the particles, and later, exchanged with two

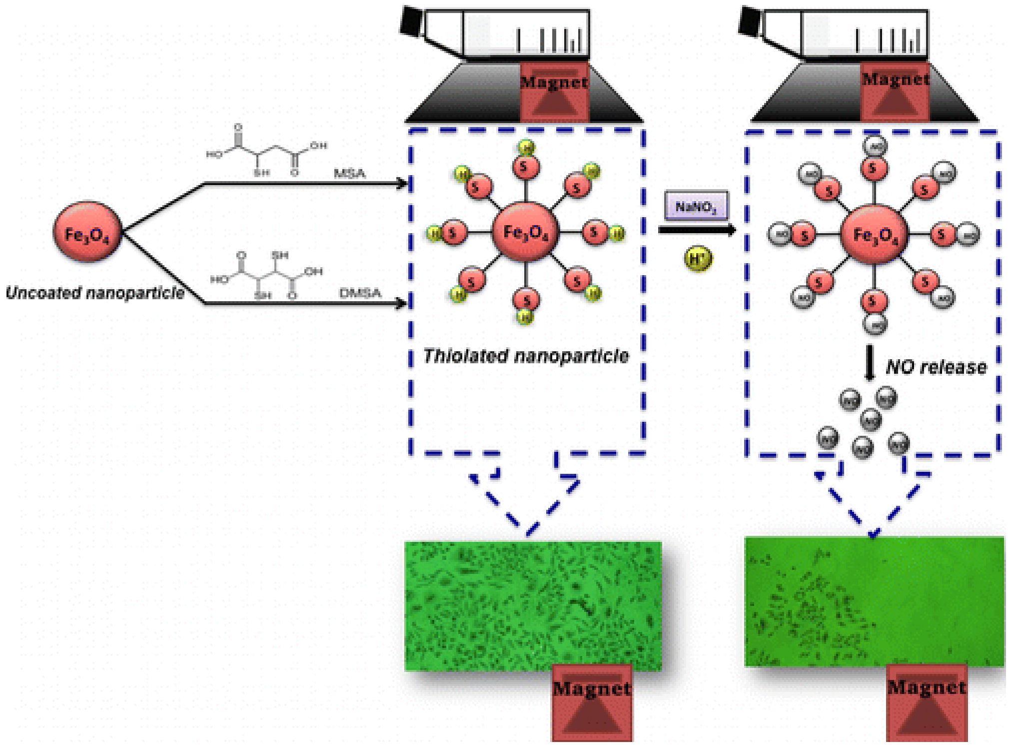

Figure **1.8**. Schematic of mercaptosuccinic acid (MSA) or dimercaptosuccinic acid (DMSA) functionalization of Fe_3O_4 nanoparticles. The thiolated nanoparticles were then *S*-nitrosated by incubation in acidic sodium nitrite, forming NO-donating *S*-nitroso-MSA or *S*-nitroso-DMSA-Fe_3O_4 nanoparticles. Localization of the nanoparticles in a culture of human lymphocytes was achieved using a focused magnetic field and demonstratied site specific cytotoxicity with the NO-donating formulation.[171]

different thiol-containing dicarboxylic acid ligands: mercaptosuccinic acid (MSA) or 2,3-dimercaptosuccinic acid (DMSA) in a 1:40 solution of MNP:SA, producing stable aqueous dispersions of thiolated nanoparticles (SH-MNPs). Nitration of the free thiol (SH) groups by the way of nitrous acid produced *S*-nitrosothiol modified dicarboxylate ligands on the surface of MNPs. The NO-releasing MNPs demonstrated room-temperature superparamagnetism and produced 160 mmol L^{-1} of NO in aqueous solution at 25°C which can be enhanced in the presence of visible light. The cytotoxicity of SH-MNPs and NO-releasing MNPs were evaluated against human lymphocytes by 1 h incubation in solutions containing 0.1 mg mL^{-1} MNPs and produced a 20-30% inhibition of cellular growth. The results of this work indicate that NO-releasing MNPs may provide a useful platform for NO-delivery in biomedical applications, such as a radio-sensitizer for the treatment of neoplasia.

1.7.2 NO releasing Gold Nanoparticles

The use of gold nanoparticles (GNPs) as drug delivery vehicles relies on of the enhanced permeation and retention (EPR) effect to localize and then release therapeutic molecules within neoplastic tissue.[172] Due to the rapid growth of certain tumor masses, the vascularization of the tumor body takes place in a rapid uncontrolled fashion and demonstrates enhanced permeation compared to healthy vasculature. GNPs that meet the minimal biomedical requirements of small size, water solubility, and stability are expected to permeate through the leaky vasculature of tumor masses and be retained within the tumor tissue where they can release their drug payload. The high surface to volume ratio and water solubility of GNPs provides an efficient light harvesting center for the transfer of photo-energy to surface functionalized ligands. Sudhesh *et al.* have recently reported the photoactivated release of NO from gold nanoparticles (GNPs) containing surface-bound 2-mercapto-5-nitro benzimidazole (MNBI) ligands (Figure 1.9).[173] An alkaline solution containing tetrachloroauric acid stabilized with 2-

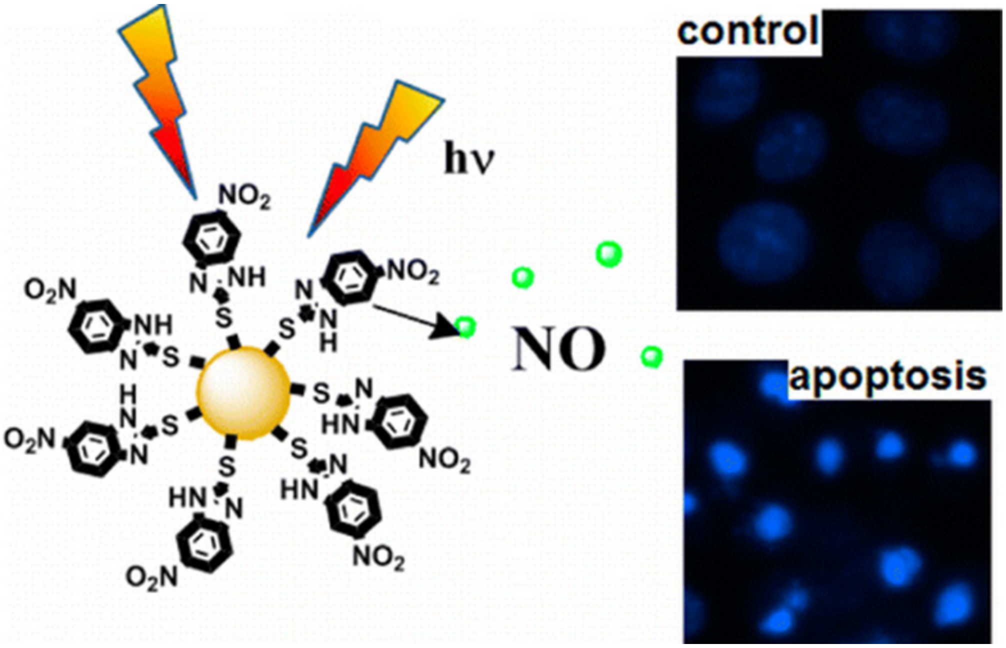

Figure **1.9**. 2-mercapto-5-nitro benzimidazole functionalized gold nanoparticles released NO upon visible-light irradiation. Increased cytotoxicity was observed in a culture of human cervical cancer cells upon illumination of the NO-releasing GNPs.[173]

mercapto-5-nitro benzimidazole was rapidly stirred for 1 h, and then, reduced by the addition of $NaBH_4$, in order to precipitate MNBI-GNP. Surface-attached benzimidazoles act as bridging ligands between the light-harvesting gold core (7 nm) and appended nitro groups facilitating nitro-to-nitrite photo-rearrangement and O-NO bond rupture to produce a phenoxy radical and release NO. The absorption spectra of MNBI-GNPs demonstrated a decrease in intensity in a photoband centered at 350 nm after continuous illumination with visible light, indicating that the photochemical transformation of the NO_2 group resulted from the transfer of photo-energy from the gold core. The concentration of NO released from 0.5 ml MNBI-GNP (4 μg mL^{-1})

under irradiation with a 40 W fluorescent lamp was 22 μM NO, as measured using the Griess reagent. The 95% cytotoxic dose of MNBI-GNP under irradiation with a 40 W fluorescent lamp against human cervical cancer cells was 80% lower (by weight) than that of the common cancer drug cisplatin. Of note, the 95% cytotoxic dose of MNBI-GNP also demonstrated 60% cytotoxicity in the absence of light indicating an inherent toxicity of MNBI-GNP independent of NO release. Ramla et.al have reported the anti-tumor effects of benzimidazole compounds and concluded that the cytotoxic effect is mainly due to interactions with the nitro group.[174]

1.7.3 NIR Activated Up-Converting Nanocrystals

Although considerable interest exists in the development of photoactivated NO-delivery methods, there are relatively few photochemical NO precursors with sufficient adsorptivity in the visible to NIR region (where tissue penetration is the greatest) to drive NO-releasing photoreactions at an adequate rate.[175] In order to enhance the rate of photoactivated NO-release, strongly absorbing molecular and supramolecular assemblies can be conjugated to photochemical NO-precursors to function as light harvesting antennae and provide the necessary photo-energy to drive NO-release.[176] Semiconductor quantum dots (QDs) have been used for such purposes due to their high adsorptivity in the ‘phototherapeutic window’ (600-1000 nm), large two-photon absorption cross-sections, tunable spectral properties, and readily functionalized surfaces for the binding of targeting and passivating ligands.[177] Ford and co-workers have conjugated a cationic, dinitrito Cr(III) complex, *trans*-[Cr(cyclam)$(NO_2)_2$](BF_4) (**9**), to a water soluble CdSe/ZnS core/shell QD by exploiting electrostatic interactions

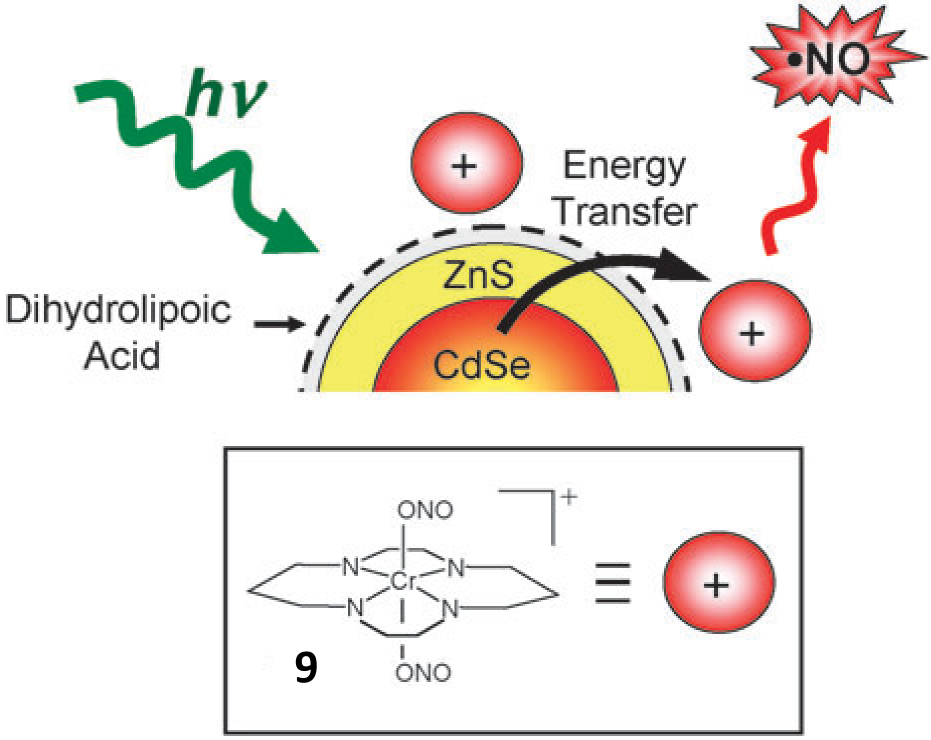

Figure **1.10**. A cationic Cr(III) nitro complex (**9**) was electro-statically absorbed onto the anionic surface of dihydrolipoic acid functionalized CdSe/ZnS core/shell quantum dots (QDs). The photo-luminescent QDs functioned as a light-harvesting antennae that transferred sufficient visible-light photo-energy to the Cr(III) complex to promote a NO-releasing photoreaction.[178]

with the negatively charged QD surface (Figure 1.10).[178] Although the Cr(III) complex is only weakly absorbing in the near-UV and visible light regions, the photo-release of NO from **9** upon illumination with < 460 nm light increased 15-fold after conjugation to the semiconducting QDs. The enhanced NO release from **9** was attributed to energy transfer through a FRET type mechanism from the conduction band of optically excited QDs to a slightly lower energy band corresponding to the excited quartet state of the ion-paired Cr(III) complex. Then, internal conversion to the lowest-energy, reactive doublet state results in the labilization of NO from the Cr(III) complex. This proof-of-concept study provides a useful technique for sensitizing NO photo-donors using QDs as light-harvesting antennas.

The quest for NIR promoted NO-delivery techniques in recent years has recruited innovative modes of photoexcitation, in addition to new materials. Ford and Zhang *et al.* have reported on $NaYF_4$ nanocrystals doped with lanthanide cations that up-convert 980-nm laser light (from a NIR diode laser) into the UV and visible range.[179] These up-converting nanocrystals (UPNCs) were first coated with silica, then functionalized with terminal amines, and finally conjugated to **RBS** to afford UPNCs@SiO2-**RBS**, a composite material that releases NO upon irradiation with 980-nm NIR light in aqueous solution (pH 5). A modification of this NO-donating system has recently been reported by the same workers. The system consists of a polydimethylsiloxane disk containing UPNCs that have been infused with **RBC** to afford NO releasing **PD_UPNC_RBS**. [180] An unique experimental setup employing a light filter composed of porcine tissue was used to determine the ability of **PD_UPNC_RBS** to release physiological relevant doses of NO at subcutaneous locations upon irradiation with an extracorpeal source of NIR light. Irradiation of the disks with 980 nm light for 10 to 80 s through the tissue filter generated 18 to 4,200 pmol NO, demonstrating the utility of the device as a subcutaneous photo-controlled NO-delivery system. Taken together, these results indicate that novel composite materials with incorporated metal nitrosyls combined with innovative techniques for photo-activation could provide breakthrough treatment modalities for the photo-controlled delivery of NO.

1.7.4 NO-donating Material Composites with Incorporated Metal Nitrosyl

Although a variety of compounds exhibit accelerated NO-release under visisble light, many of these compounds are sensitive to other biological stimuli preventing their use as light-controlled reservoirs for NO-delivery systems.[115] Metal nitrosyls have been reported by our group and others, especially $\{Mn\text{-}NO\}^6$ and $\{Ru\text{-}NO\}^6$ complexes, that stably bind NO as a ligand under physiological conditions, until excitation by visible and NIR light.[114] The encapsulation of these metal nitrosyls in various biocompatible matrices has afforded composite materials capable of delivering NO to a targeted site under the strict control of light.[116,181] For example, Borovik and co-workers functionalized the phenolato ring of a salen ligand coordinated to [Ru(Cl)(P-salen)(NO)] (**10**) with an ether-linked styryloxy unit containing a terminal vinyl group.[182] Copolymerization of the vinyl group of **10** with methacrylate monomers formed a covalent tether between the Ru nitrosyl and the polymerized methacyralate matrix, affording **P-10** (Figure 1.10). Although the encapsulation technique resulted in slightly slower NO release kinetics, the composite material, **P-10** does not exhibit recombination of the released NO even in coordinating solvents (e.g., MeCN or H_2O). In phosphate buffer, **P-10** readily delivers NO to reduced myoglobin upon exposure to visible light. Gomes and coworkers reported the encapsulation of *trans*-$[Ru(NO)(NH_3)_4(py)](BF_4)_3$ (**11**) in PLGA particles via a double emulsion process, which, unfortunately, suffered from a low encapsulation efficiency (maximum 30%)

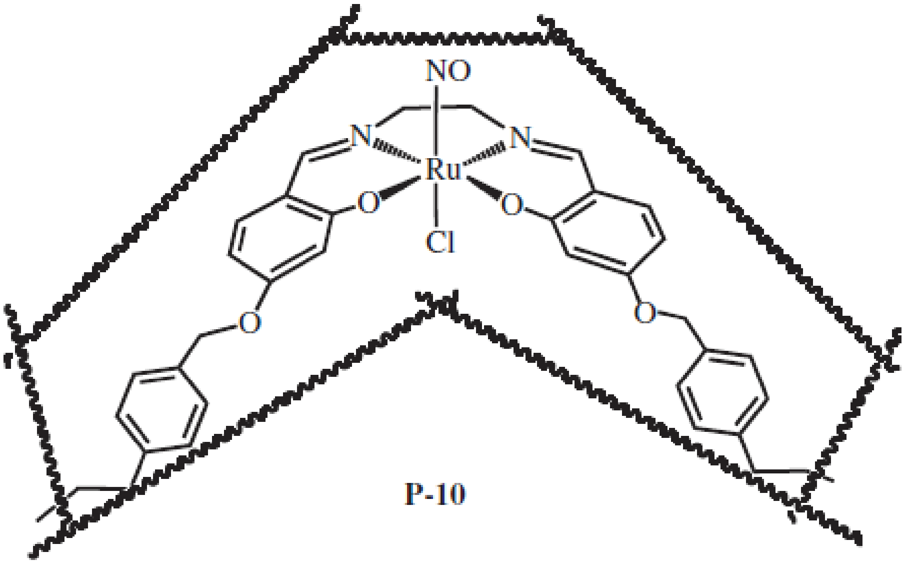

P-10

Figure **1.10**. Copolymerization of the vinyl group of [RuCl(P-salen)(NO)] (**10**) in a methacyralate matrix afforded the photoactive NO-donating material **P-10**.

and a polydisperse particle size (avg. diameter of 1.6 mm).[183] Schiller and co-workers reported the incorporation of a $\{Ru\text{-}NO\}^6$ complex, [RuCl(impb)(NO)] (**12**), containing a *N*-methyl imidazole derivative of H_2bpb into poly(L-lactide-*co*-D,L-lactide) nanofibers with the aid of electrospinning.[184] Non-woven scaffolds derived from such fibers release NO upon illumination with UV light (366 nm) and exhibit low toxicity against 3T3 mouse fibroblasts.

1.7.5 Site-specific Delivery of Photo-controlled NO

In order to deliver NO in a site-specific manner, we have incorporated our designed photoactive metal nitrosyls into various polymer matrices to produce nitrosyl–polymer composites.[169] Optically transparent and NO permeable materials were selected as hosts to minimize inhibition of the quantum efficiency and rate of NO release from the incorporated metal nitrosyls. Furthermore, to ensure the therapeutic utility of the nitrosyl composites, the host matrices were limited to those with known biocompatibility. The mild reaction conditions of sol-gel chemistry and the ability to control important properties, such as the optical transparency, biocompatibility, chemical and thermal stability, and morphology, was used for the encapsulation of the highly efficient NO donors $[Mn(PaPy_3)(NO)](ClO_4)$ **3** and $[Mn(PaPy_2Q)(NO)](ClO_4)$ **4**, in an inert silica matrix (Figure 1.11).[150,185] The transparent and flexible green **3·SG** and maroon **4·SG** patches were coated with a layer of polyurethane, a biocompatible and NO permeable polymer, to inhibit leaching of the incorporated nitrosyls and their photoproduct(s) while permitting $NO_{(g)}$ diffusion. Precise spatial control of NO-release from the composite materials was evident when a photomask was placed in between

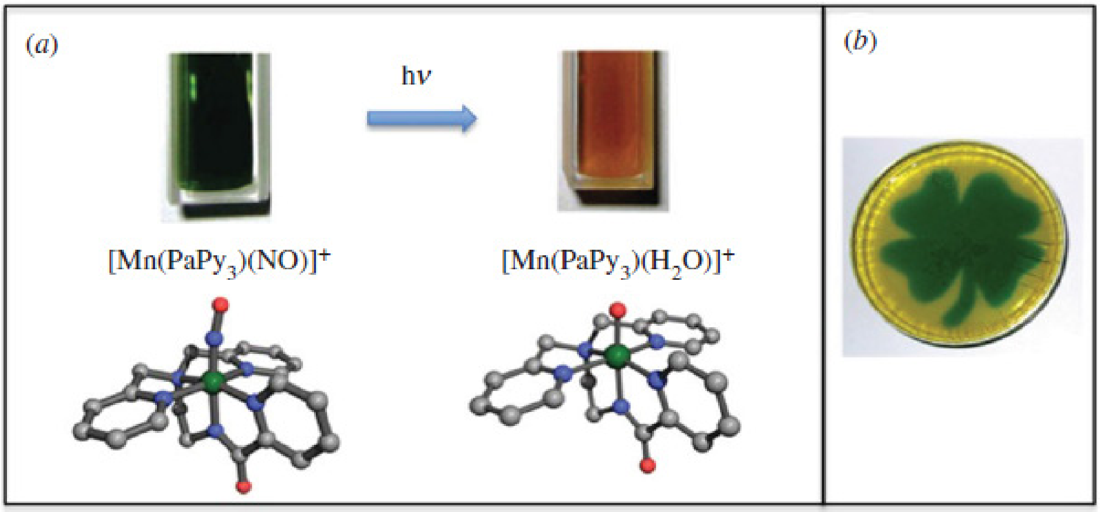

Figure **1.11**. (*a*) Change of colour due to photorelease of NO upon exposure of **3 • SG** to visible light (10 mW). (*b*) Spatial control on light-triggered NO release shown with a patch of **3 • SG** using a shamrock photo-mask placed between the patch and the light source.

the light source and the sol–gel patch. Sol–gel encapsulation of the nitrosyl resulted in only modest inhibition of the quantum yield of NO release for both nitrosyls. For example, irradiation of aqueous solutions containing thin disks of the composite materials with low-power (10mW) visible light resulted in rapid NO-release with quantum efficiencies of ϕ_{532} = 0.25 for **3·SG** and 0.55 for **4·SG**, comparable to those of the free nitrosyls, ϕ_{550} = 0.38 and 0.69 for **3** and **4**, respectively (measured in H_2O, 10mW of 550 nm light).[150] Exposure of **4·SG** to 40 mW of 780 nm monochromatic light readily nitrosylated reduced myoglobin in physiological buffer, while **3·SG** demonstrated a considerable reduction in NO-release rates in the NIR region. The $\{Mn\text{-}NO\}^6$ sol-gel composite, **4·SG**, represents the first reported example of an NO-releasing material derived from a photoactive metal nitrosyl that could be activated with NIR light.

Although NO exhibits strong antimicrobial activity in the treatment of chronic infections by Gram-positive, Gram-negative, and antibiotic-resistant bacteria, photo-activation is generally not amendable to the treatment of microbial infections in deep tissue and body cavities, especially in cases of pneumonia and UTI.[186] Av-Gay and co-workers have reported the extended release of high doses (5 mM to 166 μM) of $NO_{(g)}$ from NO-impregnated Foley urinary catheters which was sufficient to prevent bacterial colonization and biofilm formation on the catheter surfaces, and inhibit the growth of *E. coli* in the surrounding media.[187] In order to target NO-release to remote sites under the complete control of light, an endoscopic device was constructed by casting a small (4 mm in diameter and 5 mm in length) cone-shaped, sol-gel monolith containing embedded $[Mn(PaPy_3)(NO)](ClO_4)$ (**3**) on the polished end of fiber-optic line, and then, coating the monolith with a thin layer of polyurethane.[188] When the free end of the fiber-optic line was coupled to a light source, light was guided through the line to the sol-gel tip and activated NO-release from the embedded $\{Mn\text{-}NO\}^6$ complex. When the endoscope was immersed in narrow tubes containing bacterial cultures, and illuminated with light guided through the fiber optic line, a high dose (5 μM) of NO was released from the sol-gel tip for 10 min causing almost complete eradication of clinically significant (10^5 CFU mL^{-1}) loads of *S. aureus*, *P. aeruginosa*, and *E. coli*. These results demonstrate the utility of this modality of remote NO-delivery for the treatment of infections by Gram-positive and Gram-negative bacteria in subcutaneous and deep tissue (such as infected body cavities in ventilator-related infections), while avoiding common issues that can arise during the administration of $NO_{(g)}$.

Hydrogels based on poly(2-hydroxyethyl methacrylate) (pHEMA) are widely used in biomedical applications, especially as dressings for tissue burns, owing to their excellent oxygen permeability, as well as their capacity to adsorb wound exudate and retain moisture in the wound bed. [166] In addition to the beneficial effects provided by pHEMA dressings, the delivery of NO directly to the wound site has been shown to accelerate the healing process by accelerating angiogenesis and increasing the production of extracellular matrix, in addition to its antimicrobial properties.[189] In order to combine the beneficial effects of NO and pHEMA dressings on the wound healing process, the photoactive Mn nitrosyl, $[Mn(PaPy_3)(NO)](ClO_4)$ **3**, has been incorporated into a pHEMA matrix along with methylene blue (MB; a light-activated singlet oxygen generating photosensitizer). The composite material was cut into thin disks to afford $\mathbf{3_{MB}}$·pHEMA.[190] Upon illumination with visible light, $\mathbf{3_{MB}}$·pHEMA released a combination of NO and singlet oxygen, which is thought to rapidly form RNS, with potent antibiotic activity against liquid cultures of *P. aeruginosa* and *E. coli*. Although patches of $\mathbf{3_{MB}}$·pHEMA provide an effective NO-releasing wound dressing, the composite material required a coating of polyurethane to retain the metal nitrosyl and its photoproduct(s) within the porous hydrogel matrix. This requirement was circumvented in another approach to incorporate the photoactive $\{\text{Ru-NO}\}^6$ nitrosyl, $[(Me_2bpb)Ru(NO)(4\text{-vpy})](BF_4)$ (**11**) containing the tetradentate ligand frame $Me_2bpb^{2-}$and 4-vinylpyridine (4-vpy) as the sixth ligand, *trans* to NO. [191] The stable, NO-donating material, **11**·pHEMA, was formed by the radical-induced copolymerization of the 4-vpy ligand of **11** with HEMA and ethyleneglycoldimethacrylate (a cross-linker), which covalently attached the nitrosyl to the cross-linked polymer backbone. The nearly transparent **11**·pHEMA composite readily released NO upon exposure to low-power UV light (5mW) while securely retaining the NO-donor and its photoproduct to the polymer backbone. Since NO is known to accelerate wound healing, the pHEMA–nitrosyl composites could serve as excellent wound dressings with strong wound-healing properties, in addition to light-controlled antibiotic properties.

1.7 Thesis Outline

A variety of nitrosyl–material conjugates have been reported by our group that demonstrate light-controlled NO-release and stability under physiologically relevant conditions. Based on early results of the antimicrobial properties of such materials demonstrating their antimicrobial activity against pathogenic bacteria, the work presented in this thesis was aimed towards further improving and demonstrating the biomedical utility of NO-donating composite materials containing photoactive nitrosyls for the light-controlled delivery of NO to sites of infection. In the first set of materials reported by our group, sol–gel (SG) chemistry (employing silicon alkoxides) was utilized for entrapping photo-active nitrosyls. Evaporation of solvent from the pores of SG materials (e.g. **3·SG** or **4·SG)** affords a brittle, glass-like silica xerogel that is highly susceptible to fragmentation. In chapter 2, a method is described for utilizing the solvent-evaporated xerogels to prepare NO-donating polyurethane films with dispersed xerogel particles containing up to 3 mol% of **3** entrapped in a silica matrix and swelled with excess moisture. The uncured viscous mixture of polyurethane and xerogel particles was spin-cast onto glass slides forming a thin layer that was allowed to cure for 16 h, and then, dip-coated with an outer, passive layer of polyurethane. The resulting flexible green film (**PUX-NO**) rapidly releases NO under irradiation with visible light (300 mW cm^2). When PUX–NO films containing various concentrations of **3** were placed over nutrient-rich agar plates inoculated with 10^5 CFU mL^{-1} of various bacterial pathogens common to skin and soft-tissue infections (including a strain of methicillin-resistant *S. aureus*) and then illuminated for 1–2 h, a dose-dependent decrease in bacterial colonies was observed.

Mesoporous silicates are an attractive option for immobilizing photo-active nitrosyls for NO administration since the silicate matrix is chemically inert and does not react with gaseous free radicals. Chapter 3 details the incorporation of a photoactive Mn nitrosyl (**3**) in the mesopores of a MCM-41 type silicate. To increase the interaction between **3** and the MCM-41 pore walls, an aluminosilicate-based material (Al-MCM-41) was used with 3 mol% Al^{III} substituted for tetrahedral Si^{IV} sites, which introduced negative point charges that electrostatically interact with the cationic nitrosyl. Homegenous loading of 25 wt.% **3** throughout the hexagonally packed, uni-dimensional pores of Al-MCM-41 was determined using various analytical techniqus including ICP-MS, FAAS, PXRD, N_2 sorption isometry, UV-vis DRS, FTIR, and SEM-EDX. Exposure of **3**@Al-MCM-41 to visible light of similar intensity to sunlight on a bright day (100 mW cm^{-2}) released high fluxes of NO that effectively eradicated a multi-drug resistant strain of *Acinetobacter baumannii.* In another study, described in Chapter 4, the powdery material was used to demonstrate the effect of NO on the dimorphic fungal pathogen, *Candida albicans*. Since the virulence of *C. albicans* is dependent on the ability of the fungus to switch growth from an ovoid yeast form to an elongated hyphal form, careful studies on the dose-dependent effect of NO released from **3**@Al-MCM-41 on morphologically pure cultures of *C. albicans* in the yeast and hyphal forms have revealed that the hyphal form is more susceptible to NO. Results of this work suggest that photo-activated NO-donating materials of this type could prevent commensal populations of *C. albicans* from invading vulnerable tissue by blocking the over-growth of the tissue penetrating hyphal form of the fungus.

1.8 References

1. Palmer, R. M. Ferrige, A. G. Moncada, S. *Nature* 1987, *327*, 524–526.
2. Kreuzer, L. B. Patel, C. K. N. *Science* **1971**, *173*, 45–47.
3. (a) Rubbo, H. Darley-Usmar, V. Freeman, B. A. *Chemical Research in Toxicology* **1996**, *9*, 809–820. (b) Martínez-Ruiz, A. Cadenas, S. Lamas, S. *Free Radical Biology and Medicine* **2011**, *51*, 17–29. (c) *Nitric Oxide: Biology and Pathobiology*; Ignarro, L. J., Ed; Academic Press: San Diego, 2000.
4. Ignarro, L. J. Buga, G. M. Wood, K. S. Byrns, R. E. Chaudhuri, G. *Proc. Natl. Acad. Sci. U.S.A.* **1987**, *84*, 9265–9269.
5. Palmer, R. M. Ferrige, A. G. Moncada, S. *Nature* **1987**, *327*, 524–526.
6. E. D. Garcin, C. M. Bruns, S. J. Lloyd, D. J. Hosfield, M. Tiso, R. Gachhui, D. J. Stuehr, J. A. Tainer, E. D. Getzoff, *J. Biol. Chem*. **2004**, *279*, 37918.
7. M. Aoyagi, A.S. Arvai, J.A. Tainer, E.D. Getzoff, *EMBO J.* **2003**, *22*, 766.
8. Daff, S. *Nitric Oxide*, **2010**, *23*, 1.
9. (a) Stuehr, D. J.; Kwon, N. S.; Nathan, C. F.; Griffith, O. W.; Feldman, P. L.;Wiseman, J. *J. Biol. Chem.* **1991**, *266*, 6259; (b) Stuehr, D. J. *Biochim. Biophys. Acta Bioenerg.* **1999**, *1411*, 217.
10. Li, H. Y. Shimizu, H. Flinspach, M. Jamal, J. Yang, W. P. Xian, M. Cai, T. W. Wen, E. Z. Jia, Q. A. Wang, P.G. Poulos, T. L. *Biochemistry*, **2002**, *41*, 13868.

11. (a) Fischmann, T. O. Hruza, A. Niu, X. D. Fossetta, J. D. Lunn, C. A. Dolphin, E. Prongay, A. J. Reichert, P. Lundell, D. J. Narula, S. K. Weber, P. C. *Nat. Struct. Biol.* **1999**, *6*, 233; (b) Raman, C. S.; Li, H.Y.; Martasek, P.; Kral V.; Masters, B. S. S.; Poulos, T.L. *Cell*, **1998**, 95, 939.

12. Kalsner S. *Nitric Oxide and Free Radicals in Peripheral Neurotransmission*; Birkhäuser: Boston, 2000.

13. *Nitric oxide and Infection*; Fang, F. C., Ed; Kluwer Academic/Plenum Publishers: New York, 1999.

14. *Nitric Oxide and Cell: Proliferation, Differtiation and Death*. Moncada S., Higgs, E. A., Bagetta, G., Eds; Portland Press: London, 1998.

15. Matter, H. Kumar, H. S. A. Fedorov, R. Frey, A. Kotsonis, P. Hartmann, E. Frohlich, L. G. Reif, A. Pfleiderer, W. Scheurer, P. Ghosh, D. K. Schlichting, M. Schmidt, H. *J. Med. Chem.* **2005**, *48*, 4783.

16. Nathan, C. Xie, Q. W. *Bioi. Chem*. **1994,** *269,* 13725-28

17. Espey, M. G.; Miranda, K. M.; Pluta, R. M.; Wink, D. A.. *J. Biol. Chem*. **2000**, *275*, 11341–11347;.

18. Stuehr, D. J.; Santolini, J.;Wang, Z. Q.;Wei, C. C.; Adak, S. *J. Biol. Chem*. **2004**, *279*, 36167–36170;.

19. Chen, X. Buerk, D. G. Barbee, K. A. Jaron, D. *Ann. Biomed. Eng*. **2007**, *35*, 517–529.

20. Hofseth, L. J. Saito, S. Hussain, S. P. Espey,M. G. Miranda, K.M. Araki, Y. Jhappan, C. Higashimoto, Y. He, P. Linke, S. P. Quezado,M.M. Zurer, I. Rotter,

V. Wink, D. A. Appella, E. Harris, C. C. *Proc. Natl. Acad. Sci. USA*. **2003**, *100*, 143–148.

21. Laurent, M. Lepoivre, M. Tenu, J. P. *Biochem. J.* **1996**, *314*, 109–113;.
22. Wink, D. A. Ford, P. C. *Methods: A Companion to Methods Enzymol.* **1995,** *7*,14–20.
23. Doyle, M. P. Hoekstra, J. W. J. *Inorg. Biochem.* **1981**, ***14*,** 351–356.
24. Yu, A. E. Hu, S.; Spiro, T. G. Burstyn, J. N. *J. Am. Chem. Soc.* **1994**, *116*, 4117–4118.
25. Stone, J. R. Marletta, M. A. *Biochemistry* **1994**, *33*, 5636–40.
26. Murad, F. *Recent Prog.. Horm. Res.* **1994**, *49,* 239–248.
27. Forstermann, U. Ishii, K. Measurement of cyclic GMP as an indicator of nitric oxide production, In: *Methods in nitric oxide research.* Feelisch, M.; Stamler, J., eds. New York: Wiley; 1996: 555–566.
28. Hofmann, F. *J. Biol. Chem.* **2005**, *280,* 1–4.
29. Kharitonov, V.G. Russwurm, M. Magde, D. Sharma, V.S. Koesling, D. *Biochem. Biophys. Res. Commun*. **1997**, *239*, 284-6.
30. Guijre, A. Sarti, P. D'Itri, E. Buse, G. Soulimane, T. Brunori, M. *J. Biol. Chem*. **1996**, *271*, 33404-8.
31. Kharitonov, V.G. Sharma, V.S. Magde, D. Koesling, D. *Biochemistry* **1997**, *36*, 6814-8.
32. Henry, Y. Guissani, A. Ducastel, B. *Nitric Oxide Research from Chemistry to Biology: EPR Spectroscopy of Nitrosylated Compounds,* Springer-Verlag,

Berlin, 1997.

33. Chang, C.K. Dolphin, D. *Proc. Natl. Acad. Sci. USA* **1976**, *73*, 3338-42.

34. Cassoly, R. Gibson, Q.H. *J. Mol. Biol.* **1975**, *91*, 301-13.

35. (a) Chen, X.; Buerk, D. G.; Barbee, K. A.; Jaron, D. *Ann. Biomed. Eng*. **2007**, *35*, 517–29. (b) Lancaster, J. *Proc. Natl. Acad. Sci. USA* **1994**, *91*, 8137–41.

36. Azarov I, He X, Jeffers A, Basu S, Ucer B, Hantgan RR, Levy A, Kim-Shapiro DB. *Nitric Oxide* **2008**, *18*, 296–302.

37. (a) Vaughn, M. W. Huang, K. T. Kuo, L. Liao, J. C. *J. Biol. Chem.* **2000**, *275*, 2342–8. (b) Azarov I, Huang KT, Basu S, Gladwin MT, Hogg N, Kim-Shapiro, D. B. *J. Biol. Chem.***2005**, *280*, 39024–32. (c) El-Farra, N. H. Liao, J. C. *Ann. Biomed. Eng.* **2003,** *31*, 294–309.

38. Hurshman, A. R. Marletta, M. A. *Biochemistry* **1995**, *34*, 5627–34.

39. Sternlicht, M. D. Werb, Z. *Annu. Rev. Cell Dev. Biol.* **2001**, *17,* 463–516.

40. Siwik, D. A. Colucci, W. S. *Heart Fail. Rev*. **2004**, *9,* 43–51.

41. Addison, A.W. Stephanos, J.J. Biochemistry **1986**, *25*, 4104-13.

42. Gorbunov, N. V. Osipov, A. N. Day, B. W. Zayas-Rivera, B. Kagan, V. E. Elsayed, N. M. *Biochemistry* **1995**, *34*, 6689–99.

43. Wink, D. A. Cook, J. Pacelli, R. DeGraff, W. Gamson, J. Liebmann, J.

44. Krishna, M. Mitchell, J. B. *Arch. Biochem. Biophys.* **1996**, *331,* 241–8.

45. Kanner, J. Harel, S. Granit, R. *Lipids* **1992**, *27,* 46–9.

46. Padmaja, S. Huie, R. E. *Biochem. Biophys. Res. Commun.* **1993**, *195,* 539–44.

47. Wink, D. A. Cook, J. A. Krishna, M. C. Hanbauer, I. DeGraff, W. Gamson, J.

Mitchell, J. B. *Arch. Biochem. Biophys.* **1995**, *319,* 402–7.

48. (a) Stanbury, D. M. *Adv. Inorg. Chem.* **1989**, *33*, 69-138. (b) Kemp-Harper B.K. *Antioxid. Redox Signal.* **2011**, *14*, 1609–13.

49. Huie, R. E. Padmaja, S. *Free Radic. Res. Commun.* **1993**, *18*, 195–9.

50. Ford, P. C.; Wink, D. A.; Stanbury, D. M. *FEBS Lett.* **1993**, *326*, 1–3.

51. Liu, X.; Miller, M. J. S.; Joshi, M. S.; Thomas, D. D.; Lancaster, J. R. J. *Proc. Natl. Acad. Sci. USA* **1998**, *95*, 2175–9.

52. Wink, D. A. Darbyshire, J. F. Nims, R. W. Saveedra, J. E. Ford, P. C. *Chem. Res. Toxicol.* **1993**, *6*, 23–7.

53. Lamkin-Kennard, K. A. Buerk, D. G. Jaron, D. *Microvasc. Res.* **2004**, *68,* 38–50.

54. Wink, D. A.; Grisham, M.; Mitchell, J. B.; Ford, P. C. *Methods Enzymol.* **1996**, *26,* 12–31.

55. Lancaster, J. *Proc. Natl. Acad. Sci. USA* **1994**, *91*, 8137–41.

56. Shiva, S. Oh, J. Y. Landar, A. L. Ulasova, E. Venkatraman, A. Bailey, S. M. Darley-Usmar, V.M. *Free Radic. Biol. Med.* **2005**, *38,* 297–306.

57. Eiserich, J. P. Hristova, M. Cross, C. E. Jones, A. D. Freeman, B. A. Halliwell, B. van der Vliet, A. *Nature* **1998**, *391,* 393–7.

58. Radi R. *J. Biol Chem.* **2013**, *288,* 26464–72.

59. Lancaster J. R. *Chem. Res. Toxicol.* **2006**, *19*, 1160-74.

60. Lim C.H. Dedon, P.C. Deen, W.A. *Chem. Res. Toxicol.* **2008**, *21*, 2134-47.

61. Bowman, L. A. H. McLean, S. Poole, R. K. Fukuto, J. M. *Adv. Microb. Physiol.* **2011**, *59*, 135-219.

62. Toledo, J.C. Augusto, O. *Chem. Res. Toxicol.* **2012**, *25*, 975-89.

63. Dedkova, E. N. Blatter, L. A. *Am. J. Physiol. Cell Physiol.* **2005***, 289,* C836–C845.

64. Riobó, N. A. Clementi, E. Melani, M. Boveris, A. Cadenas, E. Moncada, S. Poderoso, J. J. *Biochem. J.* **2001**, *359*, 139–45.

65. Brune, B. *Antioxid. Redox Signal.* **2005**, *7*, 497–507.

66. Ridnour, L. A.; Thomas, D. D.; Mancardi, D.; Espey,M. G.; Miranda, K. M.; Paolocci, N.; Feelisch, M.; Fukuto, J.; Wink, D. A. *Biol. Chem.* **2004**, *385*, 1–10.

67. Murphy, M. P. *Biochimica et Biophysica Acta - Bioenergetics*. **1999**, *1411*, 401–14.

68. Bagci, E. Z. Vodovotz, Y. Billiar, T. R. Ermentrout, B. Bahar, I. *PLoS One* **2008**, *3*, e2249.

69. Häcker, G. *Microb. Infect*. **2013**, *15*, 640–4.

70. Olson, J. S. Foley, E. W. Rogge, C. Tsai, A.-L. Doyle, M. P. Lemon, D. D. *Free Rad. Biol. Med.* **2004,** *36*, 685-97.

71. Gardner, P. R. Gardner, A. M. Martin, L. A. Salzman, A. L. *Proc. Natl. Acad. Sci. USA* **1998,** *95*, 10378-10383.

72. Zumft, W. G. *J. Inorg. Biochem.* **2005,** *99*, 194-215.

73. Wasser, I. M. deVries, S. Moënne-Loccoz, P. Schröder, I. Karlin, K. D. *Chem. Rev.* **2002,** *102*, 1201-1234.

74. (a) Mellmann, A. Harmsen, D. Cummings, C. A. Zentz, E. B. Leopold, S. R. Rico, A. Prior, K. Szczepanowski, R. Ji, Y. Zhang, W. *PLoS ONE* **2011**, *6*, e22751. (b) Frank, C. Werber, D. Cramer, J. P. Askar, M. Faber, M. an der Heiden, M. Bernard, H. Fruth, A. Prager, R. Spode, A. *N. Engl. J. Med.* **2011**, *365*, 1771-80.

75. Eich, R. F.; Li, T. Lemon, D. D. Doherty, D. H. Curry, S. R. Aitken, J. F. Mathews, A. J. Johnson, K. A. Smith, R. D. Phillips, G. N. Jr. Olson, J. S. *Biochemistry* **1996,** *35*, 6976-83.

76. Bang, I.S. Liu, L. M. Vazquez-Torres, A. Crouch, M. L. Stamler, J. S. Fang, F. C. *J. Biol. Chem.* **2006**, *281*, 28039-47.

77. Stevanin, T. M. Poole, R. K. Demoncheaux, E. A. G. Read, R.C. *Infect. Immun.* **2002**, *70*, 4399-405.

78. Robinson, J. L. Brynildsen, M. P. *PLoS Comput. Biol.* **2013**, 9(5), e1003049.

79. Darwin, K. H. Nathan, C. F. *Infect. Immun.* **2005**, *73*, 4581-7.

80. (a) Warren J.B., Loi R., Rendell N.B., Taylor G.W. *Biochem. J.* **1990**, *266*, 921-3. (b) Poole, R. K. *Biochem. Soc. Trans.* **2005**, *33*, 176-80.

81. Miller, C. C. Rawat, M. Johnson, T. Av-Gay, Y. *Antimicrob. Agents Chemother.* **2007**, *51(9)*, 3364-3366.

82. Helmick, R. A. Fletcher, A. E. Gardner, A. M. Gessner, C. R. Hvitved, A. N. Gustin, M. C. Gardner, P. R. *Antimicrob. Agents Chemother.* **2005**, *49*, 1837-43.

83. Hyduke, D. R. Jarboe, L. R. Tran, L. M. Chou, K. J. Liao, J. C. *Proc. Natl. Acad. Sci. USA* **2007**, *104*, 8484–9.

84. Chen, X. Buerk, D. G. Barbee, K. A. Jaron, D. *Ann. Biomed. Eng*. **2007**, *35*, 517–29.

85. Abu-Soud, H. M. Hazen, S. L. *J. Biol. Chem.* **2000**, *275*, 37524–32.

86. (a) Niu, X-P. Smith, C. W. Kubes, P. *Circ. Res.* **1994**, *74*, 1133-40. (b) Kanner, J. Harel, S. Granit, R. *Arch. Biochem. Biophys.* **1991**, *289*, 30-6.

87. Schafer, F. Q. Buettner, G. R. *Free Radic. Biol. Med.* **2001**, *30*, 1191–212.

88. Schairer, D. O. Chouake, J. S. Nosanchuk, J. D. Friedman, A. J. *Virulence* **2012**, *3*, 271-9.

89. (a) Ignarro, L. J. Napoli, C. Loscalzo, J. *Circ. Res.* **2002**, *90*, 21–8. (b) Muscara, M. N. Wallace, J. L. *Am. J. Physiol. Gastrointest. Liver Physiol.* **1999**, *276*, 1313–16.

90. Napoli, C. Ignarro, L. J. *Nitric Oxide* **2001,** *5*, 88–97.

91. Moncada, S.*Ann. NY Acad. Sci.* **1997**, *811*, 60–7.

92. Eiserich, J. P. Patel, R. P. O'Donnell, V. B. *Mol. Aspects Med.* **1998**, *19*, 221–357.

93. Ignarro, L. J. Cirino, G. Casini, A. Napoli, C. *J. Cardiovasc. Pharmacol.* **1999**, *34*, 879–86.

94. Gasco, A. Fruttero, R. Rolando, B. *Mini-Rev. Med. Chem.,* **2005**, *5*, 217-29.

95. Brunton, T. L. *Lancet* **1867**, *2*, 97–8.

96. Katsuki, S. Arnold, W. Mittal, C. Murad, F. *J. Cyclic Nucl. Res*. **1977**, *3*, 23–35.

97. (a) Furchgott, R. F. Zawadzki, J. V. *Nature* **1980**, *288*, 373–6. (b) Ignarro, L. J. Buga, G. M. Wood, K.S. Byrns, R.E. Chaudhuri, G. *Proc. Natl Acad. Sci. USA* **1987**, *84*, 9265–9. (c) Ignarro, L. J. Byrns, R. E. Buga, G. M. Wood, K. S. *Circ. Res*. **1987**, *61*, 866–79.

98. Moncada, S. Palmer, R. Higgs, E. *Pharmacol. Rev*. **1991**, 43, 109–42.

99. Toledo, Jr. J. C. Augusto, O. *Chem. Res. Toxicol*. **2012**, *25*, 975–89.

100. Mocellin, S. Bronte, V. Nitti, D. *Med. Res. Rev*. **2007**, *27*, 317–52.

101. (a) Dhein S. Salameh, A. Berkels, R. Klaus, W. *Drugs* **1999**, *58*, 397-404. (b) Yang, J. Fukuo, K. Morimoto, S. Niinobu, T. Suhara, T. Ogihara, T. *Hypertension* **2000**, *35*, 82–5.

102. Ding, Y. Vaziri, N. D. *J. Pharmacol. Exp. Ther.* **2000**, *292*, 606–9.

103. Stilo, A. Visentin, S. Cena, C. Gasco, A. M. Ermondi, G. Gasco, A. *J. Med. Chem*. **1998**, *41*, 5393-401.

104. (a) Fruttero, R. Boschi, D. Stilo, A. Gasco, A. *J. Med. Chem*., **1995**, *38*, 4944-9. (b) Boschi, D. Stilo, A. Cena, C. Lolli, M. Fruttero, R. Gasco, A. *Pharm. Res.* **1997**, *14*, 1750-8.

105. (a) Mombouli, J. V. Vanhoutte, P. M. *J. Mol. Cell. Cardiol.* **1999**, *31*, 61–74. (b) Taylor-McCabe, K. J. Erasahin, C. Simmons, W. H. *J. Hypertens.* **2001**, *19*, 295–9.

106. Luscher, T. F. Spieker, L. E. Noll, G. Cosentino, F. *J. Cardiovasc. Pharmacol.* **2001**, *38*, S3–111.

107. (a) Liu, Y. H. Xu, J. Yang, X. P. Yang, F. Shesely, E. Carretero, O. A. *Hypertension* **2002**, *39*, 375–81. (b) Cleophas, T. J. *J. Clin. Med.* **1998**, *2*, 2–25.

108. Jessup, W. *Curr. Opin. Lipidol.* **1996**, *7*, 274–80.

109. Cooke, J. P. Oka, R. K. *Curr. Atheroscler. Rep.* **2001**, *3*, 252–59.

110. (a) Lerman, A. Burnett, J. C. Jr. Higano, S. T. McKinley, L.J. Holmes, D. R. Jr. *Circulation* **1998**, *97*, 2123–8. (b) Tousoulis, D. Davies, G.J. Tentolouris, C. Crake, T. Katsimaglis, G. *Am. J. Cardiol.* **1998**, *82*, 1110–13.

111. Blum, A. Hathaway, L. Mincemoyer, R. Schenke, W. H. Kirby, M. *Circulation* **2000**, *101*, 2160–64.

112. (a) *Nitric Oxide Donors for Pharmaceutical and Biological Applications*, Wang, P. G. Cai, T. B. Taniguchi, N. Eds. Wiley–VCH: Weinheim, Germany; 2005. (b) Degoute, C. S. *Drugs* **2007**, *67*, 1052. (c) Keefer, L. K., Nims, R. W., Davies, K. M., and Wink, D. A. *Chem. Res. Toxicol.* **1996**, *6*, 895–9.

113. Mascharak, P. K. *Ind. J. Chem.*, **2012**, *51(A)*, 99.

114. Rose, M. J. Mascharak, P. K. *Curr. Opin. Chem. Biol.*, **2008**, *12*, 238.

115. (a) Eroy-Reveles, A.A. Mascharak, P.K. *Future Med. Chem.* **2009**, *1*, 1497. (b) Halpenny GM, Mascharak PK. *Antiinfect. Agents Med. Chem*. **2010**, *9*, 187–97.

116. Heilman, B. J. Mascharak, P. K. *Phil. Trans. R. Soc. A* **2013**, *371*, 20120368.

117. (a) Cheng, L. Goodwin, C. A. Schully, M. F. Kakkar, V. V. Claeson, G. *Circulation* **1965**, *3*, 755–66. (b) Chen,, Z. Foster, M. W. Zhang, J. Mao, L. Rockman, H. A. Kawamoto, T. Kitagawa, K. Nakayama, K. I. *Proc. Natl. Acad. Sci. USA* **2005**, *102*, 12159–64. (c) Flaherty, J. T. *Am. J. Cardiol.* **1992**, *70*,

73B–81.

118. (a) Molina, C. R. Andresen, J. W. Rapoport, R. M. Waldman, S. Murad, F. *J. Cardiovasc. Pharmacol.* **1987**, *10*, 371–78. (b) Munzel, T. Sayegh, H. Freeman, B. A. Tarpey, M. M. Harrison, D. G. *J. Clin. Invest.* **1995**, *95*, 187–94.
119. Munzel, T. Kurz, S. Rajagopalan, S. Thoenes, M. Berrington, W. R. *J. Clin. Invest.* **1996**, *98*, 1465–70.
120. Drago R. S.; Karstetter B. R. *J. Am. Chem. Soc.* **1961**, *83*, 1819–22.
121. Keefer, L. K. *ACS Chem Biol.* **2011**, 6, 1147–55.
122. (a) Al-Sádoni, H. H. Ferro, A. *Rev. Med. Chem*. **2005**, *5*, 247–54. (b) Loscalzo, J. Smick, D. Andon, N. Cooke, J. P. *J. Pharmacol. Exp. Ther.* **1989**, *249*, 726–29.
123. Leopold, J. A. Loscalzo, J. S-nitrosothiols. In *Nitric Oxide and the Cardiovascular System* Humana Press: New York City, New York; 2000, 411-29.
124. Zai, A. Rudd, M. A. Scribner, A. W. Loscalzo, J. *J. Clin. Invest.* **1999**, *103*,393–9.
125. Jaworski, K. Kinard, F. Goldstein, D. Holvoet, P. Trouet, A. *Eur. J. Pharmacol.* **2001**, *425*, 11–9.
126. Napoli, C. Ignarro, L.J. *Annu. Rev. Pharmacol. Toxicol*. **2003**, *43*, 97–123.
127. Tfouni, E. Truzzi, D. R. Tavares, A. Gomes, A.J. Figueiredo, L. E. Franco, D. W. *Nitric Oxide* **2012**, *26*, 38-53.
128. Barabas, K. Milner, R. Lurie, D. Adin, C. *Vet. Comp. Oncol.* **2008**, *6*, 1-18.

129. Toledo, J. C. Neto, S. L. Franco, D. W. *Coord. Chem. Rev.* **2005**, *249*, 419.

130. Enemark, J. H. and Feltham, R. D. *Coord. Chem. Rev.*, **1974**, *13*, 339.

131. Lewandowska H. Kalinowska, M. Brzóska, K. Wójciuk, K. Wójciuk, G. Kruszewski, M. *Dalton Trans*. **2011**, 40, 8273-89.

132. Tinker, J. H. and Michenfelder, J. D. *Anesthesiology* **1976**, *15*, 340.

133. Bates, J. N. Baker, M. T. Guerra, Jr. R. Harrison, D. G. *Biochem. Pharmacol.* **1991**, *42*, S157.

134. Lockwood, A. Patka, J. Rabinovich, M. Wyatt, K. Abraham, P. *J. Clin. Trials* **2012**, *2*, 133.

135. Coppens, P. Novozhilova, I. Kovalevsky, A. *Chem. Rev.* **2002**, *102*, 861.

136. Robertson, C. S., Clifton, G. L., Taylor, A. A., Grossman, R. G. *J. Neurosurg.* **1983**, *59*, 455-60.

137. Lynch, M. S. Cheng, M. van Kuiken, B. E. Khalil, M. *J. Am. Chem. Soc.* **2011**, *133*, 5255.

138. Singh, R. J. Hogg, N. Neese, F. Joseph, J. Kalyanaraman, B. *Photochem. Photobiol.* **1995**, *61*, 325-30.

139. Flitney, F. W. Megson, I. L. Thomson, J. L. M. Kennovin, G. D. Butler, A. R. *Br. J. Pharmacol.* **1996**, *117*, 1549.

140. Ford, P. C. Bourassa, J. Miranda, K. Lee, B. Lorkovic, I. Boggs, S. Kudo, S. Laverman, L. *Coord. Chem. Rev.* **1998**, *171*, 185.

141. Mitchell, J. B. Wink, D. A. DeGraff, W. Gamson, J. Keefer, L. K. Krishna, M. C. *Cancer Res.* **1993**, *53*, 5845.

142. Rose, M. J. Mascharak, P. K. *Coord. Chem. Rev*. **2008**, *252*, 2093.

143. Fry, N. L. Mascharak, P. K. *Acc. Chem. Res.* **2011**, *44*, 289.

144. (a) Fry, N. L. Mascharak, P. K. *Dalton Trans.* **2012**, *41*, 4726. (b) Merkle, A. C. Fry, N. L. Mascharak, P. K. Lehnert, N. *Inorg. Chem*. **2011**, *50*, 192–212.

145. (a) Patra, A. K. Rowland, J. M. Marlin, D. S. Bill, E. Olmstead, M.M. Mascharak, P. K. *Inorg. Chem*. **2003**, ***42***, 6812–23. (b) Patra, A. K. Afshar, R. K. Olmstead, M. M. Mascharak, P. K. *Angew. Chem. Int. Ed*. **2002**, *41*, 2512–5.

146. (a) Nagashima, S. Nakasako, M. Dohmae, N. Tsujimora, M. Takio, K. Odaka, M. Yohda, M. Kamiya, N. Endo, I. *Nat. Struct. Biol.* **1998**, *5*, 347. (b) Song, L. Wang, M. Z. Shi, J. J. Xue, Z. Q. Wang, M. X. Qian, S. J. *Biochem. Biophys. Res. Commun.* **2007**, *362*, 319.

147. Patra, A. K. Olmstead, M. M. Mascharak, P. K. *Inorg. Chem*. **2003**, *42*, 7363–5.

148. (a) Szundi, I. Rose, M. J. Sen, I. Eroy-Reveles, A. A. Mascharak, P. K. Einarsdottir, O. *Photochem. Photobiol*. **2006**, *82*, 1377–84. (b) Madhani, M. Patra, A. K. Miller, T. W. Eroy-Reveles, A. A. Hobbs, A. Fukuto, J. M. Mascharak, P. K. *J. Med. Chem*. **2006**, *49*, 7325–30.

149. Ghosh, K. Eroy-Reveles, A. A. Avila, B. Holman, T. R. Olmstead, M. M. Mascharak, P. K. *Inorg. Chem*. **2004**, *43*, 2988–97.

150. Eroy-Reveles, A. A. Leung, Y. Beavers, C. M. Olmstead, M. M. Mascharak, P. K. *J. Am. Chem. Soc*. **2008**, *130*, 4447–58.

151. Zheng, W. Wu, S. Zhao, S. Geng, Y. Jin, J. Su, Z. Fu, Q. *Inorg. Chem.* **2012**, *51*, 3972.

152. Hoffman-Luca, C. G. Eroy-Reveles, A. A. Alvarenga, J. Mascharak, P. K. *Inorg. Chem*. **2009**, *43*, 9104–11.

153. Patra, A. K. Rose, M. J. Murphy, K. Olmstead, M. M. Mascharak, P. K. *Inorg. Chem*. **2004**, *43*, 4487–95.

154. Fry, N. L. Heilman, B. J. Mascharak, P. K. *Inorg. Chem.* **2011**, *50*, 317.

155. Rose, M. J. Olmstead, M. M. Mascharak, P. K. *J. Am. Chem. Soc*. **2007**, *129*, 5342–3.

156. Rose, M. J. Fry, N. L. Marlow, R. Hinck L. Mascharak, P. K. *J. Am. Chem. Soc*. **2008**, *130*, 8834-46.

157. Fry, N. L. Wei, J. Mascharak, P. K. *Inorg. Chem.* **2011**, *50*, 9045.

158. Ettenson, D. S. Edelman, E. R. *Vasc. Med.* **2000**, *5*, 97–102.

159. Bertrand, O. F. Sipehia, R. Mongrain, R. Rodes, J. Tardif, J. C. *J. Am. Coll. Cardiol.* **1998**, *32*, 562–71

160. Pulfer, S. K. Ott, D. Smith, D. J. *J. Biomed. Mater. Res.* **1997**, *37*, 182–9.

161. (a) Maalej, N. Albrecht, R. Loscalzo, J. Folts, J. D. *J. Am. Coll. Cardiol* **1999**, *33*, 1408–14. (b) Stamler, J. S. Simon, D. I. Osborne, J. A. Mullins, M. E. Jaraki, O. *Proc. Natl. Acad. Sci. USA* **1992**, *89*, 444–8.

162. Jen, M. C. Serrano, M. C. van Lith, R. Ameer, G. A. *Adv. Funct. Mater.* **2012**, *22*, 239–60.

163. Nablo, B. J. Rothrock, A. R. Schoenfisch, M. H. *Biomaterials* **2005**, *26*, 917-24.

164. Hetrick, E. M. Prichard, H. L. Klitzman, B. Schoenfisch, M. H. *Biomaterials* **2007**, *28*, 4571–80.

165. Nablo, B. J. Schoenfisch, M. H. *Biomaterials* **2005**, *26*, 4405–15.

166. Wang, Y. X. Robertson, J. L. Spillman, W. B. Claus, R. O. *Pharmaceut. Res.* **2004**, *21*, 1362-73.

167. (a) Wheatley, P. S. Butler, A. R. Crane, M. S. Fox, S. Xiao, B. Rossi, A. G. Megson, I. L. Morris, R. E. *J. Am. Chem. Soc.* **2006**, *128*, 502−9. (b) Fox, S. Wilkinson, T. S. Wheatley, P. S. Xiao, B. Morris, R. E. Sutherland, A. Simpson, A. J. Barlow, P. G. Butler, A. R. Megson, I. L. Rossi, A. G. *Acta Biomater* **2010**, *6*, 1515−21.

168. Tfouni, E. Doro, F. G. Gomes, A.J. da Silva, R.S. Metzker, G. Benini, P.G.Z. Franco D.W. *Coord. Chem. Rev.* **2010**, *254*, 355-71.

169. Heilman, B.J. Gonzalez, M.G. Mascharak, P.K. *Progress in Inorganic Chemistry, vol 58,* Karlin, K.D. Ed. John Wiley & Sons: San Diego, Ca; 2014.

170. Haddad, P. S., Seabra, A. B. Biomedical Applications of Magnetic Nanoparticles, in *Iron Oxides: Structure, Properties and Applications.* Martinez, A. I. Ed. Nova Science Publishers, Inc.: New York; 2012, 165−188.

171. Seabra, A. B. Pasquôto, T. Ferrarini, A. C. F. Santos, M. D. C. Haddad, P. S. de Lima, R. *Chemical research in toxicology*, **2014**, *27*, 1207-18.

172. Nazir, S. Hussain, T. Ayub, A. Rashid, U. MacRobert, A. J. *Nanomed. Nanotechnol.* **2014**, *10*, 19−34.

173. Sudhesh, P., Tamilarasan, K., Arumugam, P., & Berchmans, S. *ACS applied materials & interfaces*, **2013**, *5*, 8263-6.

174. Ramla, M. M. Omar, M. A. El-Khamry, A. M. El-Diwani, H. I. *Bioorg. Med. Chem.* **2005**, *14*, 7324−32.

175. Dougherty, T. J. Marcus, S. L. *Eur. J. Cancer* **1992**, *28A*, 1734-42.

176. DeRosa, F. Bu, X. Ford, P. C. *Inorg. Chem.* **2005**, *44*, 4157-4165

177. (a) Pinaud, F. Michalet, X. Bentolila, L. A. Tsay, J. M. Doose, S. Li, J. J. Iyer, G. Weiss, S. *Biomatererials* **2006**, *27*, 1679-87. (b) Larson Daniel, R. Zipfel, W. R. Williams, R. M. Clark, S. W. Bruchez, M. P. Wise, F. W. Webb, W. W. *Science* **2003**, *300*, 1434-1436.

178. Neuman, D. Ostrowski, A. D. Mikhailovsky, A. A. Absalonson, R. O. Strouse G. F. Ford, P. C. *J. Am. Chem. Soc.* **2008**, *130*, 168.

179. Garcia, J. V., Yang, J., Shen, D., Yao, C., Li, X., Wang, R., Stucky, G. D., Zhao, D., Ford, P. C. and Zhang, F. *Small* **2012**, *8*, 3800–5.

180. Burks, P. T. Garcia, J. V. GonzalezIrias, R. Tillman, J. T. Niu, M. Mikhailovsky, A. A. Zhang, J. Zhang, F. Ford, P. C. *J. Am. Chem. Soc.* **2013**, *135*, 18145–52.

181. Tfouni, E. Doro, F. G. Figueiredo, L. E. Pereira, J. C. Metzker, G. Franco, D. W. *Curr. Med. Chem*. **2010**, *17*, 3643-57.

182. Mitchell-Koch, J. T. Reed, T. M. Borovik, A. S. *Angew Chem. Int. Ed.* **2004**, *43*, 2806.

183. Gomes, A. .J. Barbougli, P. A. Espreafico, E. M. Tfouni, E. *J. Inorg. Biochem.* **2008**, *102*, 757-66.

184. Bohlender, C. Wolfram, M. Goerls, H. Imhof, W. Menzel, R. Baumgaertel, A. Schubert, U. S. Mueller, U. Frigge, M. Schnabelrauch, M. Wyrwa, R. Schiller, A. *J. Mater. Chem.* **2012**, *22*, 8785.

185. Eroy-Reveles, A. A. Leung, Y. Mascharak, P. K. *J. Am. Chem. Soc.* **2006**, *128*, 7166.

186. Franz, M. Heorl, W. H. *Nephrol. Dial. Transplant*. **1999**, *14*, 2746–53.

187. Regev-Shoshani, G. Ko, M Miller, C. Av-Gay, Y. *Antimicrob. Agents Chemother.* **2010**, *54*, 273–9.

188. Halpenny, G. M. Gandhi, K. R. Mascharak, P. K. *ACS Med. Chem. Lett.* **2010**, *1*, 180.

189. Masters K. S. B. Leibovich, S. J. Belem P. West J.L. Poole-Warren, L.A. *Wound Rep. Reg.* **2002**, *10*, 286-94.

190. Halpenny, G. M. Steinhardt, R. C. Okialda, K. A. Mascharak, P. K. *J. Mater. Sci. Mater. Med*. **2009**, *20*, 2353–60.

191. Halpenny, G. M. Olmstead, M. M. Mascharak, P. K. *Inorg. Chem*. **2007**, *46*, 6601–6.

Chapter 2

Light-Controlled Antibiotic Effects of a Polyurethane Film Containing Silica-Xerogel Particles with Encapsulated Photoactive Manganese Nitrosyl

2.1 Background

Skin and soft-tissue infections (SSTI) can be extremely problematic in open cutaneous wounds arosomg from traumatic injury or surgical procedures.[1] Such wounds compromise the integrity of the epidermis and serve as an open portal for the colonization of the underlying cutaneous and soft-tissue layers by pathogenic microbes. Although the presence of colonizing microbes usually has no immediate clinical significance on the outcome of the wound, their unabated growth can severely disrupt the wound healing process causing abnormal tissue repair such as aberrant scarring, non-healing chronic wounds, or tissue necrosis.[2] The ability of a microbial population to progress from colonization to infection is dependent on the inoculum size and virulence but inhibited by the competency of the local and systemic host defenses.[3] However, in certain cases of skin and soft-tissue injury such as those that present certain anatomical deficiencies (e.g. avascular tissue burns or neuropathic diabetic ulcers) or a concurrent health condition (e.g. immunodeficiency or peripheral vascular disease), the limited potential for a sufficient immune response often necessitates clinical intervention to mitigate the almost certain onset of infection.

One of the most important aspects of wound care is the expeditious and proper dressing of the wound, which can facilitate rapid hemostasis and protect the open wound site from further contamination or trauma.[4] Although wound dressings were initially designed to act solely as a protective barrier against further damage and infection, their passive role in wound care rapidly transformed following a seminal report by Winter in 1962.[5] In order to assess the effects of moisture retention on the healing process of open cutaneous wounds, he observed the progress of two superficial incisions on the back of a porcine model, one covered with a moisture impermeable polyethylene film and the other left uncovered. In addition to providing protection from external contaminates, the polyethylene films dramatically decreased the moisture vapor transmission rate (MVTR) from the wound bed which caused a significant change in the physiology of the healing process compared to the exposed wound. Histological examination of the incisions 24 h post-wounding demonstrated that the exposed wound underwent severe dehydration of the wound bed and several layers of the dermis while the occlusive film retained a high level of moisture in the wound bed and maintained the viability of the underlying tissue including a healthy population of basal cells attached to an intact basement membrane. The high moisture content of the occlusively dressed wound greatly enhanced the degradation of the collagen bundles by matrix metalloproteinases secreted during the advancement of autolytic leukocytes through the granular tissue and facilitated the subsequent migration of keratinocytes. In order to restore the epidermis, basal cells detach from the basement membrane and differentiate into a migratory keratinocyte cell type which follow the leukocytic front towards the surface of the wound. Upon reaching the last layer of granular tissue with adequate moisture to support re-epithelialization, keratinocytes differentiate and form cellular contacts characteristic of a healthy epidermis. The regeneration of the epidermis at the wound surface accelerates maturation of the underlying granular tissue through the activity of autolytic macrophages and migratory keratinocytes which transform the randomly oriented ‘mat’ of type-III collagen granules into an organized matrix of cross-linked type-I collagen fibrils that are aligned with the tension lines of the peripheral tissue. This new extracellular matrix will eventually support a cellular population similar to the surrounding tissue and reach a tensile strength of >80% of the pre-wound site.[6] Such processes are inhibited in the exposed wound as a result of the thick, rigid granular layer formed by the dehydration of the wound bed and several layers of the underlying dermis. Since the dehydrated incision lacks a viable basement

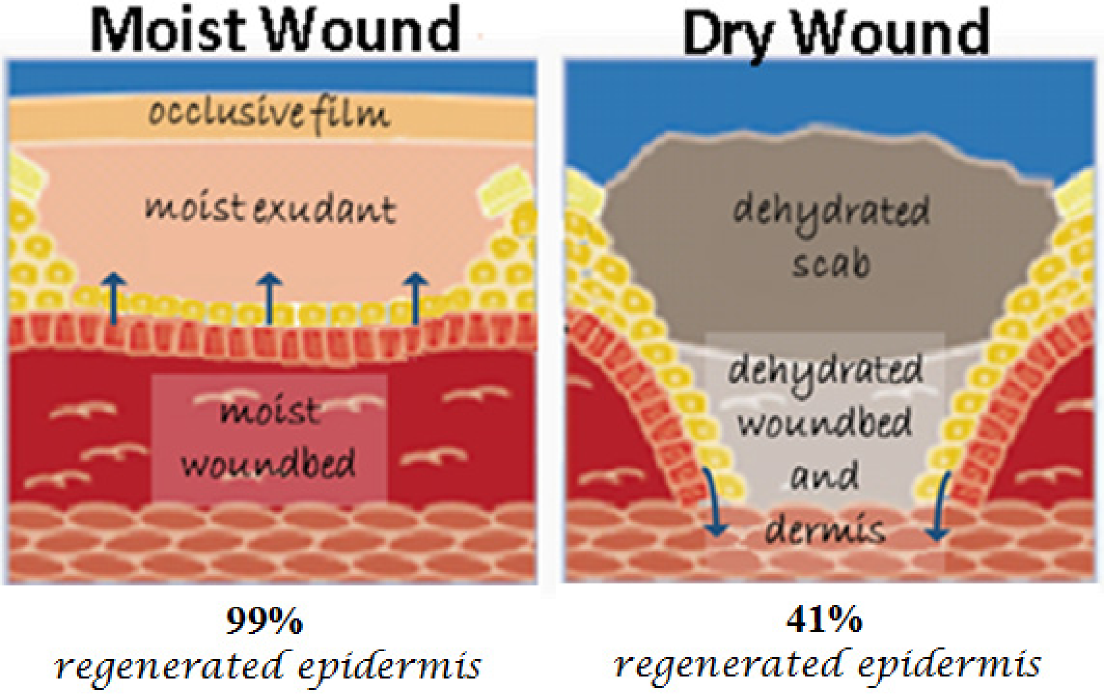

Figure **2.1** – Wound re-epithelialization under moist conditions produced by an occlusive film dressing was 99% complete after 3 days post-wounding (left), while re-epithelialization under dry conditions resulting from the exposure of the wound to the air was only 41% complete after 3 days post-wounding (right). The depictions illustrate the observations reported by Winter on the enhanced re-epithelialization of superficial wounds in a procine model as a result of wound occlusion using a polyethylene film. Adapted from Ref 5.

membrane, re-epithelialization occurs through the lateral migration of keratinocytes from the perphieral tissue through the outer layer of hydrated dermis across the epidermal gap. As the keratinocytes migrate underneath the impenetrable scab covering the wound bed they must degrade the ECM of the healthy tissue to prepare a wound bed that will support the repair process, resulting in a considerable delay of re-epithelialization compared to that of the hydrated wound (Figure 2.1). The enhanced mobility of keratinocytes at the surface of occluded wounds increases the rate of re-epithelialization nearly two-fold. Recent clinical evidence has shown that the increased moisture content of occluded wounds poses no significant risk of infection, in contrast to previous assumptions which discouraged the use of occlusive films for nearly two decades after Winter's report.

Since the first report by Winter on the ability of occlusive film dressings to retain moisture in the wound bed and increase the rate of re-epithelialization in Porcine models, numerous clinical studies using human patients have produced similar results with the preponderance of current evidence demonstrating that occlusive dressing of acute wounds increases the rate of re-epithelialization by ~40%.[7] However, a lack of evidence from well executed and unbiased clinical trials have prevented a reliable analysis of the benefits and risk of occlusive dressings for chronic, non-healing wounds.[3] One well designed, moderate sized clinical study found that occlusive dressing of venous leg ulcers enhanced the formation of healthy granular tissue in the wound bed by 81% while only 46% (19 out of 36) of patients treated with occlusive dressings demonstrated enhanced ulcer re-epithelialization.[8] These results suggest that occlusive dressing of chronic wounds may be beneficial in promoting tissue granulation and remodeling, but less effective for promoting re-epithelialization. This could result from the accumulation of senescent fibroblasts (common cellular phenotype in chronic wounds that is unable to replicate and shows altered functionality) that produce dramatically lower levels of epidermal growth factors (EGF), effectively halting keratinocyte proliferation despite the presence of a well granulated wound bed.[9]

In order to induce re-epithelialization in such wounds, the impregnation of EGF and other growth factors (GFs) into primary dressings that exchange fluids with the wound bed in combination with a secondary occlusive film dressing may be a promising method for inducing re-epithelialization in chronic wounds that fail to heal under moist conditions alone.[10] However, the clinical use of GF-based therapy in wound care is still limited by an inadequate understanding of the cellular and molecular abnormalities that occur in chronic, non-healing wound, as well as the limitations of current delivery methods which lack the ability to deliver a precise dose of GFs to the desired target. and targeting of exogenous GFs to the desired receptor and/or cell type.[10] Some of the major technical hurdles in developing a successful delivery platform for GFs include the degradation of GFs by proteolytic enzymes that are present in high concentrations in the exudant of chronic, non-healing wounds, the required *in situ* activation of GFs by matrix metalloproteinases and/or hetero/homo-dimerization with protein activators such as herapin, and the multiple receptors and/or cell types that are responsive to a single GF.[11] A thorough understanding of the temporal and sequential requirements of single or, preferably, multiple GF therapies is also needed as many GFs can generate signal cascades that affect multiple downstream cellular processes when appropriate feedback is not provided.[12] Most clinical investigators agree that the GF therapy is a promising treatment for restoring normal cellular function in chronic, non-healing wounds,[13] but they also agree that it should be pursued with the utmost care since many of the same growth factors required for proper wound healing are also implicated in carcinogenesis.[14] Therefore, future work should focus on identifying wound healing–specific pathways and the development of GF delivery methods capable of the precise activation of those pathways.[15]

Another signaling molecule with a complex role in nearly all phases of wound healing is nitric oxide (NO). The central role of NO in the re-epithelialization process has been demonstrated by the following observations: (a) keratinocyte proliferation is iNOS-dependent (inducible nitric oxide synthase) as revealed by the limited replication of keratinocytes following L-NAME supplementation (L-N^G-Nitroarginine methyl ester, an iNOS inhibitor),[16] (b) exogenous NO induces keratinocyte proliferation and differentiation to a locomotive phenotype,[17] and (c) wound re-epithelialization proceeds at an [NO] dependent rate (with potential mediation through downstream vascular endothelial growth factor (VEGF) signaling).[18] Clinical evidence for the ability of NO to induce re-epithelialization in humans was demonstrated, anecdotally, by a case study that investigated the effect of NO therapy to treat a non-healing venous leg ulcer that had shown no response to 2 years of prior, best available treatment.[19] Healthy granular tissue was observed on the surface of the ulcer after just 3 days of NO therapy delivered over eight separate one hour treatment courses involving enclosure of the wounded leg in an inflatable plastic boot which was flushed at a rate of 1.0 L min^{-1} with 200 ppm $NO_{(g)}$. On day 14, the wound became almost completely re-epithelialized at which point treatment was discontinued. However, the wound continued to progress and was declared clinically healed 26 weeks after the start of NO therapy (normal healing times are much longer for similar sized chronic wounds). In addition to its effect on epidermal regeneration, NO is also a vital signaling molecule for coordinating the production of extracellular matrix by fibroblasts and has been shown to induce collagen synthesis and promote an overall increase in the rate of extracellular matrix production through various signaling pathways.[20] Another important phase of wound healing, contraction, which reduces the size of the epidermal gap that must be closed by keratinocyte proliferation and migration, is also NO-dependent as demonstrated by the delayed contraction of excisional wounds in iNOS knockout murine models.[21] In light of the multi-faceted role of NO in the wound healing process, the measurement of decreased levels of NO metabolites in the exudant of non-healing diabetic wounds (compared to properly healing wounds) strongly indicates an association at some level between disrupted NO signaling and the delayed healing process observed in chronic wounds.[22] This association is further substantiated by the ability to partially restore the healing capacity of non-healing diabetic wounds through an increase in dietary L-arginine (substrate for NO synthesis by NOS).[23] Together these observations indicate a vital role for NO signaling in nearly all phases of the wound healing process, and suggest that exogenous NO therapy could be an effective treatment to induce healing in chronic wounds or to increase the rate of healing in open wounds that present a significant health-risk due to their potential for severe infection or other complications.[24]

Similar to the role of growth factors in the wound healing process, NO signaling during inflammation and healing is complex and requires precise temporal regulation to properly induce the correct sequence of cellular functions involved in wound healing.[25] Given that disruption in the sequence of wound healing phases can precipitate a cycle of dysfunctional cellular activity similar to cellular dysfunction in non-healing wounds, it seems possible that unregulated delivery of exogenous NO to the wound site (a powerful mediator of cellular function involved all phases of wound healing) could produce a similar state of cellular dysfunction.[26] In order to address such concerns, methods for delivering a precise dose of NO in a temporally and spatially controlled manner are required to provide investigators the necessary tools to establish a thorough understanding of the cellular and mechanistic effects of exogenous NO on the wound healing process.[25] Such knowledge is vital for the establishment of safe and effective treatment parameters for the development of future NO-based therapies for the treatment of SSTI and non healing wounds. Recognizing the lack of NO-delivery systems capable of achieving such rigorous demands, the Mascharak lab has performed extensive research over the last few years to develop advanced NO-delivery methods through the incorporation of photoactive transition metal nitrosyls into stable, biocompatible matrices to afford NO-releasing composite materials capable of rapidly delivering the desired dose of NO to the targeted site by stimulation with low-power visible light.[27]

Through the rational design of multidentate metal chelating ligands, our lab has synthesized the stable {Mn-NO}^{6} nitrosyls, [Mn(PaPy$_3$)(NO)](ClO$_4$)[28] and [Mn(PaPy$_2$Q)(NO)](ClO$_4$)[29], which rapidly release NO upon irradiation with low power visible and infrared light, respectively. The incorporation of these nitrosyls in optically transparent and NO-permeable matrices has afforded composite materials that are well-suited for the site specific, rapid delivery of high doses of NO under the complete control of light. In addition, we have utilized robust encapsulating matrices to serve as physical barriers to minimize any negative interactions between the application site and the metal based complex. Due to the mild reaction conditions of sol-gel based chemistry using alkoxysilicates, our laboratory has made extensive use of sol-gel chemistry for the encapsulation of photoactive metal nitrosyls within a highly stable and biologically inert silica matrix.[27] The encapsulation of [Mn(PaPy$_3$)(NO)](ClO$_4$) and [Mn(PaPy$_2$Q)(NO)](ClO$_4$) within a silica-gel matrix was achieved without degradation of the encapsulated nitrosyl by dissolving the nitrosyls in a pre-polymerized solution of tetraethoxysilicate in ethanol and water followed by the addition of a mild acid catalyst to promote polymerization of the silicate monomers into a sol-gel.[30, 29] After gelation the solution, the resulting nitrosyl-gel composites were cut into disks and coated with a thin, transparent layer of medical grade polyurethane to prevent leaching of the nitrosyl from the sol-gel pores. The sol-gel based encapsulation method used for these materials resulted in only modest attenuation of the quantum yield values of NO release in comparison to the free nitorysls owing to the highly transparent and NO permeable nature of the silica-gel matrix.[27] Sol-gel chemistry was also utilized to encapsulate $[Mn(PaPy_3)(NO)](ClO_4)$ within a sol-gel monolith cast on the polished end of a fiber optic line that permitted remote activation of the nitrosyl by the transmission of light from the opposite end of the fiber optic line to the sol-gel tip.[31] To demonstrate the utility of this platform for the treatment of infection in internal sites (*e.g.* urinary tract infections), the nitrosyl-gel tip was submerged in a narrow Eppendorf tube containing liquid culture with different pathogens which had been grown to the clinically defined confluencey of infection ($>10^5$ CFU mL^{-1}) and illuminated by a remote light to activitate NO release for ~10 min. The treated cultures were swabbed onto agar plates along with negative controls and incubated for 16 h. The plates were then visually assessed for microbial clearing which demonstrated the ability of the photoreleaseed NO to cause complete eradication of *P. aeruginosa* bacterial loads, near eradication of *Escherichia coli* and methicillin susceptible *S. aureus*, and a significant reduction in methicillin-resistant *S. aereus* (MRSA).

Although the aforementioned nitrosyl-gel composites demonstrated efficient release of NO from functionally well-designed materials, the tendency of the solvent to evaporate from the silica-gel interior of the composites during handling resulted in the formation of a brittle glass-like material that was highly susceptible to fragmentation.[29-31] The potential fragmentation of these materials during therapeutic application could be detrimental and severely limits the shelf life of the composite materials. To address such concerns, we now report a flexible, polyurethane (PU) based film containing a dispersion of silica xerogel particles (~100 μm) incorporated with 3 mol% of the photoactive Mn-nitrosyl $[Mn(PaPy_3)(NO)](ClO_4)$ (henceforth abbreviated $\{Mn\text{-}NO\}^6$).[32] The polyurethane based xerogel-nitrosyl films (PUX-NO) demonstrated rapid NO photorelease upon exposure to low-power visible light which was able to cause complete eradication of several gram-positive and gram-negative pathogenic bacteria including a strain of methicillin-resistant of *S. aureus*. As described in the following sections, the properties of the PUX-NO films serve as a proof of concept to demonstrate their utility as a NO-releasing occlusive film for the treatment of SSTI or chronic, non-healing wounds. Since the NO-release rate from the films can be modulated by simple adjustment of the intensity of the light source, the films could be used to first clear the microbial burden from the wound site using high fluxes of NO and then provide a moderate, sustained flux of NO through modulation of the illumination intensity in order to accelerate the initial phases of the wound healing process to induce rapid re-epithelialization and mitigate the potential for recurrent infections.[10]

Since the desired outcome of wound care is not only the prevention or clearance of infection but also complete healing of the wound, methods to deliver antimicrobial agents, such as NO, to the wound site should not abate the healing process (unless the risk for severe infection is eminent and its clearance must be prioritized). Although NO therapy alone aids the wound healing process independent of other treatment factors, the maximum benefit to the outcome of the wound will be achieved by merging NO-delivery systems with clinical standards of wound care, which focus heavily on optimizing the wound bed to facilitate and promote re-epithelialization. In discussing the importance of wound bed management in conjunction with the topical administration of biological factors, Sibbald *et al.* stated that:

> "A single biologic factor in a fixed concentration without the ideal local wound bed properties will often fail…"[33]

In this proof of concept study we focused solely on the synthesis and characterization of a single layer polyurethane film that could be used as a primary dressing for low exudant, superficial to partial thickness wounds, or as a secondary backing for an absorbent, primary dressing. Since the onset of SSTI often results in an abrupt increase in wound exudant due to the overexpression of pro-inflammatory cytokines,[34] occlusive dressings for infected wounds usually consist of a primary dressing to absorb excess exudant which otherwise could cause peri-wound tissue maceration due to the presence of soluble bacterial toxins. To extend the wear time of the primary dressing and promote wound occlusion, a secondary polyurethane film backing with an appropriately adjusted moisture vapor transmission rate (MVTR) to wick absorbed moisture from the wound contacting, primary dressing is often used. [35] The reduced frequency of dressing changes limits the exposure of the wound to infectious agents and mitigates damage to newly formed wound tissue that often adheres to the primary layer. OPSITE® Post-Op Visible is a commercially available, transparent dressing manufactured by Smith & Nephew consisting of a polyurethane film backing with an adhered lattice structured, absorbent foam pad that allows monitoring of the wound site and absorption of moderate exudant over an extended period of time, reducing the frequency of dressing changes by 60% compared to standard gauze.[36] The use of the

PUX-NO formulation for the polyurethane backing of such films could be easily achieved allowing for SSTI treatment regimens in which wound and infection progress could be monitored before and after NO exposure without disturbing the wound bed.

2.2 Synthesis and Optimization of PUX-NO films

2.2.1 Encapsulation of [Mn(PaPy$_3$)(NO)](ClO$_4$) in Silica-Xerogel Particles

The incorporation of [Mn(PaPy$_3$)(NO)](ClO$_4$) ({Mn-NO}^{6}) into a polyurethane (PU) film was first attempted without encapsulating the compound into a silica matrix. This was pursued by dissolving the nitrosyl in a liquid PU solution, casting the film, and allowing it to cure overnight (12 h). The cured films were immediately checked for their ability to retain the incorporated nitrosyl within the PU matrix by submersion of the film in water which resulted in immediate leaching of the compound from the polymer film. In the next phase, the nitrosyl was first entrapped in silica particles that were of adequate size for immobilization within the PU matix. A visual schematic of the step by step assembly process is shown in Figure **2.3**. Assembly of PUX-NO films was achieved by first dissolving the desired mass of {Mn-NO}^{6} (2-18 mg) into an aqueous sol of tetramethylorthosilicate (1.15 mL) that had been rapidly stirred until homogenized. The nitrosl-sol mixture was allowed to gelate and the nitrosyl-gel composite was then allowed to dry at room-temperature until most of the solvent had evaporated to form a brittle glass-like xerogel (48-72 h, depending on the concentration of {Mn-NO}^{6}). Next, the green xerogel glass was crushed in a mortar and pestle to obtain silica particles ranging from 1–100 μm in diameter. Tecoflex® SG-80A thermoplastic polyurethane (PU) beads composed of alternating soft and hard segments of macromolecular tetramethyleneglycol chains (soft) and 4,4-methylenedicyclohexyl diisocyanate condensed with 1,4-butanediol (hard) (Figure **2.2**) were dissolved in tetrahydrofuran (THF) (1g PU to 10 mL, 10%) with stirring until a homogenous, viscous liquid was obtained. The silica particles with embedded {Mn-NO}^{6} were finally dispersed into a solution of 10% PU in THF at ratio of 1:4 by mass (xerogel:10% PU in THF) and an aliquot of 400 mg of the final solution was spin-coated onto round glass slides (22 mm ø). The films were allowed to cure in the dark overnight (~12 h) at room temperature affording a flexible polyurethane film. To ensure that surface exposed silica particles did not become dislodged from the films or leach the nitrosyl to the contacting media during application, the films were dip-coated with a thin formulation of 5% PU in THF to passivate the films with an outer layer of non-medicated polyurethane. The PUX-NO films thus produced are quite flexible and were readily cut with a razor blade to any shape. Cross sections of the film were visually inspected using bright field microscopy to demonstrate an even dispersion of the silica

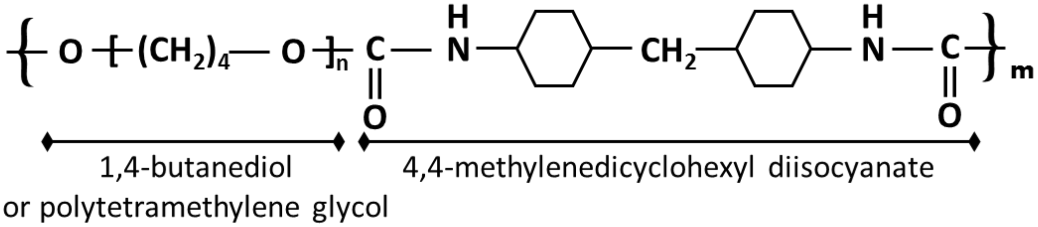

Figure **2.2** – Chemical formula of Tecoflex ® SG-80A thermoplastic polyurethane chains, where n is 1 for 1,4-butandiol or macromolecular for the glycol chains.

particles throughout the films (Figure **2.3(F)**, inset). In repeated preparations using the above outlined procedure, we obtained ~200 µm thick films although films of greater thickness can be assembled.

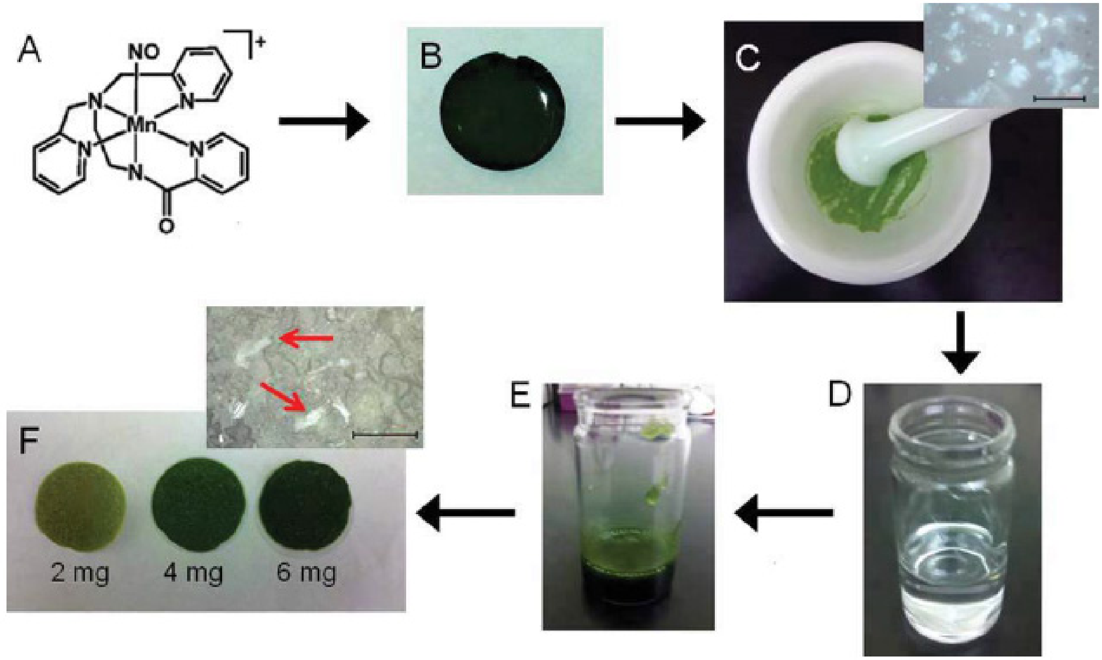

Figure **2.3** - Schematic of the synthesis of PUX-NO films. (A) $[Mn(PaPy_3)(NO)]^+$ $\{Mn\text{-}NO\}^6$; (B) $\{Mn\text{-}NO\}^6$ -incorporated into silica xerogel; (C) Crushed xerogel. Inset: 100x magnification of crushed silica particles. Scale bar is 40 µm.; (D) Pre-swelled solution of polyurethane in THF; (E) Crushed xerogel dispersed in polyurethane solution; (F) Cured polyurethane disks of PUX-NO on glass support containing various amounts of $\{Mn\text{-}NO\}^6$. Inset: 20x magnification of the surface of a PUX-NO film showing dispersion of silica particles. Red arrows show embedded silica particles. Scale bar is 200 µm.

2.2.2 Optimization of the Moisture Content of PUX-NO Films to Achieve Maximum NO Release

In determining the optimal procedure for preparing the PUX-NO films, accelerated curing of the films was attempted by baking the freshly cast films in an 80°C oven for 1 h. The resulting films were notably dry during handling and no significant moisture content (q%, section 2.8.2) was measured in the films. Additionally, illumination of the dry films with 300 mW of visible light over a period of 1 h produced no photorelease of NO as monitored by an NO-sensitive electrode. The lack of photoactivity from the dry films can be explained by the role of an outer sphere solvent molecule in the $\{\text{Mn-NO}\}^6$ photoreaction. Following photoexcitation of $\{\text{Mn-NO}\}^6$ in the ground state to an Mn-NO antibonding excited state, an outer sphere solvent molecule displaces NO from the inner coordination sphere of the excited state complex which rapidly oxidizes in the presence of oxygen to form the Mn(III) photoproduct $[\text{Mn(PaPy)}_3\text{(solv)}]^{2+}$, according to eq (**1**):[28]

$$[\text{Mn(PaPy)}_3\text{(NO)}]^{+} + \text{solv} + h\nu \xrightarrow{O_2} [\text{Mn(PaPy)}_3\text{(solv)}]^{2+} + \text{NO}\cdot \qquad \textbf{(1)}$$

This observation suggests that the moisture content of the PUX-NO films has a significant influence on the NO photorelease capability of the entrapped nitrosyl. Therefore, pre-swelling of the polyurethane films was pursued by the addition of 1 mL of water into 10 mL of 10% PU in THF with stirring until homogenous followed by the addition of the nitrosyl-silica particles. The pre-swelled films were cured overnight by storage in the dark at room temperature (~12 h) and then dip-coated in a solution of 5% PU in THF. The moisture content (q%) of the pre-swelled films approached 30 wt%

while the moisture content of the films prepared without pre-swelling stayed within a range of 10–20 wt%.

The effect of the moisture content from the pre-swelling step on the NO photo-release capability of the PUX-NO films was monitored using a NO-specific electrode (Figure **2.4(A)**). The curve labeled ‘‘with water’’ (film pre-swelled with water) reaches a steady state of [NO] within 10 min of illumination which is sustained for > 2 h, while the curve labeled ‘‘no water’’ (no pre-swelling of film) never reaches a steady state of [NO] but instead peaks after 20 min of illumination and then drops off approaching baseline after 1 h. We hypothesize that the use of THF (a dehydrating solvent) [37] in the fabrication of the PUX-NO film dehydrates the silica particles and reduces the hydration shell of the embedded Mn nitrosyl to the determinant of the solvent-dependent, NO-releasing photoreaction (**1**). In contrast, pre-swelling of the PU films, with saturation of the water adsorption capacity of the hydrophilic silica-xerogel particles (> 30 wt% during storage in a moisture saturated atmosphere (100% RH)) [38], appears to adequately hydrate the embedded Mn nitrosyl and ensure quantitative NO release.[39] Additionally, pre-swelling of the polyurethane matrix with water has an effect on the rate of NO release from PUX-NO films by altering the permeability of the medium to NO. Meyerhoff and coworkers have reported the diffusion coefficient of NO (D_{NO}) in various media.[40] For Tecoflex SG-80A solvent cast polyurethane films, D_{NO} was found to be 2.74 x 10^6 cm^2 s^{-1} while for water D_{NO} was 4.8 x 10^6 cm^2 s^{-1}, suggesting that films with a higher water content should exhibit enhanced NO permeability. Thus, all further preparations of PUX-NO films included the pre-swelling step and all remaining measurements were performed using films prepared with the pre-swelling step.

2.3 Light-activated NO release from PUX-NO films

2.3.1 NO Photo-release Rate and Duration from PUX-NO

NO photo-release from 5 x 5 mm squares of PUX-NO during illumination with 300 mW cm^{-2} white light was measured using an NO-sensitive electrode in 1.5 mL of PBS buffer. The rate and duration of NO release from the PUX-NO squares was varied by increasing the concentration of $\{Mn\text{-}NO\}^6$ incorporated into the silica-xerogel partices but could also be varied by adjusting the intensity of the light source. Upon illumination, the PUX-NO squares rapidly released NO for 30–120 min depending on the concentration of $\{Mn\text{-}NO\}^6$ in the film. The curve labeled ‘‘with water’’ in Figure **2.4(A)** demonstrates typical release kinetics of a film containing 18 mg of $\{Mn\text{-}NO\}^6$. As shown, the film rapidly released NO reaching a peak concentration of ~400 µM NO in 1.5 mL of water within 10 min and maintained a steady NO concentration greater than 300 µM for 2 h. This volume of water (1.5 mL) was chosen as it represents the volume of agar beneath the area covered by the films on the inoculated agar plates (25 Ml in 90 mm ø plates) used for the antimicrobial assay. Figure **2.4(B)** demonstrates the

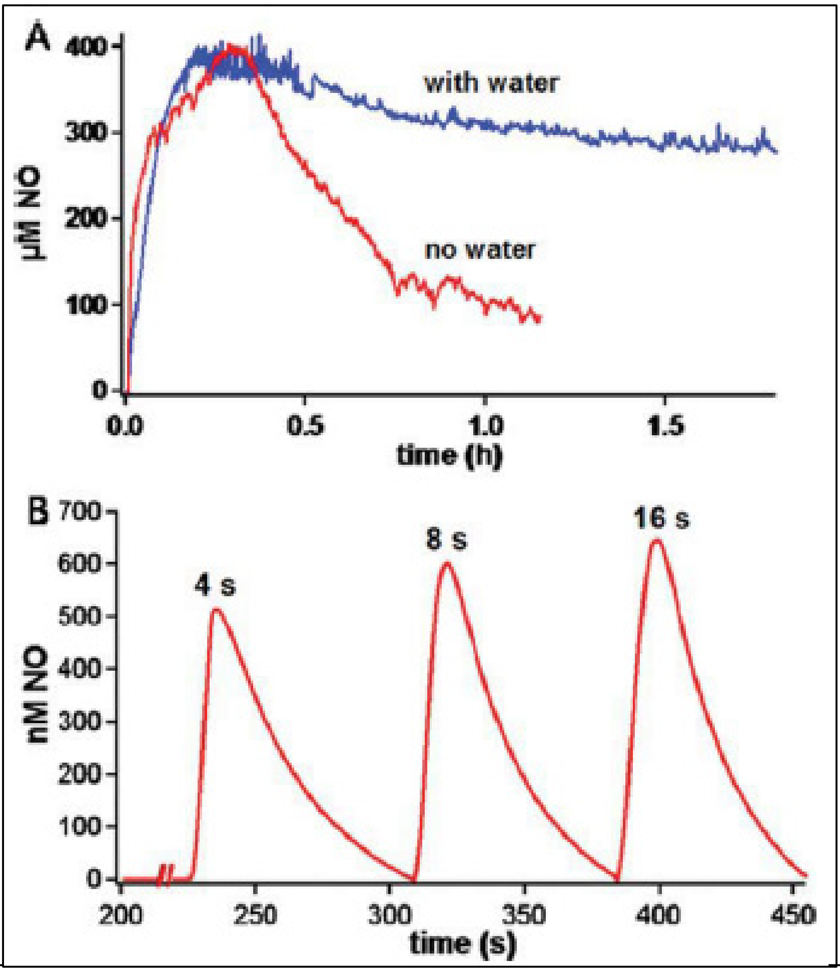

Figure **2.4** - NO photorelease (300 mW cm^{-2}) from 5 mm x 5 mm patches of PUX-NO films containing 18 mg of {Mn-NO}^{6} measured by an NO-specific electrode in PBS buffer at 25ºC. (A) Improved steady-state NO photorelease was observed from films fabricated by pre-swelling (with water) the polyurethane. (B) NO release was not observed from PUX-NO in the dark for 200 s, however, irradiation with brief pulses of light for 4, 8, and 16 s triggered rapid NO photorelease.

light controlled release of NO from PUX-NO in stirred PBS buffer at 25ºC. During the first 200 s, the film was left in the stirred solution containing the NO-sensitive electrode and kept in the dark to determine whether any NO was released in the absence of light at room temperature. No response was measured above background until after 200 s when the light was rapidly pulsed on and off for the specified time which produced bursts of NO as seen by the sharp peaks in the graph shown in Figure **2.4(B)**.

2.3.2 Visualization of the Diffusion of NO Released from PUX-NO in an Agar Matrix

The Griess test is an indirect colorimetric test for the presence of NO consisting of an aqueous solution containing 0.2% naphthylethylenediamine, dihydrochloride, 2% sulphanilamide and 5% phosphoric acid that forms a pink azo-dye following reaction of sulphanilamide with NO_2^-, formed in solution from the autooxidation of NO by dissolved O_2.[41] The Griess solution was incorporated into 20 mL 1.5% (w/v) liquid agar (45^{O}C) at a concentration of 0.5% which was poured into 90 mm petri dishes. After cooling, the solidified agar was overlayed with 6 mL of 0.7% (w/v) liquid agar (45^{O}C) containing 3.2% Griess solution. Illumination of a PUX-NO film on the surface of the plate resulted in the formation of the pink azo-dye in the agar which allowed visualization of the diffusion of NO released from the film into the surrounding media. As seen in Figure **2.5(A)**, at a dose of 4 mg of $\{Mn\text{-}NO\}^6$ per film, NO released from PUX-NO was localized to the agar directly underneath the film and a narrow, faint peripheral ring. When the dose was increased to 10 mg of $\{Mn\text{-}NO\}^6$, the boundaries of the pink dye spread well beyond the area covered by the patch, and the agar directly underneath the film turned pale yellow (Figure **2.5(B)**) due to nitration of the azo-dye from excess NO in the aqueous gel forming high concentrations of NO oxidation products such as N_2O_5 and HNO_2.[41] Such results demonstrate that although peripheral effects are seen around the site of application (radius of 2.2 cm), the spreading of NO to the surrounding media can be limited by controlling the NO release rate by varying the concentration of incorporated nitrosyl or by modulation of the intensity of the illuminating light.

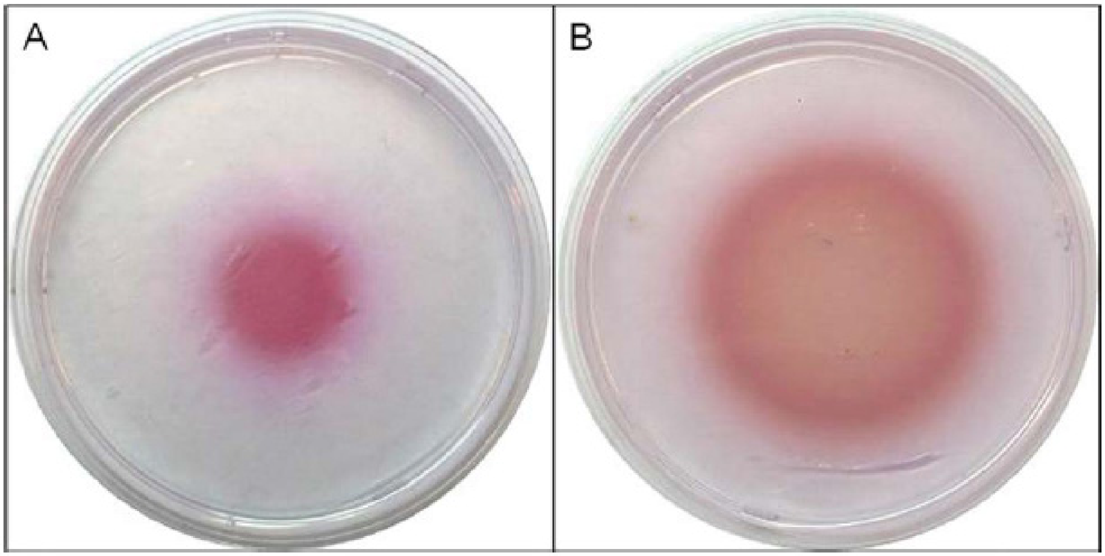

Figure **2.5** –The diffusion of NO released from PUX-NO films was visualized in an agar matrix by the formation of a pink azo-dye from the Griess reagent. (A) Area of NO diffusion from a film containing 4 mg of $\{Mn\text{-}NO\}^6$ illuminated for 20 min. (B) Area of NO diffusion from a film containing 10 mg of $\{Mn\text{-}NO\}^6$ illuminated for 20 min (300 mW cm^{-2} visible light).

The Griess agar plates were also used to check the thermal stability of PUX-NO at physiological temperature (37°C). This was achieved by placing a film on top of a Griess agar plate and transferring the plate with the film to a 37°C incubator for 16 h in the dark. The film was then removed from the agar, and the plate was exposed to light for 1 h to trigger NO release from any nitrosyl that had leached from the film into the agar. No pink azo dye was formed using films containing even the highest concentration of {Mn-NO}^{6}. These observations demonstrate that NO release from PUX-NO can only be triggered by light under physiological conditions and that the PUX-NO formulation is effective for immobilizing {Mn-NO}^{6} within an optically transparent and NO permeable material.

2.4 Optimal Storage Conditions for PUX-NO Films

As discussed in the introduction to this chapter, the motivation for this study was to address issues with the long-term stability encountered with prior NO-releasing silica-gel based materials reported by this laboratory which became brittle and lost their functionality after prolonged handling due to the loss of solvent.[29-31] Loss of moisture from the PUX-NO films is also the main concern in determining the optimal storage conditions for and shelf-life of the films. Such parameters are important to investigate as they can affect NO release rates as described earlier. All PUX-NO films were stored in 1 L Ziplock ® brand resealable LDPE bags which were wrapped in aluminum foil after the contents had been sealed inside and placed in the dark under three different storage conditions to determine the optimal conditions to maximize their shelf-life and to ensure a predictable NO release profile after storage. The three storage conditions were (1) room temperature without added moisture to the sealed bags, (2) room temperature with 1 mL of added water inside the 1 L bag, and (3) 4°C with 1 mL added water. After 3 months of storage under these conditions, the NO release profiles of the PUX-NO films were determined with the aid of the NO-specific electrode. From these measurements (Table **2.1**), the most important storage variable to ensure predictable NO release was the additional moisture in the bag. No significant difference in the NO release profiles between films stored with added moisture at room temperature and at 4°C was observed. Films that were stored with added moisture at room temperature and 4°C had average moisture content of 27 ± 1 and 29 ± 2%, respectively, after 3 months of storage. Those stored at room temperature with no added water lost a considerable amount of moisture after 3 months of storage and had a water content of 17 ± 2%. The NO release profile was similar for films stored with added moisture to the freshly prepared films, while those stored with no added moisture exhibited considerable lag in the time required to reach a steady state of NO release. For example, films with 18 mg of $\{Mn\text{-}NO\}^6$ per film stored under dry conditions took ~20 min to reach a steady state of NO release while the same formulation stored under moist conditions reached a steady state of NO release in only 10 min. These results indicate that PUX-NO films can be stored under moist conditions for months in sealed, photo-blocking packaging

Table **2.1** – Moisture content (q(%)) from storage after 3 months under various conditions (RT is room temperature). The last column shows the mass of adsorbed moisture in films with (+PS) and without (-PS) pre-swelling, and the calculated mass of adsorbed moisture in silica particles assuming q=30%.

Storage Conditions	**q(%) after 3 months storage**	**Mass of q(%) ± Preswelling (PS)**
RT (25°C) + no H_2O	27 ± 1 %	q(+PS) = 30 wt% = 0.034 g
RT (25°C) + 1 mL H_2O	29 ± 2 %	q(-PS) = 20 wt% = 0.022 g
Refrig. (4°C) + 1 mL H_2O	17 ± 2 %	q(+PS) - q(-PS) = 10 wt% = 0.012 g
		q(silica, 0.08 g) = 30 wt% = 0.024 g

(similar to the storage conditions of commercially available, soft-plastic contact lenses) and hence have excellent shelf life.

2.5 Antibacterial Properties of PUX-NO Films

2.5.1 Antibacterial Activity of PUX-NO Films using a Modified Agar Diffusion Method

To determine the efficacy of NO-photoreleasing polyurethane films as antimicrobial occlusive wound dressings, PUX-NO films were tested against both gram-positive and gram-negative bacterial pathogens that are commonly associated with SSTI using a modified agar diffusion assay and an agar overlay assay. The modified agar diffusion assay was performed as follows: 20 μL aliquots of working stock for each bacteria grown separately in tryptic soy broth (TSB) to log-phase of *Pseudomonas auregonisa*, *Acinetobacter baumannii*, *Staphylococcus aureus*, and methicillin-resistant *S. aureus* (MRSA) was dropped on the center of TSB agar plates and spread evenly across the surface of the agar by the rolling of sterile glass beads. The spread plates were then incubated for 2 h at 37^{o}C to stimulate microbial attachment and colonization. A PUX-NO film sterilized with ethanol and rinsed copiously with sterile water was then placed directly on top of the bacterial ‘‘lawn’’ of each microbe. NO photorelease from the films was triggered by illumination with 300 mW cm^{-2} of white light for the desired duration, and then the films were carefully removed and the treated plates were incubated for 16 h at 37^{o}C. Negative controls were also performed following the same procedure except for the illumination step. Plates containing PUX-

NO films with active nitrosyl of the desired concentration were kept in the dark for 1 to 2 h. The extent of microbial clearing after incubation was visually inspected for each

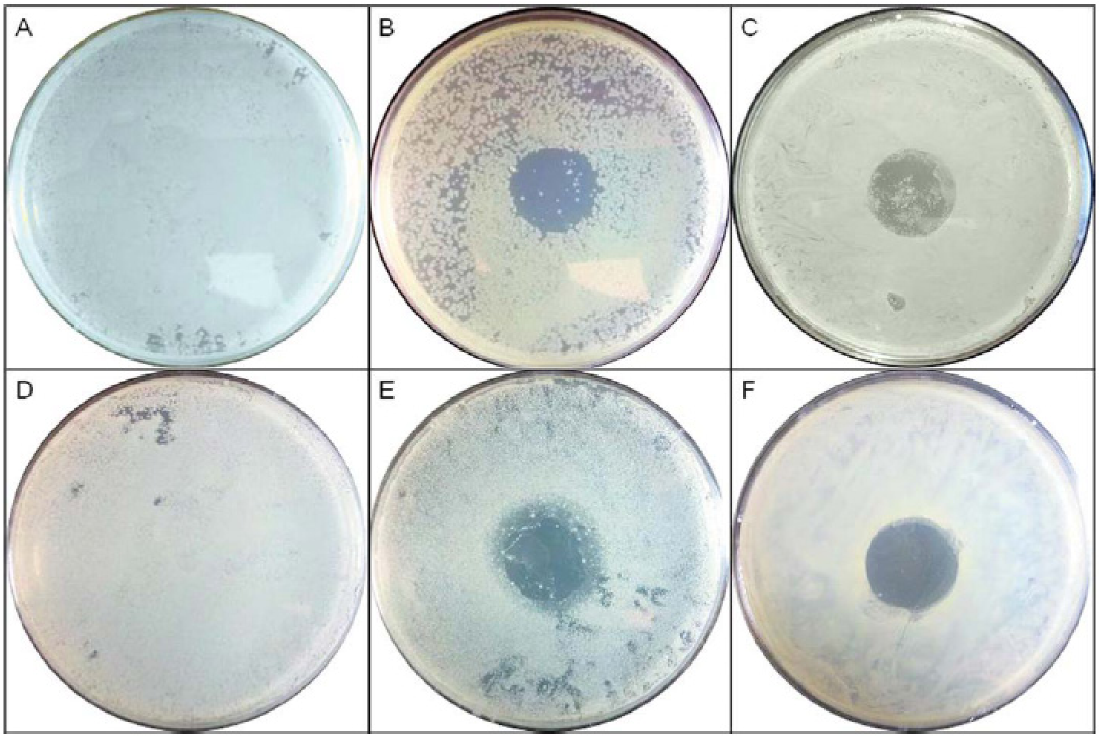

Figure **2.6 -** Antimicrobial effects of NO photorelease upon illumination of PUX-NO films on bacteria inoculated on the surface of TSB agar plates (300 mW cm^{-2} of visible light). (A) Negative control for *P. aeruginosa* in the dark; (B) *P. aeruginosa* growth inhibition with a film containing 10 mg of {Mn-NO}^{6} illuminated for 0.5 h; (C) *A. baumannii* growth inhibition with a film containing 18 mg of {Mn-NO}^{6} illuminated for 2 h; (D) Negative control for *S. aureus* in the dark; (E) *S. aureus* growth inhibition with a film containing 18 mg of {Mn-NO}^{6} illuminated for 2 h; (F) MRSA growth inhibition following two consecutive treatments with two films each containing 18 mg of {Mn-NO}^{6} illuminated 2 h each time. Results shown are typical of triplicate measurements.

plate. The negative controls all produced a uniform bacterial lawn with no clearing of the bacterial culture in each case with only slight smearing of the bacterial colonies due to perturbation from the placement and removal of the films. Each strain was tested with a range of doses to establish an unofficial minimum inhibitory concentration (regarding the content of $\{Mn\text{-}NO\}^6$ in the film and the duration of illumination) (MIC) defined as clearing of <90% of microbial colonies at the site of application as visually assessed. Then, triplicate plates and a negative control for each strain were treated using films and illumination periods corresponding to unofficial MIC for the strain. The triplicate measurements for each strain gave uniform zones of growth inhibition for all three plates in most cases (MRSA ran twice) while the negative controls demonstrated no antimicrobial effect. A representative plate of the triplicate measurements for each strain is shown in Figures **2.6**. The negative controls for *P. aeruginosa* and *S. aureus* are shown in panels A and D of Figure **2.6** and demonstrate the uniform bacterial growth achieved from the inoculation procedure and the lack of any antimicrobial effect from the film surface or the sterilization technique. In contrast, illumination of the films produced potent antibacterial doses of NO that demonstrated dramatic reduction in the microbial loads of the gram-negative bacteria *P. aeruginosa* and *A. baumannii*, as shown in panels B and C of Figure **2.6**. A circular zone of growth inhibition in the center of the plates of the same diameter of the PUX-NO films (22 mm) corresponds exactly with the application site of the PUX-NO films during illumination demonstrating that the NO released from the films was able to eradicate nearly all of the bacterial inoculum underneath the site of application with minimal cytotoxic effects to the peripheral cells. The dose required to cause such clearing of *P. aeruginosa* was 10 mg of $\{Mn\text{-}NO\}^6$ with 0.5 h of illumination while a similar effect for A. baumannii required a dose of 18 mg of $\{Mn\text{-}NO\}^6$ with 2 h of illumination.

PUX-NO films also exhibited strong antimicrobial effects against two strains of the gram-positive bacterium *S. aureus,* namely a methicillin susceptible strain (denoted *S. aureus*) and a methicillin-resistant strain (MRSA), as seen in panels E and F of Figure **2.6**, respectively. At low doses of NO (doses able to eradicate P. aureginosa), these bacteria showed little susceptibility. However starting at doses of 12 mg of $\{Mn\text{-}NO\}^6$ with 1 h illumination, clearing of *S. aureus* and MRSA became evident. A dose of 18 mg of $\{Mn\text{-}NO\}^6$ illuminated for two hours was sufficient to cause nearly complete growth inhibition of *S. aureus*. This dose showed a drastic reduction of the colony density when tested against MRSA but to obtain complete growth inhibition of the inoculum at the site of the film application, two consecutive treatments with PUX-NO films each containing 18 mg of $\{Mn\text{-}NO\}^6$ and illumination for two hours was required. This was accomplished by placing a second film on the same area of application as the first film immediately after the first film had photobleached (2 h illumination) and then illuminating the second film for an additional 2 h. To check whether two applications of PUX-NO films to the same area had any factors other than the cytotoxic effects of NO that contributed to the clearing of bacterial colonies, a control was ran by placing a sterile film onto an agar plate inoculated with MRSA and leaving it in the dark for 2 h. The first film was then removed and another film was placed on the same area, left in the dark for 2 h and removed before incubating the plate for 16 h. The control plate showed only a slight increase in smearing of bacterial colonies at the site of application compared to negative controls ran with just one film but no sign of growth inhibition was observed.

2.5.2 Antimicrobial Activity of PUX-NO Films against *Escherichia Coli* using the Agar Overlay Method

`	The antibiotic effect of PUX-NO against *E. coli* (a gram-negative bacterium) was assessed using an agar overlay assay. In this assay, the working stock of the bacterium was inoculated in 45ºC liquid soft agar (0.7 % (w/v) agar in a 1% NaCl NO films to penetrate the agar medium and cause bactericidal effects below the surface. Using the same treatment protocol as the agar diffusion assay, triplicate measurements using films with 14 mg of {Mn-NO}^{6} illuminated for 0.5, 1 and 2 h were performed to demonstrate how modulation of the light duration can be used to achieve a dose of NO

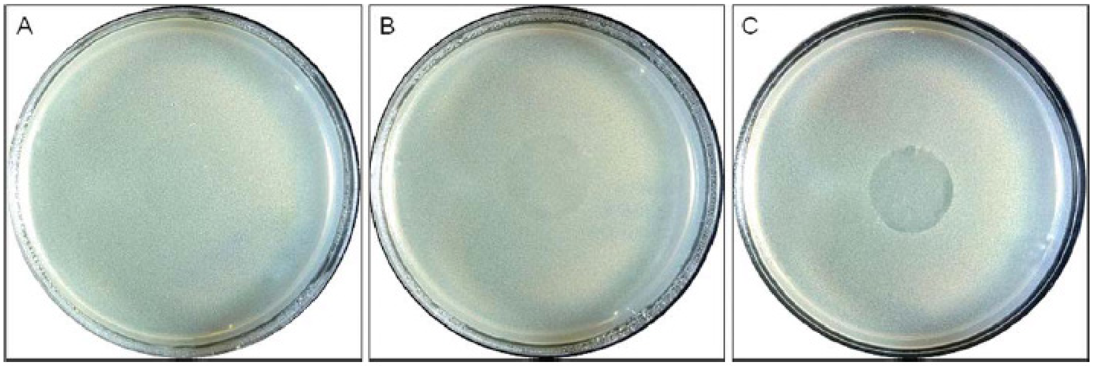

Figure **2.7** – Antimicrobial activity of PUX-NO films containing 14 mg of {Mn-NO}^{6} against *E. coli* colonies suspended in a 1.1 mm thick layer of soft agar (0.7% (w/v)). Illumination of the films with 300 mW cm^{-2} for (A) 0.5 h (B) 1 h and (C) 2 h caused growth inhibition proportional to the duration of illumination. Results shown are typical of triplicate measurements.

capable of effectively reducing *E. coli* microbial loads. As seen in Panel A of Figure **2.7**, only light thinning of the colony density was noted after 30 min of illumination. The clearing of bacterial colonies increased with 1 h of illumination (Panel B) and became significant after 2 h (Panel C).

2.6 Merits of PUX-NO as an Antimicrobial Occlusive Film Dressing

2.6.1 Merits of PUX-NO Films as a Controlled Dose Antimicrobial Delivery System

The fabrication process for PUX-NO films facilitates the encapsulation of a significant amount of the highly efficient NO-donor $[Mn(PaPy_3)(NO)](ClO_4)$ (quantum yield at 550 nm = 0.385)[28] in a primary matrix of biocompatible silica and a secondary, skin contacting layer of medical grade polyurethane while maintaining its rapid NO photorelease capabilities.[42] The flexible green polyurethane films are very durable and resist cracking or breaking even after repeated bending. In addition, pre-swelling of the polymers produces sufficient moisture within the local matrix encapsulating $\{Mn\text{-}NO\}^6$ molecules providing adequate solvation of the nitrosyl to ensure rapid NO photorelease. The composition of hydrophilic silica particles within a hydrophobic polyurethane matrix results in a high moisture retention capacity which ensures maintenance of the films NO release capabilities after 3 months of storage when sealed in a moist environment. The material composition of PUX-NO films also provides efficient NO diffusion rates that are capable of achieving NO concentrations in solution of >300 μM for up to two hours with a high consistency of NO release rates from batch to batch.[40] This concentration of NO is nearly 3x greater than that measured during the neutrophil produced respiratory burst in response to inflammatory signaling during microbial infection which is capable of generating sustained NO concentrations in the range of ~100 μM causing bactericidal effects to a wide range of bacteria.[43]

One of the most desirable properties of PUX-NO films over many other NO-releasing materials reported in the literature is the tight control over NO-release by photostimulation which is the only mechanism under physiological conditions that results in cleavage of the Mn-NO bound releasing free NO. The results of several experiments reported here confirm this unique property. For example, NO release did not occur during submersion of the films in a stirred PBS bufferat 25°C for 200 s as demonstrated by the lack of response from the NO-specific electrode as shown in Figure **2(B)**. However, the same film then rapidly released NO when exposed to short pulses of visible light producing a dramatic response by the NO-electrode (Figure **2(B)**). In addition, PUX-NO films did not release NO or leach the incorporated $\{Mn\text{-}NO\}^6$ nitrosyl during storage of the films on the surface of agar plates containing the Griess reagent over a period of 16 h at 37°C, as indicated by the lack of pink azo-dye formation even after exposure of the plates to light for 1 h. Aho *et al.* also prevented leaching of NONOate modified silica particles from an NO releasing glucose sensor membrane using a solution cast Tecoflex SG-80A polyurethane coating of 37 μm nearly identical to the passivating outer PU layer of PUX-NO films.[39] The secure immobilization of the nitrosyl within the highly biocompatible polyurethane film would prevent any potentially negative interactions between the nitrosyl and the healing tissue during therapeutic application to the wound. Negative side effects from overexposure to NO which could occur during spontaneous NO release from molecular stores such as S-nitrosothiols or NONOates, can also be mitigated using PUX-NO films as a delivery platform for NO therapy since the desired dose of NO could be delivered to the wound site in multiple deliveries with monitoring of the wound progression in between treatments. This method of NO therapy could limit peripheral effects to the surrounding tissue by delivering the minimal amount of NO required to treat the infection. A multiple delivery regimen with NO(g) was proposed by Miller and coworkers as a treatment option for pulmonary infections that would potentially reduce side effects to lung tissue in comparison to a continuous exposure regimen.[44] This regimen involved exposing bacteria intermittently to 160 ppm of NO(g) for 30 min intervals with a 3.5 h gap in between exposures. Since the treatment was shown to be 100% lethal after four rounds of NO exposure to all bacteria studied, it was evident that intermittent delivery regimens maintain the bactericidal effects of NO. In such intermittent treatment regimens, the concentration of $\{Mn\text{-}NO\}^6$ required in the film would likely be lower than the concentrations used in this study to achieve effective bacterial clearing after only 0.5-2 h of illumination. Use of a lower concentration of $\{Mn\text{-}NO\}^6$ in PUX-NO films would help maintain the transparency of the PU matrix which is highly beneficial in clinical practice since it allows continuous monitoring of the wound progress without the need to remove the dressing from the wound site which can cause damage to freshly generated tissue.[36] Treatment regimens with PUX-NO films in which wound and infection progress could be monitored in between multiple exposures therefore appears as a viable option for treating SSTI with an alternative broad-spectrum antibiotic.

The NO delivered from PUX-NO showed strong antimicrobial effects against both gram-positive and gram-negative bacteria. *P. aeruginosa* was the most susceptible to the treatment by NO among all the bacteria studied in this work. This opportunistic pathogen often complicates treatment of burn victims with infection of avascular tissues where systemic antibiotics have little efficacy.[45] Hence, topical antimicrobial delivery is generally required for treating such infections with silver sulfadiazine being the currently favored agent.[46] Treatment of P. aeruginosa with NO could be especially important since strains displaying resistance against silver sulfadiazine have been isolated.[47] Other identified silver-resistant strains include *E. coli, Enterobacter cloacae, Klebsiella pneumoniae, A. baumannii, Salmonella typhimurium,* and *Pseudomonas stutzeri*.[48] In fact a silver-resistant *Salmonella* species caused the closure of the burn unit at Massachusetts General Hospital after septicemia and death in three patients.[49] As seen in Figure **2.5(A)**, a dose of 10 mg of $\{Mn\text{-}NO\}^6$ per film was sufficient to eradicate nearly all colonies of bacteria underneath the film. PUX-NO films also showed potent antibiotic effects against another gram-negative species *A. baumannii* that has a high rate of antibiotic-resistance especially amongst nosocomial acquired strains (see Figure **2.4(B)**).[50] In particular, strains containing genes encoding the New Delhi metallo-beta-lactamase enzyme are of increasing concern. This enzyme provides resistance to the carbapenem family of antibiotics which are considered a last resort antibiotic for the treatment of life-threatening infections by multidrug resistant strains of bacteria. The increased dosage of NO required to eradicate *A. baumannii* (18 mg of {Mn-NO}^{6}) compared to the dose required for *P. aeruginosa* {10 mg of {Mn-NO}^{6}) may the result of induction of the flavohemoprotein, nitric oxide dioxygenase, which detoxifies NO by catalyzing its oxidation by dioxygen to nitrate.[51] This enzyme has been shown to provide some protection against the cytotoxic effects of NO by catalyzing the oxidation of NO to nitrate. However, the present results demonstrate that PUX-NO films can deliver sufficient NO to overwhelm the NO detoxifying mechanisms of A. baumannii causing drastic reduction of the bacterial load.

The gram-positive bacterium *S. aureus* and its methicillin-resistant variant (MRSA) which shows resistance to the beta-lactam family of antibiotics are the most common bacteria isolated from SSTI in North America, accounting for 44.6% of cases from 1998-2004.[52] Primary infections by S. aureus and MRSA commonly occur through open wounds, and with the assistance of tissue degrading exotoxins, they can invade deeper tissue causing necrosis and within 72 h, secondary infections in the lungs, heart valves, and bones, possibly leading to death.[53] Systemic infection by MRSA requires the difficult administration of the antibiotic vancomycin through a venous catheter. Unfortunately, vancomycin resistant strains of *S. aureus* (VRSA) are emerging in some environments.[54] The results shown in Figure **2.5(E,F)** demonstrate that the NO-releasing PUX-NO films cause drastic reduction of both *S. aureus* and MRSA colonies upon illumination. These bacteria required a relatively high dose of {Mn-NO}^{6} compared to *P. aeruginosa* potentially due to their ability to employ nitric oxide dioxygenase enzymes to mitigate the toxic effects of NO.[55] However, the results of this study demonstrate that these bacteria are quite susceptible to high doses of NO and hence PUX-NO films could be a viable method for treatment against complicated dermal infections by *S. aureus* and MRSA.

Among the gram-negative bacteria studied in the present work, both *E. coli* and *A. baumannii* required comparatively high doses of NO (Figures 2.5(C) and 5, respectively). The antibiotic effect of PUX-NO against *E. coli* was studied using an agar overlay assay. The bacteria in this assay are suspended in a ~1.1 mm thick layer of soft agar (0.7% (w/v)) to assess the ability of the NO delivered from PUX-NO to penetrate the media and cause antibiotic effects below the surface. The significant clearing of *E. coli* colonies from the 1 mm thick agar at the highest dose suggest that NO released from PUX-NO may be effective in passing the epidermis (~1 mm thick) and treating infections residing within the dermis and underlying soft-tissue. In line with our previous work, *E. coli* demonstrated a significant resistance to NO which likely arises from their particularly active NO-scavenging flavohemoprotein, Hmp. A recent computional study by Robinson and Brynildsen, demonstrated that slow release of NO from an N,N-diazeniumdiolate (NONOate) (producing $[NO]_{max} = 9$ μM) in a culture of *E. coli* resulted in 78.1% of the total released NO to be consumed by Hmp detoxification which mitigated [Fe-S] cluster damage by 2-4 fold. [56] However, when a fast NO releasing NONOate (producing $[NO]_{max} = 34$ μM) was used only 8.4% of total NO release was consumed by Hmp detoxification due to inhibition of the Fe-center caused competitive binding of NO before O_2. In this experimental setup, [Fe-S] cluster damage was predicted to be reduced by only 5% through Hmp activity and a nearly 2 h delay in the initiation of log-phase growth of E. coli cells was observed in comparison to slow NO release (which was nearly identical to control). These results demonstrate that rapid NO release kinetics are vital to overwhelming bacterial NO detoxification and repair mechanisms in order to allow sufficient accumulation of intercellular damage to produce cytotoxic effects. Thus, careful selection of the NO donor and the encapsulating matrix are required to produce NO donating materials which produce broad spectrum antimicrobial effects as reported with the formulation of PUX-NO. However, the release of higher doses of NO are likely to increase the risk of negative effects to the wound site and the surrounding tissue. Thus, tight control over the dose of NO delivered to the infected wound using PUX-NO films would be beneficial if NO is to be used in the treatment of SSTI. In this regard, PUX-NO has a distinct advantage over many other NO-releasing formulations reported thus far.

2.7 Conclusions

The rise of bacterial resistance to traditional antibiotic as well as the ability of microbes to form protective biofilms upon colonization of host tissue necessitates the development of novel antimicrobial therapies.[57] Due to the broad-spectrum antimicrobial effect of NO coupled with its ability to disperse biofilms and overwhelm bacterial detoxification and repair mechanisms, NO therapy may provide a means to effectively treat infections by drug-resistant organisms which currently “threatens the achievements of modern medicine” according to a recent report by the WHO on the state of antimicrobial resistance.[58] We have now developed PUX-NO, a flexible polyurethane-based film that contains silica-xerogel particles with embedded [Mn(PaPy$_3$)(NO)](ClO$_4$) as the light activated NO donor, and demonstrated its potent antibiotic effects against a broad spectrum of bacteria (*P. aureginosa*, *A. baumannii*, *E. coli*, *S. aureus,* and MRSA). The polymer film is durable, maintains its NO-releasing capacity for over 3 months of storage, and exhibits no leaching of the incorporated manganese nitrosyl. The rate of NO release from the films can be readily controlled through the facile adjustment of the amount of NO donor incorporated into the films or through the use of a variable intensity light source. The most notable advantage of this NO-delivering material over similar systems is the complete control of NO release under physiological conditions (37^{o}C, PBS solution) through the modulation of light intensity or duration. This feature would allow for the rapid release of the desirable dose of NO to the infection site while minimizing the peripheral effects to surrounding tissue. As a consequence, we purpose that PUX-NO films would be an effective antimicrobial occlusive film for the primary dressing of infected and non-healing wounds or as a secondary dressing to provide structural support and antimicrobial properties to primary absorbent dressings.

2.8 Experimental Methods

[Mn(PaPy$_3$)(NO)](ClO)$_4$ was synthesized according to previously reported procedures.[28] Tecoflex SG-80A polyurethane was a gift from Noveon, Wilmington, MA. *E. coli* (ATCC #25922), *P. aeruginosa* (ATCC #27853), *S. aureus* (ATCC #25923), and methicillin-resistant *S. aureus* (MRSA, ATCC #BAA-44) were obtained from the American Type Culture Collection (Manassas, VA). *A. baumannii* (NCIMB 12457) was obtained from Microbiologics (St. Cloud, MN).

2.8.1 Preparation of Polyurethane Films with Embedded Silica Particles Containing $[Mn(PaPy_3)(NO)](ClO_4)$

A batch of 750 μL tetramethylorthosilicate (TMOS, 4.63 mmol) was added to 400 μL deionized water (22.2 mmol) and the mixture was vigorously stirred (500 rpm) until a homogenous sol was obtained. The desired mass of $\{Mn\text{-}NO\}^6$ (Figure 2.3(A)) was then added to the solution and allowed to dissolve before transferring to a 22 mm well in a 12 well polypropylene plate. The solvent was allowed to evaporate from the sol-gel mixture for 48 h at room temperature in the dark to form green, glass-like xerogel disks (Figure 2.3(B)). The xerogel disks were then crushed in a mortar to obtain a fine powder with granule size of 1–100 μm (Figure 2.3(C)). A 10% (w/v) polyurethane solution in THF was prepared by vigorous stirring of 1.00 g of Tecoflex SG-80A beads in 10 mL of THF until fully dissolved (Figure 2.3(D)). After the solution became homogenous, the polyurethane was pre-swelled with water to ensure a desirable moisture content of the final polymer film by the addition of 1 mL of deionized water into the polyurethane solution and subsequent homogenization via stirring. The silica powder with encapsulated $\{Mn\text{-}NO\}^6$ was then dispersed into the liquid polyurethane at a ratio of 1:4 by weight via stirring with a glass rod (Figure 2.3(E)). Batches of 400 mg of the hybrid material were then spin-coated onto circular glass slides (diameter ¼ 22 mm) at 1000 rpm for 6 s and dried in the dark at room temperature to obtain circular patches of flexible, green polyurethane film (Figure 2.3(F)). To prevent leakage of surface exposed silica particles, the films were dip-coated twice with polyurethane (0.50 g Tecoflex SG-80A beads per 10 mL of THF) and allowed to dry in the dark. The polyurethane films with embedded xerogel particles containing $\{Mn\text{-}NO\}^6$ (abbreviated PUX-NO) were visualized using optical microscopy (Zeiss Axiovert 200, Chester, VA) for uniform dispersion of silica particles and thickness of the film. In the following discussion, the final amount of the $\{Mn\text{-}NO\}^6$ donor incorporated in each film is indicated by its weight. For example, a film containing 16 mg of $\{Mn\text{-}NO\}^6$ indicates that the 400 mg of the hybrid material used each time to make the film contained particles of xerogel with a total of 16 mg of $\{Mn\text{-}NO\}^6$. The amount of NO released from such a film will thus correspond to the total mole equivalent of NO in 16 mg of $[Mn(PaPy_3)(NO)](ClO)^4$ (0.03 mmol).

The moisture content of PUX-NO was measured by weighing the films obtained as synthesized, and after storage, (Wi) and then lyophilizing the films and recording the dry weight (Wd). The moisture content q(%) was then calculated according to the equation:

$$q = \frac{W_i - W_d}{W_d} x\ 100\% \qquad (2)$$

2.8.2 NO release measurements

A NO-sensitive electrode (inNO-T NO-measuring system, Harvard Apparatus) was employed to monitor NO release from PUX-NO. The NO release profile of the polyurethane film was determined by placing a 5 x 5 mm square cut from PUX-NO [which represents only 6% of the total surface area of the patches (1520 mm^2) shown in (Figure 2.3(F)) on the bottom of a glass vial containing 1.5 mL PBS buffer and placing the electrode tip 1 cm above the disk. The disk was illuminated with a 300 mW white light and the content of the vial was magnetically stirred during the measurement.

The ability of PUX-NO to deliver NO to an agar plate (to mimic the experimental setup employed in the antimicrobial assay) was visualized chemically by incorporation of the Griess reagent into a 1.5% (w/v) agar solution. 20 mL of the mixture was poured into a polystyrene Petri dish (100 x 15 mm^2) and allowed to solidify. A second layer of soft agar (also containing the Griess reagent) was cast on top of the firm agar much like the experimental setup used in the suspension assay described below. This was achieved by pouring 6 mL of 0.8% agar with 200 μL of Griess reagents on top of the firm agar. The polyurethane film was laid directly onto the agar plates containing the Griess reagent and illuminated. Reaction of the released NO with the Griess reagent quickly turned the agar pink providing an easy visualization of the permeability and range of photo-released NO in our experimental set up.

2.8.3 Storage conditions and stability of polyurethane film

Since solvation of the metal complex has an effect on the NO release kinetics of $[Mn(PaPy_3)(NO)](ClO_4)$,[28] the moisture content of PUX-NO films was found to affect the NO-releasing parameters of the designed material. The proper storage conditions of the material to ensure desirable moisture content and thus NO release abilities were determined by storing the polymers in sealed low-density polyethylene (LDPE) bags with and without added moisture at room temperature and 4°C. The ability of PUX-NO to release NO after storage under varying conditions for 3 months was determined by the NO-specific electrode and compared to newly cast films.

2.8.4 Antimicrobial effects of PUX-NO films

Strains of *E. coli*, *P. aeruginosa*, *S. aureus*, *A. baumannii*, and MRSA were received as freeze-dried cultures. From these cultures, single colonies were selected, grown in trypticase soy broth (TSB) to an A_{600} of 0.63 (UV–vis 1601 Shimadzu spectrometer) and frozen as working stocks according to procedures detailed in our previous work.[31] Two different assays were performed to demonstrate the antimicrobial ability of PUX-NO.

The ‘‘streaking assay’’ was performed by thawing frozen working stock of *P. aeruginosa*, *A. baumannii*, *S. aureus*, and MRSA and streaking 20 lL of the stock onto 20 mL TSB agar plates. These streaks were incubated at 37°C for 2 h before the antibiotic experiments were run to bring the microbes into their log growth phase. Patches of the polyurethane film, sterilized with 70% ethanol and rinsed copiously with MQ water, were placed directly onto the bacterial colonies grown on agar plates. The plates were then illuminated with 300 mW of white light. After the desired illumination time, the films were carefully removed and the plates were incubated at 37°C for 16 h and qualitatively assessed for antimicrobial effects. Negative controls were run by placing films on to agar plates loaded with bacteria and leaving the plate in the dark for 1 h before removing the film. The plates were then incubated as described above.

The ‘‘suspension assay’’ was performed by diluting 100 μL of the *E. coli* working stock with 900 μL of TSB and incubating this culture at 37°C until an A_{600} of 0.7 was reached. 50 μL of this solution was added to 100 mL of 0.8% (w/v) agar with 1% NaCl, which had been autoclaved and cooled to 47°C before the addition of the culture. 6 mL of the liquid agar-bacterial suspension was spread evenly across the surface of a 20 mL solid 1.5% (w/v) TSB agar plate (100 x 15 mm^2). The soft agar-bacterial suspension was allowed to solidify and incubated at 37°C for 2 h before antibiotic experiments were run. The antimicrobial experiments were carried out similar to the streaking method.

2.9 References

1. Edwards, R. and Harding, K.G. *Curr. Opin. Infect. Dis.* **2004**, *17*, 91–6.
2. Robson, M.C. *Surg. Clin. North Am*. **1997**, *77*: 637–50.
3. Demidova-Rice, T.N. Hamblin, M.R. Herman, I.M. *Adv. Skin Wound Care*. **2012**, *25*, 349–70.
4. Cho, C.Y. and Lo, J.S. *Dermatol. Clin*. **1998**, *16*, 25–47.
5. (A) Winter, G.D. *Nature.* **1962**, *193*, 293-4.
6. Levenson, S.M. Geever, E.F. Crowley, L.V. Oates, J.F. Berard, C.W. Rosen, H. *Ann. Surg*. **1965**, *161*, 293–308
7. (A) Eaglstein, W.H. and Mertz, P.M. *J. Invest. Dermatol.* **1978**, *71*, 382-4. (B) Hinman, C.D. and Maibach, H. *Nature.* **1963**, *200*, 377-8.
8. Falanga, V. *Arch. Dermatol.* **1988**, *124*, 872- 7.
9. Telgenhoff, D. and Shroot, B. *Cell Death Differ.* **2005**, *12*, 695–698.
10. Murphy, P.S. and Evans, G.R.D. *Plast. Surg. Int.* **2012**, *2012*, 1–8.
11. (A) Riley, K.N. and Herman, I.M. *J. Burns Wounds.* **2005**, *4*, e8. (B) D'Alessio, S. Gerasi, L. Blasi, F. *J. Cell Sci.* **2008**, *121*, 3922-32. (C)Pastore,

S. Mascia, F. Mariani, V. Girolomoni, G. *J. Invest. Dermatol.* **2008**, *128*, 1365-74. (D) Schultz, G. Rotatori, D.S. Clark, W. *J. Cell Biochem.* **1991**, *45*, 346-52. (E) Chen, L. Tredget, E.E. Wu, P.Y. Wu, Y. *PLoS ONE.* **2008**, *3*, e1886.

12. Werner, S. and Grose, R. *Physiol. Rev*. **2003**, *83*, 835-70.
13. (A) Galeano, M. Deodato, B. Altavilla, D. Cucinotta, D. Arsic, N. Marini, H. Torre, V. Giacca, M. Squadrito, F. *Diabetologia* **2003**, *46*, 546–555. (B) Eming, S.A. Medalie, D.A. Tompkins, R.G. Yarmush, M.L. Morgan, J.R. *Hum. Gene Ther.* **1998**, *9*, 529-39.
14. Turner, N. and Grose, R. *Nat. Rev. Cancer.* **2010**, *10*, 116-29.
15. Deodato, B. Arsic, N. Zentilin, L. Galeano, M. Santoro, D. Torre, V. Altavilla, D. Valdembri, D. Bussolino, F. Squadrito, F. Giacca, M. *Gene. Ther.* **2002**, *9*, 777–85.
16. Frank, S. Madlener, M. Pfeilschifter, J. Werner, S. *J. Invest. Dermat.* **1998**, *111*, 1058-64.
17. Ulland, A. E. Shearer, J. D. Coulter, C. Caldwell, M. D. *J. Surg. Res.* **1997**, *70*, 84–88.
18. Lee, P. C. Salyapongse, A. N. Bragdon, G. A. Shears the 2nd, L. L. Watkins, S. C. Edington, H. D. Billiar, T. R. *Am. J. Physiol.* **1999**, *277*, H1600-8.
19. Miller, C. C. Miller, M. K. Ghaffari, A. Kunimoto, B. *J. Cutan. Med. Surg.* **2004**, *8*, 233-38.

20. Thornton, F. J. Schaffer, M. R. Witte, M. B. Moldawer, L. L. MacKay, S. L. Abouhamze, A. Tannahill, C. L. Barbul, A. *Biochem Biophys Res Commun* **1998**, *246*, 654–659.
21. Stallmeyer, B.; Kampfer, H.; Kolb, N.; Pfeilschifter, J.; Frank, S. *J Invest Dermatol* **1999**, *113*, 1090–1098.
22. (A) Schaffer, M. R.; Tantry, U.; Gross, S. S.; Wasserburg, H. L.; Barbul, A. *J Surg Res* **1996**, *63*, 237–240. (B) Schaffer, M. R.; Tantry, U.; Efron, P. A.; Ahrendt, G. M.; Thornton, F. J.; Barbul, A. *Surgery* **1997**, *121*, 513–519.
23. Shi, H. P.; Most, D.; Efron, D. T.; Witte, M. B.; Barbul, A. *Wound Repair Regen* **2003**, *11*, 198-203.
24. Witte, M. B. and Barbul, A. *Am. J. Surg.* **2002**, *183*, 406–412.
25. Koshland, D.E. *Science* **1993**, *262*, 1953.
26. (A) Heck, D. E.; Laskin, D. L.; Gardner, C. R.; Laskin, J. D. *J Biol Chem* **1992**, *267*, 21277–21280. (B) Cui, X. L.; Iwasa, M.; Iwasa, Y.; Ogoshi, S. *JPEN J Parenter Enteral Nutr* **2000**, *24*.
27. (A) Heilman, B. J. and Mascharak, P. K. *Phil. Trans. R. Soc.* **2013**, *371*. (B) Halpenny, G. M. and Mascharak, P. K. *Anti-Infect. Agents Med. Chem.* **2010**, *9*, 187-197. (C) Eroy-Reveles, A. A. and Mascharak, P. K. *Future Med. Chem.* **2009**, *1*, 1497-1507.
28. Ghosh, K. Eroy-Reveles, A.A. Avila, B. Holman, T.R. Olmstead, M.M. Mascharak, P.K. *Inorg. Chem*. **2004**, ***43***, 2988–2997.

29. Eroy-Reveles AA, Leung Y, Beavers CM, Olmstead MM, Mascharak PK. *J. Am. Chem. Soc*. **2008**, *130*, 4447–4458.
30. Eroy-Reveles, A.A. Leung, Y. Mascharak, P. K. *J. Am. Chem. Soc*. **2006**, *128*, 7166-7
31. Halpenny G. M. Gandhi, K. R. Mascharak, P. K. *ACS Med. Chem. Lett*. **2010**, *1*, 180–183.
32. Heilman, B.J. Halpenny, G.M. Mascharak, P.K. *J. Biomed.Mater. Res. B.* **2011**, *99B*, 328–37.
33. Okan, D. Woo, K. Ayello, E.A. Sibbald, R.G. *Adv. Skin Wound Care*. **2007**, *20*, 39-5
34. Lundqvist, K. Herwald, H. Sonesson, A. Schmidtchen, A. *Thromb. Haemost.* **2004**, *92*, 281-7.
35. Thomas, S. and Fram, P. *J. Tissue Viability* **2001**, *11*, 145-60.
36. O'brien, G. Buckley, K. Vanwaleghem, G. Vanrenterghem, D. Dharma, H. Winter, R.L. Douglass, J. *Int. Wound J.* **2010**, *7*, 3-10.
37. Windholz, M. ed. *The Merck index: An encyclopedia of chemicals and drugs*, *9th edition*. Rahway, N.J.: Merck; **1976.**
38. Rogojevic, S. Jain, A. Gill, W.N. Plawsky, J. *Electrochem Solid-State Lett* **2002**, *5*, F22–3.
39. Koh, A. Riccio, D. A. Sun, B. Carpenter, A. W. Nichols, S. P. Schoenfisch, M. H. *Biosensors and Bioelectronics* **2011**, *28*, 17–24.
40. Mowery, K.A. and Meyerhoff, M.E. *Polymer.* **1999**, *40*, 6203–6207.

41. Thomas, M.D. Macleod, J.A. Robbins, R.C. Goettelman, R.C. Eldridge, R.W. Rogers, L.H. *Anal. Chem*. **1956**, *28*, 1810–1816
42. Lelah, M.D. and Cooper, S.L. ed. *Polyurethanes in Medicine.* Boca Raton: CRC Press; 1986.
43. Fang, F.C. *Nat. Rev. Micro.* **2004**, *2*, 820–832.
44. Miller, C. McMullin, B. Ghaffari, A. Stenzler, A. Pick, N. Roscoe, D. Ghahary, A. Road, J. Av-Gay, Y. *Nitric Oxide.* **2009**, *20*, 16–23.
45. Glasser, J.S. Guymon, C.H. Mende, K. Wolf, S.E. Hospenthal, D.R. Clinton, K.M. *Burns.* **2010**, *36*, 1172–1184.
46. Atiyeh, B.S. Costagliola, M. Hayek, S. N. Dibo, S. A. *Burns*. **2007**, *33*, 139–148.
47. Fuller, F.W. *J. Burn Care Res.* **2009**, *30*, 464–470.
48. (A) McHugh, G. L. Moellering, R. C. Hopkins, C. C. Swartz, M. N. *Lancet*. **1975**, *1*, 235–40. (B) Deshpande, L.M. and Chopade, B. A. *BioMetals*, **1994**, *7*, 49–56. (C) Hendry, A. T. and Stewart, I. O. *Can. J. Microbio.* **1979**, *25*, 915–21. (D) Haefeli, C. Franklin, C. Hardy, K. *J. Bacteriol.* **1984**, *158*, 389–92.
49. Gupta, A. Matsui, K. Lo, J.F. Silver, S. *Nat. Med.* **1999**, *5*, 183–8.
50. Romanelli, R. M. de C. Jesus, L. A. de Clemente, W. T. Lima, S. S. S. Rezende, E. M. Coutinho, R. L. Moreira, R. L. F. Neves, F. A. C. Brás, N. de J. *Braz. J. Infect. Dis.* **2009**, *13*, 341–347.

51. Soares, N. C. Cabral, M. P. Gayoso, C. Mallo, S. Rodriguez-Velo, P. Fernández-Moreira, E. Bou, G. *J. Proteome Res.* **2010**, *9*, 1951–1964.
52. Moet, G.J. Jones, R.N. Biedenbach, D.J. *Diagn. Microbiol. Infect. Dis.* **2007**, *57*, 7–13.
53. Raygada, J.L. and Levine, D.P. *Infect. Med.* **2009**, *26*, 49–58.
54. Larkin, E.A. Carman, R.J. Krakauer, T. Stiles, B.G. *Curr. Med. Chem*. **2009**, *16*, 4003–19.
55. Gardner, P.R. Gardner, A.M. Martin, L.A. Salzman, A.L. *Proc. Natl. Acad. Sci. USA.* **1998**, *95*, 10378–83.
56. Robinson, J. L. and Brynildsen, M. P. *PLoS. Comput. Biol.* **2013**, *9*, e1003049.
57. (A) Taubes, G. *Science.* **2008**, *321*, 356–61. (B) Hall-Stoodley, L. Costerton, J.W. Stoodley, P. *Nat. Rev. Microbiol.* **2004**, *2*, 95–108. (C) Smith, A.W. *Adv. Drug Deliv. Rev.* **2005**, *57*,1539–50.
58. World Health Organization - Antimicrobial resistance: global report on surveillance **2014**. http://www.who.int/drugresistance/documents/surveillancereport/en/ (accessed Jun 12, 2014).

Chapter 3

Light-triggered Eradication of a Multidrug Resistant Pathogen by Rapid Delivery of NO from a Porous Material with Entrapped Manganese Nitrosyl

3.1 Introduction

Over the past decade, targeted drug delivery systems (DDSs) have emerged as a potential solution for the two most commonly issues cited by the FDA in their rejection of ~40% of new drug formulations, poor bioavailability and off-target side-effects.[1] A great deal of current research in DDS technology has focused on the development of nanocarrier scaffolds.[2] Due to the rapid advancement of nanotechnology, a range of nanocarriers with diverse sizes, architectures and surface functionalities are available including micelles, dendrimers, and nanoparticles made of polymers, iron oxide, quantum dots, or gold.[3] To achieve enhanced accumulation of nano-DDSs at targeted sites, both nonspecific (the enhanced permeability and retention (EPR) effect in neoplastic tissue) and specific mechanisms (through the attachment of target-specific ligands) are pursued.[4] However, the ability to achieve targeted drug delivery through either the EPR effect or ligand recognition in the clinic remains questionable. Such concerns arise from the stochastic nature of ligand–receptor interactions and the nonspecific, Fickian controlled diffusion of the drug.[5] In contrast, stimulus-responsive DDSs are capable of delivering therapeutic agents in a spatial-, temporal- and dosage-controlled fashion. Drug delivery systems that are responsive to stimulation by extracorporeal sources, such as electromagnetic fields, light, or ultrasound, are well suited for the targeted delivery of therapeutic agents to diseased sites throughout the body.[6] Furthermore, systems produced by the incorporation of a stimulus-responsive therapeutic into a suitable biocompatible carrier often demonstrate on-demand (*on/off*) drug release with reliable, sustained pharmcokinetics even under the dynamic conditions experienced *in vivo.*[7] In addition, stimulus-responsive therapeutics can often be functionalized with image contrast agents to monitor their biodistribution and coordinate stimulation.[8] The incorporation of such therapeutics into biocompatible carriers that undergo a molecular or supramolecular conformational change under pathological conditions such as ischemia or inflammation can produce systems that demonstrate multiple layers of functionality.[9]

The unique structural and textural properties of mesoporous silicates such as their high surface area, large pore volume, tunable pore diameters, and narrow pore size distribution has made them highly desirable as drug delivery scaffolds.[10,11] The high surface area and specific pore volume of mesoporous silicates imparts a high drug loading capacity to the material which helps to minimize particle-induced toxicity.[12] The tunable pore diameters of these materials also makes them interesting scaffolds for multidrug delivery, for example to achieve simultaneous delivery of chemotherapeutic agents and multidrug-resistance silencing genes.[13] Continued development of new synthetic techniques has produced mesoporous materials demonstrating increasingly sophisticated pore networks with 1D-3D structuring, hierarchical (multimodal) pore size distributions and varying interconnectivities.[14] The structural diversity of most mesoporous materials can be achieved through the appropriate variation of a few synthetic conditions, namely: (1) the chemical composition and structure of directing agent(s) (SDA) which includes any combination of surfactants and non-surfactant molecules capable of assembling into a periodic phase(s) (2) the relative and molar concentration of SDAs (3) the temperature, pH and polarity of the solvent(s) medium

(4) the properties of the condensing inorganic phase monomer and (5) the degree of interaction between the SDA and inorganic phases.[15] A unique class of mesoporous materials called periodic mesoporous organosilicas (PMOs) has recently been reported utilizing dipodal alkoxysilane [$(RO)_3Si$-R'-$Si(OR)_3$] monomers as the condensing inorganic phase where R' is a rigid aromatic bridge that restricts the silica monomer in a rigid orientation producing long range ordering parallel to the crystallographic c-axis of the mesoporous channels.[16] The long range order demonstrated by PMOs produces crystalline domains in contrast to the highly disordered silicate framework of classically synthesized mesoporous silicates. The structure shown in Figure 3.1 was synthesized using cetyltrimethylammonium bromide (CTAB) as the SDA and a symmetrically substituted phenyl group for the bridging unit of the organosilica monomer (e.g. 1,4-bis(triethoxysilyl)benzene). The high density of well-ordered silanol groups on the pore walls of crystalline PMOs makes them desirable as drug delivery scaffolds since the silanol groups can serve as non-covalent binding sites for adsorbents and reactive groups for the covalent tethering of drug molecules.

In the present report, a purely inorganic and non-crystalline, M41S-phase analog of the PMO shown in Figure 3.1 is used for the immobilization of a photoactivated metal nitrosyl to afford a stimulus-responsive DDSs that is capable of delivering a sustained dose of nitric oxide (NO) to a targeted site under the complete control of light. Since the pharmaceutical development of stimuli-responsive DDSs becomes exceedingly difficult with the complexity of the DDS, especially in terms of the manufacturing process, reproducibity, and quality control, the synthetic technique

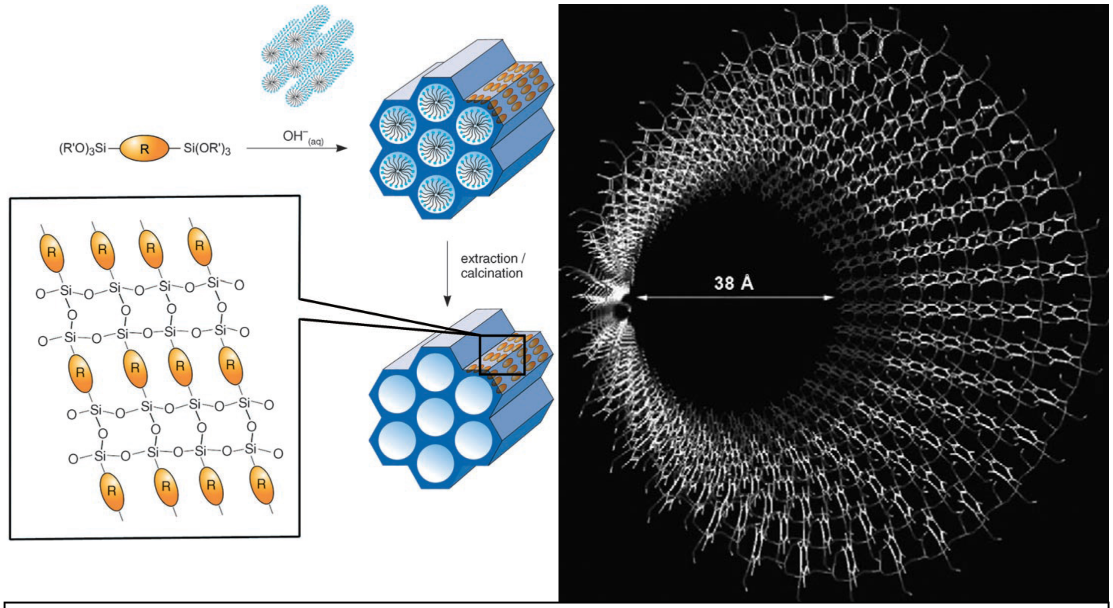

Figure 3.1 – (Left panel) Schematic depicting the synthesis of PMOs with a crystal-like arrangement of the bridging organic units R in the pore walls with an idealized orientation (slight tilting or twisting of R units with respect to each other is often observed). (Right panel) Model of the pores of a 1,4-bis(trimethyoxysilyl)benzene PMO. The benzene bridges and the condensed silicate groups connecting the organosilica monomers form alternating rings that are concentric with the pore axis. Adapted from Ref. 16

described herein was developed as an efficient and highly reproducible method for the immobilization of photoactive nitrosyls within a biocompatible and chemically inert matrix.[2] The mesoporous MCM-41 structure consisting of a hexagonal array of uni-dimensional pores with narrowly dispersed pore diameters that can be tuned from 2-10 nm was identified as a desirable material for the immobilization of the photoactive NO donor [Mn(PaPy$_3$)(NO)](ClO$_4$) ({Mn-NO}, λ_{max} = 635 nm). From analysis of the x-ray crystal structure, the furthest distance between two atoms in the structure of {Mn-NO} was determined to be ~12 Å.[17] Therefore, the > 2 nm diameter mesopores of the MCM-41 structure should permit facile diffusion of the nitrosyl along the length of the uni-dimensional channels. Hydrogen bonding between hydrogen bond acceptors present on the {Mn-NO} ligand set and silanol groups on the pore walls (2-4 groups/nm) of the MCM-41 host provides a potential means for immobilizing the nitrosyl within the MCM-41 mesopores. In order to modulate the guest adsorption behavior of mesoporous silicates, a variety of silanization techniques have been developed to modify the pore walls with organic functional groups which preferentially interact with guest molecule.[18] Such systems often rely-on amino-carboxylate electrostatic interactions between the guest and silane tethered functional groups on the host due to the charged nature of these groups at physiological pH and the prevelance of these functionalities in pharmaceuticals and biomolecules. However, there is usually little difference in the adsorption/release profiles of acidic molecules from amino/carboxylate functionalized and bare silica hosts.[19] For example, both the co-condensation of an amino functionalized silane, (3-aminopropyl)triethoxysilane (APTES), with a silica precursor, tetraethyoxysilane, used to produce the MCM-41 framework and the post-synthetic condensation of APTES with silanol groups on the surface of calcined MCM-41 particles produced no significant impact on the zeta-potential of the particle compared to bare silica at physiological pH. Such results can be explained by the isoelectric point (IEP) of isolated silanol groups (compared to viscinal and germinal) on silica surfaces which is ~1.5 compared to that of aminopropyl groups on silica (7-8).[20] Therefore, under physiologically relevant conditions (pH 7.4, high ionic strength), the relative abundance of charged, deprotonated to protonated silanol groups is 10^6 while only half of the amino groups will be in the protonated, charged state. Even after modification of the surface of silica particles through organic group functionalization, the vast majority of chemical groups present on the surface of silica particles are still silanol groups. Recently, Rosenholm and Lindén have reported a unique surface polymerization technique to generate an abundance of amino groups on the surfaces of MCM-41 particles compared to silanol groups.[20] Still, the adsorption/desorption profiles of salicylic acid from the amino-functionalized host was not significantly changed from those of the bare silica host. When permanent immobilization of the guest molecules is desired, covalent tethering of the guest to the silica framework by condensation of amino/carboxylate groups forming an amide bond between the host and guest has been attempted.[21] However, the irreversible binding of guest molecules at the pore openings can prevent loading of the pore space and severely diminish the loading capacity of the material. The isomorphous substitution of Al(III) for tetrahedral Si(IV) centers in porous silicates produces a stable, negatively charged aluminosilicate framework with a low content of charge balancing hydroxy-aluminum species when the Al content of the material is kept below 0.25 Al:Si.[22] Such materials demonstrate a sharp exponential increase in the abundance of negatively charged sites from pH 6-9 which are charge-balanced by exchangeable, extra-framework cations. Aluminosilicate MCM-41 (Al-MCM-41) materials often demonstrate a considerable increase in the adsorption capacity of cationic molecules at physiological pH compared to purely siliceous MCM-41 (Si-MCM-41).[23] Loading of {Mn-NO} into Al-MCM-41 and Si-MCM-41 has been pursued in the present work to determine the influence of the negative Al sites on the loading capacity of the cationic nitrosyl by the mesoporous MCM-41 materials. The metal nitrosyl utilized in this work is especially well-suited for this kind of host−guest chemistry as the photoproduct obtained after NO photolysis from the manganese center becomes doubly charged ($[Mn(PaPy_3)(H_2O)]^{2+}$) in the presence of oxygen and therefore is expected to bind even tighter to the negatively charged walls of the porous host. The adsorption capacities and desorption rates of the silicate and aluminosilicate-based {Mn-NO}@MCM-41 host−guest systems have been determined in this study.

Composite materials consisting of a porous silica-based scaffold and a NO source have recently been reported as DDSs for the delivery of NO to biological targets. Porous silicates are an attractive option for NO administration since the silicate carrier is chemically inert and does not react with gaseous free radical. One of the first systems, described by Wheatley and co-workers in 2006, was produced by the coordination of NO to framework Co or Zn sites in transition metal substituted zeolite-A.[24, 25] The Zn-substituted zeolite-A had a NO adsorption capacity of 1 mmol of NO per gram of zeolite-A and demonstrated quantitative release of the adsorbed NO over a period of ~40 min from the hydrolysis of the metal-NO bond in the presence of moisture-rich air. Similar to the other NO releasing porous silicate reported thus far, the endogenous nature of the drug releasing stimulus (moisture) results in the nonspecific release of NO thus eliminating the ability of such materials to function as targeted NO donors.[26,27] In this report, we describe a technique for generating a photoactived DDS that releases bactericidal amounts of NO under the complete control of mW levels of visible light. The mesostructured MCM-41 supports and the {Mn-NO}-loaded composites have been characterized by wide angle powder X-ray diffraction (PXRD), FT-IR spectroscopy, diffuse reflectance UV-vis spectroscopy (DRS-UV-vis), N_2 adsorption-desorption isometry, scanning electron microscopy coupled with energy dispersive X-ray analysis (SEM-EDX), and tunneling electron microscopy (TEM), while the NO releasing capacities of the composite materials were determined using electrochemical methods. The clinical utility of the DDS for the treatment of infection by the highly drug-resistant pathogen *Acinetobacter baumannii* is also reported.

NO has been recognized through numerous studies as a potent antibiotic against drug-resistant bacterium such as methicillin-resistant Staphylococcus aureus (MRSA).[28-30] However, the rise of multidrug-resistant (MDR) bacteria has sparked great interest in the development of novel antibiotic agents, such as NO, to combat the diverse antibiotic resistance mechanisms employed by bacteria.[31] Thus, the true utility of NO as an antibiotic agent may reside in its ability to treat infections by MDR bacteria since the drug-resistance mechanisms employed by MDR bacteria are not effective in mitigating the cytotoxic effects of NO. The gram-negative pathogen, *A. baumannii*, is genetically poised to rapidly develop multidrug resistance through a variety of defense mechanisms many of which demonstrate cross resistance to several antibiotic agents allowing the bacterium to rapidly achieve resistance to nearly the entire spectrum of clinically available antibiotics (in one study, 14% of clinical isolates were resistant to at least eight different antibiotics).[32-34] *A. baumannii* also demonstrates robust phenotypic resistance through the formation of biofilms which reduce the susceptibility of the bacterium to nearly all forms of traditional antibiotics, irregardles of previous exposure.[35] The high transmission rate of infection by *A. baumannii*, especially in hospital settings, compounds the problematic resistance demonstrated by MDR *A. baumannii*.[36,37] Following the admission of coalition soldiers wounded during tours in Operation Iraqi Freedom and Operation Enduring Freedom in Afghanistan to military and civilian hospitals, there was a large increase in the occurrence of *A. baumannii* infection amongst all admitted patients in these hospitals.[38–40] It was later discovered that the ability of *A. bauamannii* to form biofilms allows the pathogen to persist in sterile environments outside of the host and facilitates the spread of *A. baumannii* throughout entire hospital wards. Our interest in developing NO-donating materials to treat infections by microbial pathogens prompted us to study the effects of NO on MDR *A. baumannii* and evaluate the utility of a photosensitive NO delivery platform in the treatment of *A. baumannii* infection. [29,41,42] Based on the problematic infection of skin and soft-tissue injuries in soldiers wounded on the battlefield in the Middle East, we have developed an antimicrobial assay which promotes bacterial growth in a manner similar to the growth observed in skin and soft-tissue infections (SSTI). The assay is believed to provide a more reliable assessment of the efficacy of the tested antimicrobial agent for the treatment of SSTI.

3.2 Synthesis of {Mn-NO}@MCM-41.

The synthesis of the photoactive manganese nitrosyl, [Mn(PaPy$_3$)(NO)](ClO$_4$) (denoted as {Mn-NO} for both the perchlorate salt and cationic forms), was performed following previously published methods.[17] The incorporation of {Mn-NO} into mesoporous MCM-41 particles of two different compositions, a neutral silicate (Si-MCM-41, $SiO_2{\cdot}xH_2O$) and an anionic aluminosilicate-based material (Al-MCM-41, variant formula $(SiO_2)_{0.9875}(Al_2O_3)_{0.0125}{\cdot}xH_2O$), was performed to investigate: (A) the extent of electrostatic interaction between the cationic {Mn-NO} guest and the anionic tetrahedral $(AlO_4)^-$ sites of the Al-MCM-41 host structure; (B) the influence of such an electrostatic interaction on the physicochemical properties of the composite material; and (C) the photochemical properties of the pore-confined nitrosyl. Since the purely siliceous material lacks a formal charge, the loading of {Mn-NO} into the uni-dimensional pores of the Si-MCM-41 particles is thought to proceed though a passive, diffusion based mechanism. In contrast, the electrostatic interaction between the host and guest in the Al-MCM-41 composite material facilitates the diffusion of guest molecules into the porous structure by an ion-exchange mechanism. Here, the $[Mn(PaPy_3)(NO)]^+$ cations in solution displace loosely interacting Na^+ counter-ions from $(AlO_4)^-$ sites in the pore walls of Al-MCM-41, and hence the extent of loading is facilitated by a combination of ion exchange and passive diffusion. However, if the {Mn-NO} content loaded by Al-MCM-41 exceeds the number of $(AlO_4)^-$ binding sites (3 mol% total Al), further loading of {Mn-NO} would likely proceed through a diffusion-based mechanism similar to that proposed for Si-MCM-41.

Prior to loading of the MCM-41 particles, the Al-MCM-41 powder was washed in an aqueous solution containing 2% (w/v) NaCl to induce a concentration driven Na^+-exchange of any extra-framework hard metal ions (e.g. Ca^{2+} or Mg^{2+}) which strongly bind to $(AlO_4)^-$ sites, potentially inhibiting the {Mn-NO} ion-exchange process. The Si-MCM-41 and Na-exchanged Al-MCM-41 powders were then dried at 80°C for 24 h and pulverized to a fine dust with a mortar and pestel to break any aggregate particles. The dry MCM-41 powders (100 mg) were then added to separate Shlenk flasks containing dry acetonitrile (5 mL). The slurries were thoroughly degassed before freezing the solution prior to the neat addition of the desired quantity of {Mn-NO} (100 or 200 mg) under blowing $N_{2(g)}$. After thawing, the contents were stirred in the dark at 25°C for 3 days under elevated pressures of $N_{2(g)}$ (~3 bar), then collected on a glass frit, and rinsed with several portions of MeCN, followed by tetrahydrofuran until no {Mn-NO} was detected in the filtrate by UV-vis spectroscopy (LOD ~10^{-6} M). The resulting light green powders were dried *in vacuo* overnight and stored in the dark under dry conditions until use.

Loading of both the Si-MCM-41 and Al-MCM-41 host structures was performed with a low concentration of {Mn-NO} (100 mg {Mn-NO} per 100 mg MCM-41) and a high concentration (200 mg {Mn-NO} per 100 mg MCM-41). Thus, four formulations of loaded material were prepared and denoted by subscripting the mass of nitrosyl (mg) used during the loading process as follows: $\{Mn\text{-}NO\}_{100}$@Si-MCM-41, $\{Mn\text{-}NO\}_{200}$@Si-MCM-41, $\{Mn\text{-}NO\}_{100}$@Al-MCM-41, and $\{Mn\text{-}NO\}_{200}$@Al-MCM-41 (collectively referred to as {Mn-NO}@MCM-41). The $\{Mn\text{-}NO\}_{200}$@Al-MCM-41 formulation appears to achieve the maximum loading capacity for the MCM-41 materials since soaking of the host in solutions containing higher concentrations of {Mn-NO} (e.g. 300 mg {Mn-NO} per 100 mg MCM-41) did not significantly increase the {Mn-NO} content of the composite material.

3.3 Characterization of {Mn-NO}@MCM-41

3.3.1 Determination of the {Mn-NO} Content of {Mn-NO}@MCM-41

The actual mass of {Mn-NO} loaded in each host-guest formulation was determined by measuring the Mn content of an acid digested solution of the loaded MCM-41 particles. The acid digest was performed according to a modification of the protocol described by Yang and co-workers.[43] The MCM-41 frameworks were broken down by heating the particles in a solution of aqua regia (1:3 HCl to HNO_3) and 40% (v/v) HF in H_2O at 150°F for 4 h in a pressurized, Teflon lined autoclave bomb (an excess of HF was used based on the molar stoichiometry of Si to prevent formation of volatile $SiF_{4(g)}$). After the 4 h period, the silicate and aluminosilicate structures were completely dissolved and the organic ligand frame of {Mn-NO} was mineralized, producing a soluble Mn(II) nitrate complex.[44] Elemental analysis of the Mn concentration in the digest solutions was performed to determine the {Mn-NO} content in the original samples. To assess the consistency of the loading process, the digest procedure was performed in duplicate for each formulation of {Mn-NO}@ MCM-41 using samples obtained from separate synthetic batches, and the Mn concentration of each batch measured using different techniques, one by FAAS and the other by ICP-OES. The Mn content of each formulation as measured by FAAS and ICP-OES, and the average of the two measurements expressed as the weight percent of {Mn-NO} in the loaded materials are listed in Table 3.1. The batch-to-batch consistency of the loading technique was confirmed by the close agreement in the Mn content reported for the two synthetic batches analyzed for each of the four formulations of {Mn-NO}@MCM-41 with no clear bias in the values reported for the FAAS and ICP-OES analyses. As expected, higher loading of {Mn-NO} was observed for both formulations of Al-MCM-41 compared to the corresponding Si-MCM-41 based materials. The difference in the {Mn-NO} content of the silicate and aluminosilicate materials was more significant in the materials prepared with a high concentration of {Mn-NO}, achieving guest contents of 23.4(5) wt% {Mn-NO} (1.32 wt% NO) for {Mn-NO}$_{200}$@Al-MCM-41 and 20.0(3) wt% {Mn-NO} (1.13 wt % NO) for {Mn-NO}$_{200}$@Si-MCM-41. Soaking of the MCM-41 particles in solutions containing a lower concentration of {Mn-NO} did not produce a significant difference in the loading of the silicate material, {Mn-NO}$_{100}$@Si-MCM-41 (19.0(2) wt% (1.07 wt % of NO)). However, a significant decrease in the loading of the aluminosilicate material, {Mn-NO}$_{100}$@Al-MCM-41 (19.6(5) wt% (1.11 wt % of NO)) was noted. The higher loading capacity of Al-MCM-41 compared to Si-MCM-41 indicates that the uptake of {Mn-NO} by the mesoporous materials occurs through different mechanisms which are proposed as follows: an advantageous, ion-exchange of the [Mn(PaPy$_3$)(NO)] cation for extra-framework bound Na^+ in the case of Al-MCM-41 and a less efficient passive diffusion of the {Mn-NO}/(ClO_4) ion-pair into the pores of Si-MCM-41. The higher loading capacity achieved through ion-exchange of {Mn-NO} by Al-MCM-41 was likely driven by thermodynamics but may have been facilitated by a more efficient packing of guest molecules directed throughout the length of the uni-dimensional pores by their attraction to uniformly (randomly) dispersed $(AlO_4)^-$ surface sites. However, in certain systems, a strong host-guest interaction has the potential to inhibit uniform guest loading throughout the length of the uni-dimensional MCM-41 mesopores. Stathi and coworkers noted that loading of Cd^{2+} ions by a dithiocarbamate functionalized MCM-41 silicate material inhibited subsequent loading of Cu^{2+} ions due to the blocking of the pore entrances by the large hydration shell of adsorbed Cd^{2+} ions (consisting of four layers of water molecules).[45] Since ion-pairing reduces the hydration energy of ions in solution, the formation of an {Mn-NO}/(AlO_4) ion-pair should weaken the hydration sphere of the ion-exchanged guest molecules and prevent such blocking.[46]

Table **3.1** – Elemental analysis of the {Mn-NO} content of the loaded Si-MCM-41 and Al-MCM-41 materials determined by ICP-OES and FAAS analysis of the acid digested particles.

Method	$\{Mn\text{-}NO\}_{\mathbf{100}}$@ **Si**-MCM-41	$\{Mn\text{-}NO\}_{\mathbf{200}}$@ **Si**-MCM-41	$\{Mn\text{-}NO\}_{\mathbf{100}}$@ **Al**-MCM-41	$\{Mn\text{-}NO\}_{\mathbf{200}}$@ **Al**-MCM-41
ICP-OES (wt% Mn)	1.97(1)	2.07(1)	2.04(3)	2.39(4)
FAAS (wt% Mn)	1.97(2)	2.15(4)	2.02(4)	2.47(4)
Avg (wt% {Mn-NO})	19.0(2)	20.0(2)	19.6(5)	23.4(5)

3.3.2 Stability of the {Mn-NO}@MCM-41 Host-Guest Interaction Under Physiological Conditions

The stability of the host-guest interaction of {Mn-NO}@MCM-41 under physiologically relevant conditions was tested by prolonged soaking of the loaded materials in an aqueous 137 mM NaCl solution and monitoring of the extent of {Mn-NO} leaching over time. A saline solution was chosen for this experiment, instead of the more commonly employed PBS buffer, due to the potential formation and precipitation of an insoluble Mn-phosphate complex. The rate of {Mn-NO} leaching from the composite materials was determined from the results of triplicate measurements performed by suspending equal masses of the loaded materials in three separate saline solutions and gently agitating the suspensions by shaking. Small aliquots were taken at specific time-points from each solution (insignificant to the total volume), diluted with 1% HNO_3, and filtered through a 45 μm polymer membrane. The Mn concentration of each time-point was measured by ICP-OES analysis and normalized according to the total {Mn-NO} content of the \ materials. The average results from the triplicate measurements performed for each formulation are plotted in Figure 3.2. The rate of {Mn-NO} leaching from the two materials was quite steady over the entire 24 h period. A slightly higher rate is observed within the first two hours resulting in the leaching of 1.80(3)% of the total guest content of $\{\text{Mn-NO}\}_{200}$@Al-MCM-41, while $\{\text{Mn-NO}\}_{200}$@Si-MCM-41 leached 2.04(1)% over the same two hour period. Interestingly, the amount of {Mn-NO} leached in the first 2 h was greater than the total {Mn-NO} leached over the remaining 22 h for both formulation. At the end of 24 hours, the two samples had leached an equal mass of {Mn-NO} (6.9 μg per mg of particles in solution) but based on the higher loading of $\{\text{Mn-NO}\}_{200}$@Al-MCM-41 this value represents only 2.92(3)% of the guest content versus 2.44(6)% of the guest content of $\{\text{Mn-NO}\}_{200}$@Si-MCM-41. The distinct inflection in the leaching rate after 2 h (Figure 3.2) suggests that leaching of {Mn-NO} from the MCM-41 pores within this time period occurs through two processes. In such a scenario, leaching during the first two hours has a considerable contribution from the rapid desorption of weakly bound {Mn-NO} that were not removed during the washing procedure. Upon depletion of this population (~2 h), a rapid decline in the leaching rate is observed with continued leaching of {Mn-NO} occurring through a much slower partitioning of strongly bound guest molecules from the surface to the solution phase. The presence of two unique binding sites on the surface of fsilicate based material was first described by Ong et al. as isolated (pKa 4.9, site I (S_I)) and vicinal (pKa 8.5, site II (S_{II})) silanol groups with populations of 19% and 81%, respectively.[47] While the vicinal silanol groups remain largely protonated due to their ability to directly hydrogen bond with a vicinal neighbors or through a single water molecule bridge, the distance between isolated silanol groups allows them to exist in the deprotonated state. The isolated silanol groups were later sub-categorized into site I (S_I) silanol groups without any neighboring silanol groups over an area of ~120 cm^2 and site II (S_{II}) silanol groups with a much higher surface density.[48] Using the cationic dye, crystal violet (CV^+), Fan and coworkers were able to demonstrate that deprotonated S_I silanol groups ($Si\text{-}O^-$) strongly bound CV^+ molecules through an electrostatic interaction with a ΔG_{abs} roughly twice that of CV^+ bound to $Si\text{-}O^-$ groups at S_{II} types.[49] The discrepancy in the binding strength of CV^+ to the two sites despite their similar electrostatic interactions is attributed to repulsion of

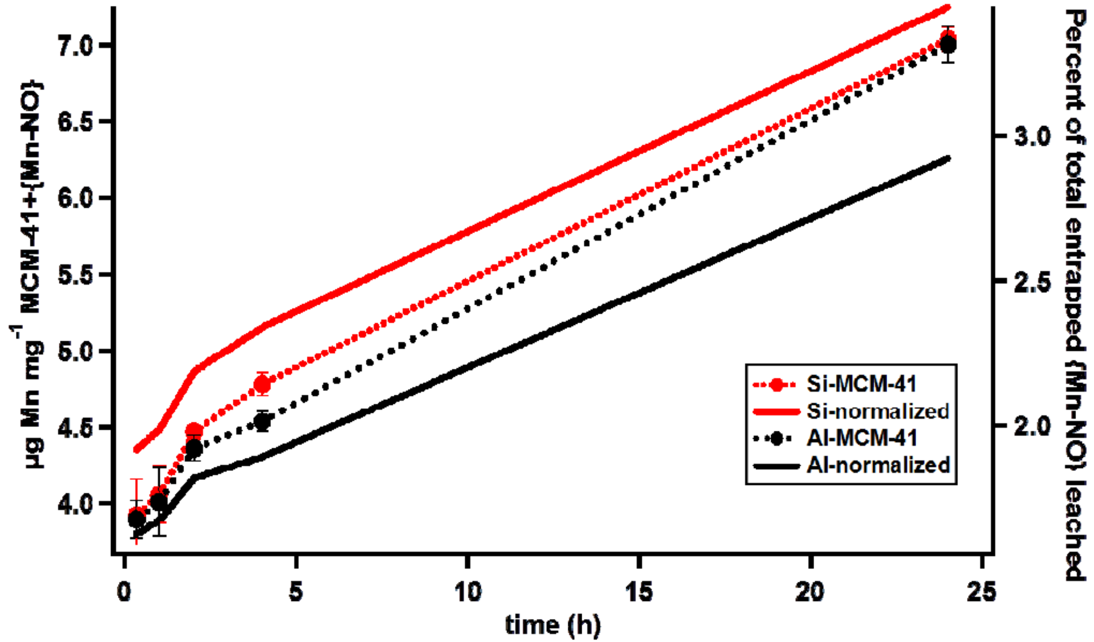

Figure 3.2. Leaching of {Mn-NO} from the mesopores of $\{Mn\text{-}NO\}_{200}$@Si-MCM-41 and $\{Mn\text{-}NO\}_{200}$@Al-MCM-41 during soaking in a physiologically relevant saline solution (10 mg sample in 2 mL of 137 mM NaCl) as measured by ICP-OES analysis (LOD = 6 ng/mL) of aliquots taken from the soak solution at 0, 1, 2, 4, and 24 h. The data points with error bars (n=3) are scaled to the left axis by normalizing the measured amount of {Mn-NO} in solution to the total amount of {Mn-NO}@MCM-41. The right axis takes into account the higher loading capacity of Al-MCM-41 by normalizing the measured amount of leached {Mn-NO} to the total amount of {Mn-NO} present in the ~10 mg samples.

the cationic complex from nearby SiOH groups. The presence of strong and weak binding sites produced a biphasic desorption isotherm due to the rapid desorption of CV^+ from S_{II} sites and the slow desorption of CV^+ from S_I sites. The similar features of the biphasic desorption isotherm reported by Fan and coworkers with the currently reported desorption isotherm of {Mn-NO}@MCM-41 may reflect the rapid desorption of {Mn-NO} from S_{II} sites within the first two hours of the experiment and the slow desorption of strongly bound guest molecules at S_I sites over the remaining 22 h period. In addition to S_I and S_{II} binding sites, the Al-MCM-41 material contains two additional binding sites for cationic guest molecules, those characterized as Lewis acid sites (AlO_4^-) and Brønsted acid sites (Al-OH-Si) which have approximate relative abundances of 0.4 Brønsted-to-Lewis acid sites (depending on prior treatments, such as calcination temperature and moisture content).[50] Further investigation will be required in order to determine the exact nature of the interaction of {Mn-NO} with the Al-MCM-41 and Si-MCM-41 frameworks. A semi-quantitative analysis of the binding-strength of {Mn-NO} with the MCM-41 frameworks could be obtained by monitoring the desorption rate of {Mn-NO} from the composite material in a solution containing competing mono- and multi-valent metal cations with well characterized binding strengths to silicate and aluminosilicate materials.[51] Queiroz and coworkers have also noted similar stabilization of a host-guest structure due to electrostatic interaction between a cationic Ir(III) guest complex, $[Ir(dfptrBn)_2(dmbpy)]^+$, and AlO_4^- sites in the pores of an aluminosilicate based xerogel glass. In contrast, attempts to immobilize the same Ir(III) complex in a neutral, silica-based xerogel glass failed due to excessive leaching of the guest compound in solution.[52] This was attributed to the lack of a strong dipole moment in the highly symmetrical Ir(III) structure which prevents the formation of a polar host-guest interaction. In the present study, polar groups on the ligand set of the {Mn-NO} complex are capable of forming strong polar

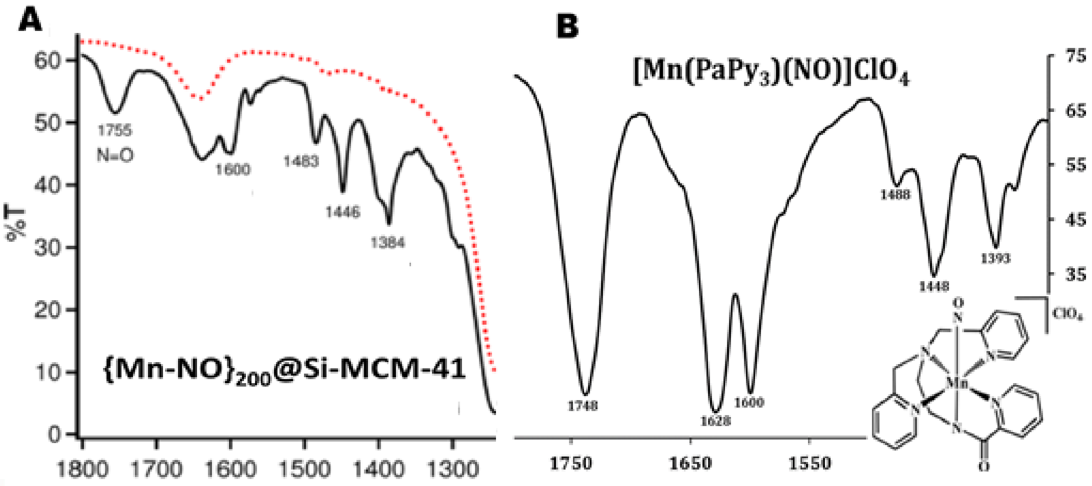

Figure 3.3. (A) FTIR spectra of Si-MCM-41 (dotted line) and $\{Mn\text{-}NO\}_{200}$@Si-MCM-41 (solid line) in the region from 1200 to 1800 cm^{-1}. **(B)** FTIR spectrum of free $[Mn(PaPy_3)(NO)](ClO_4)$ from 1200 to 1800 cm^{-1} (inset, structure of $[Mn(PaPy_3)(NO)](ClO_4)$).

interactions with surface silanol groups on the Si-MCM-41 framework. Thus, minimal leaching of the {Mn-NO} guest was observed from both $\{Mn\text{-}NO\}_{200}$@Si-MCM-41 and $\{Mn\text{-}NO\}_{200}$@Al-MCM-41 composite materials.

3.3.3 FTIR spectra of $\{Mn\text{-}NO\}_{200}$@Si-MCM-41 and $\{Mn\text{-}NO\}_{200}$@Al-MCM-41

The incorporation of {Mn-NO} within the MCM-41 hosts generated new absorption bands in the IR region which were not present in the spectra of the unloaded materials. The most notable of these bands were observed in the region between 1380−1780 cm^{-1} which encompasses the absorption bands of several functional groups present on the {Mn-NO} ligand set. The most notable of these bands is the NO stretching band ν_{NO} which can be easily identified in the FTIR spectra of $\{Mn\text{-}NO\}_{200}$@Si-MCM-41 at 1755 cm^{-1} (Figure 3.3 **A**), which is slightly blue shifted from the ν_{NO} of the free nitrosyl, $[Mn(PaPy_3)(NO)](ClO_4)$ (ν_{NO} = 1745 cm^{-1}, Figure 3.3 **B**).[40]

Due to the hydroscopic nature of the silicate and aluminosilicate based MCM-41 materials, samples exposed to the atmosphere quickly adsorbed moisture from the air producing a broad δ_{H2O} band (1630 cm^{-1}) which overlapped the ν_{NO} peak, making it indistinguishable. Incremental drying of the samples *in vacuo* revealed a low intensity, broad peak corresponding to ν_{NO} which sharpened as the moisture content of the composite material decreased. In order to obtain a well-defined ν_{NO} band in the FTIR spectra of the loaded materials, it was imperative that the samples be placed under high vacuum (10^{-5} torr) overnight prior to analysis. The broadening of the ν_{NO} band in the presence of atmospheric moisture can be attributed to hydrogen bonding between the nitrosyl group and adsorbed water on the pore walls. The prominent bands at 1446 and 1483 cm^{-1} as well as the small peak at 1572 cm^{-1} have been assigned to ring vibration modes of the pyridyl groups on the $PaPy_3^-$ ligand, based on the peak positions in the IR spectrum of coordinatively bonded pyridine ($C_5H_5N{\bullet}BF_3$) adsorbed to a silica surface.[53] Assignment of the band at 1600 cm^{-1} was complicated by the overlap of the δ_{H2O} band (1630 cm^{-1}). While we had previously assigned this band to ν_{CO} of the carboamide moiety red-shifted from 1622 cm^{-1} in the spectrum of the free nitrosyl (based on previous reports of a similar ~25 cm^{-1} red-shift in ν_{CO} upon adsprortion of a guest molecule to a silica surface), the band at 1600 cm^{-1} was likely produced by a pyridine ring vibration in the proximity of a lewis acid site (1600-1620 cm^{-1} reported for $C_5H_5N{\bullet}BF_3$ adsorbed aluminosilicate based zeolites). If this assignment of the 1600 cm^{-1} band is correct, the ν_{CO} band of $PaPy_3^-$ is likely overlapped by the strong δ_{H2O} band

and the decreased intensity stretching bands corresponding to H-bond accepting groups on silica supports.

3.3.4 Diffuse Reflactance Spectra of the {Mn-NO}@MCM-41 Materials

The diffuse reflectance UV−vis spectrum (DRS-UV-vis) of {Mn-NO}, {Mn-NO}$_{200}$@Si-MCM-41, and {Mn-NO}$_{200}$@Al-MCM-41 across the visible region are shown in Figure 3.4 Compared to the solution phase spectrum, the reflectance spectrum of the solid phase nitrosyl is less featured, displaying a single high energy band around 450 nm which is split into two bands (420 and 440 nm) in the solution phase spectra. However, the low energy band ~650 nm is quite similar in both phases. The high energy band also remains relatively unchanged upon confinement in the Al-MCM-41 mesopores, however, a slight narrowing of the band is observed upon confinement of

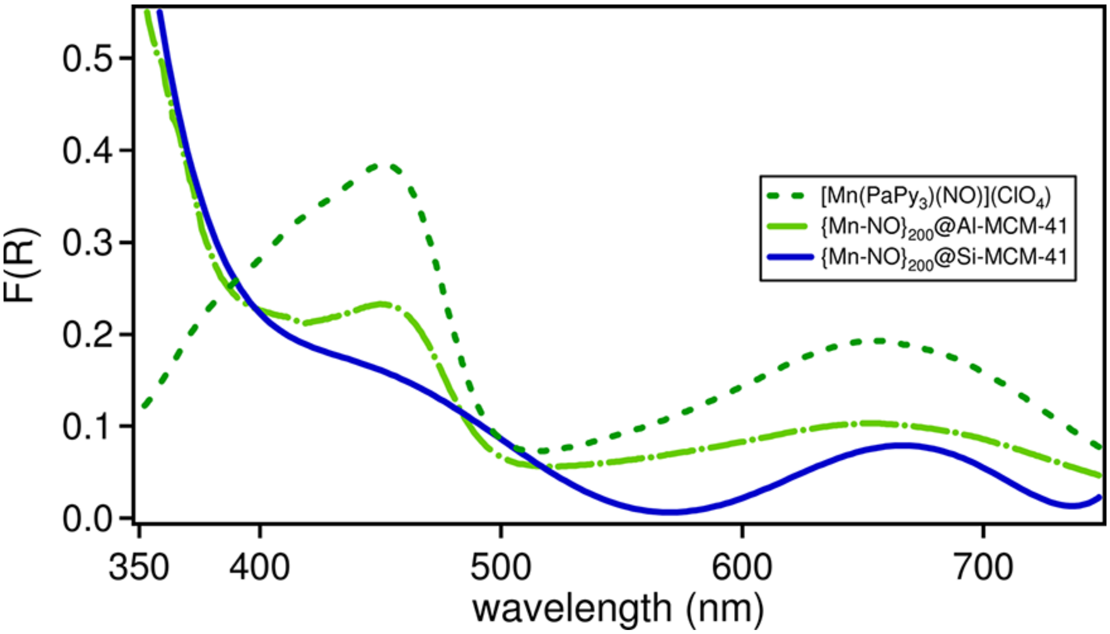

Figure 3.4. Diffuse reflectance UV-vis spectra of {Mn-NO} (dashed line), {Mn-NO}$_{200}$@Al-MCM-41 (dash-dot line) and {Mn-NO}$_{200}$@Si-MCM-41(solid line).

the nitrosyl in the Si-MCM-41 mesopores. Since no major distortion of the absorption bands is observed upon incorporation of the nitrosyl in the mesoporous materials, it is likely that the coordination structure of the nitrosyl remains intact upon confinement of the nitrosyl in the MCM-41 mesopores.[57]

3.3.5 Probing the Pore Environment of {Mn-NO}@MCM-41 by N_2 Sorption Isometry

The textural and morphological properties of the MCM-41 mesopores hybrid materials were probed by N_2 sorption isometry. Isometry experiments were performed by sealing a ~30 mg sample of the porous materials in stainless steel vessels and cooling the samples to 77.25 K (the boiling point of N_2). The vessels were then evacuated to ~10^{-5} mmHg prior and kept in a cryobath during the incremental filling of the vessel of the vessel with $N_{2(g)}$. The pressure inside the vessel was allowed to equilibrate for 45 s after each addition before measurement. The quantity of N_2 adsorbed ($cm^3\ g^{-1}$ STP) by the sample during filling and evacuation of the vessel with N_2 was plotted against the relative pressure in the vessel (P/P_o, ratio of the measured pressure to the atmospheric pressure, P_o) to afford adsorption/desorption isotherms.

The N_2 adsorption/desorption isotherms for $\{Mn\text{-}NO\}_{200}$@Si-MCM-41 (red) and $\{Mn\text{-}NO\}_{200}$@Al-MCM-41 (blue) are shown in Figure 3.5 (adsorption branches are solid lines and desorption are dotted lines). The isotherms for both materials demonstrate typical IUPAC defined type-IV profiles characteristic of ordered, mesoporous materials containing uni-dimensional pores with narrow pore size distributions. A schematic representation of the various adsorption and desorption processes and their effect on the isotherm behavior is shown in Figure 3.6 C.[58] The adsorption of N_2 on the MCM-41 samples can first by observed by the negative curvature in the isotherms after several additions of N_2 (~0.001 P/P_o). Adsorption of N_2 on the MCM-41 materials continues at a decreasing rate during the completion of the monolayer as marked by the ‘knee’ in the pressure range 0.001-0.1 P/P_o (point A in Figure 3.6 C). Completion of the monolayer adsorption process is marked by the beginning of a linear trend in the data of both materials which extends to ~0.2 P/P_o and corresponds to multilayer adsorption (point B in Figure 3.6 C). Inflections in the isotherms observed just above 0.2 P/P_o mark the initiation of the capillary condensation process in the narrowest mesopores. The sharp, linear trend following the inflection and extending to ~0.3 P/P_o is termed the condensation step and marks the pressure range of rapid condensation of liquid N_2 within the nucleated mesopores.[59] The condensation step in the isotherm of $\{Mn\text{-}NO\}_{200}$@Si-MCM-41 is well defined with a steep slope indicating a relatively sharp distribution of mesopore diameters, while that of $\{Mn\text{-}NO\}_{200}$@Al-MCM-41 is rather broad with a low slope indicating a wider distribution of *effective* mesopore diameters possibly due to heavy guest loading. Interestingly, neither isotherm demonstrates hysteresis within the pressure range of the condensation step which is usually observed in the isotherms of mesoporous materials containing independent pores with $ø \geq 2.4$ nm.[60] The hysteresis loops observed for the {Mn-NO} composites start at atmospheric pressure ($P/P_o = 1$) and close at ~0.7 P/P_o for $\{Mn\text{-}NO\}_{200}$@Si-MCM-41 and ~0.5 P/P_o for $\{Mn\text{-}NO\}_{200}$@Al-MCM-41. The uncommon hysteresis demonstrated by these materials is likely the result of the inhibited diffusion of N_2 during filling and evacuation of the uni-dimenstional channels due to adsorbed {Mn-NO} along the length of the channels.[61] The effective diffusion (D_{eff}) of N_2 within a mesoporous domain at atmospheric pressure (*i.e.* $P_{N2}/P_o \sim 1$) is inversely proportional to the tortuosity (τ) which is a measure of the detours in the trajectory of a diffusing molecule confined within a pore due to the walls and adsorbed guest molecules occupying a portion of the pore volume (ϕ).[62] The term τ of a diffusing molecule within a mesopore is calculated by:

$$\tau = \frac{1+\phi}{1-\phi} \qquad (1)$$

τ can then be used to determine D_{eff} of a diffusing molecules within a mesopore at ambient pressures

$$D_{eff} = \frac{D_{bulk}}{\tau} \qquad (2)$$

Based on the results presented in the next paragraph, the fraction of the total pore volume occupied by {Mn-NO} in the loaded Si-MCM-41 and Al-MCM-41 structures is 0.46 and 0.56, respectively, resulting in $\tau \sim 2.21$ and 3.54, for $\{Mn\text{-}NO\}_{200}$@Si-MCM-41 and $\{Mn\text{-}NO\}_{200}$@Al-MCM-41, repsectively. Therefore, the D_{eff} of N_2 during the evacuation of the {Mn-NO} occupied mesopores will be reduced by 38% in the pores of $\{Mn\text{-}NO\}_{200}$Al-MCM-41 compared to $\{Mn\text{-}NO\}_{200}$@Si-MCM-41. These results appear to be in line with the hysteresis observed in the isotherms of the {Mn-NO} loaded materials which is more pronounced in the isotherm of $\{Mn\text{-}NO\}_{200}$@Al-MCM-41 compared to $\{Mn\text{-}NO\}_{200}$@Si-MCM-41. In addition to the inhibited diffusion of N_2 due to the occupation of the pore space by {Mn-NO}, the pore confined guest molecule can also produce features called “constrictions” which describes the

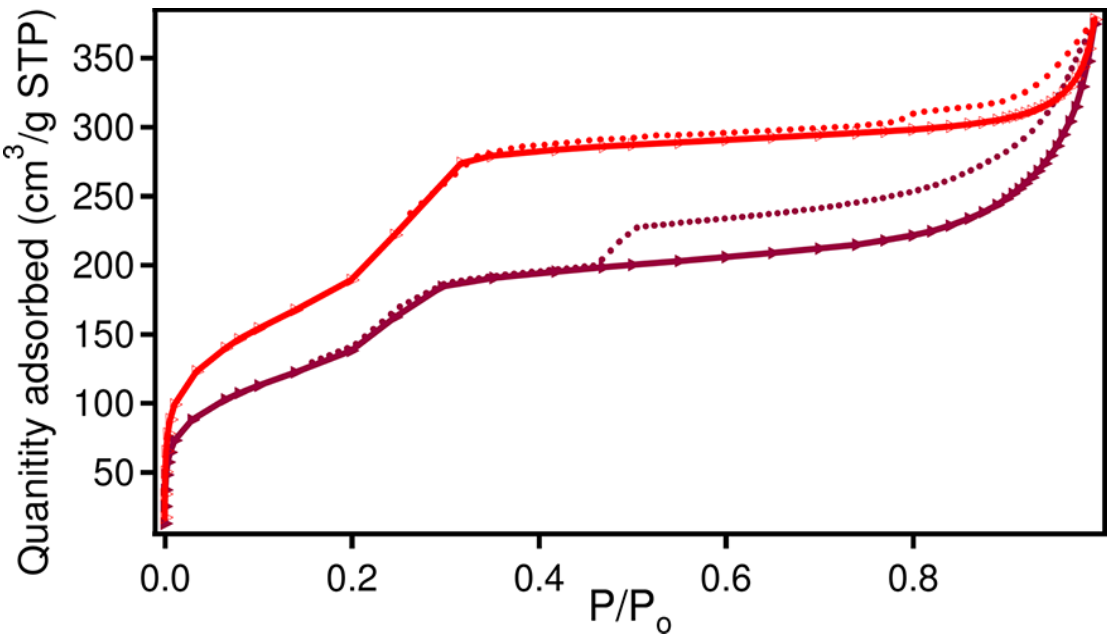

Figure 3.5. N_2 adsorption (solid lines with triangles) and desorption isotherms (dotted lines) of {Mn-NO}$_{200}$@Si-MCM-41 (red trace, open triangles) and {Mn-NO}$_{200}$@Al-MCM-41 (maroon trace, filled triangles).

narrow space between the pore wall and the confined guest.[63] Multiple constrictions within a pore can produce a ‘cavity’ which defines the space between two constrictions. Condensation of N_2 in cavities (which have the same diameter as the unmodified pores) occurs through a unique process involving the formation of a “nanobubble” upon merger of the condensed N_2 in the constrictions and the adsorbed layer(s) of N_2 on the walls of the cavity.[63] The spherical shape of nanobubbles provides a low energy curvature which facilitates condensation at a reduced pressure compared to that of the unoccupied mesopores. An abundance of disordered features in the mesopore space, such as constrictions and cavities, can smooth out many of the vertical features that would be observed in the adsorption isotherm of unconstricted meso- and macroporous materials. It is, therefore, possible that the lack of vertical features in the isotherm of

$\{Mn\text{-}NO\}_{200}$@Al-MCM-41 compared to that of $\{Mn\text{-}NO\}_{200}$@Si-MCM-41 maybe the result of the higher {Mn-NO} content in the mesopores of the aluminosilicate composite material.

Evacuation of constricted mesopores during the desorption phase of the isometry measurements can occur through two different mechanisms depending on the diameter of the constriction (d_c) (12.5 Å for {Mn-NO}) relative to the diameter of the mesopore (d).[65] When $d_c \sim d$, *pore blocking* is observed due to the inhibited evaporation of condensate trapped in an internal cavity until the pressure of the system is reduced to the normal evaporation point of the constrictions that isolate the cavity from the external, bulk phase. When $d_c < d$, *cavitation* occurs by the spontaneous formation of a gas bubble within in the cavity while the constrictions surrounding the cavitity remain filled. A schematic representation of the evacuation processes in disordered mesopores can be seen in Figure 3.6 C. In the case of pore blocking, the liquid in the cavity will evaporate at the same pressure as the liquid in the constriction and information regarding the diameter of the constricted space can be obtained (d_c). However, cavitation occurs at a pressure based solely on the bulk properties of the fluid (~0.42 P/P_o for N_2), thus, no information regarding the pore diameter will be obtained.[66] Since the hysteresis loop in the isotherm of $\{Mn\text{-}NO\}_{200}$@Al-MCM-41 closes at ~0.42 P/P_o, the evacuation of the disordered mesopores appears to occur through cavitation. In comparison, the hysteresis observed in the isotherm of $\{Mn\text{-}NO\}_{200}$@Si-MCM-41

Table 3.2. Average pore diameter, specific surface area (SSA), and cumulative pore volume of $\{Mn\text{-}NO\}_{200}$@Si-MCM-41, $\{Mn\text{-}NO\}_{200}$@Al-MCM-41 and the unloaded host materials.

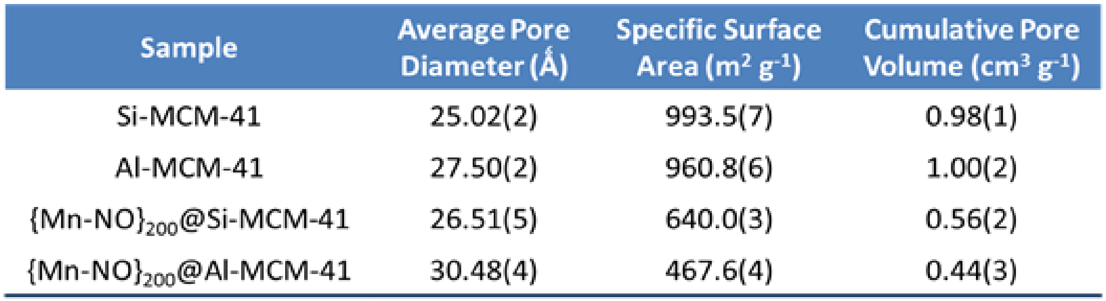

Sample	Average Pore Diameter (Å)	Specific Surface Area ($m^2\ g^{-1}$)	Cumulative Pore Volume ($cm^3\ g^{-1}$)
Si-MCM-41	25.02(2)	993.5(7)	0.98(1)
Al-MCM-41	27.50(2)	960.8(6)	1.00(2)
$\{Mn\text{-}NO\}_{200}$@Si-MCM-41	26.51(5)	640.0(3)	0.56(2)
$\{Mn\text{-}NO\}_{200}$@Al-MCM-41	30.48(4)	467.6(4)	0.44(3)

closes at 0.75 P/P_o which suggests a potential pore blocking effect or simple tortuosity effects, but seems to rule out any significant cavitation.

The BJH calculated average pore diameters of the MCM-41 materials were found to increase after loading of {Mn-NO} - from 25.02 to 26.51 Å for Si-MCM-41 and from 27.50 to 30.48 Å for Al-MCM-41 (Table 3.3). Loading of mesoporous silica nanoparticles with urea at 3% to 18.5% (w/w) also resulted in an increase in the BJH calculated pore diameters of the particles from 0.5 – 75.0 %, as reported by Gao *et al.* [67] The modified Kelvin equation formulated by Kruk-Jaroniec-Sayari was used to calculate the pore size distribution (PSD) of the loaded materials.[68] The multiple steps in the desorption branch of the isotherms generated a bimodal PSD which is not observed in the PSD calculated using the adsorption data. According to IUPAC published recommendations the desorption data should not be used to calculate the PSD of a material with constricted pores.[69] Thus, only the PSDs calculated from the adsorption data is included in the Gaussian plots in Figure 3.6 B. The Kruk-Jaroniec-Sayari geometerical equation, which utilizes the adsorption data and the spacing of the

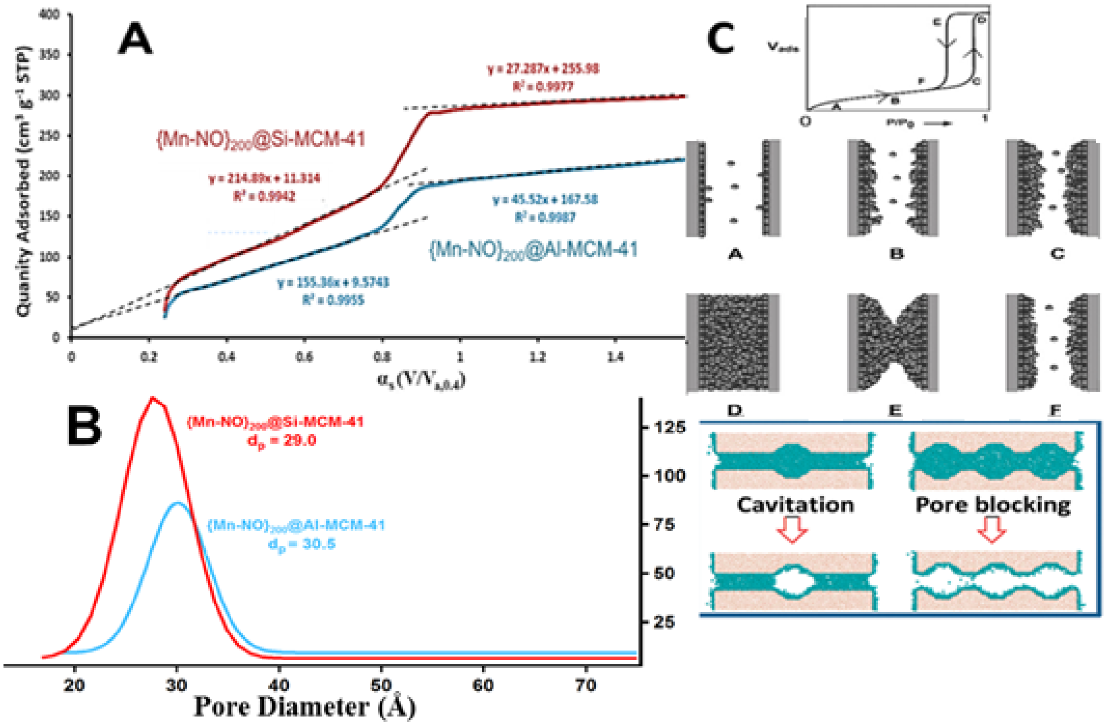

Figure 3.6. (A) High resolution α-s plot (Harkins-Jura equation) showing the quantity of N_2 adsorbed by {Mn-NO}@MCM-41 vs α - P/P_o normalized by adsorption data from an external standard, Li-Chrosorb-1000. **(B)** Gaussian plot of the pore size distributions of the loaded materials calculated from the adsorption data according to the method of Kruk-Jaroniec-Sayari. **(C)** Labeled features of a type-IV isotherm with schematics of the adsorption process. (A) Monolayer formation marked by rounded "knee". (B) Multilayer formation prior to liquid condensation showing low slope. (C) Bridging of multilayers across the center of the pore space with subsequent jump in V_{ads} due to capillary condensation. (D) Filling of pores with liquid. (E) Evaporation of liquid within the pores at a hemispherical interface with the bulk. The hysteresis loop between C and E is due to a high condensation energy. (F) Slow desorption of multilayers. Schematic

(100) peak determined by PXRD, was used to confirm the mean diameters of the PSDs (29.0 and 30.5 Å for $\{Mn\text{-}NO\}_{200}$@Al-MCM-41 and $\{Mn\text{-}NO\}_{200}$@Si-MCM-41, respectively) and yielded average pore diameters of 28.5 and 30.2 Å, for the Si-MCM-

41 and Al-MCM-41 loaded materials respectively.[68] The fairly close agreement of these values with the pore diameters calculated using the BJH method are surprising as the BJH method tends to underestimate the diameter of mesopores. The presence of micropores in the MCM-41 materials was assessed using the high resolution α-s method of Sing.[69] The ~0 intercepts of the low pressure data indicates that the samples contain no significant microporosity. The BJH calculated cumulative pore volumes of the MCM-41 host structures decreased considerably after loading of {Mn-NO}. The pore volumes of both Si-MCM-41 and Al-MCM-41 were similar prior to loading ~1 cm^3 g^{-1}, then decreased to 0.56 cm^3 g^{-1} for {Mn-NO}$_{200}$@Si-MCM-41 and 0.44 cm^3 g^{-1} for {Mn-NO}$_{200}$@Al-MCM-41 (Table 3.3). The reduction in the pore volumes of the MCM-41 hosts upon guest loading indicates that the MCM-41 structures can utilize at least 50% of their pore space for storage of guest molecules. The volume occupied by the adsorbed {Mn-NO} molecules in the Al-MCM-41 mesopores according to the BJH calculated cumulative pore volumes is 0.56 cm^3 g^{-1} which is over twice the van der Waals estimated volume of 0.27 cm^3 g^{-1} for the {Mn-NO} content of {Mn-NO}$_{200}$@Al-**x**MCM-41, as determined by ICP-MS analysis (approximating {Mn-NO} as a sphere with a diameter of 12.5 Ǻ (Table 3.4)). The discrepancy between these values was expected based on the differences in the cylindrical pore model used for BJH calculations and the disordered pore space of {Mn-NO}@MCM-41. The BET calculated specific surface area (SSA) of the unloaded and loaded Si-MCM-41 and Al-

Table 3.3 van der Waals dimensions of the {Mn-NO} cation, [Mn(PaPy$_3$)(NO)]$^+$.

Complex	x (Å)	y (Å)	z (Å)
[Mn(PaPy$_3$)(NO)]$^+$	12.4638(20) H12 to H18	10.5406(17) H3 to H9B	8.6898(13) O1 to O2

MCM-41 particles was also considerably reduced after loading of {Mn-NO}, with reductions in the SSA of Si-MCM-41 and Al-MCM-41 of 353 $m^2 g^{-1}$ and 493 $m^2 g^{-1}$, respectively (Table 3.3). The decreased surface area of Al-MCM-41 after loading corresponds to the same area occupied by ~6.2 µmol of {Mn-NO} which is close to the theoretical 4.2 µmol {Mn-NO} g^{-1} Al-MCM-41 measured by ICP-MS (assuming a cross-sectional area of 12.5 Å in diameter for {Mn-NO}).

3.3.6 PXRD and TEM Analysis of the {Mn-NO}@MCM-41 Structures

To determine if the incorporation of {Mn-NO} into the porous MCM-41 frameworks altered the structure of the MCM-41 hosts, powder x-ray diffraction (PXRD) analysis was performed on the materials before and after the loading process (Figure 3.7). The one-dimensional PXRD patterns of the unloaded materials demonstrate significant crystallinity with well-defined peaks corresponding to (100), (110), (200) and (210) reflections typical of ordered, mesoporous silicates with a hexagonal array of uni-dimensional channels with narrowly dispersed diameters.[70] The retention of a similar peak pattern in the spectra of the loaded materials demonstrates that the incorporation of {Mn-NO} into the porous materials does not severely alter the MCM-41 framework and that no long range ordering of the guest molecules occurs within the pore space. However, the introduction of electron density in the previously void pore space from the adsorption of the {Mn-NO} guest caused a dramatic reduction in the peak intensities compared to the unloaded materials. Only the low angle (100)

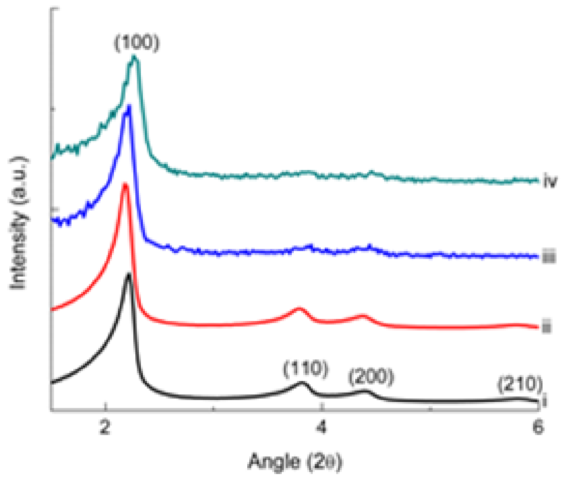

Sample	hkl	*d* (Å)	Intensity
Al-MCM-41	(100)	39.8	130422
	(110)	23.1	21968
	(200)	20.2	13537
	(210)	15.2	6085
Si-MCM-41	(100)	40.5	146313
	(110)	23.2	21732
	(200)	20.2	14837
	(210)	15.2	5858
{Mn-NO}$_{200}$@Al-MCM-41	(100)	39.8	635
	(110)	-	-
	(200)	-	-
	(210)	-	-
{Mn-NO}$_{200}$@Si-MCM-41	(100)	39.1	511
	(110)	-	-
	(200)	-	-
	(210)	-	-

Figure **3.7.** (left) PXRD patterns of: (i) Al-MCM-41 prior to loading; (ii) Si-MCM-41 prior to loading; (iii) {Mn-NO}$_{200}$@Al-MCM-41; (iv) {Mn-NO}$_{200}$@Si-MCM-41. (right) Miller indices and d-spacing of peaks observed in the PXRD patterns.

reflection can be easily identified in the spectra of the loaded materials (I_{rel} = 0.3% for {Mn-NO}$_{200}$@Si-MCM-41 and 0.5% for {Mn-NO}$_{200}$@Si-MCM-41) while the higher angle (110) and (200) reflections are just slightly above the background.[71] The almost complete loss of intensity in the PXRD patterns of the loaded materials indicates that

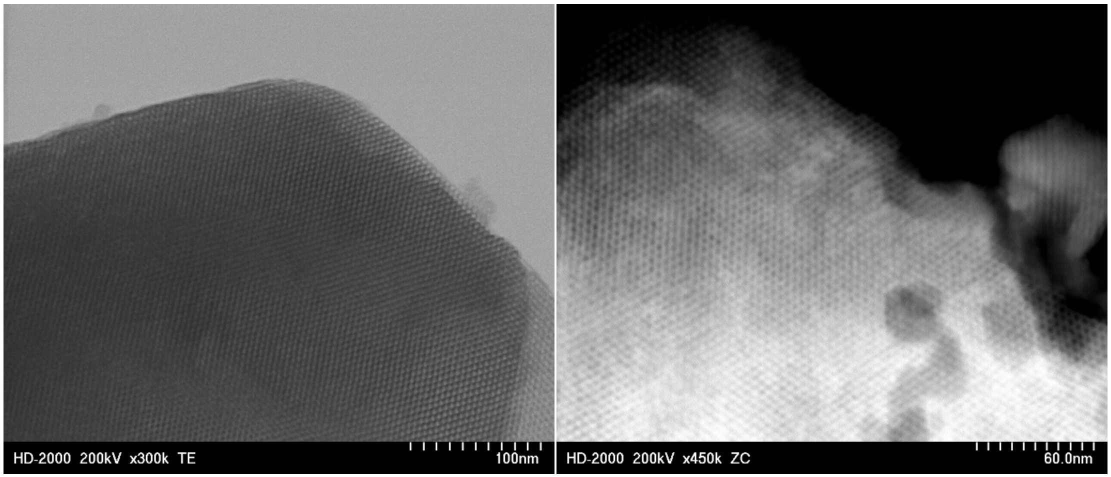

Figure 3.8. TEM micrographs of {Mn-NO}$_{200}$@Al-MCM-41 particles along the pore axis demonstrating the retention of the MCM-41 host structure.

the mean electron density (N_e/1000 Å^3) of the MCM-41 pore walls and the pore confined {Mn-NO} guest is roughly equivalent (densities within ± 0.1 e Å^{-3} eliminates any signal in the case of MCM-41 type materials).[72] However, the mesoporous structure of the MCM-41 materials can still be observed by TEM analysis. The regular hexagonal array of mesoporous channels can still be seen in the TEM micrograph of {Mn-NO}$_{200}$@Al-MCM-41 shown in Figure 3.8, which confirms that the structural integrity of the MCM-41 frameworks was maintained during guest loading.

3.3.7 SEM-EDX Elemental Mapping of {Mn-NO}@MCM-41

Cross-sectional SEM-EDX elemental mapping was performed on the {Mn-NO}$_{200}$@Si-MCM-41 and {Mn-NO}$_{200}$@Al-MCM-41 materials in order to visualize the distribution of {Mn-NO} molecules throughout a cross-section of an individual particle and to obtain a semi-quantitative analysis of the abundance of select elements present in the analyzed region. The technique for obtaining the elemental distribution maps utilizes the x-rays emitted from atoms excited by the electron beam produced by the SEM source to probe the structure of the analyte. The cross-sectional SEM-EDX single elemental (Si, O, Al, and Mn) maps of an individual particle of {Mn-NO}$_{200}$@Al-MCM-41 are shown in Figure 3.9. The even distribution of {Mn-NO} throughout the cross-section of the particle is confirmed by the correlation between the Mn elemental map (right panel, image d) and the SEM micrograph of the analyzed region (left panel). The EDX measured abundance of the elements in the analyzed cross-section (bottom right panel) closely matches the values expected on the basis of the ICP-MS and FAAS results. The considerably lower relative abundance of Cl

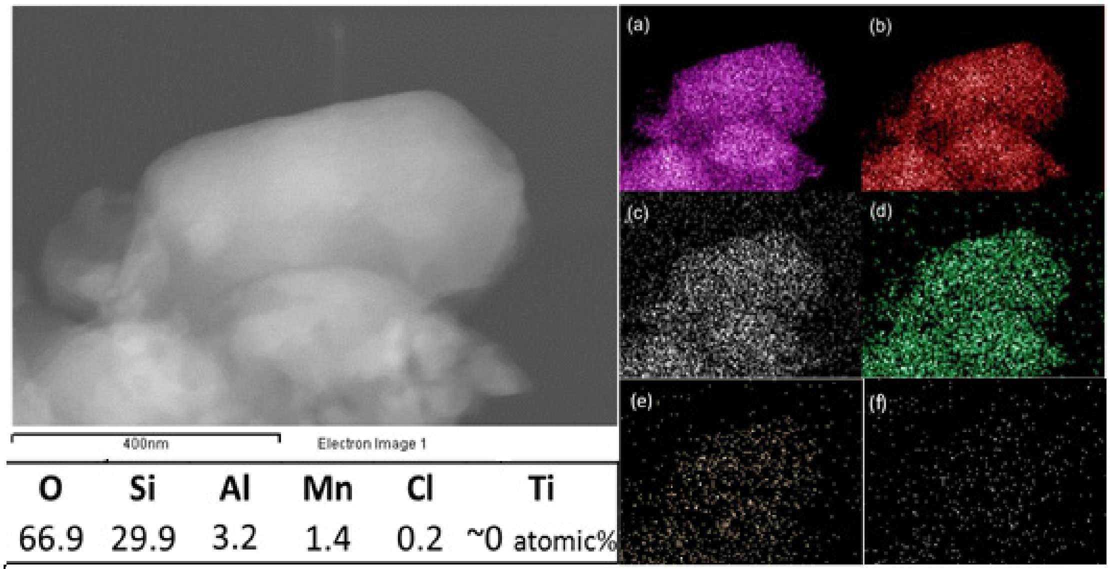

O	Si	Al	Mn	Cl	Ti	
66.9	29.9	3.2	1.4	0.2	~0	atomic%

Figure 3.9. (Left top) Cross-sectional SEM of {Mn-NO}$_{200}$@Al-MCM-41 particle and (Right) elements maps of : (a) Si, (b) O, (c) Al, (d) Mn, (e) Cl (f) Ti. (Bottom left) Relative atomic abundance of analyzed elements as measured by EDX analysis.

compared to Mn demonstrates that a majority of the {Mn-NO} content of {Mn-NO}$_{200}$@Al-MCM-41 was loaded through an ion-exchange process, promoting the dissociation of the perchlorate counter-ion. Ti mapping was performed as a control and showed negligible correlation to the particle cross-sectional area.

3.4 NO Photorelease from {Mn-NO}@MCM-41

Based on the NO photorelease capabilities of the Mn nitrosyl, $[Mn(PaPy_3)(NO)]^+$, in aqueous solutions, we hypothesized that immobilization of the nitrosyl on the hydrated pore-walls of silicate and aluminosilicate MCM-41 particles would provide the necessary conditions to support NO photorelease from the nitrosyl. The photo-dissociation of NO from the Mn center of {Mn-NO} occurs only through the following two step photoreaction under physiologically relevant conditions:

$$[\mathrm{Mn(PaPy_3)(NO)}]^+ + h\upsilon \rightarrow [\mathrm{Mn(PaPy_3)(NO)}]^{+*} \quad (3)$$

$$[\mathrm{Mn(PaPy_3)(NO)}]^{+*} + \mathrm{H_2O} \rightarrow [\mathrm{Mn(PaPy_3)(H_2O)}]^+ + \mathrm{NO} \quad (4)$$

Upon photoexcitation of {Mn-NO} by visible light ($\lambda_{max} = 635$ nm), the NO ligand of the excited state nitrosyl ($[\mathrm{Mn(PaPy_3)(NO)}]^{+*}$) becomes susceptible to displacement by donating solvents in the outer coordination sphere (e.g. water). Thus, the rate of NO photorelease (through Eqs. **3** and **4**) is dependent on adequate solvation of the nitrosyl. Due to the high moisture content (~30%) of silicate based materials, mesoporous MCM-41 type silicate and aluminosilicate particles were identified as suitable support matrices to ensure adequate solvation of pore confined {Mn-NO}.[73] In addition, such materials are highly transparent to visible light permitting adequate irradiation of the encapsulated nitrosyl, and highly porous facilitating rapid diffusion of the photoreleased NO.

The photorelease of NO from {Mn-NO}@MCM-41 suspended in aqueous saline solutions (137 mM NaCl) was monitored using a NO-specfic electrode. Typical results from such experiments are shown in Figure 3.10. The ability to rapidly trigger NO release from {Mn-NO}@MCM-41 under the complete control of light was demonstrated by irradiating the suspended particles with short pulses of visible light which induced the release of rapid bursts of NO (Figure 3.10 A). The total NO releasing capacities of $\{\text{Mn-NO}\}_{200}$@Si-MCM-41 and $\{\text{Mn-NO}\}_{200}$@Al-MCM-41 were measured during continuous illumination of the samples which produced a steady flux of NO for nearly ~1 h (Figure 3.10 B). The photo-activated release of NO from {Mn-

NO}@MCM-41 is highly desirable for the therapeutic delivery of NO since one can deliver a controlled dose of NO to the treatment site through simple illumination, and then wait for a period of time to observe the progress of the treatment site before repeating the process until the desired outcome is achieved with minimal side-effects from excess NO. NO releasing porous materials reported thus far have relied on spontaneous NO release mechanisms, such as the displacement of NO from metal centers by solvent molecules in transition metal-exchanged zeolites,[24,25] or the decomposition of NONOates (nitrosoamine functional groups) tethered to the surfaces of MCM-41 and related materials.[26] Such mechanisms allow little or no control over the amount or duration of NO release from the material. To our knowledge, {Mn-NO}@MCM-41 is the first reported inorganic porous material to demonstrate rapid NO release under the complete control of light. Furthermore, the NO-releasing capabilities (and stability) of these materials remained unchanged for at least three months when stored at room temperature in the dark.

2.4.1 NO Releasing Capacities of {Mn-NO}@MCM-41 Under Steady Illumination

The NO delivery capacities of $\{\text{Mn-NO}\}_{200}$@Si-MCM-41 and $\{\text{Mn-NO}\}_{200}$@Al-MCM-41 were determined with the aid of an inNO-T NO-electrode based measuring system. The measurements were performed by placing the tip of the electrode in a magnetically stirred suspension of the materials in 2 mL of saline solution. As shown by the red trace in Figure 3.10 B, continuous illumination of a 10 mg suspension of $\{\text{Mn-NO}\}_{200}$@Al-MCM-41 produced a maximum NO concentration of 65 μM within 10 min of illumination (100 mW cm^{-2}, visible light), and maintained a steady concentration for ~50 min thereafter. After 60 min of total illumination, complete photo-bleaching of the sample had occurred as indicated by the return of the electrode signal to the baseline and the loss of the green color from the loaded material

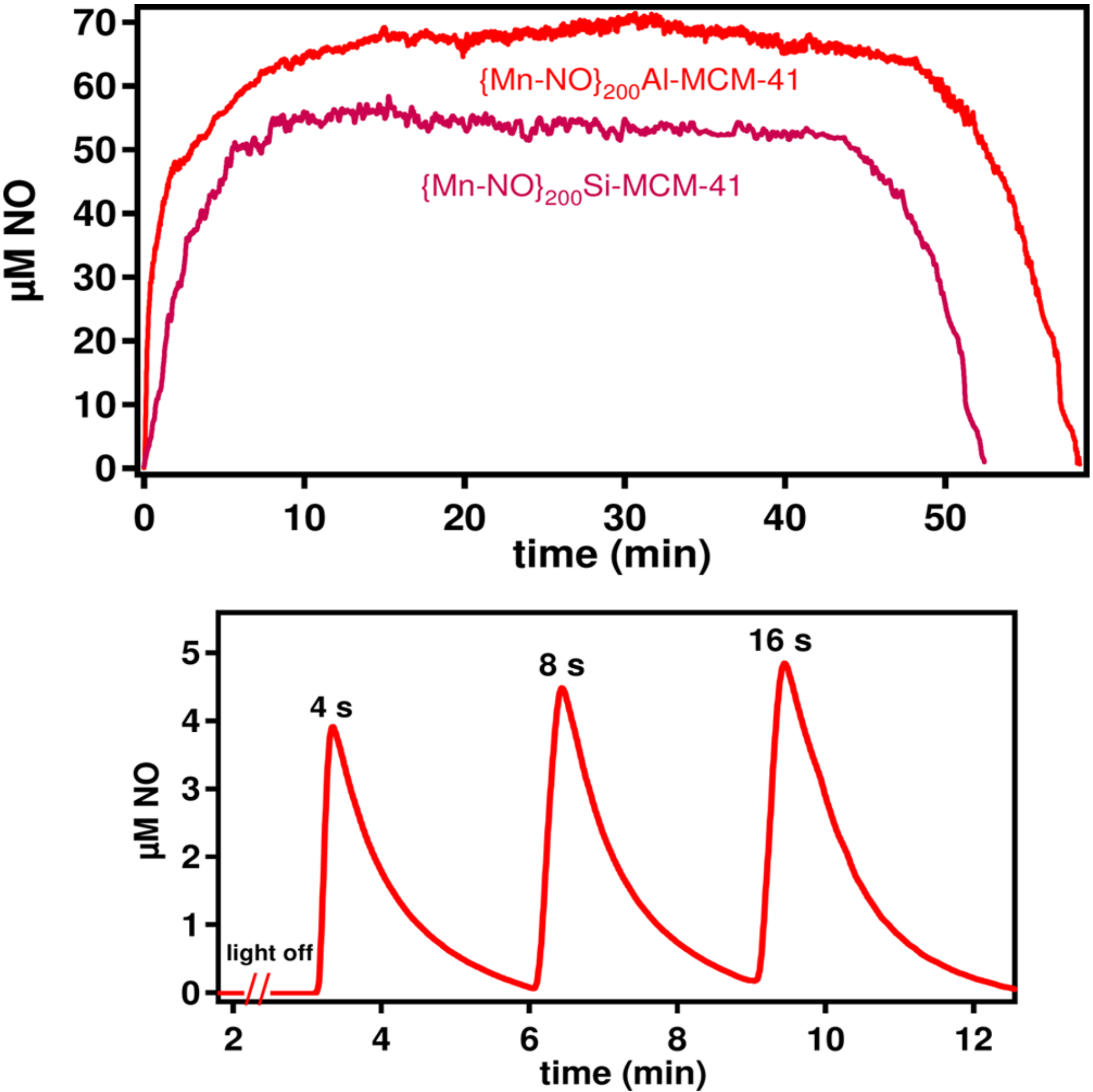

Figure 3.10 (Top panel): Light-triggered NO release from {Mn-NO}200@Si-MCM-41 and {Mn-NO}200@Al-MCM-41 suspended in saline solution (constant illumination). (Bottom panel): Bursts of NO release from {Mn-NO}200@Al-MCM-41 triggered by light pulses (duration time in s).

due to the photodissociation of $[Mn(PaPy_3)(NO)]^+$ and the accumulation of the tan colored photoproduct, $[Mn(PaPy_3)(H_2O)]^+$. The total NO released from the 10 mg sample of $\{Mn\text{-}NO\}_{200}$@Al-MCM-41 over the 60 min illumination period (as determined by the Griess reagent) was 4.3(2) μmol, close to the total NO content of the sample (4.4 μmol) as determined from the results of ICP-MS analysis. Similar measurements with$\{Mn\text{-}NO\}_{200}$@Si-MCM-41 resulted in a maximum concentration of 50 μM of NO after ~7 min of illumination, which was maintained for nearly 40 min. The release of rapid bursts of NO from $\{Mn\text{-}NO\}_{200}$@Al-MCM-41, as seen in Figure 3.10 A, was achieved by the illumination of a 5 mg sample with pulses of light with increasing durations of 4-16 s producing bursts of NO with concentrations from 4−6 μM.

The ability of {Mn-NO}@MCM-41 to produce μM concentrations of NO suggests that the material would exhibit antimicrobial properties. Such concentrations of NO have previously been shown bactericidal activity against a range of pathogenic organism and is close to the suggested concentration of NO experienced by microbes in the phagolysosome.[74,75] Ghaffari and Miller reported that exposure of bacterial cultures in liquid media to a continuous-flow of 200 ppm $NO_{(g)}$ caused a 98% reduction in the viability of cultures grown to 10^5 cfu mL^{-1}.[74,75] The uptake of NO by the acellular media delivered through the continuous-flow system was determined to be ~80 μM NO h^{-1}. However, consideration of such results should take into account the variability in such measurements due to the intrinsic error in determing the rate of gaseous NO uptake by liquid media and the variable susceptibility of bacteria to a given concentration of NO based on the culturing technique.[76] Notably, the growth phase of bacterial cultures has a drastic effect on the cytotoxicity of NO. Soares and coworkers have shown that cultures of *A. baumannii* grown to either the log or stationary phases then treated with the same 1 mM dose of the NO donor, sodium nitroprusside (SNP), caused complete eradication of the log phase culture while the stationary phase culture maintained 85% viability.[77] It was reported that such concentrations of SNP produced [NO] of 50 μM for ~ 1 h. The discrepancy in the cytotoxic effects of NO on bacteria in different growth phases was explained by the change in the gene expression patterns and the decrease in cellular uptake that are observed when a bacterial culture reaches the stationary growth phase. Such results emphasis the need for an accurate assessment of the antimicrobial effects of {Mn-NO}@MCM-41, despite the known NO release rates, against bacterial cultures grown under conditions which closely mimic those of the proposed therapeutic application. Here we propose the potential application of {Mn-NO}@MCM-41 in the treatment of skin and soft-tissue infections by *A. baumannii*.

3.5 Antimicrobial effects of {Mn-NO}$_{200}$@MCM-41 against *A. baumannii*

Following measurement of the NO releasing cabalities of {Mn-NO}@MCM-41 materials, the antibiotic efficacy of the hybrid material was tested against a drug susceptible and a multi-drug resistant strain of *A. baumannii* (MDR-AB). For such experiments, the {Mn-NO}$_{200}$@Al-MCM-41 formulation was chosen over the purely siliceous material based on the greater NO releasing capacity and enhanced retention of {Mn-NO} its photoproduct(s) within the Al-MCM-41 framework. The latter attribute is vital for such experiments to eliminate potential interference from the leaching of the Mn complexes from the MCM-41 mesopores in the determination of the bactericidal effects of the photoreleased NO. Since the intended application of the {Mn-NO}@MCM-41 materials was the treatment of skin and soft-tissue infections (SSTI), antibiotic testing was performed using a model designed to mimic the growth environment of the skin and soft-tissue and induce bacterial colonization representative of SSTI. The SSTI model used in this study was constructed by inoculating 1.0% (w/v) brine-agar held in the liquid phase at 45°C, then evenly pouring the inoculated liquid agar over the surface of a 1.5% (w/v) agar plate (containing tryptic soy nutrient) generating a 1.1 mm thick top layer of soft agar with homogenously suspended bacteria at a colony density of > 10^5 CFU cm^{-1}. This top-agar SSTI model was a useful tool to test the ability of the NO released from samples of $\{Mn\text{-}NO\}_{200}$@Al-MCM-41 dispersed over a defined area to penetrate the agar matrix and eradicate bacteria at various depths corresponding to the spread of bacteria to deeper layers of tissue during the course of SSTI.

3.5.1 Skin and Soft-Tissue Infection Model for Antimicrobial Testing

The SSTI model used in this work was designed to address certain limitations of the standardized disk diffusion and agar dilution assays used for testing the antibiotic efficacy of topical therapies for the treatment of SSTI.[78] The bacterial plates used in these assays are constructed by spreading a liquid inoculum over the surface of a nutrient rich hard agar plate (1.5-2% (w/v) of agar). Bacterial growth on conventional agar plates is inadequate for testing the efficacy of antibiotics against SSTI due to several limitations. First, bacteria colonizing the surface of the skin are incapable of initiating infectious growth due to the inadequate nutrient availability on the keratinized and exfoliating cells covering the skin. Instead, SSTI does not occur until colonization of tissue layers 0.3-1 mm below the surface of the skin, corresponding to the lower epidermis or the dermis.[79] If left untreated, the infection will progress through the continual spread of bacteria into deeper regions of the cutaneous and subcutaneous tissue by the excretion of exotoxin-like proteases which break down the extracellular matrix and facilitate bacterial motility.[80] Certain virulent strains of *A.baumannii* are particularly well equipped to spread from the soft-tissue to the blood by penetrating the epithelial layer surrounding the vaculature through the activity of the outer membrane porin, AbOmpA. This protein mediates the interaction of *A. baumannii* with eukaryotic cells allowing the bacteria to bypass the epithelium and colonize the circulatory system where it can then spread to vital organs, a highly fatal condition called bacterial sepsis.[81]The standardized methods of antibiotic testing contain only surface exposed bacteria and thus provide no means for assessing the bactericidal effects of an antibiotic in the deep tissue regions where the onset of sepsis occurs. Second, the standardized assays are incapable of invoking the “ditching phenomena” which describes the penetration of surface colonized bacteria into deeper layers of agar by bacteria due to the lack of nutrients available at highly populated regions at the agar surface.[82] Finally, one of the most important considerations which is often overlooked in such experiments is the decreased partial pressure of oxygen that occurs upon heavy pathogen colonization of tissue.[83] Microbial burdens can deplete the local abundance of nutrients and decrease the availability of oxygen in infected tissue through metabolic activity and the induction of host repsonses (e.g. disruption of microvasculature, blood vessel constriction, increased activity of repair proteins).[84] Direct administration of antibiotics to surface-exposed colonies using the standardized methods ensures a plentiful source of atmospheric oxygen, therefore excluding any effect of oxygen deficiency on the antimicrobial pharmacodynamics. The importance of assessing potential oxygen deficiencies in infecting locales prior to treatment was demonstrated by the considerable increase in the MIC_{50}'s of the widely used antibioitics: tobramycin, amikacin, and aztreonam which increased by 4, 4, and 16-fold, respectively, when measured under hypoxic conditions.[85] Oxygen deficiencies in host tissue can also influence the metabolic phenotype of infecting pathogens, potentially triggering bacterial populations to shift towards a latent phenotype with a reduced metabolism, and a decreased uptake of extracellular material (including antibiotics), as demonstrated by the persistence of *Mycobacterium tuberculosis* in lung tissue granulomas with extremely low oxygen and nutrient concentrations for decades.[86] Low oxygen pressures in hypoxic tissue can also affect the competency of the innate immune response by host cells, limiting the ability of the host to clear remaining pathogens after a successful antibiotic course.[84] Despite the simple design of the SSTI model employed in the present work, it provides an effective means to address the limitations of the standardized methods outlined above.

Mukerji reported on the ability of *Acinetobacter spp.* to penetrate an agar matrix through a unique twitching motility.[87] This motion is now believed to occur through the retraction of a type IV pili and is most effective when the bacterium is cultured on soft, >1 % (w/v) agar.[88] Bacterial motility is driven by chemotaxis. In a bacterium's quest for sustenance, swimming planktonic cells will form "wolfpacks" to coordinate their efforts in search of the origin of molecular signals. Nutrient driven motility is a widely described phenomena amongst motile bacteria (termed energy taxis) and can promote bacterial 'ditching' towards subsurface nutrient reservoirs (the bottom agar layer in our SSTI model).[89] It is known that the subsurface location of nutrient rich blood vessels are targeted by *A. baumannii* through the activity of a heme-sensing signal transduction system (HbpS) which promotes *A. baumannii* populations to colonize the tissue surrounding the vasculature.[90] In the present SSTI model, the diffusion of nutrients from the bottom layer of nutrient rich agar into the nutrient deplete top agar layer is likely to generate a nutrient gradient with a maximum concentration at the interface of the two agar layers. Based on the previously observed behavior of *A. baumannii*, the energy taxis promoted motility of bacterial cells towards nutrient rich zones in the SSTI model could produce high bacterial density and metabolic activity in localized regions, depleting oxygen availability as observed during the colonization of host tissue by pathogenic bacteria *in vivo*.[91] In addition, the 1.0% agar matrix supporting the bacterial inoculum in the SSTI model has an increased permeability compared to the > 1.5% agar plates used in the standardized methods,[78] and should facilitate bacterial motility so that growth and colonization can occur in a manner similar to those of clinical SSTI.[92] During host infection, bacteria can spread in all three dimensions, penetrate tissue, and form cell-to-cell contacts, colonies, and biofilms which are all extremely important virulence factors of pathogenic bacteria and affect the organisms antibiotic susceptibility.

3.5.2 The Antimicrobial Efficacy of {Mn-NO}@MCM-41 Against *A. baumannii*

Following casting of the inoculated (> 10^5 CFU mL^{-1}) top-agar layer of the SSTI model (as described above), the plates were incubated at 37°C for two hours before application of $\{Mn\text{-}NO\}_{200}$@Al-MCM-41 to allow the inoculum to establish normal log phase growth and metabolic activity. The exceptional rate of drug resistance demonstrated by clinical isolates of *A. baumannii* has been contributed to the family of multi-drug efflux pumps expressed by the bacterium which have the combined ability to export the spectrum of clinically available antibiotics.[93] Since the expression of genes encoding efflux pumps reaches a maximum during log phase growth of *A. baumannii*, the colony density in the SSTI model should maximize the activity of this resistance mechanism.[94] After the two hour incubation, sterile samples of $\{Mn\text{-}NO\}_{200}$@Al-MCM-41 and $\{Mn\text{-}solv\}_{200}$@Al-MCM-41 (photolyzed material as a negative control) were spread over a 22 mm in diameter area on the surface of the agar plates (using an appropriately cut and sterilized paper mask) and illuminated with 100 mW cm^{-2} of visible light. The effect of the photoreleased NO on drug susceptible and drug resistant strains of *A. baumannii* are shown in Figure 3.11. The growth of both strains of *A. baumannii* was unaffected effected by the illumination of the photolyzed control (plates A and D). However, the illumination of a low dose of {Mn-NO}$_{200}$@Al-

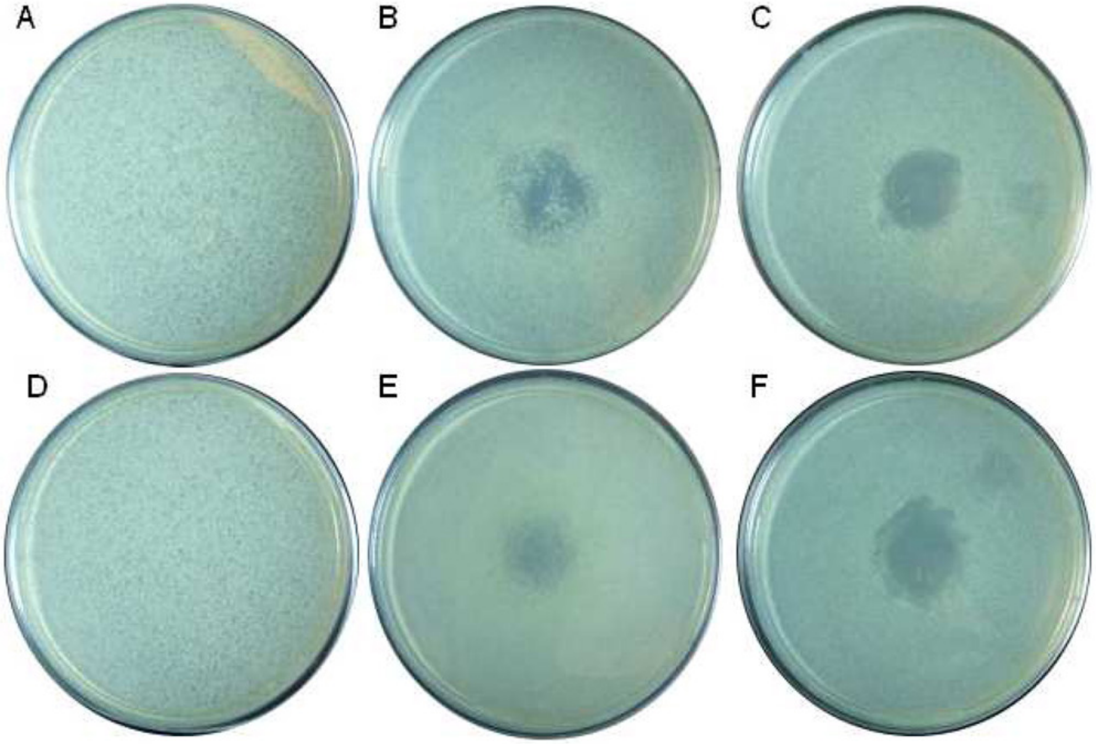

Figure 3.11 Effects of NO photoreleased from {Mn-NO}200@Al-MCM-41 on *A. baumannii* colonies. (A−C): Results with drug-susceptible strain. (D−F): Results with drug-resistant strain. Materials sprayed on the central application zone. (Plate A): Photoproduct showing no reduction of the bacterial load. (Plate B): Clearing of bacterial load with 30 mg of {Mn-NO}200@Al-MCM-41. (Plate C): Clearing with 50 mg of {Mn-NO}200@Al-MCM-41. (Plate D): Photoproduct effect on the bacteria. (Plate E): Clearing with 30 mg of {Mn-NO}200@Al-MCM-41. (Plate F): Clearing with 50 mg of {Mn-NO}200@Al-MCM-41.

MCM-41 for 1 h (30 mg, plate B) produced a significant reduction in the growth of drug susceptible *A. baumannii*, while illumination of a high dose of {Mn-NO}$_{200}$@Al-MCM-41 for 1 h (50 mg, plate C) caused complete clearing of the bacterial load. The zone of bacterial clearing caused by the photoreleased NO was mostly localized (area in contact with the powder) showing limited effects from the lateral diffusion of NO. Continued illumination of the high dose of {Mn-NO}$_{200}$@Al-MCM-41 for a total length of 1.5 h produced an excess of NO which resulted in considerable lateral effects from the treatment site and possible saturation of the contents and headspace of the petri dish (50 mg, Figure 3.12). The penetration of NO through the 1.1 mm layer of inoculated soft agar was visually apparent by the complete clearing of bacterial colonies through entire depth of the agar layer within the treatment area. To confirm that no viable cells remained in the cleared areas, full thickness excisions of a portion of the top-agar (~1 cm^2) were transferred to liquid growth media and gently homogenized. After 24 hours of incubation, the lack of growth in the transfer media confirmed that the photoreleased NO was to sufficiently penetrate and diffuse through the entire depth of the top agar layer to cause complete eradication of bacterial colonies. Since the bacterial loads used to inoculate the

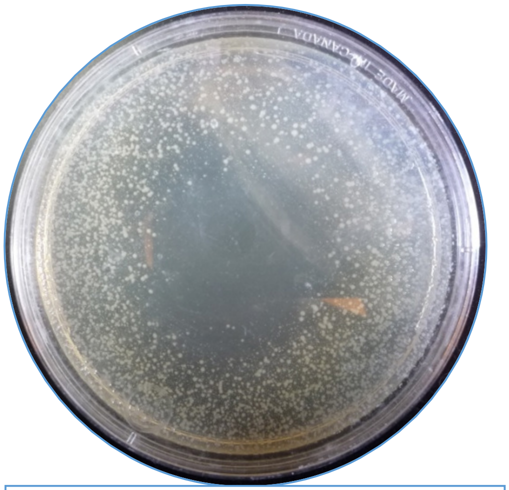
Figure 3.12 Antibacterial effects of photoreleased NO from 50 mg of {Mn-NO}$_{200}$@Al-MCM-41 after 1.5 h illumination against drug susceptible *A. baumannii*.

soft agar in the SSTI model meet the clinical definition of infection (> 10^5 CFU mL^{-1}), the results of the antimicrobial experiments provide evidence of the efficacy of {Mn-NO}$_{200}$@Al-MCM-41 for the treatment of SSTI caused by drug susceptible *A. baumannii*. The antimicrobial testing was repeated with a multidrug resistant clinical isolate of *A. baumannii* (MDR-AB) inoculated at the same initial colony density (10^5 CFU mL^{-1}). Application of 30 mg of {Mn-NO}$_{200}$@Al-MCM-41 to the surface of the soft agar followed by 1 h of illumination caused a significant reduction of the colony density (plate E). When a dose of 50 mg of the hybrid NO-donor was illuminated for 1.5 h, the clearing was nearly complete (plate F). Antimicrobial effects due to the lateral diffusion of NO were observed as a thinning of the colony density around the application site. The lateral effects at this dose are considerably attenuated compared to those observed with the drug susceptible strain indicating that MDR-AB may consume a considerable amount of NO through detoxification pathways. This would explain the increased illumination time (thus an increase in the dose of NO) required for complete clearing of MDR-AB. However, since NO is capable of inactivating proteins through active site binding/inhibition, Fe-S cluster mobilization, and amino acid modification, clearing of NO tolerant bacterium can be achieved as demonstrated here.[28] Collectively, the results of the antimicrobial testing using the SSTI model demonstrate that {Mn-NO}$_{200}$@Al-MCM-41 is an effective *in vitro* bactericidal agent against *A. baumannii* (both drug susceptible and drug resistant strains). However, *in vivo* studies will be necessary to confirm the suitability of the composite NO-donating material for the treatment of SSTI caused by these highly problematic gram-negative bacteria.

Studies by Miller and co-workers have shown doses of 200−300 ppm of NO to be nontoxic to key cells involved in tissue repair even when the exposure is continued for 48 h.[74] Exposure to even higher doses of NO for short durations are also tolerated by human cells. In a later study, Miller and coworkers have demonstrated that similar doses of NO are nontoxic to a variety of immune cells, and multiple exposure to NO could be additive to host immune response.[75] In addition, exposure to NO stimulates collagenase expression in fibroblasts.[95] As a consequence, delivery of NO to the site of SSTI can promote wound healing in addition to its antibiotic effects. The MCM-41 framework employed here is also beneficial for blood clot formation in open wounds, as demonstrated by the ability of molecular sieves and ~1 mm mesoporous silica particles to reduce clotting time by ~half.[96,97] Nitric oxide also stimulates the repair of injured skeletal muscles and promotes bone metabolism and formation at damaged sites.[98,99] We therefore anticipate that the {Mn-NO}@MCM-41-type materials could assist the healing of both infected and uninfected wounds in several way in addition to the reduction of bacterial loads.

3.6 Conclusions

In summary, loading of a photosensitive manganese nitrosyl into the porous structures of MCM-41 hosts has been achieved in the present work. In case of the neutral Si-MCM-41, the nitrosyl is entrapped within the channels of MCM-41 via interaction with groups on the channel wall. Use of Al-MCM-41 as the host promotes improved loading of the nitrosyl due to an expected ion-exchange mechanism and the formation of electrostatic interaction between the cationic guest and anionic Al sites. Leaching of the nitrosyl from the either host structure is minimal in physiological saline and is reduced further from the Al-MCM-41 host. Exposure of the hybrid materials to visible light results in rapid release of NO from the entrapped nitrosyl while the photoproducts are retained in the host structure. As a consequence, such hybrid NO-donors could be employed to deliver NO under the total control of light with very little toxicity from the biocompatible host, the pore retained nitrosyl or its photoproducts. These properties have been demonstrated in the eradication of *A. baumannii* loads using a SSTI model. Effective clearing of both drug sensitive and multi-drug resistant strains *of A. baumannii* has been observed by means of photo-triggered NO delivery. With the typical light flux of a sunny day (100 mW cm^{-2}) in mind, we have employed a 100 mW cm^{-2} light source in the measurement of the NO releasing properties and antibacterial properties of {Mn-NO}@MCM-41. It is expected that application of these nitrosyl-containing porous materials to infected wounds followed by exposure to sunlight will bring about a rapid reduction of the pathogen load. Since the chemical composition and material structure of {Mn-NO}@Al-MCM-41 is comparable to the current (kaolin powder impregnated in non-woven gauze) and past (2002-2008, zeolite granules) standards of care of the US military for the treatment of hemorrhage (major cause of battlefield causlties) using a hemostatic agent, powders of this kind (or derivates thereof) could be employed as a first line of treatment for *A. baumannii* infections in battlefield wounds.[100]

3.7 Experimental Section

3.7.1 Materials

MCM-41-type silicate and aluminosilicate molecular sieves were obtained from Sigma-Aldrich (St. Louis, MO). Antibiotic susceptible *A. baumannii* freeze-dried culture (NCIMB 12457) and MDR *A. baumannii* (BAA-1605) was obtained from Microbiologics (St. Cloud, MN). BAA-1605 is a clinical isolate from the sputum of a soldier injured in Afghanistan and sent to a Canadian hospital in 2006. The strain showed resistance to 9 of 11 antibiotics tested.

3.7.2 Synthesis Safety Note

Transition metal perchlorates should be handled with great caution and be prepared in small quantities as metal perchlorates are hazardous and may explode upon heating.

3.7.3 Synthesis of {Mn-NO}@MCM-41

All manipulations were performed in the dark. A batch of 100 mg of Si-MCM-41 or the Na-exchanged Al-MCM-41 was added to 5 mL of distilled acetonitrile in a 50 mL Schlenk flask containing a magnetic stir bar. The mixture was degassed by three cycles of freeze–pump–thaw, leaving the solution frozen on the last cycle. Next, a batch of 100 or 200 mg of microcrystalline {Mn-NO} was added to the flask under nitrogen. The solution was then allowed to thaw at room temperature and stirred in the dark for 3 days. The loaded MCM-41 material was collected by filtration using a fritted funnel.

The deep green solid was washed with 5 × 2 mL of acetonitrile and 3 × 3 mL of THF. At the end of the repeated washings, the filtrate contained no detectable amount of {Mn-NO} as discerned by electronic absorption spectroscopy. Finally, the light green powder was dried in vacuo.

3.7.4 Analysis of the Manganese Content of {Mn-NO}@MCM-41

An acid digest procedure modified from the protocol described by Yang and co-workers was used to determine the manganese content of the loaded materials. [43] Batches of 25 mg of the {Mn-NO}@MCM-41 samples were added to the Teflon vessels of autoclave bombs, and to each was added 1 mL of a 1:3 mixture of concentrated HNO_3 and HCl. The samples were then frozen by dipping the vessels in liquid N_2 before the addition of 0.125 mL of 40% aqueous HF to each vessel. Following addition of HF, the vessels were immediately sealed and allowed to warm to room temperature before placing them in a 150 °C oven for 4 h. Next, the vessels were allowed to cool to room temperature, and 12.5 mg of boric acid was added to each sample solution to complex free F^-. Finally, the samples were diluted to 50 mL using Millipore water containing 1% HNO_3 and transferred to a polypropylene flask for analysis. The total Mn content of each digest solution was measured by flame atomic absorption spectroscopy (FAAS) or inductively coupled plasma-optical emission spectroscopy (ICP-OES). To test the batch-to-batch consistency and the accuracy of the reported loading values for each formulation of the host−guest material, two separate batches of each formulation were synthesized and digested separately, and the Mn content of one digest was measured (in triplicates) by FAAS and the other by ICP-

OES. FAAS measurements were performed on a Perkin-Elmer AAnalyst100 with a hollow cathode lamp and filter set to the Mn absorption line of 279.5 nm. The slit width was set to 0.2 nm, and the nebulized digest solution was sent through a nitrous oxide–acetylene flame. ICP-OES measurements were performed on a PerkinElmer Optima 4300DV utilizing the Mn emission line at 259.372 nm and a slit width of 0.2 nm.

3.7.5 Leaching of {Mn-NO} from {Mn-NO}@MCM-41

The extent of the loss of the nitrosyl from the host was checked as follows. Vials containing 5 mg portions of $\{Mn\text{-}NO\}_{200}$@Si-MCM-41 or $\{Mn\text{-}NO\}_{200}$@Al-MCM-41 in 1 mL of 137 mM saline solution were gently agitated for a total time of 24 h. Aliquots of 10 μL were taken from each test solution at various time intervals and brought to 10 mL with Milli-Q water containing 1% HNO3. Following filtration through a 0.2 μm filter, the Mn content of each sample was determined by ICP-OES analysis. The amount of leached Mn from $\{Mn\text{-}NO\}_{200}$@Si-MCM-41 or $\{Mn\text{-}NO\}_{200}$@Al-MCM-41 for each time point was determined by averaging their values from three independent runs. The leaching of the photoproduct of {Mn-NO} left in the MCM-41 pores after NO photorelease was also examined. First, samples of {Mn-NO}@MCM-41 were completely photobleached via illumination for 2 h. The completion of this process was confirmed with a NO-specific electrode. Leaching of the Mn-photoproduct (with no bound NO) from such photolyzed samples of $\{Mn\text{-}solv\}_{200}$@Si-MCM-41 and $\{Mn\text{-}solv\}_{200}$@Al-MCM-41 (solv = solvent) in saline solution was then tested by following the procedure described above.

3.7.6 Spectroscopic Measurements

Infrared spectra of the materials (in KBr disks) were recorded on a Perkin-Elmer Spectrum-One FT-IR spectrometer. The absorption spectra were monitored with a Varian Cary 50 spectrophotometer. UV−vis diffuse reflectance spectra (DRS-UV-vis) of Si-MCM-41, Al-MCM-41, $\{Mn\text{-}NO\}_{200}$@Si-MCM-41, and $\{Mn\text{-}NO\}_{200}$@Al-MCM-41 were obtained by using a Varian Cary 5000 UV−vis−NIR spectrophotometer (Harrick Praying Mantis diffuse reflectance cell attachment, BaSO4 standard). Samples of each material (~20 mg) were spread on a bed of BaSO4. The reflectance data was analyzed using the Kubelka−Monk function, and the output of the function was plotted versus the wavelength.

3.7.7 Other Measurements

The structural order of the materials over long-range was assessed by powder X-ray diffraction (PXRD). These measurements were carried out with a Rigaku SmartLab powder diffractometer at a scan rate of 1.5 deg s−1 and step size of 0.02 deg. A Micromeritics ASAP 2020 Accelerated Surface Area and Porosimetry Analyzer was used to acquire the nitrogen adsorption and desorption isotherms (at 77 K) of $\{Mn\text{-}NO\}_{200}$@Si-MCM-41 and $\{Mn\text{-}NO\}_{200}$@Al-MCM-41 samples (run in triplicates). ~30 mg batches of the materials were first evacuated at 573 K for 4 h before the measurements. Specific surface areas were calculated using the Brunauer-Emmett-Teller (BET) method while the Barrett−Joyner−Halenda (BJH) method was used to calculate the pore volume and diameter.[101,102] distributions. The porosity and volume data of unloaded samples were also analyzed and compared with the data supplied by the manufacturer (Sigma-Aldrich). Cross-sectional analysis of the distribution of the various atoms (Si, O, Al, and Mn) in {Mn-NO}200@Si-MCM-41 and {Mn-NO}200@Al-MCM-41 was carried out with the aid of scanning electron microscopy coupled with elemental dispersive X-ray spectroscopy (SEM-EDX). The data were collected on a Hitachi HD-2000 dedicated STEM equipped with an Oxford Inca EDS system. The elemental composition of the analyzed area was determined by the Cliff Lorimer thin ratio quantitation method and normalized by total mass of all measured elements to obtain wt % and atomic % for each element. The TEM images were collected at 200 kV accelerating voltage.

3.7.8 NO Release Profile of {Mn-NO}@MCM-41

The NO release profiles of the loaded materials were recorded with a NO-sensitive electrode (inNO-T NO-measuring system, Harvard Apparatus). Samples of ~10 mg suspension of the {Mn-NO}@MCM-41 in 2 mL of PBS buffer contained in 5 mm diameter vials were used. The release of NO was induced by illumination of the sample with 100 mW/cm^2 light (irradiance intensity measured by a Coherent Field Max II power meter). The samples were exposed to the atmosphere and gently stirred with a microflea stir bar. The tip of the electrode was placed 3 cm above the stir bar, and [NO] was measured at 0.5 s intervals. The amperometric data collected by the electrode were converted into [NO] by calibrating the electrode response during illumination of standard solutions of {Mn-NO} in acetonitrile to the change in concentration of {Mn-NO} by Beer's law analysis at $\lambda = 635$ nm. The reduced concentration of {Mn-NO} was confirmed to be a result of NO photorelease by the growth of the photoproduct band around 800 nm. The conversion factor obtained (pA to nM of NO) through this method was further confirmed by comparing its value with the results of the standard calibration method of NO formation by an acidified nitrite solution as described by the manufacturer. The ability of the NO released from {Mn-NO}@MCM-41 to penetrate a 1.1 mm layer of agar (the thickness of the bacterial suspension used in the antibiotic test described below) was assessed using an agar plate containing a 1.1 mm layer of soft agar with dissolved Griess reagent which turns pink in the presence of NO. Samples (10 or 30 mg) of {Mn-NO}@MCM-41 were evenly spread in the center of the agar plates using a template with a circular opening (2.2 cm in diameter) and illuminated for 30 min. The plates were then visualized for the formation of the pink dye on the surface (and beneath) of the agar. The resulting pink circles on the plates demonstrated very little lateral spreading of the released NO from the sites of application.

3.7.9 Growth Conditions for *A. baumannii* Cultures

Freeze-dried cultures were allowed to thaw and then spread across trypticase soy agar (TSA) plates for growth and isolation single colonies of the bacteria. The TSA plates were grown overnight at 37 °C under aerobic conditions. Following incubation, a single colony was selected, grown in trypticase soy broth (TSB) to an OD600 of 0.63 (Varian Cary 50 spectrophotometer) and frozen as working stocks. The conversion factor for calculating CFU mL−1 from the OD600 for each strain of *A. baumannii* was determined by incubating single-colony isolates in trypticase soy broth (TSB) until OD600 = 0.4 and performing dilutions to achieve a density appropriate for cell counting by a hemocytometer. A conversion factor of 2.9 × 108 CFU mL−1 per unit of OD600 was found for both strains.

3.7.10 Model of Skin and Soft Tissue Infection by *A. baumannii*

Instead of using a typical agar surface inoculated with bacterial colonies for the antibacterial assays, a model of skin and soft tissue infection was designed through a ”bacterial suspension method” , adapted from the procedure of Benjamin and co-workers.[103] First, the working stock was thawed and an aliquot of 100 μL was added to 1 mL of TSB inside an Eppendorf tube. The tube was then placed on a shaker inside a 37 °C incubator and grown to an A600 of 1.40 (late stationary phase). Next, an aliquot of 200 μL of this culture was added to a flask containing 100 mL of “soft brine agar ” (0.8% (w/v) agar and 1.0% (w/v) NaCl) kept in the liquid state by storing it in a water bath maintained at 45 °C. The resultant inoculated liquid agar contained 8.1 × 105 cells mL−1. The liquid agar was gently vortexed to obtain a homogeneous suspension of the bacteria, and 6 mL of the inoculated agar was spread over a TSA plate containing 20 mL of 1.5% (w/v) agar. The soft brine agar suspension was allowed to solidify and the plate was then incubated in a 37 °C incubator for 1 h to allow the microbes to adhere to the agar and form cell-to-cell contacts. Composite agar plates of this kind were used in the bactericidal assays. Bactericidal Assays. The bactericidal efficacy of {Mn-NO}$_{200}$@Al-MCM-41 was examined on both drug-susceptible and multi-drug resistant strains of A. baumannii. The template with a circular opening (ø = 2.2 cm) was employed to facilitate the application of the powdery material to a well-defined area. The template and the {Mn-NO}$_{200}$@Al-MCM-41 powder used in the test were first sterilized by soaking in 70% ethanol followed by drying at room temperature over 30 min. The template was then placed on top of the inoculated composite agar plate and the desired mass of sterile {Mn-NO}$_{200}$@Al-MCM-41 was evenly spread over the exposed area. Following removal of the template, the whole plate was illuminated with 100 mW/cm2 of light for the desired duration. After illumination, the MCM-41 powder was gently washed off from the plate with a sterile saline solution and the treated plates were then incubated at 37 °C for 16 h. Control experiments were run following the same procedure but with photolyzed {Mn-solv}@Al-MCM-41 to assess any bacterial clearing due to the host material or any leached Mn-complex. The bactericidal effect of the NO released from the material was assessed by visually comparing the cellular density of the NO-treated plates against the control plates. When complete clearing of the bacterial load was noted, agar samples from the area of application of the {Mn-NO}@MCM-41 material were homogenized and extracted in fresh growth media, plated, and incubated at 37 °C to ensure the lack of any viable bacteria remaining in the kill-zone.

3.8 References

1. Roggers, R. Kanvinde, S. Boonsith, S. Oupický, D. *AAPS PharmSciTech.* **2014**, *15*, 1163–71.
2. Mura, S. Nicolas, J. Couvreur, P. *Nat. mater.* **2013**, *12*, 990-1003.
3. Torchilin, V. P. *Nat. Rev. Drug Discov.* **2014**, advance online publication doi:10.1038/nrd4333.

4. *Nanoparticulate Drug Delivery Systems.* Thassu, D. Deleers, M. Pathak, Y., Eds.; Informa Healthcare: USA, **2007**.
5. Trapani, G. Denora, N. Trapani, A. Laquintana, V. *J. Drug Target.* **2012**, *20*, 1–22.
6. *Nanoparticulates as Drug Carriers.* Torchilin, V. P., Ed; Imperial College Press: London, **2006**.
7. Jain, R. K. Stylianopoulos, T. *Nature Rev. Clin. Oncol.* **2010**, *7,* 653–64.
8. Rose, M. J. Fry, N. L Marlow, R. Hinck, L. Mascharak, P. K. *J. Am. Chem. Soc.* **2008**, *130*, 8834.
9. Barreto, J. A. O'Malley, W. Kubeil, M. Graham, B. Stephan, H. Spiccia, L. *Adv. Mater.* **2011**, 23, H18-40.
10. Barbe, C. Bartlett, J. Kong, L. Finnie, K. Lin, H. Q. Larkin, M. Calleja, S. Bush, A. Calleja, G. *Adv. Mater.* **2004**, *16*, 1959-65.
11. Avnir, D. Coradin, T. Lev, O. Livage, J. *J. Mater. Chem.* **2006**, *16*, 1013-18.
12. Cheng, X. Chen, D. Liu, Y. *ChemPhysChem*. **2012**, *13*, 2392–404.
13. Li, J. Huo, M. Wang, J. Zhou, J. Mohammad, J.M. Zhang, Y. Zhu, Q. Waddad, A.Y. Zhang, Q. *Biomaterials* **2012**, *33*, 2310–20.
14. Brinker, C.J. *J. Non-Cryst. Solids.* **1988**, *100*, 31–50.
15. Kjellman, T. Alfredsson, V. *Chem. Soc. Rev*. **2013,** *42,* 3777–91.
16. Inagaki, S. Guan, S. Ohsuna, T. Terasaki, O. *Nature* **2002**, *416*, 304–307.
17. Patra, A. K. Rose, M. J. Murphy, K. M. Olmstead, M. M. Mascharak, P. K. *Inorg. Chem.* **2004**, *43*, 4487.

18. Rosenholm, J. M. Sahlgren, C. Lindén, M. *Nanoscale* **2010**, *2*, 1870–83.
19. Rosenholm, J. M. *Modular design of mesoporous silica materials: towards multifunctional drug delivery systems,* doctoral dissertation in physical chemistry; Faculty of Technology, Abo Akademi University, **2008**.
20. Rosenholm, J. M. Lindén, M. *J. Control. Rel.* **2008**, *128*, 157–64.
21. Rosenholm, J. M. Peuhu, E. Bate-Eya, L. T. Eriksson, J. E. Sahlgren, C. Lindén, M. *Small* **2010**, *6*, 1234.
22. Deshpande, R. R. Eckert, H. *J. Mater. Chem.* **2009**, *19*, 3419.
23. Lee, W.F. Chen, Y.C. *J. Appl. Polym. Sci.* **2004**, *91*, 2934-41.
24. Wheatley, P. S. Butler, A. R. Crane, M. S. Fox, S. Xiao, B. Rossi, A. G. Megson, I. L. Morris, R. E. *J. Am. Chem. Soc.* **2006**, *128*, 502−509.
25. Fox, S. Wilkinson, T. S. Wheatley, P. S. Xiao, B. Morris, R. E. Sutherland, A. Simpson, A. J. Barlow, P. G. Butler, A. R. Megson, I. L. Rossi, A. G. *Acta Biomater*. **2010**, *6*, 1515−1521.
26. Shin, J. H. Marxer, S. M. Schoenfisch, M. H. *Anal. Chem.* **2004**, *76*, 4543–49.
27. Storm, W. L. Schoenfisch, M. H. *ACS Appl. Mater. Interfaces* **2013**, *5*, 4904–12.
28. Fang, F. C. *Nitric Oxide and Infection.* Kluwer Academic/Plenum Publishers; New York, **1999**.
29. Halpenny, J. M. Mascharak, P. K. *Anti-Infect. Agents Med. Chem*. **2010**, *9*, 187−97.
30. Fang, F. C. *J. Clin. Invest.* **1997**, *99*, 2818−25.

31. Taubes, G. *Science* **2008**, *321*, 356−61.

32. Sengstock, D. M. Thyagarajan, R. Apalara, J. Mira, A. Chopra, T. Kaye, K. S. *Clin. Infect. Dis.* **2010**, *50*, 1611−1616.

33. Van Looveren, M. Goossens, H. *Clin. Microbiol. Infect.* **2004**, *10*, 684−704.

34. Peleg, A. Y. Seifert, H. Paterson, D. L. *Clin. Microbiol. Rev.* **2008**, *21*, 538−582.

35. Martínez, J. L. Rojo, F. *FEMS Microbiol. Rev*. **2011**, *35*, 768−89.

36. Morgan, D. J. Liang, S. Y. Smith, C. L. Johnson, J. K. Harris, A. D. Furuno, J. P. Thom, K. A. Snyde, G. M. Day, H. R. Perencevich, E. N. *Infect. Control Hosp. Epidemiol.* **2010**, *31*, 716−21.

37. Fournier, P. E. Richet, H. *Clin. Infect. Dis*. **2006**, *42*, 692−99.

38. Center for Disease Control and Prevention. *MMWR Morb. Mortal. Wkly. Rep*. **2004**, *53*, 1063–6.

39. Murray, C. K. Roop, S. A. Hospenthal, D. R. Dooley, D. P. Wenner, K. Hammock, J. Taufen, N. Gourdine, E. *Mil. Med*. **2006**, *171*, 826−29.

40. Scott, P. Deye, G. Srinivasan, A. Murray, C. Moran, K. Hulten, E. Fishbain, J. Craft, D. Riddell, S. Lindler, L. Mancuso, J. Milstrey, E. Bautista, C. T. Patel, J. Ewell, A. Hamilton, T. Gaddy, C. Tenney, M. Christopher, G. Petersen, K. Endy, T. Petruccelli, B. *Clin. Infect. Dis*. **2007**, *44*, 1577−84.

41. Halpenny, G. M. Gandhi, K. R. Mascharak, P. K. *ACS Med.Chem. Lett*. **2010**, *1*, 180−183.

42. Heilman, B. J. Halpenny, G. M. Mascharak, P. K. J. *Biomed. Mater. Res., Part B* **2011**, *99B*, 328−337.

43. Chao, K. J. Chen, S. H. Yang, M. H. *Fresenius' Z. Anal. Chem*. **1988**, *331*, 418−22.
44. Kotz, L. Kaiser, Tschöpel, P. Tölg G. *Z. Anal. Chem.* **1972**, *260*, 207-9.
45. Stathi, P. Dimos, K. Karakassides, M. A. Deligiannakis, Y. *Journal of Colloid and interface science.* **2010**, *343*, 374–80.
46. Meng, S. Gao, S. *The Journal of Chemical Physics* **2006**, *125*, 014708.
47. Ong S. W. Zhao, X. L. Eisenthal, K. B. *Chem. Phys. Lett.* **1992**, *191*, 327-35.
48. Dong, Y. Pappu, S. V. Xu, Z. *Anal. Chem.* **1998**, *70*, 4730-5.
49. Fan, H. Li, F. Zare, R. N. Lin, K. *Anal. Chem.* **2007**, *79*, 3654-61
50. Borade, R. B. Clearfield, A. *Catal. Lett.* **1995**, *31*, 267-72.
51. Giraldo, L. Moreno-Piraján, J.C. *Mater. Res.* **2013**, *16*, 745-54.
52. Queiroz, T. B. Botelho, M. B. S. Fernandez-Hernandez, J. M. Eckert, H. Albuquerque, R. Q. Camargo, A. S. S. *J. Phys. Chem. C* **2013**, *117*, 2966−75.
53. Parry, E.P. *J. Catal*. **1963**, *2*, 371-79.
54. Lewis, D. L. Estes, E. D. Hodgson, D. J. *J. Cryst. Mol. Struct.* **1975**, *5*, 67-74.
55. Duraczyńska, D. Serwicka, E. M. Drelinkiewicz, A. Rutkowska-Żbik, D. Witko, M. Socha, R. Zimowska, M. Olejniczak, Z. *App. Catal. A.* **2012**, *427–428*, 16–23.
56. Duraczynska, D. Serwicka, E. M. Waksmundzka-Gora, A. Drelinkiewicz, A. Olejniczak, Z. *J. Organomet. Chem.* **2008**, *693*, 510-18.
57. Xu, Q. Li, L. Liu, X. Xu, R. *Chem. Mater.* **2002**, *14*, 549-55.

58. Thommes, M. *Physical adsorption characterization of ordered and amorphous mesoporous materials in Nanoporous Materials- Science and Engineering.* Max Lu, X.S Zhao, eds. Imperial College Press; London: **2004**.

59. Kresge, C. T. Leonowicz, M. E. Roth, W. J. Vartuli, J. C. Beck, J. S. *Nature* **1992**, *359*, 710−2.

60. Kärger, J. Valiullin, R. *Chem. Soc. Rev.* **2013**, *42*, 4172.

61. Thommes, M. Köhn, R. Fröba, M. *J. Phys. Chem. B* **2000**, *104*, 7932–7943.

62. M. Thommes, B. Smarsly, M. Groenewolt, P. I. Ravikovitch A. V. Neimark, *Langmuir*, **2006**, *22*, 756–764.

63. Coasne, B., Galarneau, A. Roland, J. M. Di Renzo, F. *Chem. Soc. Rev.* **2013**, *42*, 4141-71.

64. A. P. Malanoski and F. Van Swol, Phys. Rev. E: Stat., Nonlinear, Soft Matter Phys., 2002, 66, 041603.

65. Page, J. H. Liu, J. Abeles, B. Herbolzheimer, E. Deckmann, W. A. Weitz, D. A. *Phys. Rev. E.* **1995**, 52, 2763.

66. Benoit Coasne, Anne Galarneau, Roland J. M. Pellenq and Francesco Di Renzo *Chem. Soc. Rev.* **2013**, *42*, 4141.

67. H Wanyika, E Gatebe, P Kioni, Z Tang, Y *Gao Proceedings of the 2011 Jkuat Scientific, Technological and Industrialization Conference*. **2011,** ***36.***

68. Kruk, M. Jaroniec, M. Sayari, A. *Langmuir*, **1997**, *13*, 6267–73.

69. Sing, K. S. W. Everett, D. H. Haul, R. A. W. Moscou, L. Pierotti, R. A. Rouquerol, J. Siemieniewska, T. *Pure Appl. Chem.* **1985**, *57*, 603.

70. Breck, D. W. Zeolite Molecular Sieves; Wiley: New York, 1974.

71. Bottinelli, E.; Miletto, I.; Caputo, G.; Coluccia, S.; Gianotti, E. J. *Fluoresc*. 2011, 21, 901−909.

72. Marler, B. Oberhagemann, U. Vortmann, S. Gies, H. *Microporous Mater.* **1996**, *6*, 375–83.

73. Rogojevic, S. Jain, A. Gill, W.N. Plawsky, J. *Electrochem. Solid-State Lett.* **2002**, *5,* F22–F23.

74. Ghaffari, A. Neil, D.H. Ardakani, A. Road, J. Ghahary, A. Miller, C.C. Nitric Oxide,2005, 12, 129-140.

75. Ghaffari, A. Miller, C.C. McMullin, B. Ghahary, A. Nitric Oxide,2006, 14, 21-29.

76. Keynes, R. G. Griffiths, C. Garthwaite, J. Biochem. J. 2003, 369, 399–406.

77. Soares, N. C. Cabral, M. P. Gayoso, C. Mallo, S. Rodriguez- Velo, P. Fernandez-Moreira, E. Bou, G. J. Proteome Res. 2010, 4, 1951–1964.

78. CLSI. Performance Standards for Antimicrobial Disk Susceptibility Tests; Approved Standard—Eleventh Edition. CLSI document M02-A11. Wayne, PA: Clinical and Laboratory Standards Institute; **2012**.

79. Maton, A, Hopkins, J, McLaughlin, C. W., Johnson, S, Warner, M. Q., LaHart, D, et al. Human Biology and Health; Prentice Hall:Englewood Cliffs, **1993**.

80. Moreillon, P. Que, Y. A. *Lancet* **2004**, *363*, 139−149.

81. Choi, C. H. Lee, J. S. Lee, Y. C. Park, T. I. Lee, J. C. *BMC Microbiol.* **2008**, *8*, 216.

82. Barker, J. *J. Med. Microbiol.* **1975**, *8*, 443−446.

83. Mitchell, A.J. Wimpenny, J.W.T. *J. App. Microbio.* **1997**, *83,* 76–84.

84. Gottrup, F. *World J. Surg.* **2004**, *28*, 312−315.

85. King, P. Citron, D. M. David, C. Griffith, D. C. Lomovskaya, O. Dudley, M. N. *Diagn. Microbiol. Infect. Dis.* **2010**, *66*, 181−186.

86. Bentrup, K. H. Russell, D. G. *Trends Microbio.***2001**, *9*, 597–605.

87. Mukerji, S. *J. Clin. Pathol.* **1984**, *37*, 103.

88. Jacobs, A. C. Sayood, K. Olmsted, S. B. Blanchard, C. E. Hinrichs, S. Russell, D. Dunman, P. M. *FEMS Immun. Med. Microbio*. **2012**, *64* 403–12.

89. Fernando, D. Kumar, A. *J. Antimicrob. Chemo.* **2011**: doi:10.1093/jac/dkr519.

90. Zinder, S. Dworkin, M. In *The Prokaryotes*; Rosenberg, E. DeLong, E. Lory, S. Stackebrandt, E. Thompson, F. Eds. Springer: Berlin Heidelberg, **2013**; 89–122.

91. Skiebe, E. de Berardinis, V. Morczinek, P. Kerrinnes, T. Faber, F. Lepka, D. Hammer, B. Zimmermann, O. Ziesing, S. Wichelhaus, T. A. Hunfeld, K.-P. Borgmann, S. Gröbner, S. Higgins, P. G. Seifert, H. Busse, H.-J. Witte, W. Pfeifer, Y. Wilharm, G. *Int. J. Med. Microbio.* **2012**, *302*, 117–128.

92. de Orué Lucana, D. O. Groves, M. R. *Amino Acids* **2009**, *37*, 479−486.

93. Croze, O.A. Ferguson, G. P. Cates, M.E. Poon, W.C.K *Biophys J.* **2011**, *101*, 525–534.

94. Schertzer J.W., Brown S.A., Whiteley M. *Mol. Microbiol.* **2010**, *77*, 1527–1538.

95. Shekhter, A. B. Serezhenkov, V. A. Rudenko, T. G. Pekshev, A. V. Vanin, A. F. *Nitric Oxide* **2005**, *12*, 210-19.

96. Ostomel, T.A. Shi, Q. H. Stucky, G.D. *J. Am. Chem. Soc.* **2006**, *128*, 8384–5.

97. Wu, X. Wei, J. Lu, X. Lv, Y. Chen, F. Zhang Y. Liu, C. *Biomed. Mater.* **2010**, *5*, 035006.

98. De Palma, C. Clementi, E. *Mol. Neurobiol.* **2012**, *46*, 682-92

99. Baldik, Y. Talu, U. Altinel, L. Bilge, H. Demiryont, M. Aykac-Toker, G. *Clin. Orthop. Relat. Res.* **2002**, *404*, 343-52.

100. Committee on Tactical Combat Casualty Care. *Tactical combat casualty care guidelines, October 28, 2013*. http://www.naemt.org/Files/TCCC/041114/TCCC%20Guidelines_131028.pdf Accessed September 12, 2014.

101. Brunauer, S. Emmett, P. H. Teller, E. *J. Am. Chem. Soc.* **1938**, *60*, 309−19.

102. Barrett, E. P. Joyner, L. G. Halenda, P. P. *J. Am. Chem. Soc*. **1951**, *73*, 373−80.

103. Hardwick, J. B. J. Tucker, A. T. Wilks, M. Johnston, A. Benjamin, N. A. *Clin. Sci.* **2001**, *100*, 395.

Chapter 4

Selective Damage to the Hyphal Form of *Candida albicans* by the Light-Controlled Delivery of Nitric Oxide

4.1 Background

Candida albicans is a polymorphic fungus that causes opportunistic infections in humans.[1] *C. albicans* is isolated only from human and animal sources where it can grow in several morphological forms. These include an ovoid budding yeast, as elongated ellipsoid cells that remain attached at a constricted septum (pseudohyphae), as elongated parallel-sided true hyphae (or filamentous form), and as a spore-like form (chlamydospores) that have a thick cell wall.[2] *C. albicans* also undergoes phenotypic switching between white and opaque morphologies – an event which is important for mating and biofilm formation.[3] Until recently, it was thought that *C. albicans* did not have a sexual form (haploid cells), but the progression of our knowledge (largely due to genetic studies) regarding the sexual development and sporulation of C. albicans has ushered in the possibility of using mating techniques to unravel the genes that cause disease.[3] Since *C. albicans* and other fungal pathogens are eukaryotic diploids, they share many of the same basic biochemical pathways as their human hosts. This genetic similarity complicates the development of fungicides that discriminate between human and fungal target enzymes or biochemical steps and has limited the number of available low-toxic, broad-spectrum antifungal medications.

As a commensal organism in 50-80% of the population, *C. albicans* colonizes mucous and cutaneous membranes without eliciting an immune response from the host. However, at opportunistic times, such as reduced host immunocompetency or reductions in the number of microbial competitors as a result of antibacterial therapy, the fungus will initiate an infectious growth process that begins with a morphological switch to a polarized hyphal growth form that is capable of penetrating colonized epidermal or epithelial membranes.[4] The switch of cellular morphologies by *C. albicans* is sensed by host cells by the recognition of epitopes specific to the hyphal cell wall causing the release of pro-inflammatory cytokines. However, if the host immune response is insufficient or the inoculum size is large enough, the infection progresses. Due to the increasing population of immunocomprised and hospitalized individuals, opportunistic infections by fungal pathogens (*C. albicans* being the most common etiological agent) have recently emerged as a major health concern with the rate of mycoses (fungal sepsis) in the United States increasing nearly 207% from 1979 to 2000.[5] The severity of such infections also dramatically increased during this time with number of lethal cases increasing from 1,557 in 1980 to 6,534 in 1997.[3] Despite the current availability of antifungal medications and the continued effort of researchers to gain a better understanding of fungal pathogenesis, the treatment of systemic mycosis continues to have a high failure rate, as high as 30-50%.[6]

The transition between yeast and hyphal polymorphs by *C. albicans* is tightly regulated by a network of signal transduction pathways that respond to micro-environmental cues within the host making morphological switching an important virulence factor for the fungus.[7] The signaling pathways that regulate morphological switching by *C. albicans* identified thus far include a cAMP-protein kinase A (cAMP-PKA) pathway,[8] a mitogen-activated protein kinase (MAPK) pathway,[9] a cell cycle arrest pathway,[10] and a pH response pathway.[11] These pathways become activated by hyphal-inducing environmental cues such as temperature (37°C),[12] blood serum,[13] physiological CO_2 (P_{CO2} = 5%, partial pressure of CO_2 in blood),[14] neutral or alkaline pH,[12] N-acetyl-D-glucosamine,[15] nutrient limitation,[16] and the presence of amino acids.[17] The yeast-to-hypha conversion is critical for systemic infections, a premise that has been reinforced by the inability of local infections by C. albicans mutants defective in hyphal formation to spread to new tissue.[7] The hyphal form of *C. albicans* is so well-adapted for its role during infection that it can induce endocytosis by epidermal and epithelial cells by expression of the invasion, Als3, which binds cadherin and induces endocytosis so that the pathogen can rapidly bypass mucosal and cutaneous membranes, a mechanism called transcytosis. In addition to the active virulence factors discussed so far, hyphal growth-related genes are also involved in biofilm formation, an important mechanism to increase the tolerance of the organism to various antifungal agents *in vivo.*[18]

A detailed understanding of the role of hyphal morphogenesis in the early processes of opportunistic infection by previously commensal populations of *C. abicans* has been achieved using *in vitro* systems mimicking infections of the human body as closely as possible.[22,] Dietrich and coworkers have monitored the progression of candidal infection in a keratinized cutaneous model (3D collagen matrix supplemented with fetal bovine serum containing a basal fibroblast layer and seeded with human epidermal cells) with a clinical isolate; a Δefg1 null mutant, competent in pseudohyphal morphogenesis but unable to form true hyphal cells; and a Δcph1 Δefg1 null mutant, incompetent in pseudohyphal and hyphal morphogenesis.[22,23] As shown in Figure 4.1 left panel, the clinical isolate strongly adhered to the outer layer of the epithelial cells in the cutaneous model and penetrated the stratified epidermal layers with a large number of elongated hyphae. Small groups of yeast cells are observed in the basal fibroblast layer beneath the epidermal layers, possibly by navigating the paths of hyphal cells but may represent daughter cells, budded off an already penetrated hyphal cell. The Δcph1 Δefg1 mutant strain remained in the yeast form after inoculation and was unable to penetrate the epithelial layer. The Δcph1 Δefg1 mutant also showed greatly attenuated adhesion to epithelial cells after the same washing procedure applied to the hyphal and pseudohyphal competent strains. The pseudohyphal competent strain, Δefg1, was unable to penetrate the squamous layer of the epidermal equivalent but was able to penetrate an analogously constructed epithelial model of the intestine.[24] This may be due to the lack of active transport by keratinized cells on the surface of the

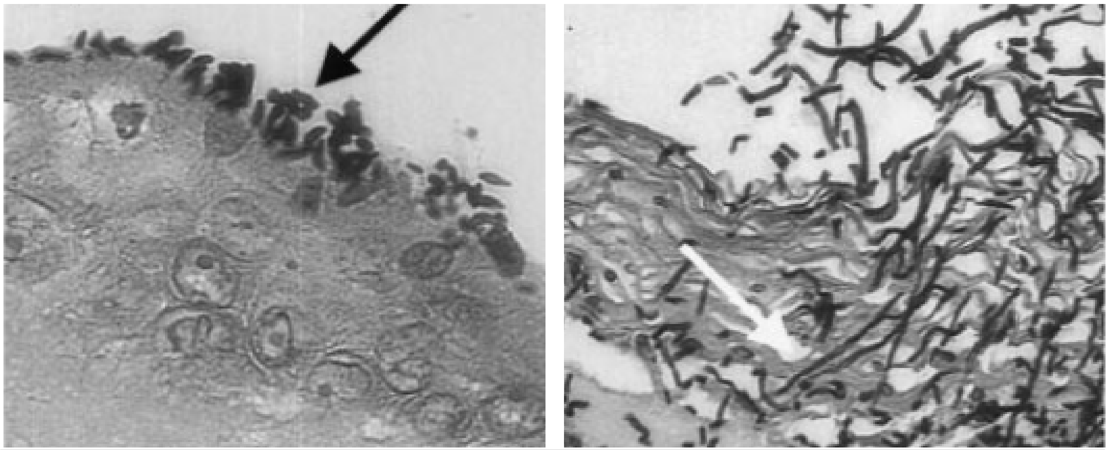

Figure 4.1. Infection of a reconstructed skin equivalent with *C. albicans* wild-type (right) and *Δcph1 Δefg1* null mutant (right) lacking necessary factors for hyphal or pseudohyphal morphogenesis. The wild-type strain penetrates the protective keratinocytic layer and invades through the epidermal layer into the fibroblast seeded basal layer, causing severe damage to the model system. (200x magnification). (Left) *Δcph1 Δefg1* null mutant is locked in the yeast and unable to penetrate or to damage the epidermal equivalent. (400x magnification)

epidermis which would prevent transcytoses, potentially the only mechanism available to pseudohyphal cells (which lack the range of proteases expressed by hyphal cells) to penetrate tissue membranes.

Whole blood and blood serum is one of the most robust cues for hyphal growth causing almost immediate hyphal morphogenesis (42% of cells within 30 min).[25] Interestingly, neutrophils which are abundant in the blood are able to repress hyphal formation by *C. albicans* in whole blood and fractions (80% yeast in whole blood containing normal neutrophil counts).[26] Removal of the neutrophil fraction of blood restored hyphal formation in 83% of all cells while co-incubation of neutrophils with *C. albicans* in hyphal-inducing blood plasma repressed hyphal formation in 95% of cells. It would appear as if neutrophil activity instead of any regulatory program of *C. albicans* controls the morphology of the fungus in the blood since hyphal formation would confer several advantageous for the fungus to increase its survival and dissemination in the blood: (1) factors secreated from hyphal cells have the potential to inhibit killing by neutrophils, (2) hypha formation could help the fungus escape from monocytes after phagocytosis, and (3) hyphal cells demonstrate enhanced adhesion to endothelial cells and are able to penetrate the endothelial membrane allowing escape from the blood, and (4) hyphal (not yeast) cells are capable of invading the tissue outside the endothelium.[25] It is known that neutrophils are the major mediator of the host immune response against systemic candidiasis and furthermore, associate with and endocytose hyphal cells at a rate four times greater than yeast cells. This raises the question of whether *C. albicans* self-regulates hyphal formation in the blood to minimize neutrophil response during septicemia. On the other hand, the ability of epithelial cells to distinguish between the invasive hyphal form and the yeast form, and activate the inflammasome in response to infectious growth by *C. albicans* but not during colonization seems to validate the hypothesis that factors produced by host cells could regulate the morphology of *C. albicans* in the blood. Nitric oxide (NO) is produced in conjugation with reactive oxygen species by host immune cells against infectious *C. albicans* and has been reported to inhibit the yeast-to-hyphal transition.[27,28]

Therapeutics that target pathogen specific virulence factors have been suggested as a new model for antimicrobial design that will stop the increasingly rapid development of strains that show resistance to new drug agents.[29] Targeting virulence factors instead of essential biological processes will eliminate the selective pressure associated with cytotoxic treatments. Antimicrobial therapies that interfere with essential biological processes.[30] Since there are a plethora of known small molecule inhibitors of morphological switching, this particular virulence factor is a very attractive option for specifically controlling *C. albicans* infections.[31] Proof of principle experiment have already demonstrated that blocking filamentation in *C. albicans* by means of gene deletion attenuates the virulence of this pathogen *in vivo*.[32] Often superficial candidiasis produces symptomatic infection due to neutrophil infiltration and is more effectively treated as an overly aggressive immune response. Since hyphal cells trigger a more robust immune response than yeast, treatments that inhibit the morphogenesis of hyphal cells could provide relief to individuals suffering from recurrent candidiasis. *C. albicans* is implicated in a number of common, superficial infections of the cutaneous and mucosal surfaces (such as candidal vulvovaginitis, affecting 1 of 3 women, and oral candidiasis, affecting two thirds of immunocompromised patients) that could be successfully treated with the appropriate inhibitor of hyphal formation.[33]

It has been demonstrated that NO production by the inducible NO synthase (iNOS) enzyme of phagocytic cells has candidacidal activity.[34] Ghaffari *et al* have shown that NO is effective against *C. albicans* even though the fungus possesses a highly inducible NO defense mechanism. Schoenfisch et al. have demonstrated the efficacy of surface-generated NO against C. albicans adhesion and biofilm formation on implanted medical devices such as indwelling catheters.[35] In burn victim units, aggressive C. albicans invasion is a serious concern. In a recent paper, Martinez et al. have reported the successful use of a NO-donating nanoparticle to treat infected burn wounds in a murine model.[36] Since NO maintains skin tissue homeostasis and aids in wound healing,[37] the NO-donating nanoparticles produced excellent healing along with strong fungicidal effects.

During the past few years, our laboratory has been engaged in developing designed metal nitrosyls (NO complexes of transition metals) that could be employed to deliver NO to biological targets under the exclusive control of light. Very recently, the photoactive NO donor, $[Mn(PaPy_3)(NO)]^+$ (denoted as {Mn-NO}) has been incorporated within the columnar pores of biocompatible Al-MCM-41 type material[38] and the powder (abbreviated as {Mn-NO}@Al-MCM-41 hereafter) has been employed to successfully eradicate multidrug-resistant strains of *Acinetobacter baumannii*.[39] The excellent antimicrobial activity of the {Mn-NO}@Al-MCM-41 powder raised our curiosity regarding the possibility of use of this composite material against *C. albicans* infection. Herein we report that the {Mn-NO}@Al-MCM-41 composite does exhibit strong NO-induced antifungal activity in vitro and the antifungal activity can be controlled in a dose-dependent fashion through illumination. In addition, our results indicate that more invasive hyphal form of *C. albicans* exhibits enhanced sensitivity to NO compared to the yeast form.

3.2. NO-donating materials: {Mn-NO}@Al-MCM-41 and PUX-NO

Since NO exists as a free radical gas in its pure form, NO releasing vehicles were utilized to investigate the cytotoxic effects of NO on the yeast, pseuodohyphal, and hyphal morphotypes of *C. albicans* as well as genetic mutants of the model organism *S. cerivisea.* The aluminosilicate based mesoporous material, {Mn-NO}@Al-MCM-41, developed by us and discussed in Chapter 2 is capable of producing high fluxes of NO under the complete control of visible light. NO release from the material results from the photo-activation of a pore confined metal nitrosyl, $[Mn(PaPy_3)(NO)]^+$, entrapped within a chemically and biologically inert aluminosilicate MCM-41 type framework. The Mn nitrosyl was synthesized as a perchlorate salt according to the published methods.[40] The cationic nitrosyl and its doubly charged photoproduct ($[Mn(PaPy_3)(H_2O)]^{2+}$) are held within the mesopores by an electrostatic interaction with negatively charged tetrahedral Al sites (3 mol%)

incorporated into the Al-MCM-41 silica framework and demonstrate negigble leaching of the Mn guest molecules under physiological conditions (less than 5% after 24 h in 137 mM NaCl). The amount of {Mn-NO} loaded by the porous Al-MCM-41 host material using the published method was estimated by measuring the concentration of {Mn-NO} remaining in the soak solution after the loading process and the amount of desorbed {Mn-NO} collected by the washing solutions. The {Mn-NO} content of the {Mn-NO}@Al-MCM-41 material used in the present study using this technique was 25 wt% {Mn-NO} which corresponds well with the value obtained by ICP-OES analysis of acid digested {Mn-NO}@Al-MCM-41 (23.1(3) wt% {Mn-NO}).[39]

The NO release profile of {Mn-NO}@Al-MCM-41 was measureed using a NO-specific electrode. The measurements were performed using the same dose (16 mg) of {Mn-NO}@Al-MCM-41 as the *C. albicans* assays. Illumination of the suspended {Mn-NO}@Al-MCM-41 particles in an aqueous solution produced a steady concentration of 130 μM of NO for at least 40 min. After 1 h of illumination, the previously green tinged material lost all color indicating complete photolysis of {Mn-NO} as a result of the photochemical reaction:

$$[\mathrm{Mn(PaPy_3)(NO)}]^+ + h\nu + \text{solvent} \rightarrow [\mathrm{Mn(PaPy_3)(H_2O)}]^{2+} + \text{solvent} \ (1)$$

The total amount of NO released from the 16 mg of sample of {Mn-NO}@Al-MCM-41 was 7.1(4) μmol after1 h of illumination, as determined by the Griess reagent.

The ability of the photoreleased NO from {Mn-NO}@Al-MCM-41 to penetrate a 1.1 mm layer of agar (the thickness of the fungal suspension used in this study) was assayed by dissolving the Griess reagent – a pro-fluorescent NO reporter mixture - in a 1% agar solution prior to casting into a 1.1 mm thick top agar layer. A batch of 16 mg of {Mn-NO}@Al-MCM-41 powder was evenly spread at the center of the Griess agar plate using a template with a circular opening (ø of 2.2 cm) and illuminated for 20 min. Visualization of the area and depth of pink azo dye formation allowed assessment of the diffusion of photoreleased NO from its photochemical source. A color filtered photograph of the Griess agar plate is shown in Figure 4.2. NO diffusion as measured by the Griess reagent was limited to an area of 100 mm in diameter, considerably different than the speculated 100 µm RMS distance of NO diffusion *in vivo*. The agar directly underneath the film turned pale yellow due to oxidative bleaching of the azo dye in the presence of high concentrations of NO or NO oxidation products. The

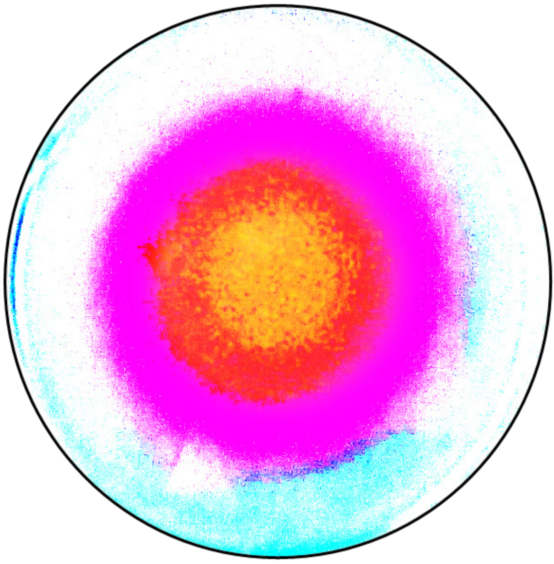

Figure 4.2 Color filtered image of a Griess agar plate showing the diffusion of photoreleased NO from **PUX-NO** films. Formation of a pink azo dye from the reaction of the Griess reagent with nitrite (oxidation product of NO formed at a constant rate under aerobic conditions) serves as an indicator for NO.

bleaching of the dye was confined to a small area that extended just outside the 22 mm application site due to the rapid consumption of NO shortly after photorelease. Care must be taken when extending these observations to the effect of NO on dense microbial populations due to the rapid consumption of NO by microbial detoxification mechanisms and the reaction of NO with biological molecules.

The synthesis, characterization, and light-controlled antibacterial properties of **PUX-NO** films have been previously reported by this laboratory.[41] The films were constructed by trapping {Mn-NO} in amorphous silica xerogel particles and casting those particles in a medical grade polyurethane film. The hybrid material demonstrated potent antibacterial effects against a broad spectrum of gram-positive and gram-negative pathogens when exposed to mW levels of visible light. PUX-NO films were synthesized for this work according to the published methods and used for the delivery of NO to wild-type strain Y190, and deletion mutants ΔYHB1 and ΔSSU1 of *S. cerevisiae* grown on top of YPD agar in order to assess the influence of these genes on the nitrosative stress tolerance of this model organism. In addition, these antimicrobial studies provide a proof-of-performance assessment of the ability of the NO-releasing materials to deliver a specific amount of NO *i.e.* an amount that is 100% lethal to the NO susceptible organsims and >100% lethal to tolerant microbes.

4.3. Growth Conditions for *C. albicans and S. cerevisiae*

C. albicans was grown in liquid broth and solid agar under specific conditions and with various supplements to induce the growth of a single morphology. The literature describes a variety of methodologies to induce the growth of C. albicans in a single, pure phase using liquid growth media.[42] Growth of *C. albicans* on solid medium, such as solid Spider medium, induces robust hyphal morphogenesis in the absence of other hyphal inducing stimuli.[43] Here we describe a unique method for the growth of morphologically pure cultures of *C. albicans* suspended in a 1% agar matrix.

4.3.1 Morphologically Selective Growth of *C. albicans* in Liquid Media

Due to the difficulty in growing morphologically pure preparations of pseudohyphal cells for study, a unique method reported by Hornby and coworkers was used to induce pseudohypha formation.[44] Following the method of Hornby, an overnight culture of *C. albicans* in YPD was transferred to modified GPP broth (containing the hyphae inducer N-acetyl-D-glucosamine) that was supplemented with 1:1 KH_2PO_4/K_2HPO_4 to achieve final concentrations in the range of 10-800 mM $[PO_4^{3-}]$. The growth of pseudohyphal cells was dominate at phosphate concentrations of 300 mM and above. However, the mycelia grown with 300 mM $[PO_4^{3-}]$ was quite elongated compared to the short, thick mycelia grown with 600 mM $[PO_4^{3-}]$, Figure 3.4 panels A and B, respectively. Concerns over the influence of such high $[PO_4^{3-}]$ on the antimicrobial effects of NO on *C. albicans* were raised based on a report by Gow and coworkers on the binding of NO to protein metal centers in the presence of elevated concentrations of phosphate.[45] Based on the hyperfine structure of the EPR spectrum of partially ligated oxy-hemoglobin, it was determined that a high phosphate concentration (100 mM) perturbs the allosteric modulation of ligand affinity by disfavoring the relaxed [R (oxy)] structure. Given the effect of 100 mM $[PO_4^{3-}]$ on the binding activity of hemoglobin, the enzymatic activity of the structurally similar flavohemoglobin protein, nitric oxide dioxygenase, may be affected if the high extracellular [PO_4^{3-}] resulted in a dramatic change of the normal intracellular concentration of ~15 mM [PO_4^{3-}].[46] Since NO dioxygenase *is* a major mediator of the nitrosative stress response of *C. albicans*, the effect of NO on *C. albicans* could be modulated in the presence of such high [PO_4^{3-}] in the growth medium.

4.3.2 Morphologically Selective Growth of *C. albicans* in Soft Agar

Growth media and conditions described by Sudbery were investigated to induce the growth of a single morphotype of *C. albicans.*[47] For this method, the pH of YPD media and the incubation Sudbery were successfully reproduced for hyphal and yeast growth but produced less robust pseudohyphal growth compared to that obtained by the elevated phosphate method of Hornby.[44] The method of Sudbery was modified for solid phase growth in the SSTI growth model by pH adjusting the soft brine agar with PIPES buffer and supplementing the soft brine agar with 20% FBS, after autoclaving. Pseudohyphal growth was achieved with satisfactory results by combining the methods of Sudbery and Hornby.[44,47] The growth of morphologically pure cultures of *C. albicans* in the SSTI model was achieved within PIPES buffered soft brine agar supplemented and temperature were optimized to promote the growth of a single polymorph. The results reported by phosphate, pH 5.5 and 35°C; and hyphae promoted with 20% FBS, pH 7 and 37°C. After 24 h of incubation under the described conditions, a full length excision of the soft agar layer was measured incubated as follows: yeast promoted by pH 6 and 30°C; pseudohyphae promoted with 600 mM onto a glass slide and imaged by light microscopy to verify the morphology of the cells. The morphology index (M_i) of Merson-Davies and Odds was used to provide a quantitative means of indexing elongated cells as hyphal ($M_i = 3.4 - 3.8$) or pseudohyphal ($M_i = 2.5 - 3.4$).[48] For each cell, the dimensions l (length), d (maximum cell diameter) and s (diameter at septal junction) were measured using Adobe Photoshop image analysis software and used to calculate M_i, according to the following equation

$$M_i = \frac{d \times s}{l^2} \qquad (2)$$

The septum marks the budding site between mother and daughter cells and consists of an association between proteins and a membrane-bound ring of 10 nm filaments and serves as a secretory passage for the transfer of new cell material from the mother to the daughter cell.[47] The arrows in Panel D of Figure 4.3 show the location of constricted septa between cells in pseudohyphal filaments. The true hyphal cells seen in Panels E and F have continuous, parallel cell walls with minimal variation in the cell diameter along the entire length of the filaments. Visual analysis of the cellular morphology and calculation of the M_i for cells displaying an ambiguous morphology was performed to determine morphological distribution of the cells grown under each of the described conditions after 4 h of incubation. As shown in Figure 4.3., the described growth media and conditions produced excellent morphological selectivity (> 90% for pseudohyphae; > 98% for hyphae and yeast).

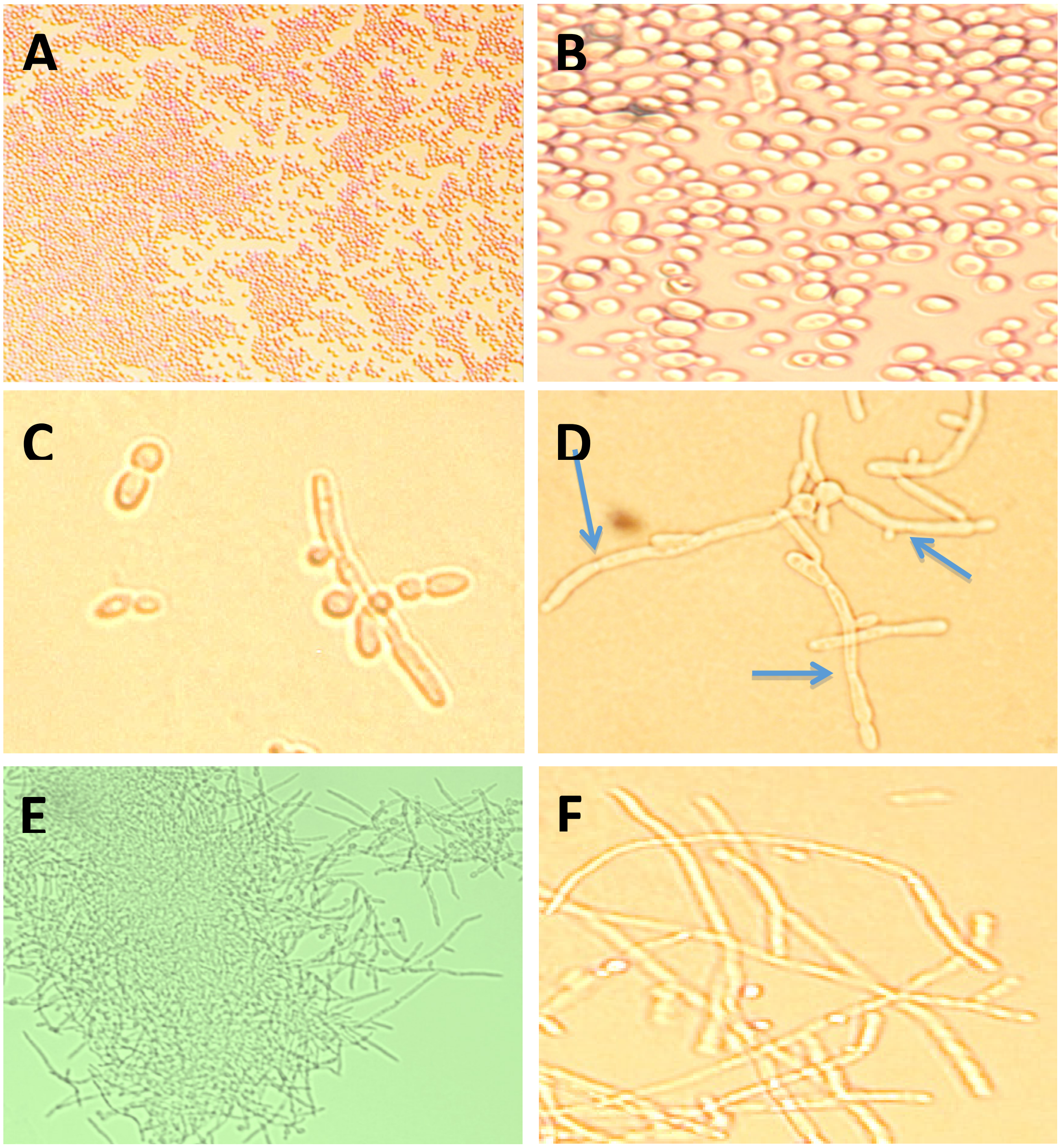

Figure **4.3.** Micrographs of *C. albicans* polymorphs induced under specific conditions in 1.0% (w/v) soft agar cast on top of hard YPD agar plate. Panes A and B yeast form grown at 35ºC in pH 6 (PIPES buffer) soft agar, 20x and 100x magnification, respectively. Panels C and D pseudohyphae grown in soft agar at pH 5.5 and 600 mM phosphate, 50x and 100x magnification, respectively. Arrows indicate constricted septum separating cells.

4.4 Antimicrobial Effect of Photorealeased NO from {Mn-NO}@Al-MCM-41 on *C. albicans*

A skin and soft tissue infection (SSTI) model as described in Chapter 2 was used instead of the standardized disk diffusion and agar dilution assays. In this model, a top agar layer (1% (v/v); 1.1 mm thick) was inoculated with 10^6 CFU mL^{-1} of *C. albicans* and incubated at the designated temperature for 4 h before application of the NO-donor. As the commitment to a cellular morphology usually occurs within 75 min of incubation, the 4 h incubation period allowed for longer mycelium growth and easier differentiation between pseudohyphae and hyphae.[47] As shown in Figure 4.4, application of 10, 14, and 16 mg of {Mn-NO}@Al-MCM-41 (applied evenly at the center of the plates) followed by illumination for 1 h resulted in a dose-dependent eradication of *C. albicans*. A 'kill zone' became apparent at a dose of 14 mg (Panel C) and complete eradication of the fungus was noted with 16 mg of the NO donor (Panel D). The clearing across the entire thickness of the soft agar layer demonstrated that the photoreleased NO exerted its fungicidal effect over the entire inoculated volume. This in turn indicated that NO did travel some distance through the agar layer. The clear "kill zone" in Figure 4.4 panel D also confirmed that the effect of NO was confined within the application zone. As a negative control for NO, a photolyzed sample of the composite material ({Mn-H_2O}@MCM-41) was applied to the surface of an agar plate and illuminated for 1 h (Figure 4.4, panel A). The complete absence of any fungicidal activity demonstrated that the composite without NO has no adverse effect on *C. albicans*.

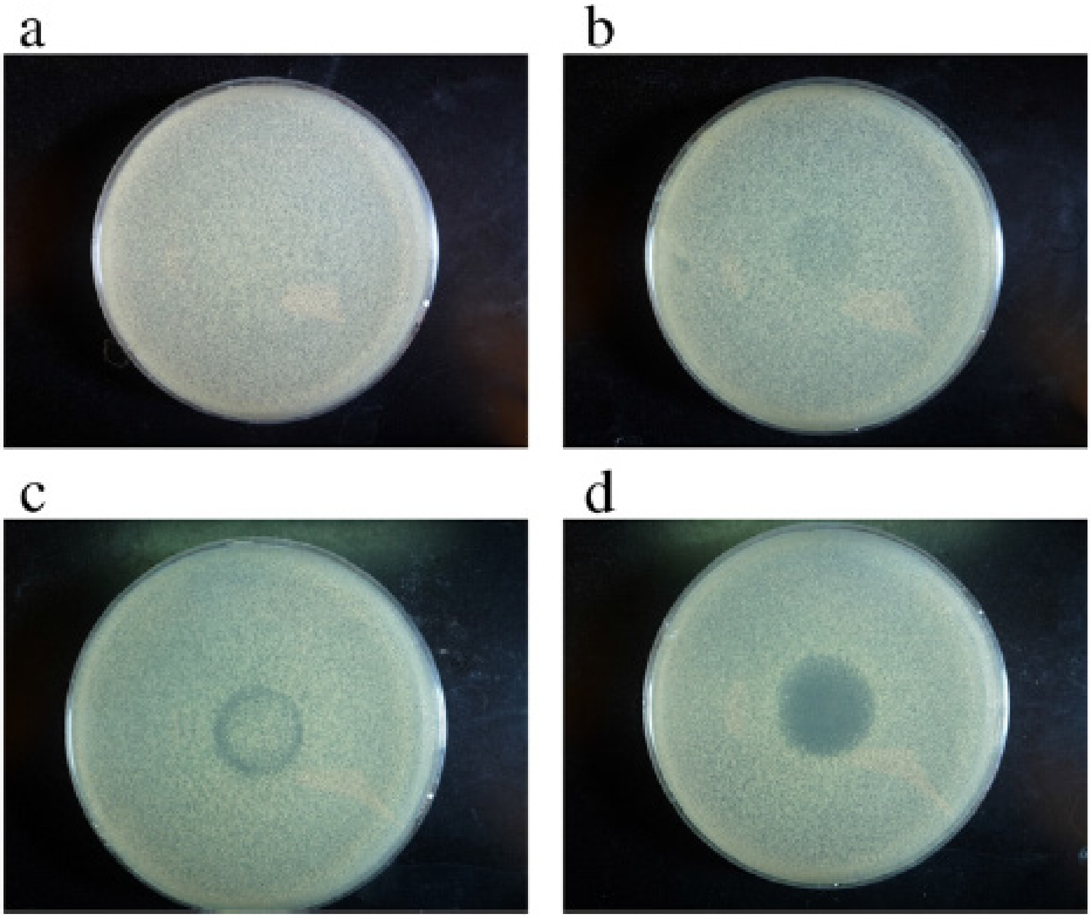

Figure **4.4** (**A**) Negative control for NO showing no adverse effects from the illumination of photolyzed {Mn-H_2O}@Al-MCM-41. Antifungal effects of 10 (**B**), 14(**C**) and 16 mg (**D**) {Mn-NO}@Al-MCM-41 illumination for 1 h with 100 mW cm^{-2} visible light.

Measurement of the NO delivery capacity of 16 mg of {Mn-NO}@Al-MCM-41 indicated that the illumination of 16 mg of the material produced a steady concentration of 130 μM of NO in the surrounding medium for at least 40 min. The material was completely photolyzed at the end of 1 h. As shown in Figure 4.4 D, illumination of 16 mg of {Mn-NO}@Al-MCM-41 for 1 h was sufficient to eradicate the fungal load colonizing a 1.1 mm thick agar layer. Since the photolyzed material does not exhibit any fungicidal activity (Figure 4.4 A), exposure to ~130 μM of NO for 1 h is cytotoxic to *C. albicans* cultured in the SSTI model. Using a continuous horizontal-flow delivery system, Ghaffari *et al*. have shown significant reduction of *C. albicans* load on TSA (tryptic soy agar) plates from exposure to 200 ppm of $NO_{(g)}$.[35] Complete eradication was observed after 4 h. In the present work, the source of NO was in close contact with the fungal colonies and the photoreleased NO had more time (static nature) to exert its effect on the fungus compared to the experimental setup employed by Ghaffari *et al*., in which the gas was allowed to flow over the fungal colonies. We believe that the results shown in Figure 4.4 confirm that a lower level of NO could eradicate *C. albicans* infection if the NO source is placed in intimate contact with the fungal colonies

It is generally accepted that the hyphal form of *C. albicans* is more invasive and the yeast-to-hyphae transition could be the trigger for conversion of the commensal fungus into a pathogenic one.[7] We therefore became interested to monitor the effects of NO on colonies of the two distinct forms of *C. albicans* grown under controlled conditions. As described in the experimental section, the yeast form was grown in our SSTI model at pH 6.5 with no FBS in the growth medium.[31] The incubation temperaturewas set at 30 °C. Growth of the hyphal colonies was stimulated by the use of 20% (v/v) FBS in the growth medium with the pH set at 7 and the incubation temperature set at 37 °C. The colonies were inspected carefully with the aid of light microscopy to confirm the exclusive presence of the individual forms in the two sets of SSTI models. As shown in Figure 4.3, the growth conditions gave rise to the two

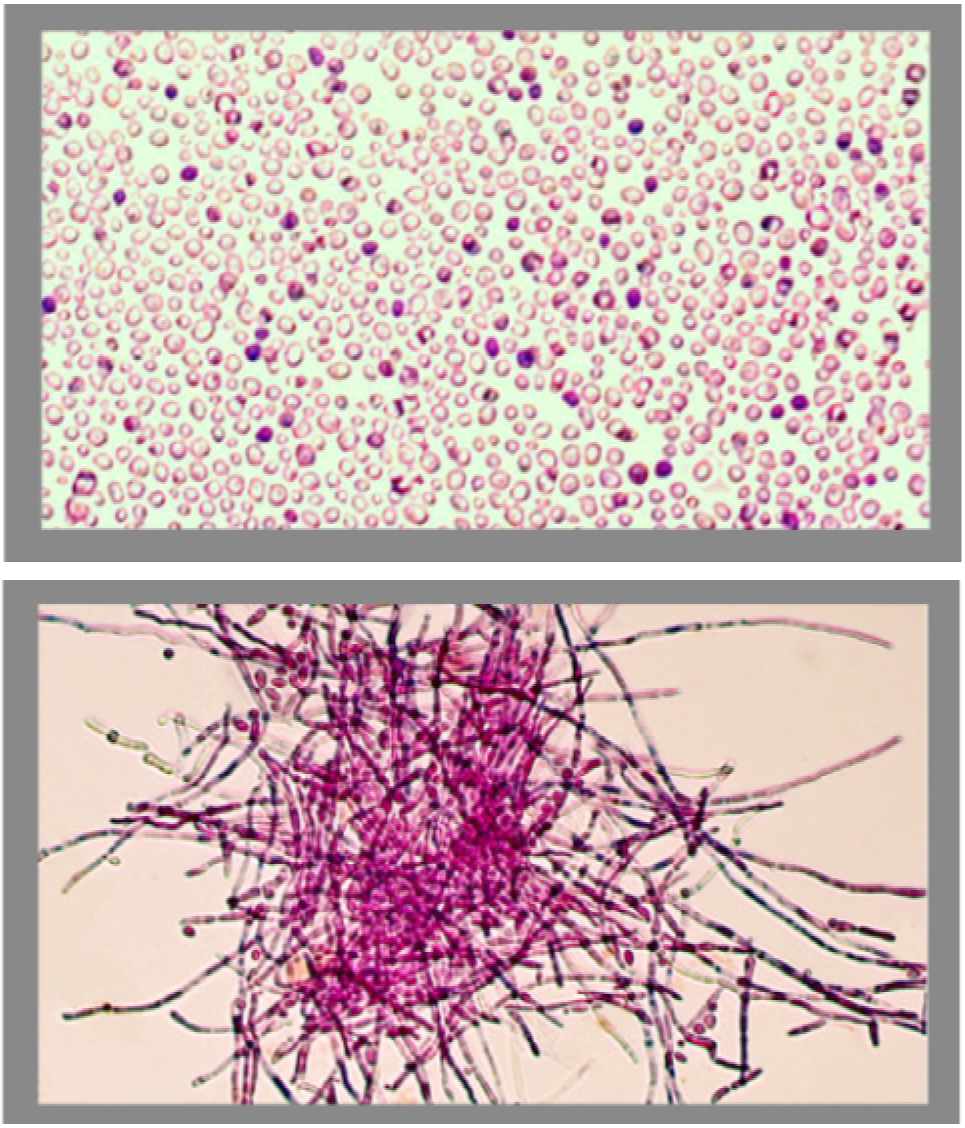

Figure **4.5** Effects of moderate dose of NO (photoreleased from {Mn-NO}@Al-MCM-41) on pure yeast form (top panel) and pure hyphal form (bottom panel) of C. albicans. The dead cells are identified by the bluish purple color (stained with

forms with >98% selectivity (n=50). In order to monitor the effect of the photoreleased NO on the two forms, we decided to employ a lower dose of {Mn-NO}@Al-MCM-41 (10 mg) to avoid complete eradication of the colonies at the site of application. Measurements with NO-electrode confirmed a steady level of 70 μM of NO for 30 min from 10 mg of the NO donor in buffer solutions. As shown in Figure 4.4, this amount of {Mn- NO}@Al-MCM-41 causes light clearing of *C. albicans* grown in the SSTI layer. When such a dose was applied to the two morphological forms separately, very different results were obtained. With the pure yeast variety, death of very few cells was noted upon exposure to NO (Figure 4.5, top). Most of the cells survived the NO exposure (no staining) and further plating confirmed their viability. However, the NO-treated yeast cells exhibited limited budding during the next 12 h of incubation. Quite in contrast, application of the same dose of the NO donor to the pure hyphal form caused extensive killing of the cells as evident by the near complete staining of the filamentous cells extracted from the kill-zone (Figure 4.5, bottom). This heightened susceptibility of the more invasive hyphal form of C. albicans to NO is quite noteworthy. Bistoni *et al.* have previously reported that supernatants from murine macrophages incubated with sodium nitroprusside (an NO donor) exhibit fungicidal activity against the hyphal (but not yeast) form of *C. albicans*.[49] The researchers, however, suggested the "likely involvement of stable nitrogen-containing compounds" in such selectivity. Our results now directly show that the hyphal form of *C. albicans* is more sensitive to NO compared to the yeast form. This inference also explains the absence of fungal hyphal structures in the NO-treated lesions of a murine burn-model infected with *C. albicans*, as reported by Martinez et al. in a recent paper.[37]

4.5 Sensitivity of *S. cerevisiae* Mutants Lacking Key Components of the Nitrosative Stress Response to Photo-released NO

The ability of the NO photoreleased from **PUX-NO** films to overwhelm key elements of the nitrosative stress response expressed by *S. cervisiea* was demonstrated using genetic mutants. Three strains of *S. cerevisiae* where used in the study: the wild-type (Y190), a knockout strain ΔYHB1 for the gene encoding the flavohemoglobin nitric oxide dioxygenase (NOD), Yhb1p, which detoxifies NO by catalyzing its oxidation to nitrate, and a knockout strain ΔSSU1 for the gene encoding the putative sulfite efflux pump, Ssu1p.[48] Orthologous proteins are found in pathogenic fungi such as *C. albicans* [49] The bacterial ortholog of Yhb1p, hmp, is expressed by the pathogens *S. aureus*, MRSA and *E. coli*.[50] This family of proteins has been shown to increase the virulence of pathogens *in vitro* and *in vivo* due to its ability to protect the organism from the nitrosative stress induced by host immune cells while knockout strains of flavohemoglobin NOD demonstrate hypersensitivity to NO.[51] The gene encoding the sulfite efflux pump, SSU1, is up-regulated by *S. cerevisiae* and *C. albicans* under conditions of nitrosative stress. However, the *C. albicans* ΔSSU1 mutant does not show enhanced susceptibility to NO or attenuated virulence in a mouse model while the *S. cerevisiae* ΔSSU1 mutant shows slightly increased susceptibility to NO donating molecules.[52] The connection between nitrosative stress and the up-regulation of SSU1 in these organisms has not been identified but represent an evolutionary artifact in *C. albicans*.

The effects of photoreleased NO from **PUX-NO** films against wild-type, ΔYHB1, and ΔSSU1 mutants of *S. cerevisiae* grown using the SSTI model of infection are shown in Figure 4.6. Films containing the indicated amount of {Mn-NO} were

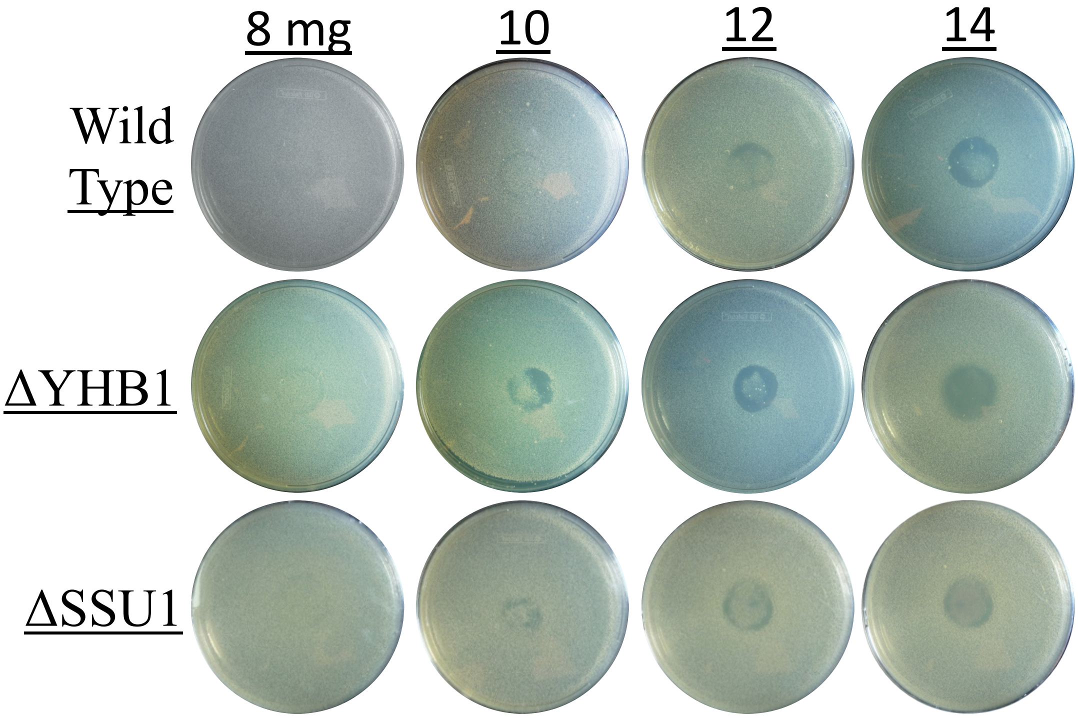

Figure **4.6** Effects of NO photoreleased by **PUX-NO** films against wild-type, ΔYHB1, and ΔSSU1 mutants of *S. cerevisiae* grown in soft agar cast on YPD plates. Films containing the indicated amount of {Mn-NO} were placed in the center of the plates and illuminated for 1 h. The treated plates where then incubated at 30°C for 12 h before visualization.

placed in the center of the plates and illuminated for 1 h. The treated plates where then incubated at 30°C for 12 h before visualization. The ΔYHB1 mutant showed enhanced susceptibility to all concentrations of NO compared to wild-type and the ΔSSU1 mutant. Comparison of the reduction in the microbial loads of ΔSSU1 and wild-type by **PUX-NO** films shows that the wild-type strain has enhanced resistance to NO through an as of yet unknown role of the sulfite efflux pump in the nitrosative stress response of *S. cervisiea*. Taken together, these results demonstrate that NO photoreleased from biocompatible materials such as **PUX-NO** films are able to overwhelm key elements of the nitrosative stress response by *S. cervisiea* Since *S. cervisiea* is often used as a model organism for pathogenic fungus like *Candida spp.* due to their evolutionary relatedness, these results are useful for assessing the suitability of NO donating materials for the treatment of infection by pathogenic fungus that infect cutaneous wounds such as *C. albicans.*[53]

4.6 Conclusions

To date, a few groups have examined the effects of gaseous NO[34] and exogenous NO donors on *C. albicans*.[35, 36] Synergistic fungicidal effects of exogenous NO donors and azoles on *Candida spp.* have also been reported.[54] Results of this study now indicate that a moderate dose of NO could prevent the spread of the hyphal form of *C. albicans* and limit the damage from the infection. Normal human tissues are not harmed by such doses of NO.[34] The NO-donating material {Mn-NO}@Al-MCM-41 (a biocompatible powder) is easy to apply compared to a continuous flowing device with a noxious gas. The NO-spent material with the entrapped $[Mn(PaPy_3)(H_2O)]^{2+}$ photoproduct can be easily removed from the infected area through wound rinsing. Because the NO delivery by the material can only be triggered by light, the doses of NO can be controlled depending on the nature and degree of virulence of the infection. We therefore believe that this material provides an opportunity to treat invasive *C. albicans* infections under the control of light.

4.7 Experimental Methods

4.7.1 Materials and physical measurements

The manganese nitrosyl [Mn(PaPy$_3$)(NO)](ClO$_4$) ({Mn-NO}) was synthesized by following the published procedure.[39] The Al-MCM@{Mn-NO} composite was prepared according to the procedure published by this group,[38] with slight modification. Briefly, a suspension of 100 mg of Na-exchanged Al-MCM-41 (Sigma-Aldrich) in 2.5 mL of acetonitrile was degassed by three cycles of freeze-pump-thaw and during the last freeze cycle, 200 mg of {Mn-NO} was added to the flask under N2. After bringing the solution to room temperature, the flask was sealed under N_2 atmosphere and allowed to stir for 48 h. The {Mn-NO}-impregnated Al-MCM-41 powder was collected on a ceramic filter and the green solid was washed with acetonitrile until no {Mn-NO} was detected in the wash solution (as monitored by electronic absorption spectroscopy). The light green powder was finally rinsed with tetrahydrofuran and dried in vacuo. The amount of {Mn-NO} retained within the pores of the sample was estimated by measuring the increase in mass of the dry powder after the loading procedure. The increase in mass corresponded to the chemical analysis of thematerialwith the aid of ICP-MS as described previously.[38] The {Mn-NO}@Al-MCM-41 sample employed in the present work contained 25 wt.% of nitrosyl.

The NO release profile of the {Mn-NO}@Al-MCM-41 sample was recorded with a NO-sensitive electrode (inNO-T NO-measuring system, Harvard Apparatus). A batch of 16 mg of {Mn-NO}@Al-MCM-41 was suspended in 2 mL of PBS buffer in a 5 mm diameter vial and NO release was initiated by illuminating the vial with a 100 mW cm$^-$

^{2} light source. The solution was stirred in the open vial and the tip of the NO-electrode was placed 3 cm above the stir bar and the concentration of free NO in solution was measured at 0.5 s intervals. The electrode assembly was calibrated against known NO donors and acid/nitrite solution according to standard methods. The sample afforded a steady level of 130 µM of NO within 5 min of illumination and the level was maintained for 30 min thereafter. The total amount of NO released from the sample, determined by Griess reagent, was 7.1(4) µmol after 1 h of illumination.

The ability of the NO released from {Mn-NO}@Al-MCM-41 to penetrate a 1.1 mm layer of agar (the thickness of the fungal suspension used in this study) was assayed by using a control agar plate consisting of a 1.1 mm layer of soft agar with dissolved Griess reagent which turns pink in the presence of NO. A batch of 16 mg of {Mn-NO}@Al-MCM-41 powder was evenly spread at the center of the agar plate using a template with a circular opening (2.2 cm dia) and illuminated for 1 h. The plate was then visualized for the formation of the pink dye on the surface (and beneath) of the agar. The resulting pink circle on the plate demonstrated very little lateral spreading of the released NO from the site of application.

4.7.2 Growth and maintenance of *C. albicans*

C. albicans freeze-dried culture (ATCC 10231) was obtained from Microbiologics (St. Cloud, MN). The freeze-dried culture was thawed and spread across the surface of 2% agar plate containing 1% yeast extract, 2% peptone, and 2% dextrose (YPD). The YPD agar plate was then incubated at 30 °C until single colonies were observed. A single colony was transferred to 6 mL of YPD broth and grown overnight at 30 °C on a rotary shaker until the cells reached stationary phase (OD_{600} ~10, Varian Cary 50 spectrophotometer). Frozen stock was obtained from the overnight culture by adding 15% (v/v) glycerol to the fungal culture and transferring 1 mL of the stock solution to individual vials. The vials were then frozen and stored at −80 °C. At the beginning of every week, a vial of frozen stock was thawed and plated onto fresh YPD agar. Isolated single colonies were grown at 30 °C and maintained throughout the week by storage at 4 °C. Subsequent experiments were performed using overnight cultures grown from single colonies isolated from such plates and grown to stationary phase. The cellular density as a function of the OD_{600} of C. albicans ATCC 10231 cultures in YPD broth was found to be 7.8(2)×108 cells mL^{-1} @ OD_{600}=1.0 as determined by hemocytometry and confirmed by the plate drop method.

4.7.3 Dose-dependent NO delivery to C. albicans and evaluation of the fungicidal activity

The dose dependent growth inhibition and fungicidal activity of the NO released from various dosages of {Mn-NO}@Al-MCM-41 during illumination with white light (100 mW cm^{-2}) was determined by using an in vitro model of the invasion and colonization of epithelial layers by *C. albicans*. Because epithelial layers serve as a vital barrier to protect the body from foreign agents and pathogens, they are the initial site of attack and invasion by *C. albicans* that have received environmental signals to switch its mode of growth from commensal to invasive form. Such a skin and soft tissue infection model (SSTI)[38] was constructed by the inoculation of a molten solution of 1% agar and 1% NaCl maintained at 45°C with an overnight culture to achieve a cellular density of 106 CFU mL^{-1}. The appropriate volume of inoculated agar (~2 mL) was then spread across the surface of an YPD agar plate to create a thin layer of soft agar (1.1 mm) of similar thickness to the human epidermal layer (~1 mm). The intimate contact of the soft agar layer to the YPD agar layer allowed facile diffusion of YPD from the bottom layer to the nutrient deplete top layer containing the suspended fungus to promote the polarized growth of C. albicans cells toward the nutrient reservoir, a phenomenon termed as “ditching” [30]. These plates were then incubated at 37 °C for 2 h to allow attachment of the cells to the agar matrix and the formation of cell-to-cell contacts. Such growth conditions stimulated modest germ tube formation (~25% of cells had an elongated morphology). Next, the plates containing fungal suspensions were treated with varying masses of {Mn-NO}@Al-MCM-41 powder evenly distributed at the center of the plates through the use of a circular template with a central opening of 2.2 cm in diameter and illuminated for 1 h. After illumination, the photolyzed material was gently washed off from the plate with a sterile saline solution and the treated plates were then incubated at 37 °C for 16 h. The fungicidal effect of the NO released from the material was assessed by visually comparing the cellular density of the NO-treated plates against the control plates. When complete clearing of the fungal load was noted, agar samples from the area of application of the {Mn-NO}@Al-MCM-41 material were homogenized and extracted in fresh growth media, plated, and incubated at 37 °C to ensure the lack of any viable cell(s) remaining in the kill-zone. A control plate was also exposed to 16 mg of the NO-spent material ({Mn-

H_2O}@Al-MCM-41) and illuminated for 1 h to determine fungicidal activity (if any) of the photolyzed material.

4.7.4 Growth of the yeast and hyphal forms of *C. albicans*

To determine the effects of photoreleased NO on the two morphological forms of *C. albicans,* the yeast and the hyphal form were grown on our SSTI model under different growth conditions. The temperature, pH and presence of blood serumwere all adjusted to set up growth conditions selective for each phenotype. The soft 1% agar layer used for both forms contained 137 mM of NaCl and 20 mM of piperazine-N,N′-bis(2-ethanesulfonic acid) (PIPES) buffer in Millipore water and was inoculated with a cellular density of 106 CFU mL^{-1}. The yeast form grew selectively when the pH of the soft agar layer was adjusted to 6.5 and incubated at 30 °C for 4 h without any fetal bovine serum (FBS) in the growth layer. The growth of hyphal cells was achieved with >95% selectivity by adjusting the pH of the soft agar layer to 7 and the addition of 20% (v/v) FBS to the growth layer. The bilayer plates were then incubated at 37°C for 4 h to allow sufficient elongation of the hyphal cells. The soft agar layers from both cases were then smeared on microscopic slides and cells of the two morphologies were visualized by light microscopy (Zeiss Axiovert 200 fitted with an AxioCam MRc5 camera).

4.7.5 Studies of the effects of NO on the two forms of *C. albicans*

A batch of 10 mg of {Mn-NO}@Al-MCM-41 was added to the two morphological forms of *C. albicans* grown in the SSTI model using the circular template with a 2.2 cm hole at the center and illuminated for 1 h with visible light (100 mW cm−2). The treated plates were then incubated for 8 h at 30 °C for the yeast and 37 °C for the hyphal form. Next, the cells were removed from the agar suspension by careful delamination of the soft agar layer from the bottom YPD agar layer and homogenization of the extracted agar into a pH 7.4 Tris·HCl buffer solution. The cells were stained with Trypan blue (0.04 wt.%) and photographed with the aid of a Zeiss Axiovert 200 microscope fitted with an AxioCamMRc5 camera. Because the viable cells do not absorb the vital stain, they were easily distinguished from the dead cells which exhibited distinct bluish purple color due to passage of the dye through the membrane and accumulation within the cellular envelope.

4.8 References

1. Odds, F. C. *Candida and Candidosis.* Balliere Tindall: London, 1988.
2. Runke, M. *Candida and Candidiasis.* (ed) Calderone, R. ASM Press: Washington, D.C.; 2002, 307-325.
3. Hickman, M. A. Zeng, G. Forche, A. Hirakawa, M. P. Abbey, D. Harrison, B. D. Wang, Y.M. Su, C. H., Bennett, R. J. Wang, Y. Berman, J. *Nature* **2013**, *7*, 55-9
4. Gow, N *Mycologist* **2002**, *16*, 33-5.
5. Martin, G. S., Mannino, D. M. Eaton, S. Moss. M. *N. Engl. J. Med.* **2003**, *348***,** 1546–54.
6. McNeil, M. M., Nash, S. L. Hajjeh, R. A. Phelan, M. A. Conn, L. A. Plikaytis, B. D. Warnock. D. W. *Clin. Infect. Dis*. **2001**, *33*, 641-7.

7. Lo, H. J. *Cell* **1997**, *90*, 939–49.

8. Feng, Q. H., Summers, E., Guo, B. Fink, G. *J. Bacteriol.* **1999**, *181*, 6339–46.

9. Leberer, E. *Mol. Microbiol.* **2001**, *42*, 673–87.

10. El Barkani, A. *Mol. Cell Biol.* **2000**, *20*, 4635–47.

11. Sellam, A. *Eukaryot. Cell* **2010**, *9*, 634–44.

11. Sudbery, P. E., Gow, N. A. R. Berman, J. *Trends Microbiol.* **2004**, *12*, 317–24.

12. Buffo, J., Herman, N. Soll, D. R. *Mycopathologia* **1985**, *85*, 21–30.

13. Mardon, D., Balish, E. Phillips, A. W.*J. Bacteriol.* **1969**, *100*, 701–7.

14. Simonneti, N., Stripolli, V. Cassone, E. A. *Nature* **1974 250**, 344–346 (1974).

15. Brown, D. H. Jr, Giusani, A. D., Chen, X. Kumamoto, C. A. *Mol. Microbiol.* **1999**, *34*, 651–62.

16. Lee, K. L., Buckley, H. R. Cambell, C. C. *Sabouraudia* **2004,** *13*, 148–153

17. Chen, H., Fujita, M., Feng, Q. H., Clardy, J. Fink, G. R. *Proc. Natl Acad. Sci. USA* **2004**, *101*, 5048–52.

18. Hogan, D. A. Kolter, R. *Science* **2002**, *296*, 2229–32.

19. Hogan, D. A. *Eukaryot. Cell* **2006**, *5*, 613–9.

20. Schaller, M., Schackert, C., Korting, H. C., Januschke, E. Hube, B. *J. Invest. Dermatol.* **2000**, *114*, 712-7.

21. Dieterich, C. Schandar, M. Noll, M. F. Johannes, J. Brunner, H. Graeve, T. Rupp, S. *Microbiology* **2002**, *148*, 497–506.

22. Jacobsen, I. D. Wilson, D. Wächtler, B. Brunke, S. Naglik, J. R. Hube, B. *Expert Rev. Anti. Infect..Ther.* **2012**, *10,* 85-93.
23. Falgier, C. Kegley, S. Podgorski, H. Heisel, T. Storey, K. Bendel, C.M. Gale, C.A. *Proc. Natl. Acad. Sci. USA* **2014**, *111*, 811–6.
24. Fradin, C. De Groot, P. MacCallum, D. *Mol. Microbiol.* **2005**, *56*, 397–415.
25. Urban CF, Reichard U, Brinkmann V, Zychlinsky A. *Cell Microbiol.* **2006**, *8*, 668–76.
26. Romani, L.; Bistoni, F.; Puccetti, P. *Current Opinion in Microbiology* **2003**, *6*, 338–343.
27. Moyes, D. L. *Cell Host Microbe* **2010**, *8*, 225–35.
28. Gauwerky, K. Borelli, C. Korting, H. C. *Drug Discov. Today* **2009**, *14*, 214–22.
29. Shareck J. Belhumeur, P. *Eukaryot. Cell* **2011**, *10*, 1004–12.
30. Hisajima, T. Maruyama, N. Tanabe, Y. *Microbiol. Immunol.* **2008**, *52*, 327–33.
31. Saville, S. P. Lazzell, A. L. Bryant, A. P. *Antimicrob. Agents Chemother..* **2006,** *50*, 3312–6.
32. Wächtler, B. Wilson, D. Hube, B. *Antimicrob. Agents Chemother.* **2011**, *55*, 4436–9.
33. Cheng, S. C. Joosten, L. A. B. Kullberg, B. Netea, M. G. *Infect. Immun.* **2012**, *80*, 1304-1

34. Ghaffari, A. Miller, C.C. McMullin, B. Ghahary, A. *Nitric Oxide* **2006**, *14* 21–9.
35. Privett, B.J. Nutz, S.T. Schoenfisch, M.H. *Biofouling* **2010**, *26,* 973–83.
36. Macherla, C. Sanchez, D.A. Ahmadi, M.S. Vellozzi, E.M. Friedman, A.J. Nosanchuk, J.D. Martinez, L.R. *Front. Microbiol.* **2012**, *3,* A193.
37. Hudson, S. Padera, R.F. Langer, R. Kohane, D.S. *Biomaterials* **2008**, *29*, 4045–55.
38. Heilman, B. J. St. John, J. Oliver, S.R. Mascharak, P.K. *J. Am. Chem. Soc.* **2012**, *134* 11573–82.
39. Ghosh, K. Eroy-Reveles, A.A. Avila, B. Holman, T.R. Olmstead, M.M. Mascharak, P.K. *Inorg. Chem.* **2004**, *43*, 2988–97.
40. Heilman, B.J. Halpenny, G.M. Mascharak, P.K. *J. Biomed. Mater. Res. B* 2011, *99*, 328–337.
41. Sudbery, P.E. *Nat. Rev. Microbiol.* **2011**, *9* 737–48.
43. Liu, H. P., Kohler, J. R. & Fink, G. R. *Science* **1994**, *266*, 1723-6.
42. Hornby, J. M. Dumitru, R. Nickerson, K. W. *J. Microbio. Methods* **2004**, *56*, 119– 24.
43. Gow, A. J. Luchsinger, B. P. Pawloski, J. R. Singel, D. J. Stamler, J. S. *Proc. Natl. Acad. Sci. Usa* **1999**, *96*, 9027–32.
44. Rothstein, A. *Electrolytes in Biological Systems*; Shanes, A. M. (ed) Amer. Physiol. Soc: Washington, DC; **1955**, 65– 100.
45. Sudbery, P. E. *Mol. Microbiol.* **2001**, *41*, 19–31.

46. Merson-Davies, L. A. Odds, F. C. *J. Gen. Microbiol.* **1989**, *135*, 3143–52.

47. de Jesus-Berrios, M., Liu, L., Nussbaum, J. C., Cox, G. M., Stamler, J. S., Heitman, J. *Curr. Biol.* **2003**, *13*, 1963–8.

48. Ullmann, B. D., Myers, H., Chiranand, W., Lazzell, A. L., Zhao, Q., Vega, L. A., Lopez-Ribot, J. L., Gardner, P. R., and Gustin, M. C. *Eukaryot. Cell* **2004**, *3*, 715–723.

49. Gardner PR, Gardner AM, Martin LA, Salzman AL *Proc Natl Acad Sci USA* **1998**, *95*, 10378–83.

50. Liu, L., Zeng, M., Hausladen, A., Heitman, J., and Stamler, J. S. Proc. Natl. Acad. Sci. USA **2000**, *97*, 4672–4676.

51. Miramón, P. Dunker, C. Windecker, H. Bohovych, I. M. Brown, A.J.P. PLoS ONE **2010**, *7*, e52850.

52. Goldstein, Alan L., McCusker, John H. *Genetics*. **2001**, *159*, 499-513.

53. McElhaney-Feser, G.E. Raulli, R.E. Cihlar, R.L. *Antimicrob. Agents Chemother.* **1998**, *42*, 2342–6.

Appendix I

The Effects of Equatorial Ligand Planarity on the Stability and NO Photorelease of Dye-Tethered Ruthenium Nitrosyls

A.1 Background

Although a variety of transition metal ions are known to form photoactive metal nitrosyls, Ru(II) centers are amongst the most well studied and promising candidates for the development of phototherapeutic NO donors.[1] The robust coordination sphere of Ru(II) complexes results in excellent thermal stability of Ru-ligand bonds, inhibiting ligand substitution reactions and non-specific release of bound NO.[2] The synthesis of photoactive Ru(II) nitrosyls usually occurs through the non-innocent binding of NO· to a Ru(III) centered precursor resulting in the transfer of an electron from NO· to Ru(III) producing a formally described Ru(II)-NO^+ moiety

$$Ru^{III}\text{-}L + NO\cdot \rightarrow Ru^{II}\text{-}NO^+ + L \qquad (1)$$

(where L is a loosely coordinated solvent molecule).[3] The resulting Ru(II)-NO^+ bond is rather complex and involves contributions from three major binding interactions between Ru and NO orbitals: (1) a σ-coordination interaction generated through the donation of two N-centered electrons from the NO(3σ) orbital to the Ru(dz^2) orbital, (2) a π-backbonding interaction from the covalent mixing of a single, doubly occupied Ru(d_{xz}, d_{yz}) orbital with the properly aligned NO($\pi^*_{x,}$ π^*_y) orbital, and (3) a π-coordination interaction that results in the donation of an electron from the singly occupied NO($\pi^*_{x,}$ π^*_y) orbital to a Ru(d_{xz}, d_{yz}) orbital, filling the Ru(t_{2g}) shell.[3] The sum of these interactions results in the loss of an electron from a NO(π^*) orbital increasing the bond order between N and O from 2.5 to 3 (i.e. $(N\equiv O)^+$).[3,4] The covalency and strength of the Ru-NO interactions listed above can vary significantly amongst different Ru(II) nitrosyls as a result of the donor/acceptor strength of the auxiliary ligand set and the geometry of the coordination sphere.[5] The variable nature of the Ru-N-O bonding complicates the assignment of both the metal and NO oxidation states (e.g. NO^+, NO·, NO^-) and prompted Enemark and Feltham to develop a singular notation for describing the oxidation state of the Ru-NO unit, $\{M\text{-}NO\}^n$, based on the sum of electrons (n) in the metal d and the NO(π*) orbitals.[3] Following the nomenclature, Ru(II)-NO^+ and Ru(III)-NO· are both described as $\{Ru\text{-}NO\}^6$ nitrosyls while the less common Ru(II)-NO· binding mode is distinguished as $\{Ru\text{-}NO\}^7$.

The synthesis of photoactive metal nitrosyls by the Mascharak group began with the design of the pentadentate ligand, $PaPy_3H$, and the synthesis of $[Fe(PaPy)(NO)](BF_4)_2$ which was the first reported nitrosyl to successfully reproduce the rapid photorelease of NO from the Fe-center of the microbial enzyme, Fe-nitrile hydratase (Fe-NHase). The structure of $PaPy_3H$ incorporated several key features of the metal coordination sphere of the protein active site including: (1) a deprotonated carboxamide-N donor which coordinated *trans* to NO in order to promote the *trans*-labilizing effect and (2) π-accepting ligands in the equatorial plane to stabilize the Fe(II)-NO^+ unit generated during the binding of NO to the Fe(III) precursor.[7] However, due to the rapid decomposition of the $\{Fe\text{-}NO\}^6$ complex in aqueous solutions, the Fe center was exchanged for its more stable congener, Ru, in the synthesis of $[Ru(PaPy)(NO)](BF_4)_2$ (Figure A.1).[8] $[Ru(PaPy)(NO)](BF_4)_2$ was the first $\{Ru\text{-}NO\}^6$ nitrosyl to demonstrate significant rates of NO photorelease upon illumination with low power UV-light under biological conditions. Previously reported photoactive $\{Ru\text{-}NO\}^6$ nitrosyls were only stable in acidic aqueous solutions ($pH < 5$) and underwent rapid hydration forming Ru-NO_2 at neutral pH.[9] In contrast, the stability of $[Ru(PaPy_3)(NO)](BF_4)_2$ under biologically relevant conditions made it useful as a photoactive NO donor in biological assays, as first demonstrated by the measurement of the NO binding and release kinetics of myoglobin and cytochrome-c using photoreleased NO produced from brief exposure (30 s) of $[Ru(PaPy_3)(NO)](BF_4)_2$ in aqueous buffer to low power UV light (7 mW/cm^2, $\lambda_{max} = 302$ nm).[10] While the unique ability of $[Ru(PaPy)(NO)](BF_4)_2$ to release NO *only* upon exposure to low-power UV-light allowed precise spatial and temporal control in the delivery of NO to biological targets such as proteins and isolated tissue, the UV-light required to activate NO photorelease from the nitrosyl limited further development of the nitrosyl as a phototherapeutic.[11] To overcome the limitations of UV-light activated $\{Ru\text{-}NO\}^6$ nitrosyls, futher use of the $PaPy_3H$ ligand involved the visible light active $\{Mn\text{-}NO\}^6$ analog, $[Mn(PaPy_3)(NO)](ClO_4)$, and its derivatives.[12]

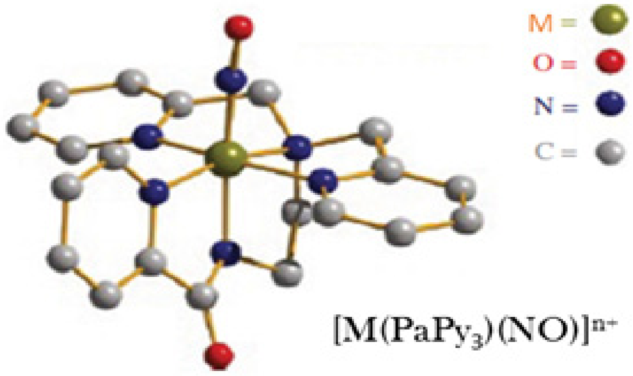

Figure **A.1** – X-ray crystal structure of $[M(PaPy_3)(NO)(Cl)]^{n+}$.[1,5,9]

While the pentadentate ligand, $PaPy_3^-$, established the influence of the axial ligand on the photoactivity of $\{Ru\text{-}NO\}^6$ through the *trans*-labilizing effect, we next sought to investigate characteristics of the equatorial donor groups of Fe-NHase that promote favorable NO photorelease. Since the equatorial plane of the Fe-NHase contains two *trans*-coordinated dicarboxamido donors from peptide bonds on the the protein backbone, this feature was incorporated into a tetradentate, dicarboxamide ligand, namely 1,2-bis(pyridine-2-carboxamido)- benzene (H_2bpb).[13] The negative charge of the deprotonated carboxamido-N donors on the bpb^{2-} frame is delocalized across a central 1,2-phenylenedicarboxamide (PDA) moiety and through the carboxamido linking groups to the terminal pyridine-N donors. This conjugated π-system maintains the bpb^{2-} ligand frame in a rigid, planar geometry during coordination to the equatorial plane of the Ru center.[14] The combination of negatively charged, σ-donating carboxamido-N and conjugated π-accepting pyridine-N donors lowers the energy gap of the NO releasing photo-transition $\pi(\text{PDA})\text{-}\pi(\text{RuNO}) \rightarrow \pi^*(\text{RuNO})\text{-}\pi^*(\text{Py})$ by increasing the electron density and raising the energy level of the HOMO, and decreasing the electron density and lowering the energy level of the LUMO.[15]

In order to enhance the effect of the admixture of the bpb^{2-} M.O.s into the Ru-NO centered photoband, the bpb^{2-} frame was modified to increase the electron donating capacity of the carboxamido-N donors and the π-accepting capacity of the pyridine-N donors. The first aim was achieved through the attachment of electron-donating groups of increasing donor strength (H < Me < OMe) to the 4 and 5 positions of the phenyl ring of the PDA moiety.[14,16] Through DFT calculations we were able to demonstrate that this modification increased the electron density of the π(PDA)-π(Ru-NO) orbital and raised its energy level.[14,17] The energy level of the LUMO orbital of the Ru-bpb^{2-} nitrosyls was achieved by enhancing the electron withdrawing strength of the pyridine groups through substitution with quinoline-N donor groups that have increased π* conjugation to better accept excited electrons from the HOMO orbital upon photo-excitation.[16] The combined effects of the lowered LUMO and raised HUMO energy levels decreased the energy gap of the NO releasing photo-transition π(PDA)-π(RuNO) → π*(RuNO)π(Py).

The ligand, Me_2bpb^{2-}, was the first modified ligand synthesized to establish the ability of peripheral ligand modifications to enhance the photoactivity of $\{Ru\text{-}NO\}^6$ nitrosyls.[14] The shifting of λ_{max} of the NO releasing photoband from 380 nm for [(bpb)Ru(NO)(Cl)] to 395 nm for [(Me_2bpb)Ru(NO)(Cl)] along with the increased rate of NO photorelease from [(Me_2bpb)Ru(NO)(Cl)] confirmed the ability of peripheral modifications to enhance the photoactivity of $\{Ru\text{-}NO\}^6$ nitrosyls. Additionally, the *trans*-labilizing effect of the Cl^- ligand bound *trans* to NO in the Ru-bpb^{2-} nitrosyls was established by the synthesis of a third nitrosyl, [(Me_2bpb)Ru(NO)(Py)], containing a pyridine (Py) ligand coordinated *trans* to NO. The greatly reduced rate of NO photorelease from [(Me_2bpb)Ru(NO)(Py)] compared to [(Me_2bpb)Ru(NO)(Cl)] confirmed the *trans*-labilizing effect of the Cl^- ligand for the bpb^{2-} based $\{Ru\text{-}NO\}^6$ nitrosyls.

In the next step of ligand modification, the pyridine arms of Me_2bpb^{2-} were substituted with quinoline groups to afford the designed ligand Me_2bQb^{2-}.[14] The increased π-accepting capacity of the quinoline rings of Me_2bQb^{2-} produced a dramatic red-shift in the photoband of the corresponding $\{Ru\text{-}NO\}^6$ nitrosyl from λ_{max} = 395 nm for [(Me_2bpb)Ru(NO)(Cl)] to λ_{max} = 455 nm for [(Me_2bQb)Ru(NO)(Cl)]. Exposure of a solution of [(Me_2bQb)Ru(NO)(Cl)] to visible light $\lambda > 465$ nm for 15 min resulted in significant NO photorelease (16%) while similar illumination conditions of the unmodified nitrosyl, [(bpb)Ru(NO)(Cl)], failed to initiate significant NO photorelease (1%). The combined effects of the appropriate electron donor and acceptor group modifications to the bpb^{2-} ligand frame, demonstrated the feasibility of sensitizing $\{Ru\text{-}NO\}^6$ nitrosyls to visible light through proper modification of the auxiliary ligands.

Following the sensitization of [(Me_2bQb)Ru(NO)(Cl)] to visible light through modification of the ligand frame, we next sought to enhance the nitrosyl's quantum yield and NO release rates through the direct coordination of a light-harvesting antennae in the form of a strongly colored dye molecule bound to the axial site *trans* to NO.[18] Previous work by Ford and coworkers had demonstrated that tethering of the chromophores protoporphyrin IX (PPIX, $\lambda_{max} \approx 400$ nm) and fluorescein (Fluor, $\lambda_{max} \approx 450$ nm) to the bridging sulfur atoms of the Fe_2S_2 center of Roussin's Red salt esters (RSE) using an extended $(CH_2)_n$ linker (generating PPIX-RSE and Fluor-RSE) resulted in only modest improvement of the iron nitrosyls' NO releasing photoactivity ($\phi \sim 0.00025\text{-}0.00052$).[19,20] Therefore, we attempted to *directly coordinate* the conjugated phenolato-O donor atom of the selected tricyclic dye chromophore, resorufin (Resf), to the Ru center of the $\{Ru\text{-}NO\}^6$ nitrosyls in an attempt to facilitate the direct transfer of energy from the dye molecule to the Ru-NO unit.[18] A series of $\{RuNO\}^6$ nitrosyls, namely [(Me_2bpb)Ru(NO)(Cl)], [(Me_2bQb)Ru(NO)(Cl)], and [($(OMe)_2$bQb)Ru(NO)(Cl)], were synthesized by removal of the Cl^- ligand with $AgBF_4$ followed by direct coordination of the deprotonated dye to the open axial site affording

[(Me$_2$bpb)Ru(NO)(Resf)], [(Me$_2$bQb)Ru(NO)(Resf)], and [((OMe)$_2$bQb)Ru(NO)(Resf)] (Figure A.2).[18] While the photobands of the Cl$^-$ bound nitrosyls had various values of λ_{max}, the photobands of the dye-sensitized nitrosyls all exhibited maximum absorption at the same wavelength (~500 nm). However, the intensity of the photoband of the methoxy modified nitrosyl, [((OMe)$_2$bQb)Ru(NO)(Resf)], was greatly enhanced (ε_{500} ~ 28 000 M^{-1} cm^{-1} in MeCN) compared to the photobands of the methyl substituted nitrosyls [(Me$_2$bpb)Ru(NO)(Resf)] and [(Me$_2$bQb)Ru(NO)(Resf)] (ε_{500} ~ 12 000 M^{-1} cm^{-1} in MeCN).[16] The quantum yield values for NO photorelease upon exposure to visible light was also greatly enhanced by coordination of the Resf dye. While the Cl$^-$ bound nitrosyls exhibited modest to negligible visible light photoactivity despite the effects of ligand modifications ($\phi_{500} < 0.025$), the dye-sensitized nitrosyls released significant amounts of NO upon illumination with 500 nm light ($\phi_{500} = 0.05$, 0.10, and 0.20 for [(Me2bpb)Ru(NO)(Resf)], [(Me2bQb)Ru(NO)(Resf)] and [((OMe)2bQb)Ru(NO)(Resf)]).

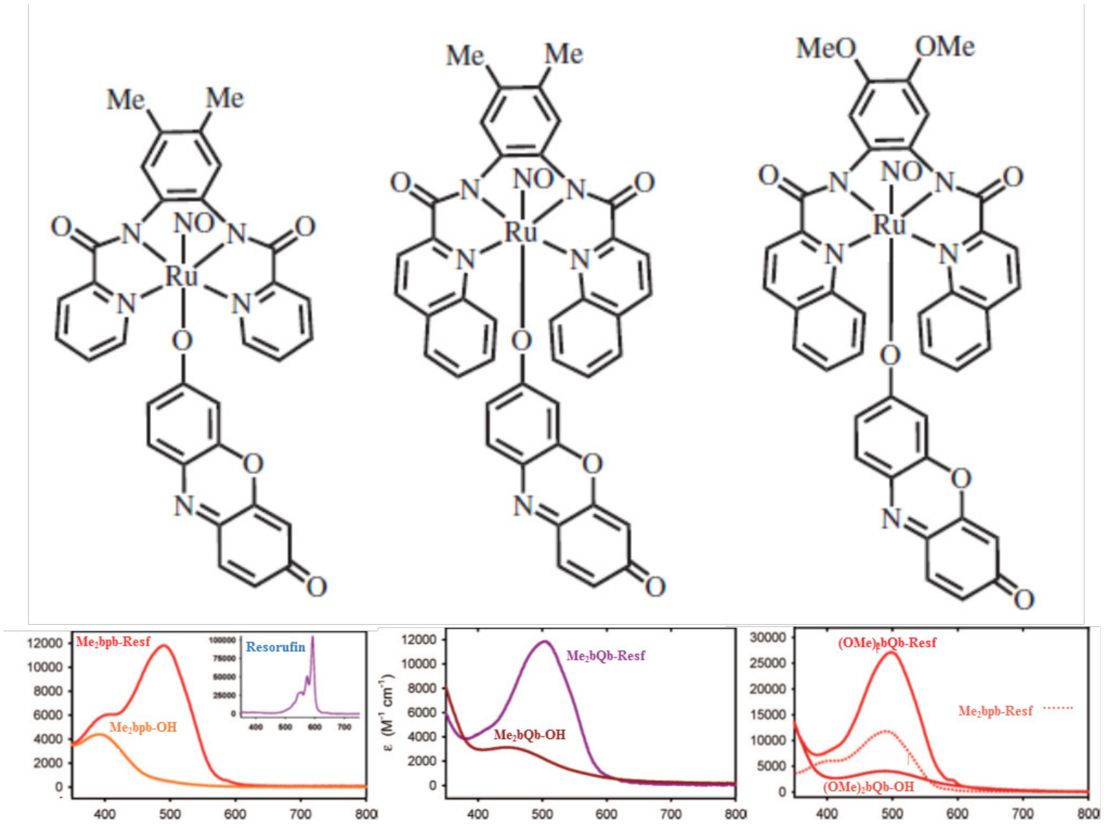

Figure **A.2** – Schematic and corresponding electronic absorption spectra of the Ru nitrosyls derived from the tetradentate, dicarboxamide ligands Me_2bpb^{2-}, Me_2bQb^{2-}, and $(OMe)_2bQb^{2-}$ with Cl^- or $Resf^-$ bound trans to NO.[16]

While the quinoline based nitrosyls $[(Me_2bQb)Ru(NO)(Resf)]$ and $[((OMe)_2bQb)Ru(NO)(Resf)]$ exhibited the greatest visible light photoactivity upon dye-sensitization, these nitrosyls lost significant amounts of the bound dye when dissolved in aqueous solutions compared to the pyridine based nitrosyls $[(Me_2bpb)Ru(NO)(Resf)]$.[16,18] For example, when the dye-sensitized nitrosyls were dissolved in aqueous solution at pH 7.4 the quinoline based nitrosyls lost ~20% of bound dye while the pyridine based nitrosyl lost only 5%. Examination of the X-ray crystal structure of the quinoline based nitrosyls revealed significant steric interaction between the quinoline arms of the ligand frame. This steric interaction generated considerable twisting of the quinoline arms out of the ligand plane, producing a nearly 35° angle between the planes of the quinoline rings (Figure A.3).[16] We hypothesized that the reduced stability of the Ru-Resf bond of the quinoline based nitrosyls was a result of the distortion of the equatorial ligand plane. To test the effect of the twisting of the ligand plane on the stability of the Ru-Resf bond as well as the visible light photoactivity of the coordinated nitrosyls, we have now synthesized two new ligands with methoxy-substituted phenylenediamine rings combined with pyridine ($H_2(OMe)_2bpb$) or 1-isoquinoline ($H_2(OMe)_2IQ1$) donors.

A.2 Syntheses of Planar Ligands $H_2(OMe)_2bQb$ and $H_2(OMe)_2IQ1$

To relieve the steric interaction of the quinoline groups observed in the structure of $[((OMe)_2bQb)Ru(NO)(Cl)]$**,** we have now synthesized two new ligands frame which have substituted the sterically hindered quinoline groups of $(OMe)_2bQb^{2-}$ with pyridine (Py) (as in $(OMe)_2bpb^{2-}$) or 1-isoquinoline moieties (IQ1, as in $(OMe)_2IQ1^{2-}$). The $(OMe)_2IQ1^{2-}$ ligand coordinates the equatorial sites of the Ru center with the fused aromatic rings of the IQ1 groups pointed away from the central C_{2v} ligand plane. This orientation maintains the extended conjugation of the equatorial ligand frame while removing the in-plane ligand twist. So that the attributes of the planar ligand frame with extended conjugation and a methoxy-substituted PDA moiety (i.e. $(OMe)_2IQ1^{2-}$) can be compared with the corresponding methoxy-substituted pyridine based ligand, we have included the synthesize and characterization of the designed ligand, $(OMe)_2bpb^{2-}$

, in this study. When coordinated, the pyridine rings of this ligand remain far apart in the equatorial plane of the nitrosyl and hence no steric interaction is expected between them.

The new ligand frames were synthesized using similar reaction conditions to those of $H_2(OMe)_2bQb$ in which triphenyl phosphite acts as the amide coupling reagent in pyridine.[16] First, the preparation of l,2-dimethoxy-4,5-phenylenediamine was achieved via reduction of l,2-dimethoxy-4,5-dinitrobenzene with excess hydrazine over Pd/C (Figure A.3).[14] The resulting diamine (which was air sensitive) was then immediately reacted with 2 equivalents of either picolinic acid or 1-isoquinolinecarboxylic acid to afford $H_2(OMe)_2bpb$ and $H_2(OMe)_2IQ1$, respectively. The pyridine containing ligand $H_2(OMe)_2bpb$ was isolated as a white solid while the extended conjugation of the 1-isoquinoline moieties of $H_2(OMe)_2IQ1$ results in a bright yellow color similar to $H_2(OMe)_2bQb$.

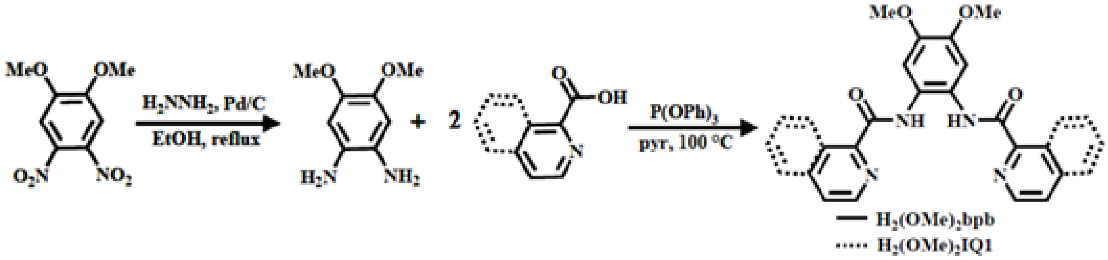

Figure **A.3** – Reaction scheme for the synthesis of $H_2(OMe)_2bpb$ (structures with solid lines) and $H_2(OMe)_2IQ1$ (structures from combination of solid and dashed lines).

A.3 Syntheses and Characterization of Cl-Bound Metal Nitroyls

The carboxamide groups of the ligands $H_2(OMe)_2bpb$ and $H_2(OMe)_2IQ1$ were deprotonated with NaH in *N,N*-dimethylformamide (DMF) creating two negatively charged carboxamido-N donor atoms. The deprotonated ligands were reacted with $RuCl_3$ in refluxing DMF. Without isolation, the resulting dichloride complexes were then converted to the nitrosyls by bubbling $NO_{(g)}$ into a refluxing solution of the dichloride metal complexes in DMF. The nitroysls, namely $[((OMe)_2bpb)Ru(NO)(Cl)]$ and $[((OMe)_2IQ1)Ru(NO)(Cl)]$, were isolated as pure compounds in good yield by removing the DMF and extracting the residues with MeCN.

A.3.1 - Structure of [((OMe)₂bpb)Ru(NO)(Cl)]

The ^{1}H-NMR and IR spectra of $[((OMe)_2bpb)Ru(NO)(Cl)]$ both confirm the synthesis of the desired nitrosyl. Coordination of the dicarboxamido ligands to the Ru(III) center can be easily monitored by the formation of the $Ru\text{-}N_{carboxamide}$ bond due to the shifting of the carbonyl stretching frequency ($\nu_{C=O}$) of the free ligand $H_2(OMe)_2bpb$ (1676 cm^{-1}) to lower energy upon formation of the nitrosyl complex (1631 cm^{-1}). Subsequent formation of the Ru-NO bond during the bubbling of NO was monitored by the appearance of a NO stretching frequency (ν_{NO}) at a wavelength (1845 cm^{-1}) indicative of bound NO in neutral $\{RuNO\}^6$ nitrosyls containing dicarboxamide tetradentate ligands and a *trans* Cl^- ligand.[14] In addition, the geometry of $((OMe)_2bpb)^{2-}$ during coordination to the equatorial plane of $[((OMe)_2bpb)Ru(NO)(Cl)]$ is inferred to be similar to the geometry of the dye-bound nitrosyl $[((OMe)_2bpb)Ru(NO)(Resf)]$. From the analysis of the crystal structure of $[((OMe)bpb)Ru(NO)(Resf)]$ (*vide infra*), the geometry of the $((OMe)_2bpb)^{2-}$ equatorial plane of $[((OMe)_2bpb)Ru(NO)(Cl)]$ is taken to be planar rather than distorted.

A.4.2 X-ray Crystal Structure of [((OMe)$_2$IQ1)Ru(NO)(Cl)]

The X-ray structure of [((OMe)$_2$IQ1)Ru(NO)(Cl)] confirms that the presence of the IQ1 moieties in ((OMe)$_2$IQ1)$^{2-}$ in place of regular quinoline moieties (as in ((OMe)$_2$bQb)$^{2-}$) allows the equitorial ligand frame to remain *strictly planar* when bound to the Ru center in contrast to the out-of-plane twisting of the quinoline arms seen in the crystal structure of [((OMe)$_2$bQb)Ru(NO)(Cl)] (Figure A.4).[16] The Cl$^-$ ligand bound *trans* to NO completes the nearly octahedral geometry about the Ru center of [((OMe)$_2$IQ1)Ru(NO)(Cl)]. Close examination of the structure of [((OMe)$_2$IQ1)Ru(NO)(Cl)] reveals that the Ru-N5(O) (1.735(3) Å) and N5-O5 (1.153(3) Å) bond lengths are very similar to those of [((OMe)$_2$bQb)Ru(NO)(Cl)] (1.7457(18) and 1.148(2) Å, respectively).[16] Both of these nitrosyls also demonstrate nearly linear Ru-N5-O5 bond angles ([((OMe)2bQb)Ru(NO)(Cl)] =175.73(19)°;[16] [((OMe)2IQ1)Ru(NO)(Cl)] = 175.9(2)°), typical of {Ru-NO}^{6} nitrosyls.

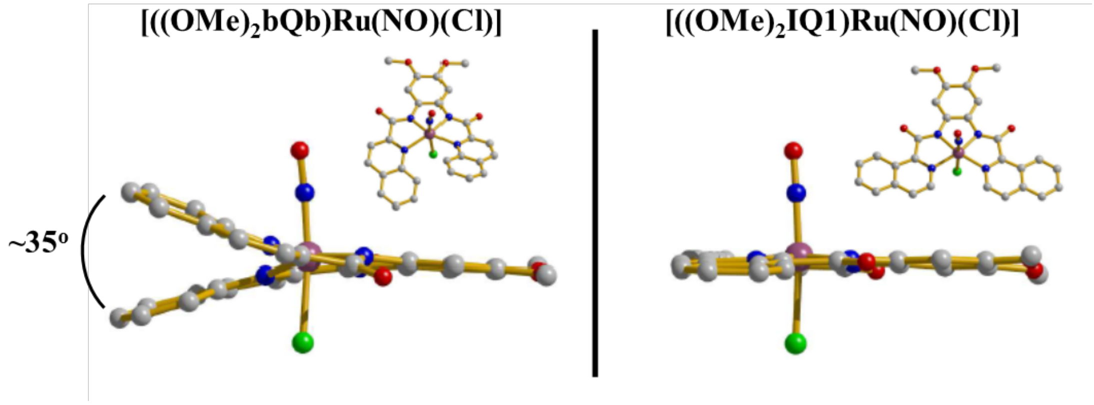

Figure **A.4 -** X-ray crystal structures of [((OMe)$_2$bQb)Ru(NO)(Cl)][16] (left) and [((OMe)$_2$IQ1)Ru(NO)(Cl)] (right), displaying the relief of the in-plane ligand twist upon substitution of the quinoline rings with 1-isoquinoline.

A.5 Comparison of Electronic Absorption Spectra of the Cl^- bound Ruthenium Nitrosyls

Comparison of the photobands of the Cl^- bound $\{Ru\text{-}NO\}^6$ nitrosyls with planar equatorial ligand frames comprised of a central PDA moiety appended with peripheral electron donors of increasing strength (H < Me < OMe) and two carboxamide tethered pyridine arms demonstrate a significant red-shift of the λ_{max} of the photobands from 380 nm to 395 nm to 420 nm following the electron donating strength of the peripheral groups (Figure A.5).[15,17] As described above, the red-shift of the photobands of these nitrosyls results from the mixing of the ligand π(PDA) M.O. with the π(Ru-NO) bonding orbital producing the mixed orbital π(PDA)-π(Ru-NO) whose energy level is directly related to the electron donor strength of the peripheral groups allowing tuning of the energy gap of the NO releasing photo-transition, π(PDA)-π(Ru-NO) → π*(Ru-NO)π*(Py).15 A similar mechanism is involved in the red-shifting of the photoband of the $\{Ru\text{-}NO\}^6$ nitrosyls containing equatorial ligand frames with quinoline based arms due to the mixing of the electron accepting π*(Q) M.O. with the π*(Ru-NO) antibonding orbital.

The electronic spectra of the Cl^- bound $\{Ru\text{-}NO\}^6$ nitrosyls with extended conjugation across Q and IQ1 groups demonstrated efficient red-shifting of their photoband due to the enhanced electron accepting capacity of the quinoline groups in comparison to the pyridine groups of $[((OMe)_2bpb)Ru(NO)(Cl)]$. For example, the addition of Q in $[((OMe)_2bQb)Ru(NO)(Cl)]$ resulted in a 70 nm red-shift from λ_{max} = 420 nm for $[((OMe)_2bpb)Ru(NO)(Cl)]$ to 490 nm,[16] while addition of IQ1 groups resulted in a red-shift of 55 nm in [((OMe)$_2$IQ1)Ru(NO)(Cl)] (λ_{max} = 475 nm) as seen in Figure 2.5. Comparison of the ε values of the methoxy substituted {Ru-NO}^{6} nitrosyls reveals another interesting trend. Relief of the in-plane ligand twist of [((OMe)$_2$bQb)Ru(NO)(Cl)] (ε_{490} = 4 000 M^{-1} cm^{-1}) by substitution of the Q groups with Py or IQ1 results in significantly higher ε values for [((OMe)$_2$bpb)Ru(NO)(Cl)] (ε_{420} = 7 800 M^{-1} cm^{-1}) and [((OMe)$_2$IQ1)Ru(NO)(Cl)] (ε_{475} = 8 700 M^{-1} cm^{-1}). These results are possibly the consequence of more efficient overlap of the atomic p-orbitals (enhancing π-conjugation) when a rigid, planar geometry is achieved in comparison to a twisted geometry in the equatorial field.

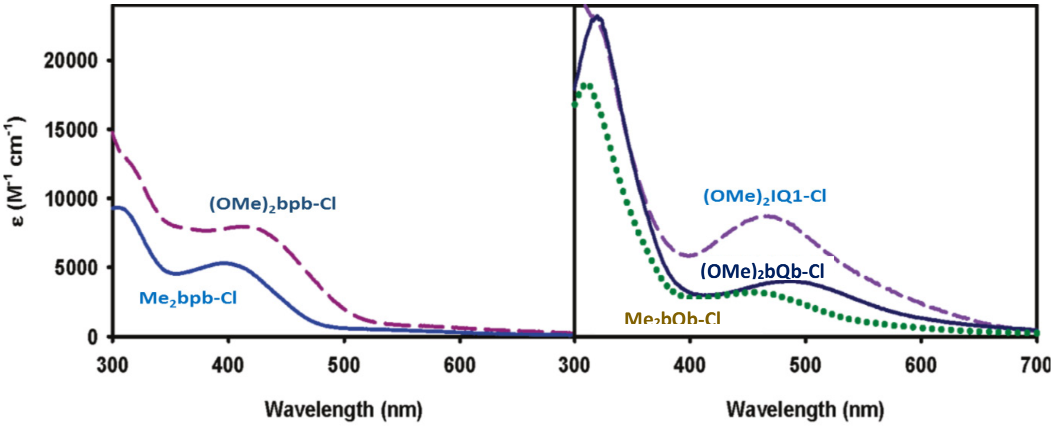

Figure **A.5 -** (left) Electronic absorption spectra of the pyridine based nitrosyls [(Me$_2$bpb)Ru(NO)(Cl)][14] and [((OMe)$_2$bpb)Ru(NO)(Cl)] in DMF. (right) Electronic absorption spectra of the quinoline based nitroysls [(Me$_2$bQb)Ru(NO)(Cl)],[14] [((OMe)$_2$bQb)Ru(NO)(Cl)],[16] and [((OMe)$_2$IQ1)Ru(NO)(Cl)] in DMF.

A.6 Syntheses and Structures of Dye Conjugated Metal Nitrosyls

The ligand frames $H_2(OMe)_2$bpb and $H_2(OMe)_2$IQ1 were designed to maintain planarity when bound to the Ru center. It was hypothesized that a planar equatorial ligand would facilitate binding of the bulky resorufin dye to the axial site *trans* to NO. Reaction of the chloride-bound $\{RuNO\}^6$ nitrosyls with $AgBF_4$ in MeCN results in the formation of the MeCN-bound intermediates which were refluxed with Resf in MeCN without isolation to yield the dye-bound nitrosyls. The solubility of [((OMe)$_2$bpb)Ru(NO)(Resf)] in MeCN allowed the removal of AgCl and $NaBF_4$ from the solution after cooling the reaction mixture to room temperature. Isolation of [((OMe)$_2$bpb)Ru(NO)(Resf)] from the filtrate was achieved by condensing, then cooling the MeCN solution forming NMR pure [((OMe)$_2$bpb)Ru(NO)(Resf)] as a red precipitate. The poor solubility of [((OMe)$_2$IQ1)Ru(NO)(Resf)] in MeCN required evaporation of MeCN and extraction of the residual solids with CH_2Cl_2 to isolate [((OMe)$_2$IQ1)Ru(NO)(Resf)] from the salt mixture.

A.6.1 X-ray crystal structure of [((OMe)$_2$bpb)Ru(NO)(Resf)]

The X-ray crystal structure of [((OMe)$_2$bpb)Ru(NO)(Resf)] reveals that the lack of steric interaction between the pyridine groups of the ligand allows (OMe)$_2$bpb^{2-} to coordinate the equatorial plane of the Ru center with a planar geometry (Figure A.6). A pseudooctahedral geometry was achieved about the Ru center with Resf bound through the deprotonated phenolato-O donor to the axial site *trans* to NO. The methoxy groups appended to the PDA moiety in [((OMe)$_2$bpb)Ru(NO)(Resf)] has little effect on the overall geometry of the nitrosyl when compared to the crystal structure of the methyl substituted nitrosyl $[(Me_2bpb)Ru(NO)(Resf)]$.[18] In both cases, the resorufin dye is bound tilted away from the axial vector with a ~120° Ru–O6–C(Resf) bond angle ([(Me2bpb)Ru(NO)(Resf)] = 128.46(11)°, [((OMe)2bpb)Ru(NO)(Resf)] = 126.0(3)°) suggesting that the phenolato-O atom of Resf is more *sp2* (ideal 120°) than *sp3* hybridized (ideal 109.5°) facilitating electronic conjugation between the Ru center and the fused aromatic ring system of the dye. The position of the dye directly underneath one of the pyridine rings of the $(OMe)_2bpb^{2-}$ frame (also observed in the methyl substituted nitrosyl) presumably facilitates π-stacking interactions between the pyridine ring and the Resf ring system. As a result of the likely stacking of these rings, the pyridine arm engaged in π-stacking is titled slightly below the equatorial plane towards the Resf plane.

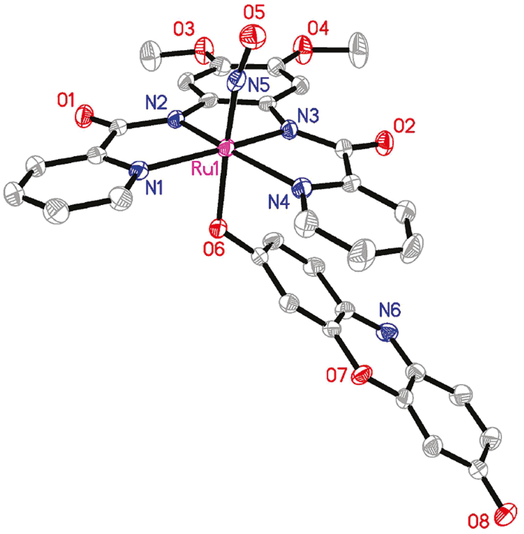

Figure **A.6** - Thermal ellipsoid (probability level 50%) plot of $[((OMe)_2bpb)Ru(NO)(Resf)]$ with select atom-labeling. H atoms are omitted for the sake of clarity.

The Ru–N5–O5 bond angle of $[((OMe)_2bpb)Ru(NO)(Resf)]$ is bent significantly to 169.3(3)° compared to the methyl substituted nitrosyl

[(Me_2bpb)Ru(NO)(Resf)] (178.13(15)°).[18] As stated in the introduction, nitrosyls with a formally described oxidation state of Ru(II)-NO^+ favor a linear Ru-N-O bond angle to facilitate π-bonding interactions, while a formally Ru(III)-NO· nitrosyl binds NO with a single σ-bonding interaction which can result in Ru-N-O bond angle as low as 120°.[4] It is more likely that the slightly bent Ru-N-O bond angle of [(($OMe)_2$bpb)Ru(NO)(Resf)] is a result of less extensive π-bonding due to the enhanced electron donation from the PDA moiety to the Ru center. However, the shorter Ru–N5(O) (1.729(4) Å) and longer N5–O5 (1.169(4) Å) bonds lengths of [(($OMe)_2$bpb)Ru(NO)(Resf)] compared to those of [(Me_2bpb)Ru(NO)(Resf)] (1.7347(16) 5 and 1.159(2) Å respectively) would suggest increased π*-backbonding interaction between the Ru and NO groups in the methoxy substituted nitrosyl.[16] However, an opposite trend was noted in the structures of the quinoline containing nitrosyls [(($OMe)_2$bQb)Ru(NO)(Resf)] (Ru-N5(O) = 1.7425(19) Å) and [(Me_2bQb)Ru(NO)(Resf)] (1.729(7) Å).[16] It was postulated in the initial report of these nitrosyls that the discrepancy in the Ru-N5(O) bond length maybe a result of the increased electron donating capacity of the methoxy groups. This is unlikely given the conflicting results reported with the pyridine based nitrosyls. Such conflicting observations indicate that the complexed nature of the Ru-NO bond requires a more holistic and in-depth evaluation of such features to provide substantial insight regarding their origin and significance which is beyond the breadth of this report.

A.6.2 Structural Characterization of [(($OMe)_2$IQ1)Ru(NO)(Resf)]

The X-ray crystal structure of [((OMe)$_2$IQ1)Ru(NO)(Resf)] is shown in Figure A.7. As predicted, the (OMe)$_2$IQ1^{2-} ligand occupies the equatorial plane of Ru with the IQ1 rings positioned away from each other facilitating a nearly planar ligand geometry. Similar to the structure of [((OMe)$_2$bpb)Ru(NO)(Resf)], the resorufin dye coordinates the axial site *trans* to NO through the phenolato-O donor with a Ru-O6-C(Resf) bond angle of 126.3(2)^o and is positioned parallel to the rings of one of the IQ1 groups. Again, the IQ1 group is angled below the equatorial plane towards the plane of the Resf rings likely to facilitate *π*-stacking interactions between the IQ1 and Resf rings. However, this tilting is not nearly as dramatic as the in-plane distortion caused by the steric interaction of the Q rings of [((OMe)$_2$bQb)Ru(NO)(Cl)].[16] The Ru-NO unit of [((OMe)$_2$IQ1)Ru(NO)(Resf)] is nearly linear with a Ru-N5-O5 bond angle of 176.5^O and Ru–N5(O) and N5–O5 bond lengths of 1.732(3) Å and 1.167(3) Å, similar to Ru-NO unit of [((OMe)$_2$bQb)Ru(NO)(Resf)].[16]

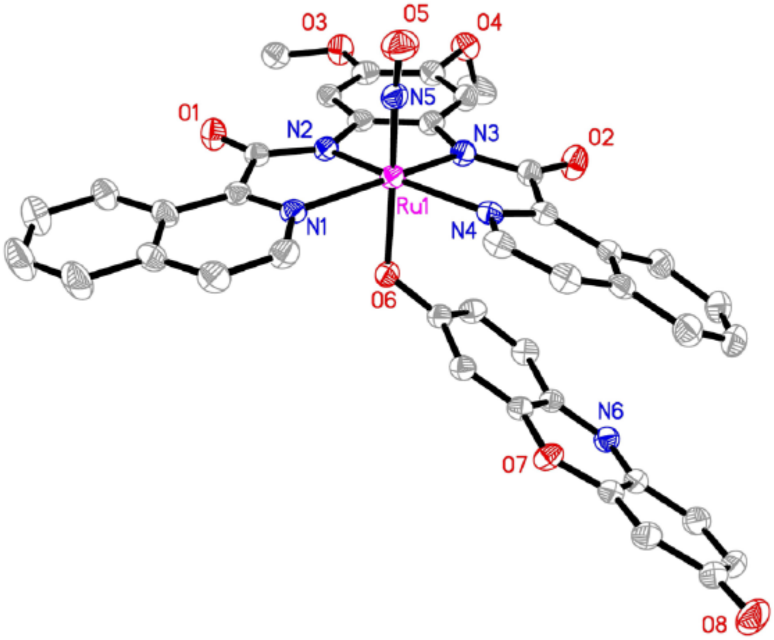

Figure **A.7 -** Thermal ellipsoid (probability level 50%) plot of [((OMe)$_2$IQ1)Ru(NO)(Resf)] with selected atom-labeling. H atoms are omitted for the sake of clarity.

A.6.3 Electron Absorption Spectra of [((OMe)$_2$bpb)Ru(NO)(Resf)] and [((OMe)$_2$IQ1)Ru(NO)(Resf)]

Substitution of the chloride ligands with the dye chromofore, resorufin, greatly enhanced the visible light sensitivity of [((OMe)$_2$bpb)Ru(NO)(Resf)] and [((OMe)$_2$IQ1)Ru(NO)(Resf)]. In contrast to the clear difference in the electronic absorption spectra of the Cl$^-$ bound conjugates (Figure 2.5), the dye-bound conjugates were found to have remarkably similar absorption bands of ε_{495} = 29 000 M^{-1}cm^{-1} and 31 000 M^{-1}cm^{-1} in MeCN for [((OMe)$_2$bpb)Ru(NO)(Resf)] and [((OMe)$_2$IQ1)Ru(NO)(Resf)], respectively (Figure A.8). Interestingly, the spectra for the dye-bound nitrosyls is quite different than that for the deprotonated, free dye (Resf$^-$, ε_{590} = 105 000 M^{-1} cm^{-1} in DMF). Coordination of the dye to the positively charged metal center results in a dramatic blue shift of the visible light absorption band with a concomitant reduction in the extinction coefficient. Similar results are observed upon protonation of Resf (ε_{470} = 20 000 M^{-1} cm^{-1} in DMF). This phenomena has been previously explained by the loss of the negative charge on the phenolato-O atom which was delocalized over the entire heterocyclic *π*-system of the dye rings.[15]

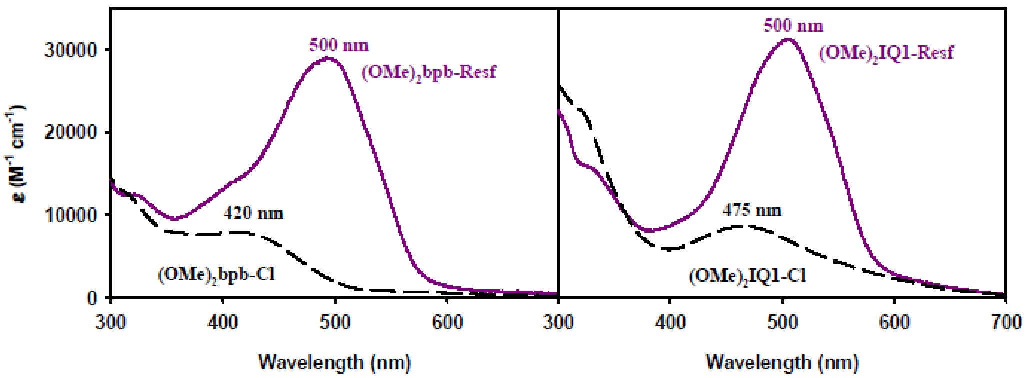

Figure **A.8** - Electronic absorption spectra for the Cl^- and dye-bound nitrosyls, $[((OMe)_2bpb)Ru(NO)(Cl)]$ and $[((OMe)_2bpb)Ru(NO)(Resf)]$ (left panel) and $[((OMe)_2IQ1)Ru(NO)(Cl)]$ and $[((OMe)_2IQ1)Ru(NO)(Resf)]$ (right panel).

Comparison of the electronic absorption spectra of the methoxy substituted dye-nitrosyl conjugates with those of the methyl substituted dye-nitrosyls reveals a uniform shift in the λ_{max} of the photoband to ~500 nm upon dye coordination to the Ru centers. However, a significant reduction in the ε_{max} values of the methyl substituted derivatives is observed compared with those of the methoxy substituted nitrosyls. Thus, the λ_{max} of the Resf-nitrosyl conjugates appears to be independent of contributions from the nitrosyl, while the ε values at λ_{max} vary significantly based on the donor strength of the PDA moiety with the methyl substituted nitrosyls $[(Me_2bpb)Ru(NO)(Resf)]$ and $[(Me_2bQb)Ru(NO)(Resf)]$ having ε_{max} values around 12 000 M^{-1} cm^{-1} and the methoxy substituted nitrosyls $[((OMe)_2bQb)Ru(NO)(Resf)]$, $[((OMe)_2bpb)Ru(NO)(Resf)]$, and $[((OMe)_2IQ1)Ru(NO)(Resf)]$ having ε_{max} values around 30 000 M^{-1} cm^{-1} (Figure A.9).[14,16] Although the planarity of the ligand frame had a substantial effect on the ε values of the photoband of the Cl^- bound nitrosyls (described above), ligand planarity seemed to have little effect on the visible light absorption efficiency of the dye-sensitized nitrosyls.

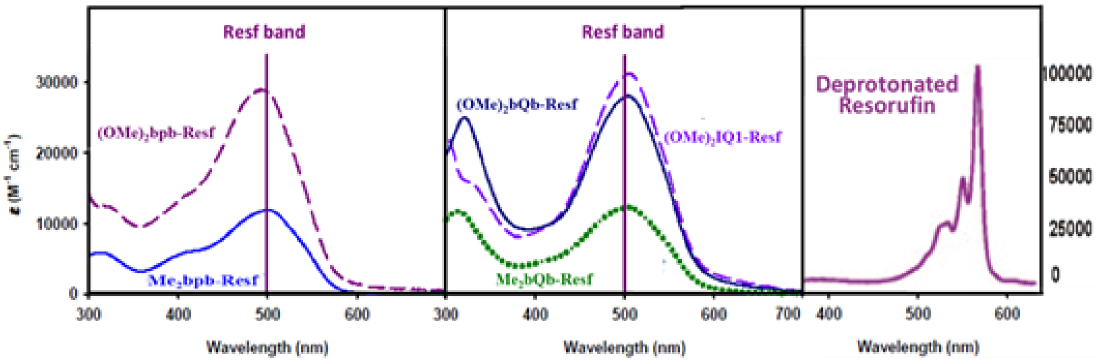

Figure **A.9 -** Electronic absorption spectra in $CHCl_3$ of dye-sensitized nitrosyls with (left) pyridine-based equatorial ligand frames, [(Me_2bpb)Ru(NO)(Resf)][18] and [($(OMe)_2$bpb)Ru(NO)(Resf)], and (middle) quinoline-based equatorial ligand frames, [(Me_2bQb)Ru(NO)(Resf)],[16] [($(OMe)_2$bQb)Ru(NO)(Resf)][15] and [($(OMe)_2$IQ1)Ru(NO)(Resf)]. (right) Electronic adsorption spectra of free, deprotonated Resorufin dye in DMF.

A.6.4 Stability of Dye-Bound Metal Nitrosyls in Aqueous Solvents

Although the Ru-Resf bonds of the dye-bound nitrosyls are indefinitely stable in weakly coordinating aprotic solvents like $CHCl_3$ and MeCN, the Ru-dye bonds slowly break when the conjugates are dissolved in aqueous solution and other coordinating solvents such as DMSO over a period of several hours. Quantitative time-course measurements of the loss of Resf from the dye bound nitrosyls were performed using UV-Vis spectroscopy. However, at physiologically pH (7.4) Resorufin (pKa ~ 6) is present in both its protonated (~4% of total Resf, λ_{max} =480 nm) and deprotonated forms (λ_{max} =571 nm) with considerable overlapping of the protonated dye bands with those of the dye-bound nitrosyls (λ_{max} ~ 500 nm). Therefore, only the concentration of deprotonated dye could be measured with certainity to obtain an estimate of the rate of dye release from the nitrosyls. Despite these limitations, the values obtained were sufficient to demonstrate a significant increase in the stability of the Ru-Resf bond upon relief of the in-plane ligand twist. For example, when the nitrosyl [((OMe)$_2$bQb)Ru(NO)(Resf)] was dissolved in an aqueous solution at pH 7.4, the nitrosyl lost ~20% of the bound Resf dye after 1 h,[16] while the IQ1 based nitrosyl, [((OMe)$_2$IQ1)Ru(NO)(Resf) lost only ~10% of its bound Resf dye after 1 h in the same solution. Interestingly, the pyridine containing nitrosyl, [((OMe)$_2$bpb)Ru(NO)(Resf)], lost even less bound dye, with only 5% of the bound dye observed in soluation after 1 h. These values demonstrate a significant increase in the stability of the Ru-Resf bond in protic media through the removal of the in-plane ligand twist.

A.7 Visible Light Triggered NO-Photorelease from the Cl$^-$ and Dye-bound Metal Nitrosyls

The photorelease of NO from the Cl$^-$ and dye-bound metal nitrosyls in 50:50 H_2O/MeCN media was monitored using an NO-sensitive electrode while the quantum yield values for NO release from the dye-bound nitrosyls was obtained by monitoring changes in the UV-vis spectra of the nitrosyls in DMF following exposure to 500 nm monochromatic light for select periods of time. The release of NO from the photoactive nitrosyls is initiated by the absorption of a photon within a range of wavelengths that stimulate an electronic transition to an excited state that relaxes through a ligand substitution reaction between NO and a solvent molecule resulting in the formation of free NO and the Ru(III) photoproduct (Ru(III)-solv) (Eq 2).

$$\text{Ru-NO} + \text{solv} + h\nu \rightarrow \text{Ru(III)-solv} + \text{NO}^{\cdot} \qquad (2)$$

Exposure of the Cl^- and dye-bound nitrosyls [$((OMe)_2bpb)Ru(NO)(X)$] and [$((OMe)_2IQ1)Ru(NO)(X)$] (where X is Cl or Resf) to brief periods of polychromatic light in a solution of H_2O/MeCN resulted in rapid NO photorelease to the surrounding media (as measured by the response of the NO-sensitive electrode (Figure 2.10, inset)). Prolonged exposure of the solution to the same light resulted in saturation of the H_2O/MeCN media with $NO^{\cdot}$ generating a steady current from the NO-sensitive electrode until a slow decay in the electrode response began upon complete photolysis of the Ru nitrosyls and the dissipation/oxidation of the total dissolved NO. The formation of a Ru(III) photoproduct from the electrode measured NO photorelease was confirmed by the appearance of an absorption band with $\lambda_{max} \sim 700$ nm in the electronic absorption spectra which had been previously assigned to a LMCT of the Ru(III) photoproduct.

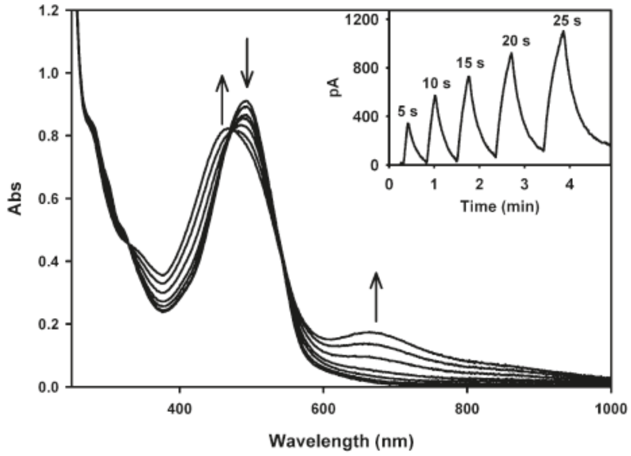

Figure **A.10** - Changes in the electronic absorption spectrum of [((OMe)$_2$IQ1)Ru(NO)(Resf)] in MeCN following illumination with visible light. Inset: NO-amperogram of [((OMe)$_2$IQ1)Ru(NO)(Resf)] in MeCN/H_2O exposed to increasing periods of light, as indicated (in seconds).

Formation of a Ru(III) photoproduct is essential to prevent recombination of the released NO (as seen in NO releasing metal porphyrins) and driven by the presence of strong σ-donors. The absorption band of the Ru(III) photoproduct (~700 nm) was used to measure the progress of the NO releasing photoreaction during measurement of the quantum yield values for the dye-bound nitrosyls. The quantum yield values for NO photorelease from the dye-bound nitrosyls in DMF upon illumination with 500 nm light in DMF were ϕ_{500} = 0.0052, 0.012, 0.206 and 0.270 for [(Me$_2$bpb)Ru(NO)(Resf)],[18] [((OMe)$_2$bpb)Ru(NO)(Resf)], [((OMe)$_2$bQb)Ru(NO)(Resf)],[16] and [((OMe)$_2$IQ1)Ru(NO)(Resf)], respectively. The observed trend in the quantum yield values of NO photorelease from the dye-bound nitrosyls was attributed to the spectral overlap between the photobands of the parent nitrosyl and the bound dye (λ ~ 500 nm). This is easily ascertained by measuring the absorption coefficient at 500 nm (ε_{500}) of the Cl^- bound nitrosyls which increased in the order: [(Me$_2$bpb)Ru(NO)(Resf)][18] < [((OMe)$_2$bpb)Ru(NO)(Cl)] < [((OMe)$_2$bQb)Ru(NO)(Cl)][16] < [((OMe)$_2$IQ1)Ru(NO)(Cl)] (as shown in Figure A.9). Thus, even though the λ_{max} of [((OMe)$_2$bQb)Ru(NO)(Cl)] was the most red-shifted at

490 nm the increased intensity of the photoband of [((OMe)$_2$IQ1)Ru(NO)(Cl)] at 500 nm resulted in a higher quantum yield for the IQ1 nitrosyl with λ_{max} = 475 nm. Thus, while the λ_{max} of the NO releasing photoband of dye-nitroysl conjugates is a useful metric in the design and development of new nitrosyl adducts, comparison of the photoactivity of dye-nitrosyl conjugates requires assessment of the molar absorptivity in the desired spectrum or more importantly the assessment of the quantum yield of NO photorelease for the desired wavelength(s).

A.8 Fluorescence Properties of Free-Dye and Metal Bound-Dye

Due to the intense fluorescence of free Resf dye in solution with pH > 6 ($\lambda_{max, fl}$ = 585 nm), it was expected that any residual fluorescence from Resf after coordination of the fluorophore to the Ru center would be sufficient to allow tracking of the nitrosyl-dye conjugate during therapeutic delivery. While significant quenching of the Resf fluorescence (~90%) occurs upon coordination to Ru as a result of the sufficient transfer of energy from Resf to the Ru-NO unit, solutions of both [((OMe)2bpb)Ru(NO)(Resf)] and [((OMe)2IQ1)Ru(NO)-(Resf)] in MeCN still exhibited broad red fluorescence emission bands of moderate intensity at 593 nm (Figure A.11). Indeed, similar fluorescence observed from [(Me$_2$bpb)Ru(NO)(Resf)] was sufficient to track the NO donor in cellular culture during the targeted NO delivery to cancer cells.[16] The loss of fluorescence upon NO delivery was also observed in this experiment serving as visual confirmation of NO delivery to the cellular targets. This was a vital observation linking the subsequent apoptosis of the treated cancer cells to the action of photoreleased NO.

The decrease in fluorescence as a marker for an event (as seen upon NO release from the Resf-nitrosyls) is deemed *turn-OFF* fluorescence signaling. The turn-off fluorescence observed upon NO photorelease from the dye-tethered nitrosyls is a result of the hemolytic breaking of the RU-NO bond during photorelease producing free NO· and a Ru(III)-solv photoproduct with a paramagnetic d^5 electronic configuration which effectively quenches all fluorescence from the bound Resf moiety. While *turn-ON* signaling is often preferred for quantitation of an event, the fluorescence of the NO bound nitrosyl-Resf adducts is useful to allow tracking of the nitrosyl to the targeted site before light activation in the treatment of localized malignancies and infection.

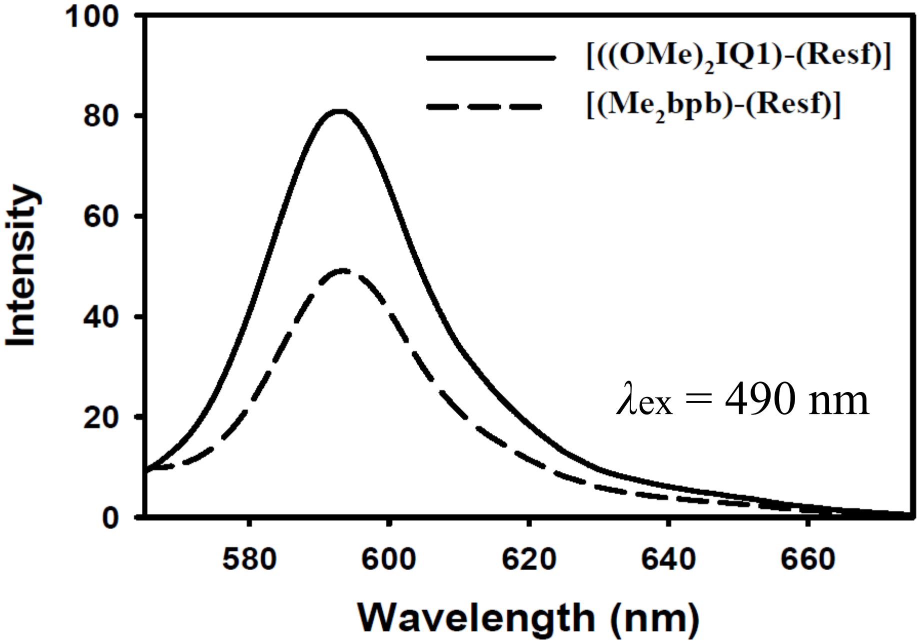

Figure **A.11** Fluorescence emission spectrum of [((OMe)$_2$IQ1)Ru(NO)(Resf)] and [(Me$_2$bpb)Ru(NO)(Resf)] in MeCN (λ_{ex}= 490 nm).

A.10 Conclusion

Two new sets of chloride-bound and Resf-bound $\{RuNO\}^6$ nitrosyls have been synthesized from two designed tetradentate ligands that allowed assessment of the effects of ligand twists in the equatorial plane of these nitrosyls. The structures of $[((OMe)_2bpb)Ru(NO)(Resf)]$, $[((OMe)_2IQ1)Ru(NO)(Cl)]$ and $[((OMe)_2IQ1)Ru(NO)(Resf)]$ have been determined by X-ray crystallography. Unlike previously reported $\{Ru\text{-}NO\}^6$ nitrosyls derived from R_2bQb^{2-} quinoline-based ligand frames that induce a twist in the equatorial ligand plane, the ligand frames in the present nitrosyls remain planar upon coordination to the Ru-center. Relief of the steric strain by the use of 1-isoquinoline moieties increases the stability of the nitrosyls in strongly coordinating solvents including water. Removal of the ligand twist also enhanced the sensitivity of the nitrosyls to visible light. As measured by the extinction coefficients and quantum yield values at 500 nm, addition of OMe substituents on the ligand frame and removal of steric interactions between the quinoline moieties of the ligand improved the sensitivity of the nitrosyls toward visible light. Thus, $[((OMe)_2IQ1)Ru(NO)(Resf)]$ exhibits the highest sensitivity to 500 nm light of the $\{Ru\text{-}NO\}^6$ nitrosyls reported from our laboratory to date. Direct coordination of the Resf dye to the Ru-center of the nitrosyls significantly quenched the fluorescence of the coordinated dye. However, the residual fluorescence of the Resf-bound nitrosyls however is sufficient for tracking the photoactive NO-donors in cellular targets. For example, the fluorescence intensity of $[((OMe)_2IQ1)Ru(NO)(Resf)])$ is similar to that of

[((OMe)$_2$IQ1)Ru(NO)(Resf)] (Figure A.11) which has already been used as trackable NO-donor in cellular studies.[16]

A.11 Experimental Section

Materials. NO gas was purchased from Spectra Gases Inc. and was purified by passing through a long KOH column prior to use. $RuCl_3 \cdot xH_2O$ (Aldrich Chemical Co.) was treated several times with concentrated HCl to prepare the starting metal salt, $RuCl_3 \cdot 3H_2O$. The solvents were dried by standard techniques and distilled. 1-Isoquinolinewas purchased from Wako Chemicals.1,2-Dimethoxy-4,5-diaminobenzene was synthesized according to the published procedure.[16] All other chemicals were purchased from Aldrich Chemical Co. and used without further purification.

Synthesis of Ligands. 1,2-Bis(pyridine-2-carboxamido)-4,5-dimethoxybenzene (H_2(OMe)$_2$bpb, H's are dissociable carboxamide protons). A mixture of 1,2-dimethoxy-4,5-diaminobenzene (0.51 g, 3.0mmol), 2 equiv of picolinic acid (0.74 g, 6.0mmol), and 2 equiv of $P(OPh)_3$ (1.87 g, 6.0 mmol) was dissolved in 20 mL of pyridine. The resulting green/brown solution turned amber after refluxing for 4 h. The solution was cooled and kept at 4°C overnight. The resulting tan precipitate was filtered and washed with EtOH and Et_2O and dried *in vacuo*. Yield: 1.04 g (55%). Selected IR bands (KBr disk, in cm-1): 3335 (w, ν_{NH}), 3285 (w), 1676 (s νCdO), 1662 (s), 1609 (w), 1527 (s), 1504 (s), 1480 (m), 1350 (m), 1210 (vs), 1093 (m), 997 (m), 751 (m), 671 (m). ^{1}H-NMR in $CDCl_3$, δ from TMS: 10.32 (s 2H), 8.57 (d2H), 8.32 (d2H), 7.91 (t 2H), 7.47 (m 4H), 3.94 (s 6H).

1,2-Bis(Isoquinoline-1-carboxamido)-4,5-dimethoxybenzene ($H_2(OMe)_2IQ1$, H's are dissociable carboxamide protons). A solution containing 1 equiv of 1,2-dimethoxy-4,5-diaminobenzene (1.27 g, 7.56 mmol), 2 equiv of 1-isoquinolinecarboxylic acid (2.62 g, 15.1 mmol), and 2 equiv of $P(OPh)_3$ (4.69 g, 15.10 mmol) was prepared in 40 mL of pyridine. The green solution turned bright red upon heating at 100°C for 4 h. The solution was partially condensed and stored at 4°C overnight. The resulting bright yellow-orange precipitate was filtered and washed several times with EtOH and Et_2O and dried *in vacuo*. Yield: 2.17 g (60%). Selected IR frequencies (KBr disk, in cm-1): 3296 (w, ν_{NH}), 1682 (s, $\nu_{C=O}$), 1526 (vs), 1478 (s), 1334 (w), 1205 (s), 1108 (w). ^{1}H-NMR in $CDCl_3$, δ from TMS: 10.46 (s 2H), 9.72 (d 2H), 8.40 (d 2H), 7.88 (d 2H), 7.82 (d 2H), 7.73 (t 4H), 7.53 (s H).

Syntheses of Metal Complexes. [$((OMe)_2bpb)Ru(NO)(Cl)$]. A pale yellow solution of $H_2(OMe)_2bpb$ (0.20 g, 0.53 mmol) in 20 mL of N,N-dimethylformamide (DMF) was treated with 2.1 equiv of NaH (0.03 g, 1.10 mmol) to generate a bright orange solution. A batch of 0.14 g (0.53 mmol) of $RuCl_3{\cdot}3H_2O$ was then added to the solution of deprotonated ligand, and the green mixture was heated to reflux temperature for 16 h. Next, it was cooled to room temperature and filtered to remove solid NaCl. The dark green filtrate was degassed and NO gas was bubbled through the solution at reflux temperature for 1 h. The resulting red/orange solution was cooled, and the solvent was removed *in vacuo*. The oily residue was triturated several times with MeCN to remove

DMF. The solid was finally washed with portions of MeCN (2 x 5 mL) and tetrahydrofuran (THF, 2 x 5 mL) to afford an orange-brown compound which was dried *in vacuo*. Yield: 0.21 g (72%). Anal. Calcd. for $C_{20}H_{16}ClN_5O_5Ru$:C 44.28, H 2.95, N 12.92; Found: C 44.53, H 3.01, N 12.89. Selected IR bands (KBr disk, in cm-1): 1845 (vs, ν_{NO}), 1631 (vs, $\nu_{C=O}$), 1596 (m), 1566 (w), 1497 (s), 1402 (m), 1368 (m), 1278 (w), 1254 (m), 1080 (w), 988 (w), 872 (w), 756 (w), 489 (w). UV/vis in DMF, λ in nm (ε in M^{-1} cm^{-1}): 319 (12 500), 420 (7 800). ^{1}H-NMR in $CDCl_3$, δ from TMS: 8.74 (d 2H), 8.49 (s 2H), 8.39 (d 2H), 8.24 (t 2H), 7.74 (t 2H), 3.98 (s 6H).

[($(OMe)_2$bpb)Ru(NO)(Resf)]. A mixture of [($(OMe)_2$bpb)Ru(NO)(Cl)] (0.10 g, 0.18 mmol) and 1 equiv of $AgBF_4$ (0.04g, 0.18 mmol) in 30 mL of MeCN was heated to reflux for 15 min and then a batch of 0.04 g (0.18 mmol) of resorufin (sodium salt) was added. The resulting red solution was heated to reflux for an additional 16 h. The red/orange mixture thus obtained was filtered and concentrated under vacuum and then stored at 4^{o}C for 12 h. The red precipitate thus obtained was filtered and washed with ether (2 x 5 mL). Yield: 0.04 mg (27%). Anal. Calcd. for $C_{32}H_{22}N_6O_8Ru$: C 53.41, H 3.06, N 11.68; Found: C 53.37, H 3.12, N 11.89. Selected IR bands (KBr disk, in cm-1): 1831 (s, ν_{NO}), 1630 (vs, $\nu_{C=O}$), 1592 (vs), 1485 (vs), 1403 (m), 1370 (m), 1322 (w), 1272 (s), 1205 (m), 1102 (m), 1082 (m), 863 (m), 758(w), 683 (w), 588 (w), 493 (m).UV/vis in MeCN, λ in nm (ε in M^{-1} cm^{-1}): 402 (14 600), 495 (29 000). ^{1}H-NMR in $CDCl_3$, δ from TMS: 8.75 (d 2H), 8.52 (d 2H), 8.32 (s 2H), 8.13 (t 2H), 7.81 (t 2H), 7.56 (t 2H), 7.30 (d 1H), 7.12 (2 1H), 6.72 (d 1H), 6.11 (s 1H), 6.08 (d 1H), 5.67 (s 1H), 4.00 (s 6H).

[((OMe)$_2$IQ1)Ru(NO)(Cl)]. A yellow solution of H$_2$(OMe)$_2$IQ1 (0.15 g, 0.31 mmol) in 20 mL of DMF was treated with 2.1 equiv of NaH (0.02 g, 0.67 mmol) to generate a red solution and to it was added a batch of 0.08 g (0.31 mmol) of RuCl$_3$·3H$_2$O. The dark brown mixture was then heated to reflux temperature for 20 h. Next, the green-brown solution was cooled to room temperature and filtered to remove NaCl. The filtrate was degassed, and NO gas was bubbled through it at reflux temperature for 2 h. The resulting red/maroon solution was cooled, and the solvent was removed in vacuo. The oily residue was triturated several times with MeCN to afford a redbrown solid. This solid was then stirred in hot MeCN and filtered to remove impurities. The dark maroon solid was finally washed with Et$_2$O and dried *in vacuo*. Yield: 0.16 g (80%). Anal. Calcd. for C$_{28}$H$_{20}$ClN$_5$O$_5$Ru: C 52.34, H 3.12, N 10.90; Found: C 52.12, H 3.22, N 10.53. Selected IR frequencies (KBr disk, in cm^{-1}): 2923 (w), 1832 (m ν_{NO}), 1614 (vs), 1585 (s), 1492 (s), 1253 (s), 1091 (s). 1HNMRin CDCl3, δ from TMS: 10.45 (d 2H), 8.72 (d 2H), 8.61 (s H), 8.06 (d 2H), 7.90 (d 2H), 7.93 (t 2H), 7.90 (t 2H), 4.05 (s 6H). UV/vis in DMF, λ in nm (ε in M^{-1} cm^{-1}): 290 (27 000), 320 sh (22 300), 475 (8 700).

[((OMe)$_2$IQ1)Ru(NO)(Resf)]. A solution of [((OMe)$_2$IQ1)Ru(NO)(Cl)] (0.13 g, 0.20 mmol) in 20 mL of MeCN was treated with AgBF$_4$ (0.04 g, 0.20mmol) and heated to reflux temperature for 3 h. Next, 0.05 g (0.20 mmol) of resorufin dye (as Na salt) was added neatly to the hot maroon solution and refluxed for 4 h. The resulting bright red solution was cooled to 4^{o}C, and the dark red precipitate was filtered. The dried precipitate was then redissolved in CH$_2$Cl$_2$ and filtered to remove AgCl and

$NaBF_4$. The filtrate was concentrated and loaded on a silica gel column. A CH_2Cl_2/THF gradient was used to elute the final product (40% THF). Yield: 0.08 g (45%). Anal. Calcd. for $C_{40}H_{26}N_6O_8Ru$:C58.61,H3.17,N10.26; Found:C58.45,H3.31, N 10.37. Selected IR frequencies (KBr disk, in cm-1): 1827 (vs, ν_{NO}), 1617 (s), 1580 (m), 1487 (s), 1323 (m), 1270 (s), 1266 (s), 1199 (m), 1095 (m), 849 (w), 491 (w). ^1H-NMR in $CDCl_3$, δ from TMS: 10.27 (d 2H), 8.78 (d 2H), 8.55 (s 2H), 8.14 (d 2H), 8.01 (d 2H), 7.92 (t 2H), 7.83 (t 2H), 7.24 (s 1H), 7.03 (d 1H), 6.72 (d 1H), 5.99 (s 1H), 5.97(d 1H), 5.36 (d 1H), 4.09 (s 6H).UV/vis in MeCN, λ in nm(ε in M^{-1} cm^{-1}): 330 (15 000), 495 (30 000).

Physical Measurements. The ^1H-NMR spectra were recorded at 298 K on a Varian Inova 500 MHz instrument. A Perkin-Elmer Spectrum-One FT-IR spectrometer was used to obtain the IR spectra of the complexes. Electronic absorption spectra were obtained with a scanning Cary 50 spectrophotometer (Varian Associates). NO photorelease from the nitrosyls in 50:50 solutions of MeCN/H_2O upon illumination was monitored using the in-NO Nitric Oxide Monitoring System (Innovative Instruments, Inc.) fitted with the ami-NO 2000 electrode. The NO amperograms were recorded in stirred solutions contained in open vials.

X-ray Crystallography. X-ray diffraction quality crystals (red blades) of [($(OMe)_2$bpb)Ru(NO)(Resf)] were obtained by vapor diffusion of diethyl ether into a solution of the nitrosyl in $CHCl_3$ at 4°C. Red crystals of [($(OMe)_2$IQ1)Ru(NO)(Cl)], suitable for diffraction study, were obtained via vapor diffusion of pentane into a solution of the nitrosyl in $CHCl_3$ at room temperature. X-ray diffraction quality red crystals of [((OMe)$_2$IQ1)Ru(NO)(Resf)] were obtained by vapor diffusion of diethyl ether into a CH_2Cl_2/THF solution of the nitrosyl at room temperature. Diffraction data for [((OMe)$_2$bpb)Ru(NO)(Resf)] · 2$CHCl_3$ · (0.5)Et_2O, [((OMe)$_2$IQ1)Ru(NO)(Cl)] · 2$CHCl_3$, and [((OMe)$_2$IQ1)Ru(NO)(Resf)] were collected at 150 K on a Bruker APEX-II instrument using monochromated Mo-Kα radiation (λ = 0.71073 Å). All diffraction data were corrected for absorption, and calculations were performed using the SHELXTL (1995-99) software package (Bruker Analytical X-ray Systems Inc.) for structure solution and refinement.

Photolysis Experiments. The quantum yield (ϕ) values were obtained using a tunable Apex Illuminator (150W xenon lamp) equipped with a Cornerstone 130 1/8 M monochromator (measured intensity of ~10 mW). Actinochrome N (475/610) was used to determine the quantum yield values at 500nm (ϕ_{500}). Solutions of the nitrosyls in DMF were prepared and placed in 2 x 10 mm quartz cuvettes, 1 cm away from the light source. All solutions were prepared to ensure sufficient absorbance (>90%) at the irradiation wavelength, and changes in the electronic spectra at 788, 650, 630, and 660 nm for [((OMe)$_2$bpb)Ru(NO)(Resf)], [((OMe)$_2$bpb)Ru(NO)(Resf)], [((OMe)$_2$IQ1)Ru(NO)(Cl)], and [((OMe)$_2$IQ1)Ru(NO)(Resf)], respectively (<10% photolysis), were used to determine the extent of photorelease of NO.

A.11 Experimental Data: IR and ^{1}H-NMR Spectra

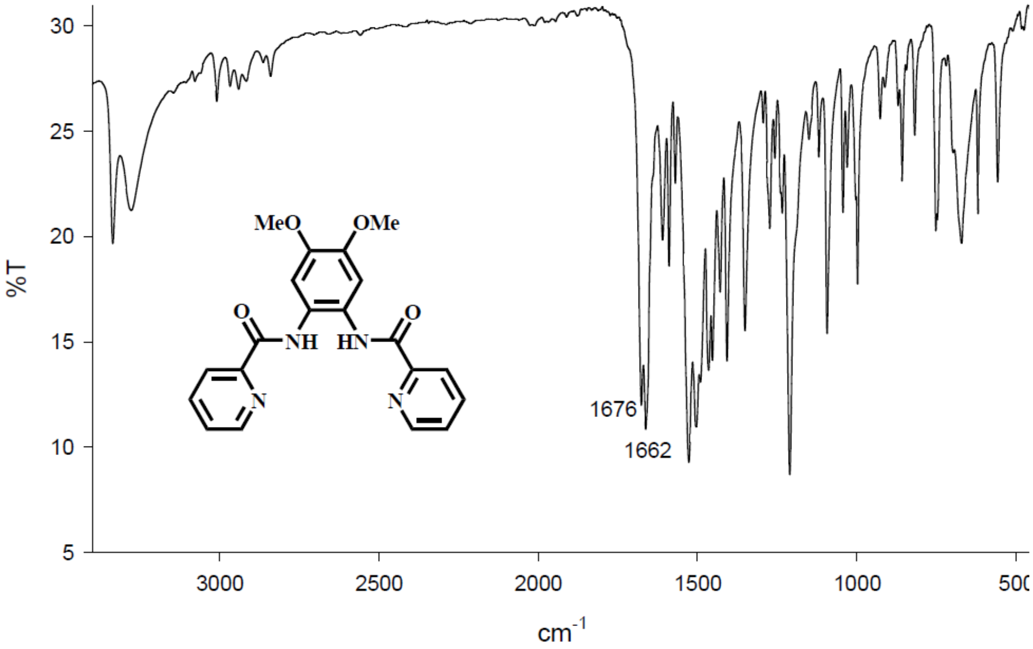

Figure **A.12** – IR spectra of $H_2(OMe)_2$bpb (KBr Pellet).

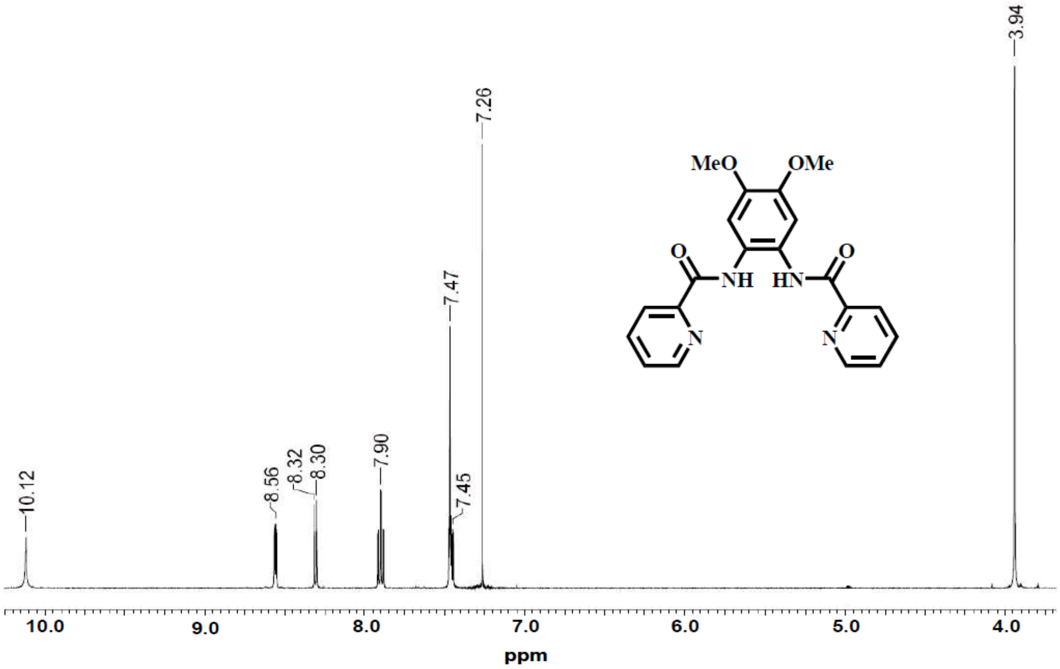

Figure **A.13** – ^{1}H-NMR spectra of $H_2(OMe)_2$bpb (3.8-10.5 ppm) in $CDCl_3$ at 298 K

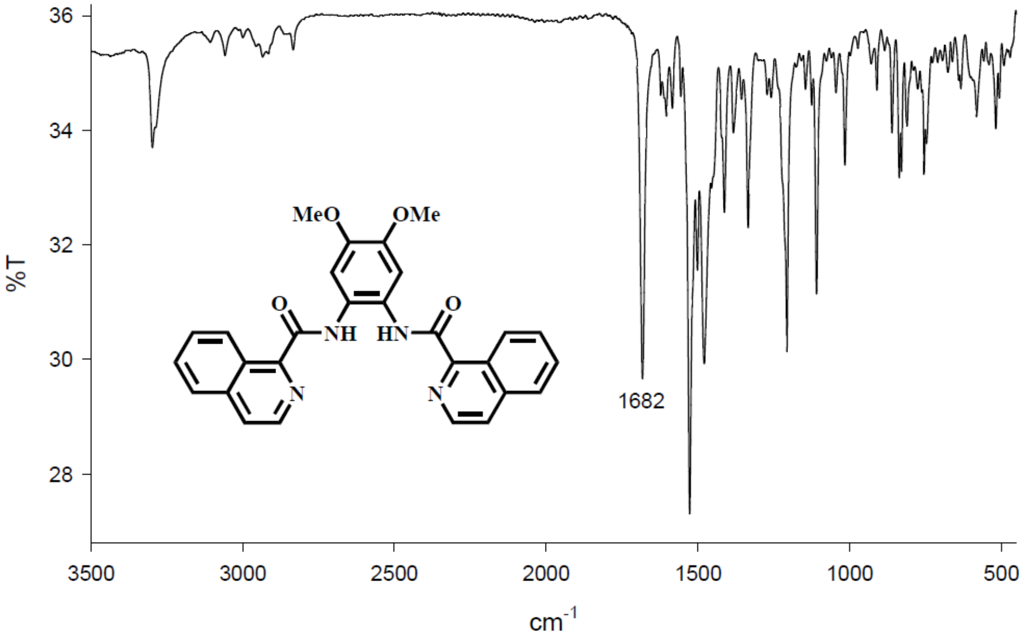

Figure **A.14** – IR spectra of $H_2(OMe)_2IQ1$ (KBr Pellet).

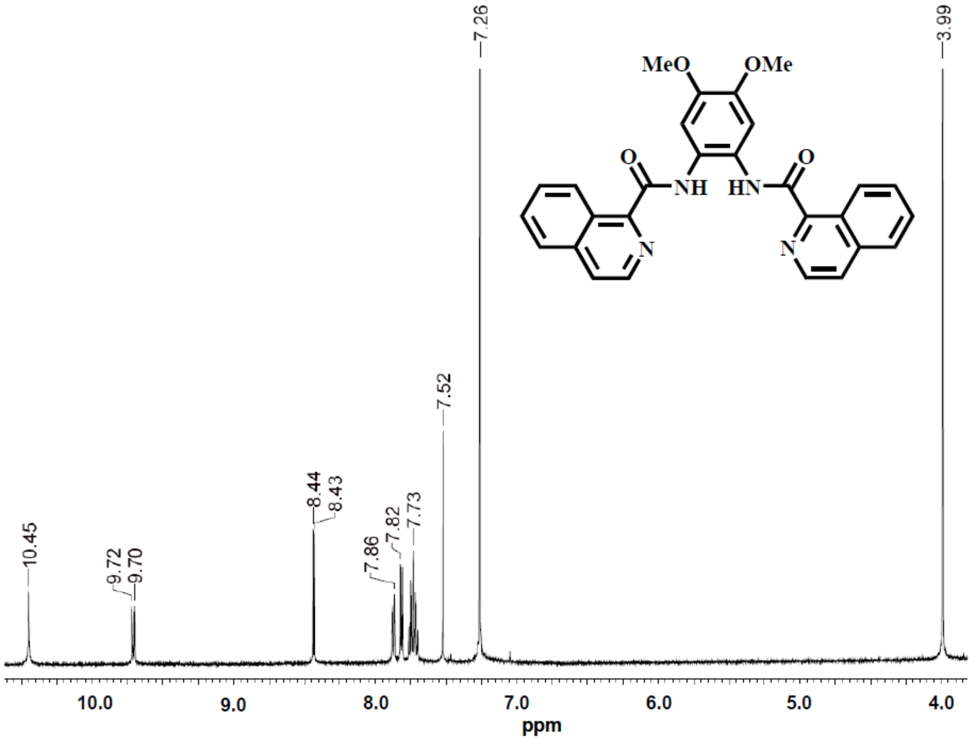

Figure **A.15** – ^{1}H-NMR spectra of $H_2(OMe)_2IQ1$ (3.8-10.5 ppm) in $CDCl_3$ at 298 K

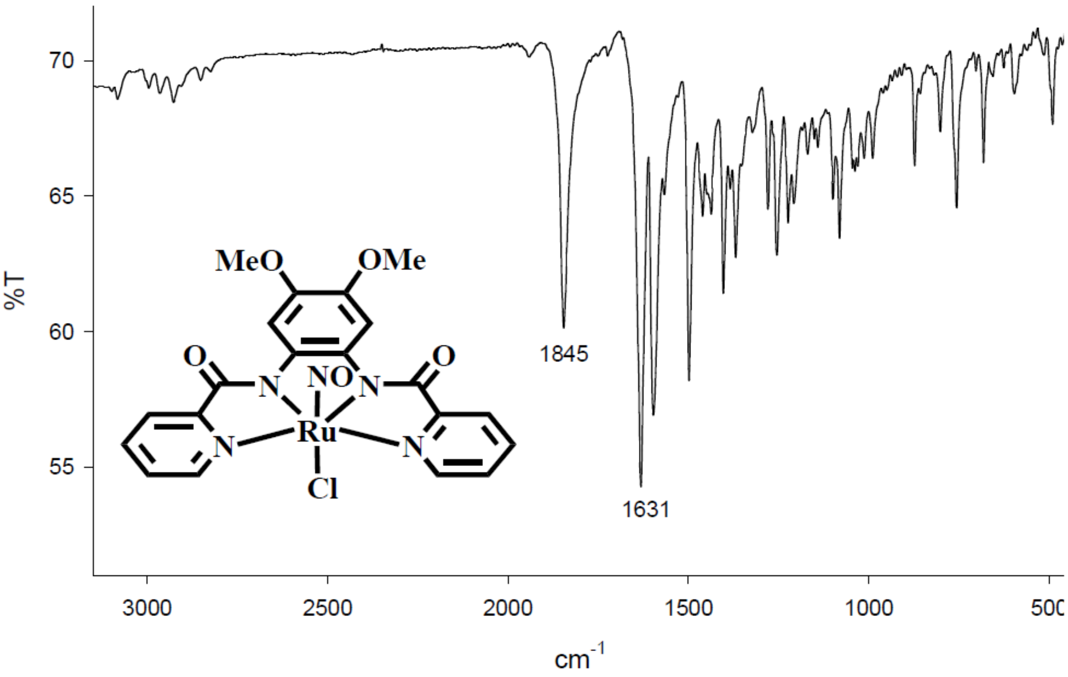

Figure **A.16** – IR spectra of [((OMe)$_2$bpb)Ru(NO)(Cl)] (KBr Pellet).

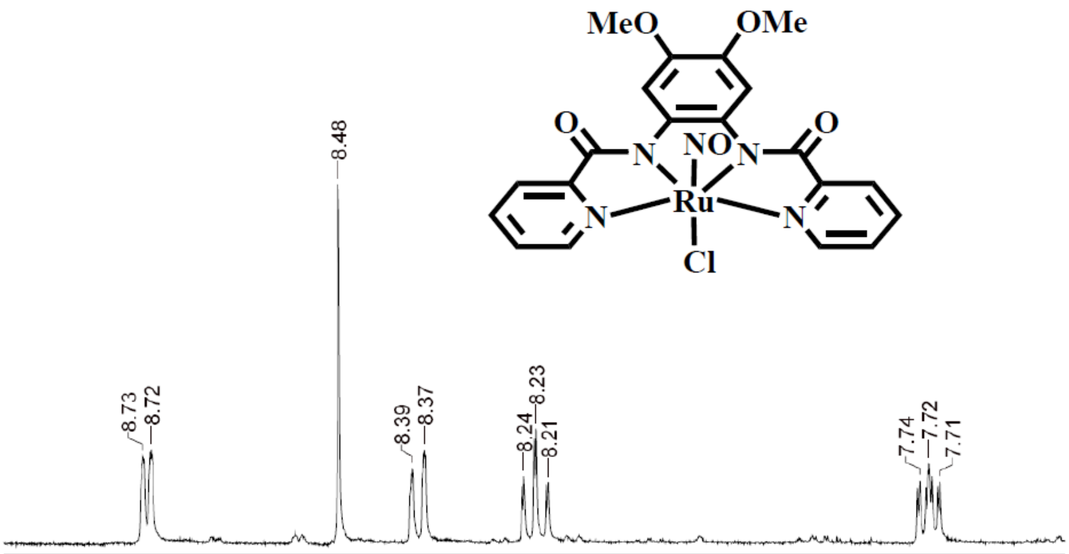

Figure **A.17** – ^{1}H-NMR spectra of [((OMe)$_2$bpb)Ru(NO)(Cl)] (3.8-10.5 ppm) in

CDCl$_3$ at 298 K.

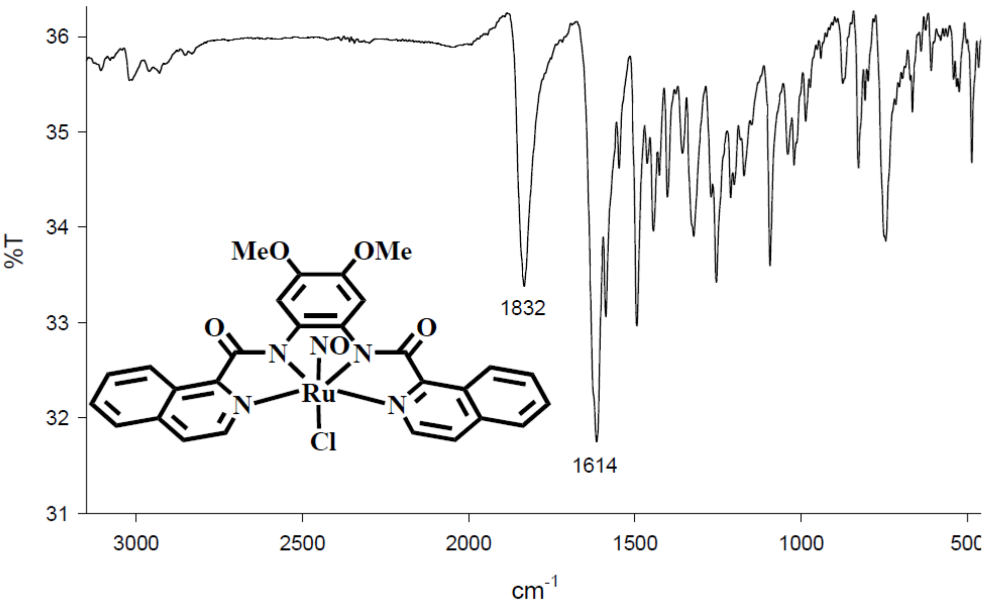

Figure **A.18** – IR spectra of [((OMe)$_2$IQ1)Ru(NO)(Cl)] (KBr Pellet).

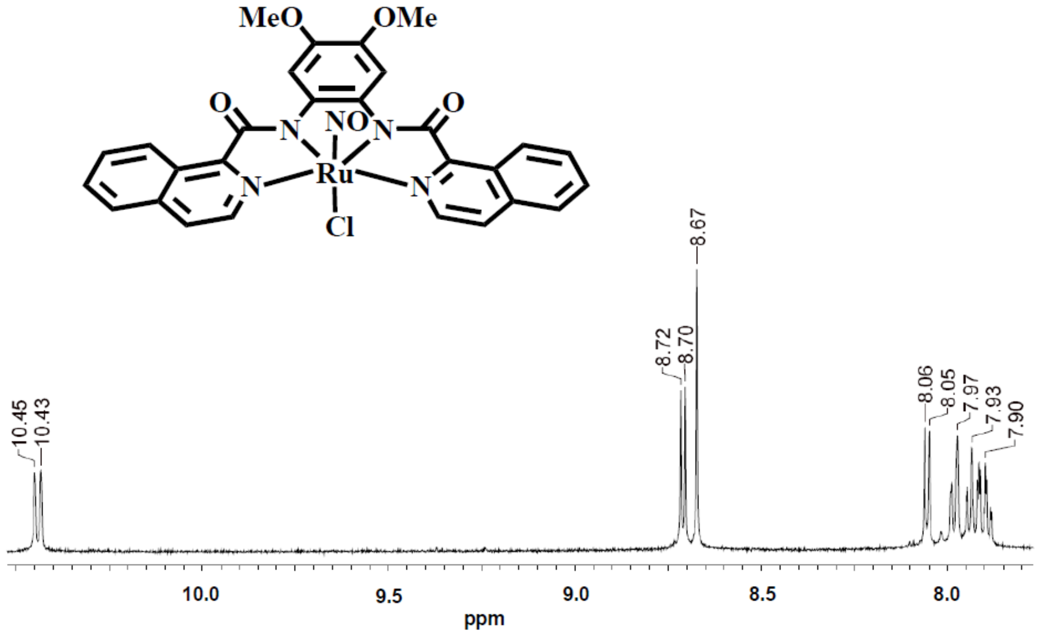

Figure **A.19** - ^{1}H-NMR spectrum (7.7-11.0 ppm) of [((OMe)$_2$IQ1)Ru(NO)(Cl)] in CDCl$_3$ at 298 K

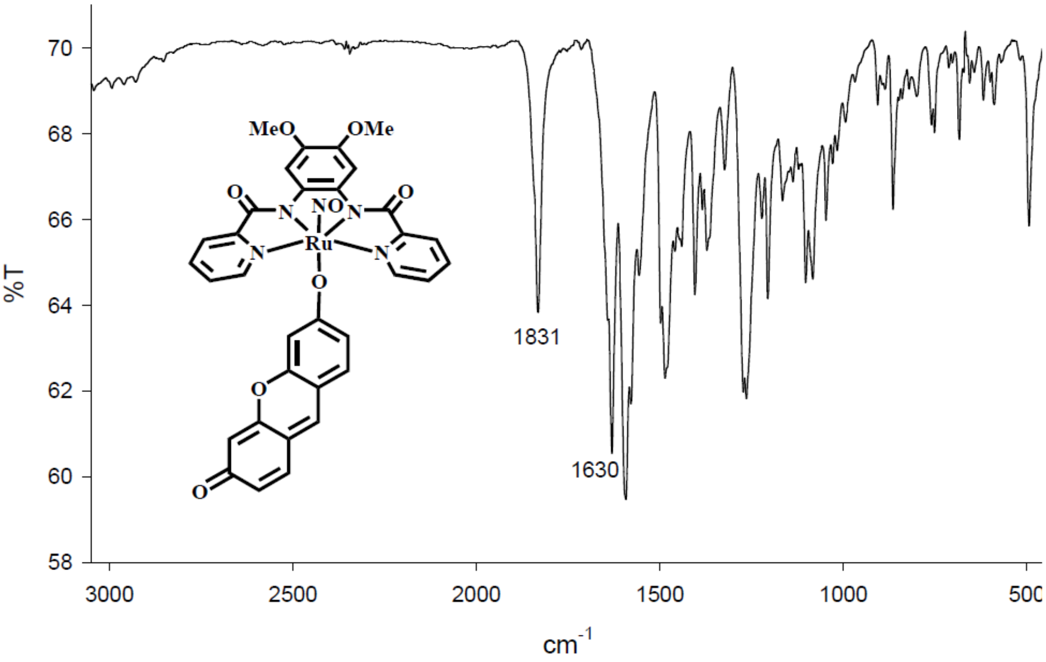

Figure **A.20 -** IR spectrum of [((OMe)$_2$bpb)Ru(NO)(Resf)] (KBr pellet).

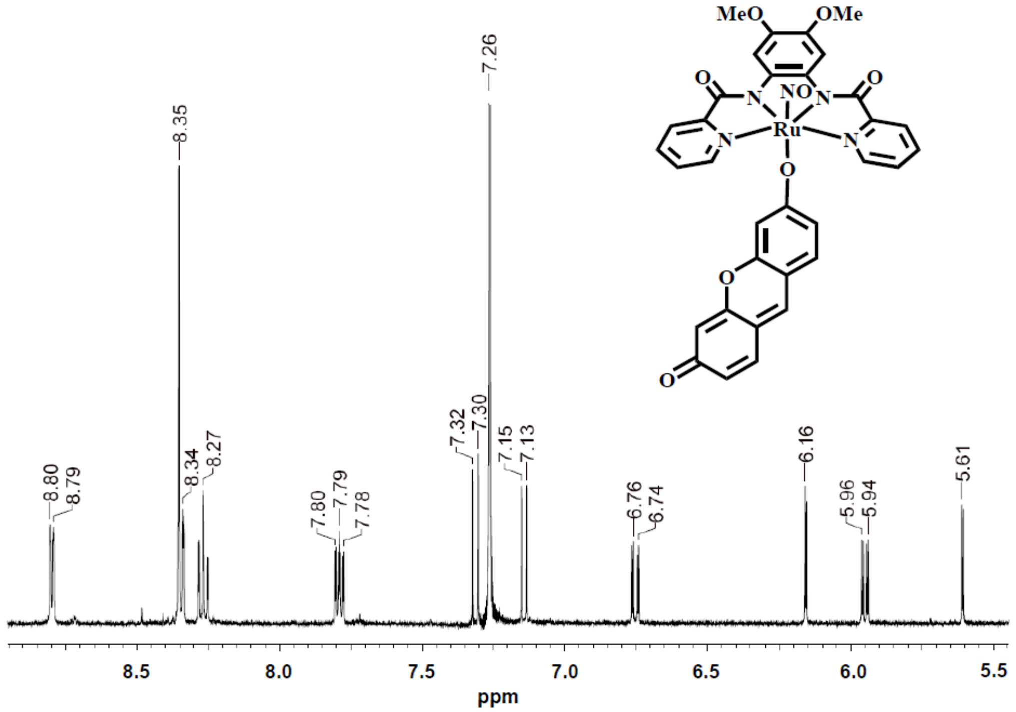

Figure **A.21 -** ^{1}H-NMR spectrum (5.5-9.0 ppm) of [((OMe)$_2$bpb)Ru(NO)(Resf)] in CDCl$_3$ at 298 K.

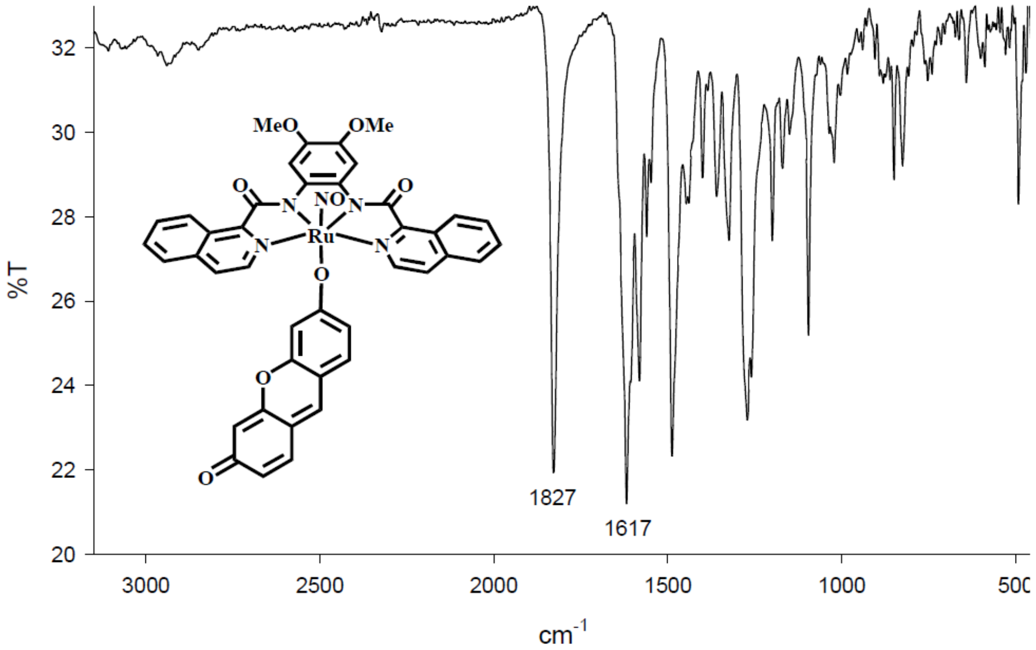

Figure **A.22 -** IR spectrum of [((OMe)$_2$IQ1)Ru(NO)(Resf)] (KBr pellet).

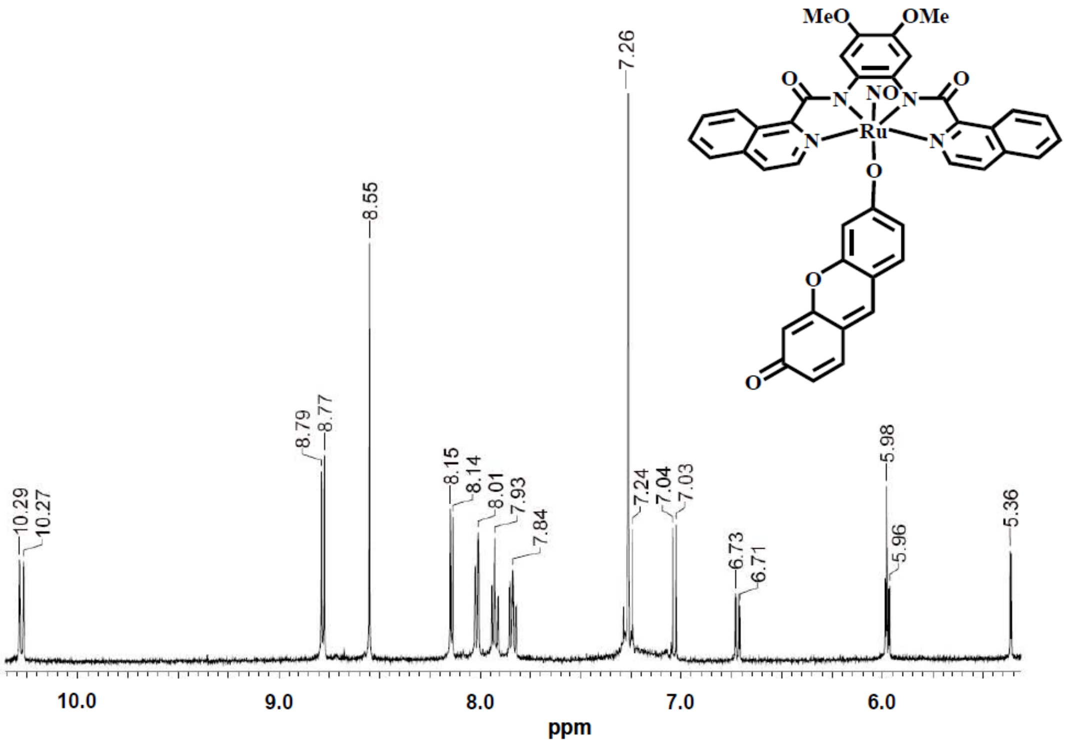

Figure **A.23 -** ^{1}H-NMR spectrum (5.1-10.4 ppm) of [((OMe)$_2$IQ1)Ru(NO)(Resf)] in CDCl$_3$ at 298 K.

A.12 References

1. a) Rose, M.J. Mascharak, P.K. *Coord. Chem. Rev.* **2008**, *252*, 2093–2114. b) Bratsos, I. Jedner, S. Gianferrara, T. Alessio, E. *Chimia*. **2007**, *61*, 692–697. c) L.J. Ignarro, Nitric Oxide: Biology and Pathobiology, Academic Press, San Diego, 2000.

2. C.K. Jorgensen, Absorption Spectra and Chemical Bonding, Pergamon Press, 1961.

3. J.H. Enemark, R.D. Feltham, Coord. Chem. Rev. **1974**, *13*, 339-406.

4. a) Quinby, M. S. and Feltham, R. D. *Inorg. Chem.* **1972**, *11,* 2468. b) Fenske, R.F. and DeKock, R.L. *Inorg. Chem*., **1972**, *11*, 437.

5. Manoharan, P.T. and Gray, H-B. *Inorg. Chem*. **1966**, *5*, 823.

6. a) Rowland, J. M. Olmstead, M. M. Mascharak, P. K. *Inorg. Chem.* **2001**, *40*, 2810-2817. b) Patra, A.K. Afshar, R.K. Olmstead, M.M. Mascharak, P.K. *Angew. Chem. Int. Ed*. **2002**, *41*, 2512–2515.
7. a) Patra, A.K. Rowland, J.M. Marlin, D.S. Bill, E. Olmstead, M.M. Mascharak, P.K. *Inorg. Chem*. **2003**, *42*, 6812–6823. b) Mascharak, P. K. *Coord. Chem. Rev.* **2002**, *225*, 201-214.
8. Patra, A.K. Mascharak, P.K. *Inorg. Chem.* **2003**, *42*, 7363–7365.

9. a) Richter-Addo, G.B. Legzdins, P. Metal Nitrosyls*,* Oxford University Press, **1992**. b) Ford, P.C. Bourassa, J. Miranda, K. Lee, B. Lorkovic, I. Boggs, S. Kudo, S. Laverman, L. *Coord. Chem. Rev.* **1998**, *171*, 185-212. c) Rose, M. J. Mascharak, P. K. *Curr. Opin. Chem. Biol.* **2008***, 12,* 238-244. d) Tfouni, E. Krieger, M. McGarvey, B. R. Franco, D.W. *Coord. Chem. Rev.* **2003**, *236*, 57–69.

10. Szundi, I. Rose, M.J. Sen, I. Eroy-Reveles, A.A. Mascharak, P.K. Einarsdottir, O. *Photochem. Photobiol*. **2006**, *82*, 1377–1384.

11. Madhani, M. Patra, A.K. Miller, T.W. Eroy-Reveles, A.A., Hobbs, A. Fukuto, J.M. Mascharak, P.K. *J. Med. Chem*. **2006**, *49*, 7325–7330.

12. a) Ghosh, K. Eroy-Reveles, A. A. Holman, T. R. Olmstead, M. M. Mascharak, P. K. *Inorg. Chem.* 2004, **43**, 2988. b) Eroy-Reveles, A. A. Leung, Y. Beavers,

C. M. Olmstead, M. M. Mascharak, P. K. *J. Am. Chem. Soc.* 2008, **130**, 4447. c) Hoffman-Luca, C. G. Eroy-Reveles, A. A. Alvarenga, J. Mascharak, P. K. *Inorg. Chem.* 2009, **48**, 9104. d) Afshar R.K. Patra, A.K. Mascharak, P.K. *J. Inorg. Biochem*. **2005**, *99*, 1458–1464.

13. Patra, A.K. Rose, M.J. Olmstead, M.M. Mascharak, P.K *J. Am. Chem. Soc.* **2004**, *126*, 4780-4781.
14. Patra, A.K. Rose, M.J. Murphy, K. Olmstead, M.M. Mascharak, P.K. *Inorg. Chem.* **2004**, *43*, 4487-4495.
15. Fry, N. L. Rose, M. J. Rogow, D. L. Nyitray, C. Kaur, M. Mascharak, P. K. *Inorg. Chem*. **2010**, *49*, 1487–1495.
16. Rose, M. J. Fry, N. L. Marlow, R. Hink, L. Mascharak, P. K. *J. Am. Chem. Soc.* **2008**, *130*, 8834–8846.
17. Fry, N.L. Mascharak, P.K. *Acc. Chem. Res*. **2011**, *44*, 289–298.
18. Rose, M.J. Olmstead, M.M. Mascharak, P.K. *J. Am. Chem. Soc.* **2007**, *129*, 5342–5343.
19. Wecksler, S.R. Hutchinson, J. Ford, P.C. *Inorg. Chem.* **2006**, *45*, 1192.
20. Conrado, C.L. Wecksler, S. Egler, C. Magde, D. Ford, P.C. *Inorg. Chem*. **2004**, *43*, 5543.